CERN-Proceedings-2012-001
5 March 2012

Organisation Européenne pour la Recherche Nucléaire
CERN European Organization for Nuclear Research

Proceedings of the 6$^{\text{th}}$ International Workshop on High-p_{T} Physics at the LHC

Edited by: K. Eskola, M. van Leeuwen, P. Lévai, A. Morsch, T. Peitzmann, J. Rak

ISBN 978-92-9083-373-4
ISSN 2078-8835

This Report should be cited as:
K. Eskola, M. van Leeuwen, P. Lévai, A. Morsch T. Peitzmann, J. Rak (Eds.), *Proceedings of the* 6^{th} *International Workshop on High-*p_{T} *Physics at the LHC*
CERN-Proceedings-2012-001 (CERN, Geneva, 2012).

Contents

1. Introduction

The International Workshop on High-p_T Physics at the LHC is a series of workshops with a limited number of participants, where various aspects of high-p_T physics in QCD at high energies are discussed. The 6th edition of this workshop took place 4-7 April 2011, in Utrecht, The Netherlands. This edition of the workshop was marked by the first results from heavy-ion running at the LHC, which sparked some lively discussions between experts from RHIC and the LHC.

We look back at a successful workshop, which consisted of 40 plenary presentations, with ample room for discussion. There was a number of shorter (20 minutes) presentations, as well as overviews from most experiments on light and heavy flavour measurements, including jets and a session on dimuon and J/ψ results. On Wednesday morning, there was a short session about future electron-ion colliders and saturation physics. At the end of the workshop, we had a few presentations about detector upgrades for particle identification in ALICE.

The organisers would like to thank all the participants for making this workshop a success. We are also grateful for support from FOM and Nikhef of the Netherlands.

Marco van Leeuwen, Thomas Peitzmann,
Kari Eskola, Péter Lévai,
Andreas Morsch, Jan Rak

High p_T particle production, hard scattering and correlations from the PHENIX Experiment

V.S. Pantuev for PHENIX Collaboration

Abstract. We present recent results from the PHENIX Experiment at RHIC on hard scattering processes in nucleus-nucleus collisions.

PHENIX extends the transverse momentum range for inclusive identified particle production by measurering η-meson spectrum for p_T up to 20 GeV/c. At such a high momentum cluster merging in the electromagnetic calorimeters is less pronounced for η than for π^0. In Fig. 1 on the left side we show nuclear modification factor R_{AA} for η-mesons at different centralities [1]. To see if the R_{AA} value rises with p_T, on the right side we present the mean R_{AA} values at two high momenta and the slope of a linear fit of this rise, if any, with centrality. Indeed, there is a small rise but withing one sigma error.

There is another strong constrain on the parton energy loss models: azimuthal assimetry, v_2 for particles at high p_T. This variable is very sensitive to model assumptions. The PHENIX extends its measurements to higher p_T up to 18 GeV/c with better statistics, see Fig. 2 [2]. Suppisingly, v_2 remains large even at highest momentum. To quatify how well different models match the data, in Fig. 3 are shown calculations of v_2 under different assumptions. We see that standard models with the quadratic rise of parton energy loss can't fit the data. Only cubic l dependence of energy losses with longitudinal expansion with time constant around 1.5 fm/c can describe the data.

Hard scattering involves two partons. Two particle correlations at high p_T can provide information on medium effects on both partons. PHENIX presented measurements of azimuthal angle correlation between π^0 particles at transverese momenta 4-12 GeV/c and associated hadrons at 0.5-7 GeV/c [3]. At high p_T the data are consistent with unmodified near and away-side jet shapes compared to $p+p$ collisions. The associated yield of hardons in the away-side peak in $Au+Au$ relative to $p+p$ (I_{AA}) is suppresed, I_{AA}=0.35-0.5, but less than for inclusive suppression (R_{AA} $\approx$0.2), see Fig. 4.

As a further investigation of the away-side suppression PHENIX have measured I_{AA} for trigger particles oriented at different angles with respect to the reaction plane [4]. A large away-side suppression for out-of-plane trigger particles, 0.26$\pm$0.2, was observed compared to the in-plane trigger orientation which is close to unity for mid-central $Au+Au$ collisions, see Fig. 5 and Fig. 6. Threse observations are qualitatively consistent

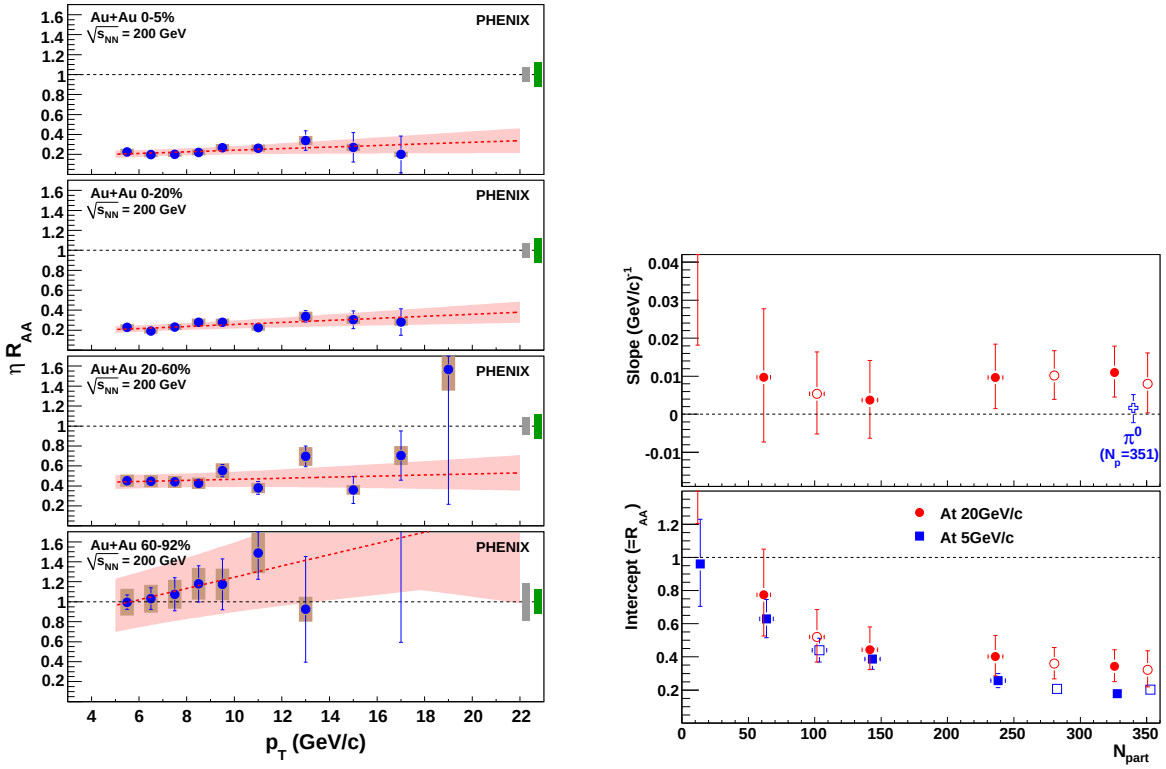

Figure 1. On the left: R_{AA} for η-mesons at various centralities. Dotted line is a liner fit to the data. On the right: (a) Slopes of the liner fit with fitting errors. Also shown: slope of the linear fit to π^0 data for most central collisions. (b) Values of R_{AA} from the fit at 5 GeV/c and 20 GeV/c.

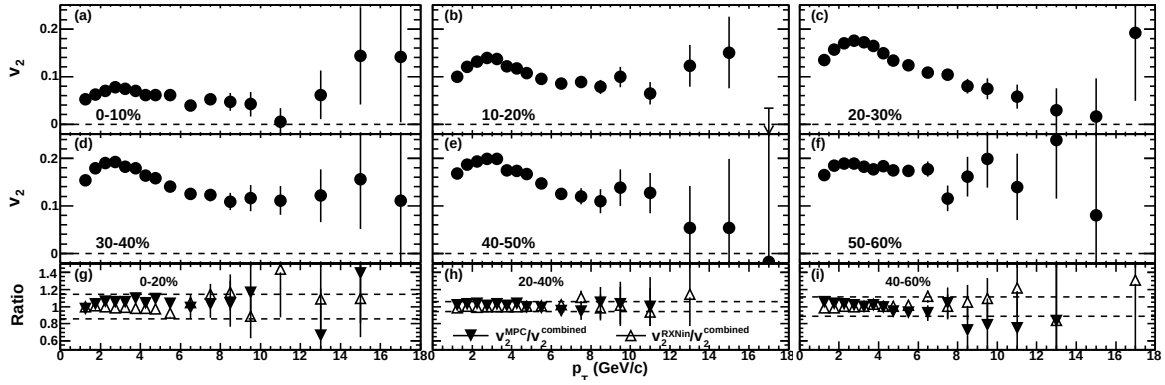

Figure 2. (a)-(f) π^0 v_2 as a function of p_T for different centralities. (g)-(i) ratios of v_2 measured by two different detectors demonstrate stability of the results.

with a picture of the increased away-side parton energy loss due to longer path through the medium.

Measurements of electrons from the decay of open-heavy-flavour mesons have shown that the yields are suppressed in $Au + Au$ collisions compared to binary-scaled $p + p$ collisions. These measurements indicate that charm and bottom quarks interact with the hot and dense matter much more than expected. PHENIX extends these studies

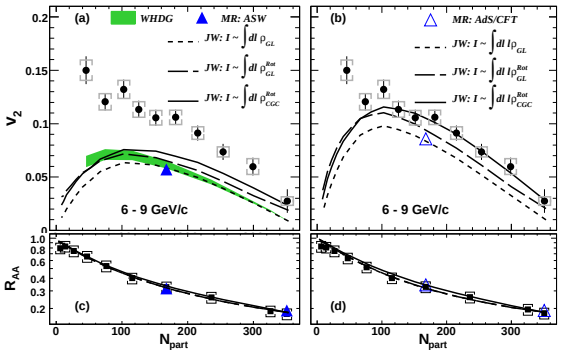

Figure 3. v_2 and R_{AA} vs N_{part} in 6-9 GeV/c range compared with various models [2]. The left panel shows quadratic and the right panel shows cubic l dependence of parton energy loss.

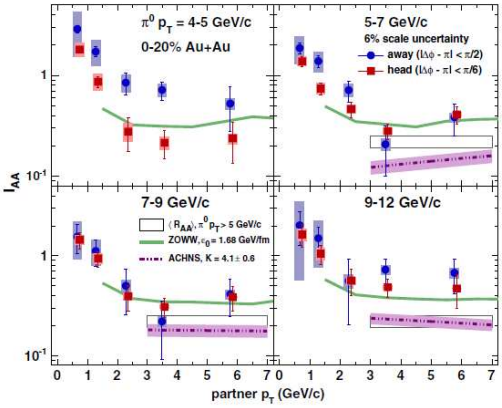

Figure 4. Away-side I_{AA} for a narrow head selection and the entire away side for different trigger range. For comparison, π^0 R_{AA} bands are included.

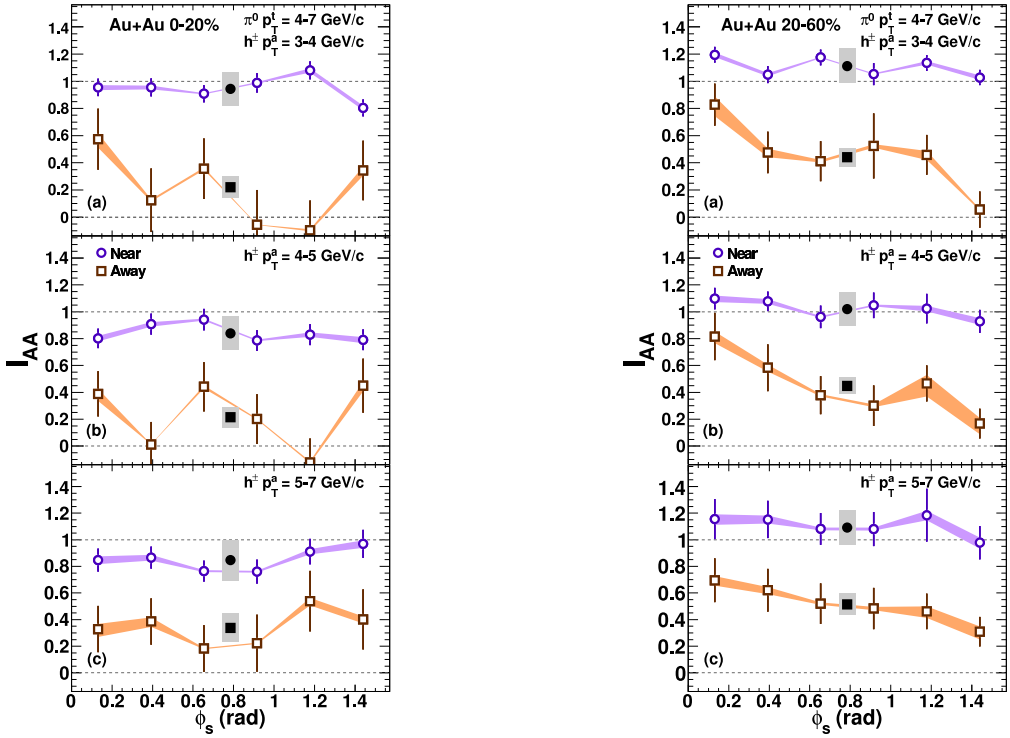

Figure 5. Nuclear jet suppression factor, I_{AA}, by angle with respect to the reaction plane for near and away-side angular selection. Solis points show trigger particle angle averaged results. The left panel shows for 0-20% centrality; right panel shows for centrality 20-60%.

to two-particle correlations where one particle is an electron from the decay of a heavy flavor meson [5]. We find the away-side jet shape and yield to be modified in $Au + Au$

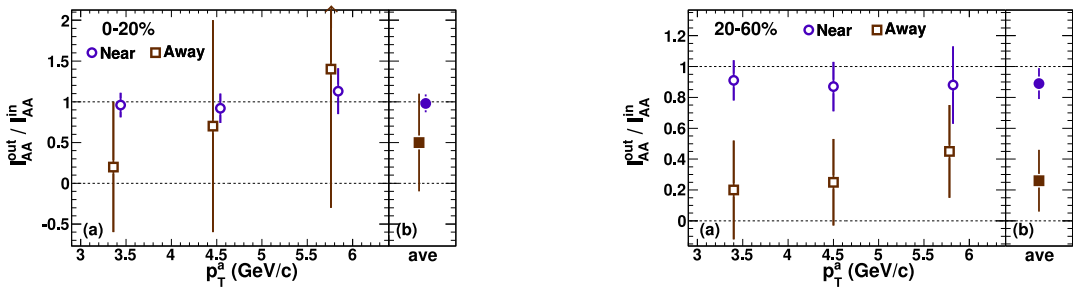

Figure 6. Nuclear jet suppression factor, I_{AA}, as a ratio between in-plane and out-of-plane trigger particles. Solis points show the averaged results. The left panel shows for 0-20% centrality; right panel shows for centrality 20-60%.

collisions compared to $p + p$ collisions, see Fig. 7. Suppression of the away-side is copareble to similar results for hadron-hadron correlations.

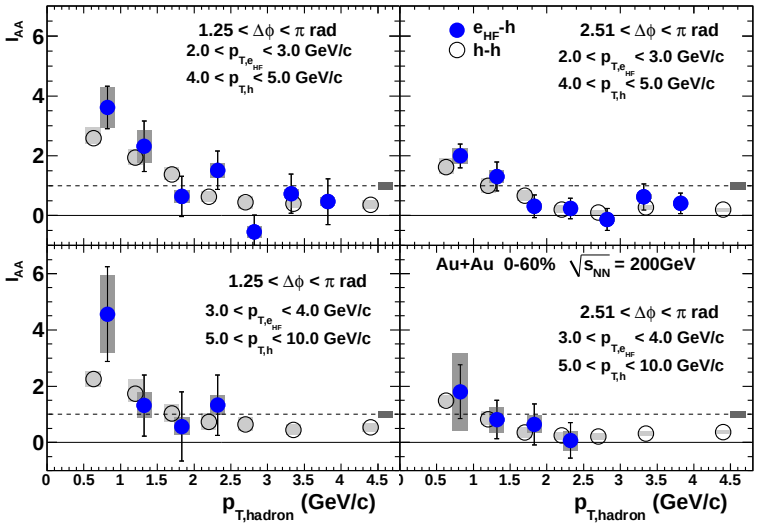

Figure 7. I_{AA} for the away-side yield with non-photonic electron trigger. Data are shown for the full away-side (left panel) and jet-like narrow region (right panel). For comparison, hadron-hadron results are shown by the open symbols.

In conclusion, the PHENIX collaboration demonstrates a wide range of capabilities for investigation of hot dense matter produced in nucleus-nucleus collisions.

[1] A. Adare *et. al.*, Phys.Rev. **C**82, 011902(R) (2010).
[2] A. Adare *et. al.*, Phys.Rev.Lett 105, 142301 (2010).
[3] A. Adare *et. al.*, Phys.Rev.Lett 104, 252301 (2010).
[4] A. Adare *et. al.*, eprint arXiv:1010.1521.
[5] A. Adare *et. al.*, Phys.Rev. **C**83, 044912 (2011).

Suppression of Particle Production at High p_T in ALICE

Philipp Luettig
for the ALICE Collaboration

Max-von-Laue-Str. 1, 60438 Frankfurt, Germany

E-mail: luettig@ikf.uni-frankfurt.de

Abstract. The ALICE experiment has measured particle production in Pb-Pb collisions at $\sqrt{s_{NN}}$ =2.76 TeV during the first heavy-ion beam time at the CERN-LHC in fall 2010. One of the most interesting observations in central collisions is a low nuclear modification factor R_{AA} for unidentified charged particles with a strong p_T dependence. Details of the analysis strategy as well as the construction of a pp reference at $\sqrt{s} = 2.76$ TeV are discussed. R_{AA} is compared to results from the STAR and PHENIX experiments.

1. Introduction

Strongly interacting matter under extreme conditions can be studied in heavy ion collisions at very high energies. At these energies, quantum chromodynamics predicts a hot and dense, deconfined state of matter which is often referred to as the Quark Gluon Plasma.

Measurements at RHIC have shown that the particle production at high p_T in heavy ion collisions (Au–Au at $\sqrt{s_{NN}} = 200$ GeV) is suppressed in comparison to the scaled particle production in pp collisions at the same energy. This is generally attributed to energy loss of partons in the deconfined state.

Now, for the first time, measurements by the ALICE Collaboration at LHC allow to investigate particle production at an energy scale of $\sqrt{s_{NN}} = 2.76$ TeV to give deeper insight into the energy loss mechanisms at play. The first comparison of the production of unidentified charged particles in Pb–Pb and pp collisions at $\sqrt{s_{NN}} = 2.76$ TeV is reported in the following.

The analysis is based on a data sample of $2.3 \cdot 10^6$ minimum bias (MB) Pb–Pb events, ~ 5 million MB events for $\sqrt{s} = 900$ GeV and ~ 28 million MB events for $\sqrt{s} = 7$ TeV. Tracks are measured using a combined tracking in the innermost two detectors of ALICE, the Inner Tracking System (ITS) and the Time Projection Chamber (TPC). The background from weak decays is excluded via a cut on the distance of closest approach to the primary vertex. Only tracks with a transverse momentum of $p_T > 0.15$ GeV/c within $|\eta| < 0.8$ are considered. The track quality is assured by requiring at least 70

out of 159 findable clusters in the TPC and at least two hits in the ITS, one of them being in the innermost part of the ITS. The Pb–Pb data sample is analyzed in different centrality selections. The centrality determination is performed by comparing the correlation between the amplitudes measured with VZERO hodoscopes and the uncorrected number of tracks measured in the TPC.

2. A pp baseline

To compare the particle production in Pb–Pb and pp collisions, a reliable pp baseline needs to be established. Before end of March 2011, no pp reference at $\sqrt{s} = 2.76$ TeV had been measured. Hence in this analysis an interpolation method between the available particle spectra measured by the ALICE experiment at $\sqrt{s} = 900$ GeV and $\sqrt{s}$ = 7 TeV has been used to determine a pp reference at $\sqrt{s} = 2.76$ TeV. The construction of this reference will be described in the following.
In a first step, input spectra for the interpolation are constructed for $\sqrt{s} = 0.9$ and 7 TeV. At low transverse momenta (p_T ¡ 2 GeV/c) the data points themselves are used. At intermediate p_T, between 2 and 5 GeV/c, the data is parametrized with a modified Hagedorn function to avoid statistical fluctuations:

$$\frac{dN^2}{d\eta dp_T} = A \cdot \frac{p_T^2}{m_T} \cdot \left(1 + \frac{p_T}{p_{T,0}}\right)^{-n}. \tag{1}$$

n, $p_{T,0}$ and A are free parameters, while m_T is assumed as

$$m_T = \sqrt{m_\pi^2 + p_T^2} \tag{2}$$

with $m_\pi = 140\ MeV/c^2$, as most of the particles produced are pions. Since the Hagedorn function does not describe the data for all p_T, for high transverse momenta (p_T ¿ 5 GeV/c) a power law function is applied to extend the range in p_T.
In a second step, the new input spectra at both energies are compared at a fixed value of p_T. ALICE has found that the particle yield as a function of the center of mass energy can be parametrized with a power law function [2]. Here it is assumed that the particle yield can be described with a power law function for a fixed range in p_T as well, interpolating the particle yield at $\sqrt{s} = 2.76$ TeV from those at $\sqrt{s} = 0.9$ and 7 TeV, parametrized with the power law function. This method will be referred to as the *interpolation method* in the following.
Naturally alternative ways to determine a reference spectrum are possible. Two of them will be discussed in the following, as they are considered as extreme cases for the pp reference later in this writeup. The first is the *NLO scaling method*. In this method, the ratio of two Next-to-Leading-Order (NLO) [3] calculations is used to "correct" the transverse momentum spectra at $\sqrt{s} = 0.9$ and 7 TeV to the spectrum at $\sqrt{s} = 2.76$ TeV:

$$\frac{\mathrm{dN}|_{2.76}}{\mathrm{d}\eta\mathrm{d}p_\mathrm{T}} = \frac{\frac{\mathrm{dN}|_{\mathrm{NLO,2.76}}}{\mathrm{d}\eta\mathrm{d}p_\mathrm{T}}}{\frac{\mathrm{dN}|_{\mathrm{NLO,x}}}{\mathrm{d}\eta\mathrm{d}p_\mathrm{T}}} \frac{\mathrm{dN}|_{\mathrm{measured,x}}}{\mathrm{d}\eta\mathrm{d}p_\mathrm{T}} \tag{3}$$

The scaled reference at $\sqrt{s} = 7$ TeV agrees with the spectrum based on the default interpolation method. The scaled reference based on the measurements at $\sqrt{s} = 900$ GeV differs from the reference obtained with the interpolation method however, and is therefore used as an estimate on the uncertainties of the construction.

The second alternative evaluation of the reference spectrum is an interpolation from CDF $\mathrm{p\bar{p}}$ data at $\sqrt{s} = 1.96$ TeV and ALICE data at $\sqrt{s} = 7$ TeV. This method is used as an alternative estimate on the uncertainties.
The CMS experiment has also performed a determination of a pp reference at $\sqrt{s} = 2.76$ TeV [4]. The resulting reference is comparable with the one discussed here, though CMS has determined the reference in a different pseudorapidity range.

3. The Nuclear Modification Factor

The comparison of the p_T spectra in Pb–Pb and pp collisions is performed for two different centrality selections, 0–5% (central) and 70–80% (peripheral) (Fig. 1 (left)). For peripheral collisions, the shape of the p_T spectrum is similar for Pb–Pb and the constructed pp reference, scaled with the number of binary collisions N_{coll}. For high transverse momenta the shape shows a power law behaviour.
In central collisions, there is a clear difference between the measured Pb–Pb p_T spectrum and the scaled pp reference. The Pb–Pb spectrum follows an exponential shape for $p_T < 5$ GeV/c. For higher transverse momenta the spectrum can be described with a power law, again.

To quantify the difference between the particle production in pp and Pb–Pb, the ratio of the particle yields is expressed in terms of the nuclear modification factor R_{AA}. The pp reference is scaled with N_{coll}:

$$R_{AA} = \frac{\frac{1}{N_{evt}} \frac{\mathrm{dN_{AA}}}{\mathrm{d}\eta \mathrm{dp_T}}}{\langle N_{coll} \rangle \frac{1}{N_{evt}} \frac{\mathrm{dN_{pp}}}{\mathrm{d}\eta \mathrm{dp_T}}} \tag{4}$$

The number of binary collisions has been determined with Glauber Monte-Carlo calculations.
Figure 1 (right) shows R_{AA} as a function of p_T. In peripheral collisions (centrality 70–80%) the particle production is slightly suppressed with a small p_T dependence. Particle production in the most central collisions (centrality 0–5%) is suppressed as well, but much stronger than in peripheral collisions. R_{AA} has a maximum for $p_T < 6$ GeV/c around $p_T \approx 2.5$ GeV/c. A strong p_T dependence is visible, a minimum of $R_{AA} \approx 0.14$ is reached for $p_T = 6 - 7$ GeV/c. R_{AA} also clearly shows the change in the shape of the Pb–Pb spectrum.
As an estimate on the uncertainty due to the pp baseline, Figure 1 (right) shows R_{AA} calculated with the two alternative baselines mentioned above: the lower grey dotted line shows R_{AA} calculated with the reference based on NLO scaling of the ALICE measurement at $\sqrt{s} = 900$ GeV. The upper grey line shows R_{AA} for the interpolated reference based on CDF and ALICE data.

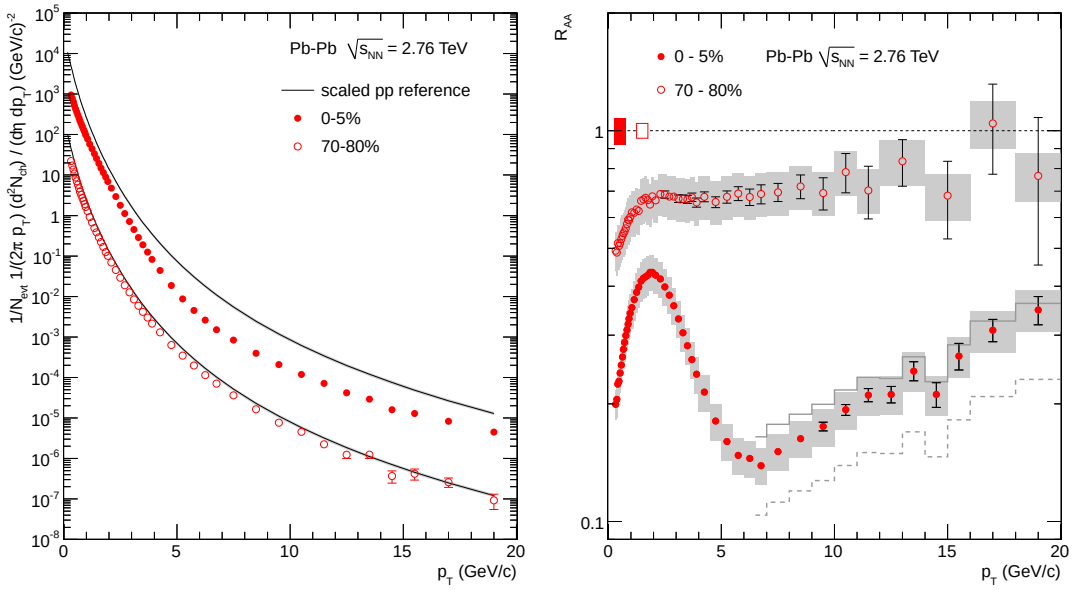

Figure 1. Left: p_T distributions of unidentified charged particles for two centrality selections together with the scaled pp reference (upper line: 0–5%, lower line: 70–80%) **Right:** Corresponding R_{AA}. Error bars indicate the statistical uncertainties. The boxes contain the systematic errors on the data and the p_T dependent systematic errors on the pp reference, added in quadrature. The histograms indicate, for central collisions only, the result for R_{AA} at $p_T > 6.5$ GeV/c using alternative pp references (see text). The vertical bars around $R_{AA} = 1$ show the p_T independent uncertainty on $\langle N_{\rm coll} \rangle$.

Finally R_{AA} can be compared to results measured by STAR and PHENIX at RHIC (Figure 2). For $p_T < 5$ GeV/c the shapes of the p_T spectra agree for all three experiments; at intermediate p_T the suppression at the LHC is stronger than at RHIC. For $p_T > 8$ GeV/c no direct comparison is possible. It has to be noted, that PHENIX has selected the 0–10% most central events, while STAR and ALICE have selected only the 0–5% most central events.

4. Summary and Outlook

Unidentified charged particle spectra for Pb–Pb collisions at $\sqrt{s} = 2.76$ TeV measured by the ALICE experiment have been presented for $0.15 < p_T < 20$ GeV/c. The construction of a pp reference at the same energy based on measured pp data at different energies has been discussed.

While the nuclear modification factor shows only a slight suppression and p_T dependence for peripheral collisions, both a strong suppression and a strong p_T dependence can be seen in central collisions.

Since the presented analysis is based only on a subset of all measured Pb–Pb collisions in the 2010 run, the p_T reach can be extended using the full statistics. In March 2011, a reference at $\sqrt{s} = 2.76$ TeV has been measured; it will provide an improved baseline.

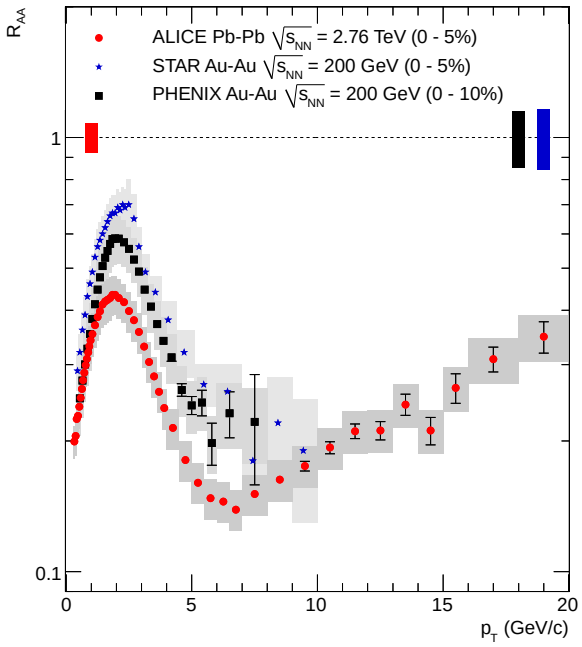

Figure 2. Comparison of R_{AA} in central Pb–Pb collisions at LHC to measurements at $\sqrt{s_{NN}} = 200$ GeV by the PHENIX [6] and STAR [7] experiments at RHIC. The error representation of the ALICE data is as in Fig. 1. The statistical and systematic errors of the PHENIX data are shown as error bars and boxes, respectively. The statistical and systematic errors of the STAR data are combined and shown as boxes. The vertical bars around $R_{AA} = 1$ indicate the p_T independent scaling errors on R_{AA}.

Furthermore, identified particles will play an important role in the detailed investigation of particle production at low transverse momenta.

[1] K. Aamodt *et al.* [ALICE Collaboration], Phys. Lett. B **696** (2011) 30-39, DOI:10.1016/j.physletb.2010.12.020
[2] K. Aamodt *et al.* [ALICE Collaboration], Eur. Phys. J. C (2010) 68: 345-354.
[3] R. Sassot, P. Zurita, and M. Stratmann, Phys. Rev. D **82** (2010) 074011.
[4] CMS Collaboration, arXiv:1104.3547
[5] R. Hagedorn, Riv. Nuovo Cim. **6** (1983) 1.
[6] S. S. Adler *et al.* [PHENIX Collaboration], Phys. Rev. C **69** (2004) 034910.
[7] J. Adams *et al.* [STAR Collaboration], Phys. Rev. Lett. **91** (2003) 172302.

Charged particle distributions and correlations in proton-proton collisions measured with the ATLAS detector

Roberto Di Nardo, on behalf of the ATLAS Collaboration

Universitá di Roma "Tor Vergata" and INFN
Via della Ricerca Scientifica 1, 00133 Rome, Italy

E-mail: Roberto.Di.Nardo@cern.ch

Abstract. We present soft-QCD measurements in proton-proton collisions at $\sqrt{s} =$ 900 GeV and $\sqrt{s} = 7$ TeV recorded with the ATLAS detector at the LHC using a single-arm minimum bias trigger. The charged particle multiplicity distribution, its dependence on transverse momentum and pseudorapidity and its correlation with the average transverse momentum will be shown. Moreover, the measurement of the underlying event properties using charged particles alone or in combination with neutral particles is discussed. Finally the measurement of the two-particle angular correlations is presented. All the measurements are compared with Monte Carlo predictions.

1. Introduction

The understanding of soft particle production in proton-proton collisions is fundamental at LHC energies since the correct modeling of soft physics is the first step toward precise high-p_T measurements. In fact, pileup events, that are unavoidable at the high LHC luminosities, are composed essentially of soft-QCD processes [1, 2] that overlay the interesting hard-scattering events. This understanding is also essential to describe the underlying event (UE) [3, 4] that consists of everything except the hard-scattering process in a hadron-hadron collisions (multi-parton interactions, beam-beam remnants and the contribution from initial and final state radiation). Moreover these soft interactions can introduce experimental biases in isolation criteria, jet trigger and jet energy scale. Perturbative QCD can correctly describe only the hard scattering between partons while phenomenological models that have to be tuned to the data are used to describe soft processes. The charged particle distributions, UE and two-particle angular correlation [5] measurements performed with the ATLAS experiment [6] at $\sqrt{s} = 900$ GeV and $\sqrt{s} = 7$ TeV in proton-proton collisions are presented. The data used for these analyses were selected by a Minimum Bias Trigger Scintillator (MBTS) single-arm trigger [7]. Efficiency corrections and unfolding are applied to data in order

to correct it back to particle level and than compared to various Monte Carlo (MC) models as fully inclusive inelastic distributions without model-dependent corrections .

2. Charged particle multiplicities.

The following charged particle multiplicity distributions[1] have been measured by the ATLAS experiment

$$\frac{1}{N_{ev}}\frac{dN_{ev}}{dn_{ch}}, \qquad \frac{1}{N_{ev}}\frac{dN_{ch}}{d\eta}, \qquad \frac{1}{N_{ev}}\frac{1}{2\pi p_T}\frac{d^2N_{ch}}{d\eta dp_T}, \qquad < p_T > vs.\ n_{ch} \tag{1}$$

where N_{ev} is the number of events with a minimum number of charged particles within the selected kinematic range, n_{ch} represent the number of charged particles in a given event, N_{ch} is the total number of charged particles in the sample and $< p_T >$ the average p_T for events with a specific value of n_{ch}. Different phase spaces have been taken into account for these measurements requiring:

- $p_T > 0.1$ GeV, $n_{ch} \geq 2$ and $|\eta| < 2.5$ for the most inclusive;
- $p_T > 0.5$ GeV, $n_{ch} \geq 6$ and $|\eta| < 2.5$ for the diffraction suppressed (used to produce the new ATLAS Minimum Bias Tune (AMBT1) [8]);
- $p_T > 0.5$ GeV, $n_{ch} \geq 1$ and $|\eta| < 2.5$, studied also at $\sqrt{s} = 2.76$ TeV;

Figure 1 shows the pseudorapidity (defined as $\eta = -\ln(\tan(\theta/2))$ where θ is the polar angle from the beam axis), p_T and n_{ch} distributions measured at $\sqrt{s}$ =7 TeV in the phase-space $n_{ch} \geq 2$, $p_T > 0.1$ GeV and $|\eta| < 2.5$. Data are compared with various MC predictions, including also AMBT1. The charged multiplicity has an approximately flat shape with a smooth dip in the central pseudorapidity and decreasing at forward pseudorapidity. Although MC predictions for $dN/d\eta$ reproduce the shape seen in data,

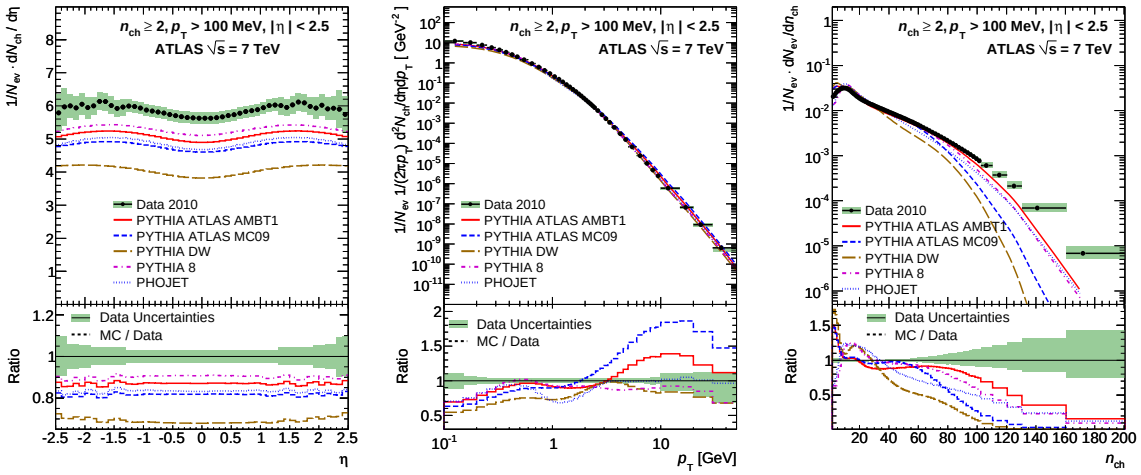

Figure 1. The measured charged particle multiplicity versus pseudorapidity (left), distribution of the transverse momentum (center) and multiplicity distribution of charged particles in the event (right) compared to different MC predictions.

all the models shown underestimate the data. The AMBT1 tune agrees well with the p_T data spectra at intermediate p_T from 0.5 to 3 GeV and all MC models agree with the data to within 20% at high p_T (with the exception of the ATLAS MC09 tune [9] that reaches 70%) and within 35% at low p_T (with the exception of the PYTHIA DW tune [10] that reaches 45%) where a larger contribution of diffractive events is expected. Finally, none of the MC models seems to be able to describe properly the charged particle multiplicity distribution per event in the low multiplicity region while, for n_{ch} $\leq$20, AMBT1 agrees well with the data distribution within 10%.

3. Underlying Event studies with charged and neutral particles.

Even if it is not possible to separate the UE from the hard scattering event-by-event, various observables sensitive to the UE properties can be studied [3]. In every event, particles are then categorized according to their $\Delta\phi$ that represent the azimuthal angular difference between charged particles and the leading particle [11]. The regions $|\Delta\phi| < 60°$ (toward region) and $|\Delta\phi| > 120°$ contain mainly particles from the hard scattering while the region $60° < |\Delta\phi| < 120°$ (transverse region) contains particles from the UE. The data are corrected for these measurements to the particle level. Figure 2 shows the $\Delta\phi$ distribution of charged particle densities ($d^2N/d\eta d\Delta\phi$) for $p_T > 0.5$ GeV and $|\eta| < 2.5$ for different values of the transverse momentum of the leading particle for data at $\sqrt{s} = 900$ GeV (left) and $\sqrt{s} = 7$ TeV (right). These distributions are compared to ATLAS Pythia MC09 predictions showing a significant difference in the shape of the distributions. Figure 3 shows the charged particle density in the transverse region as function of the p_T of the leading particle for 900 GeV and 7 TeV data. The density rises up to 4-6 GeV due to the increasing probability to have one hard collision and reaches a plateau when the UE activity stops increasing with the

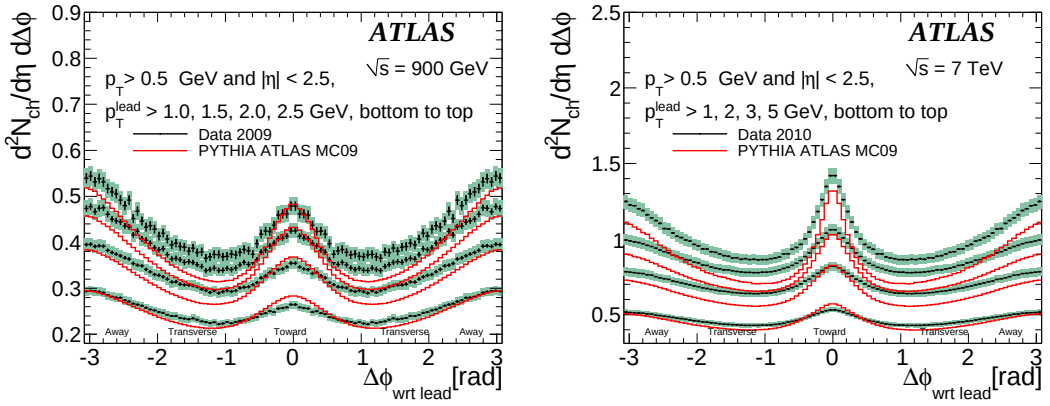

Figure 2. $\Delta\phi$ distribution of charged particle densities for $p_T > 0.5$ GeV and $|\eta| < 2.5$ compared to ATLAS Pythia MC09 predictions at $\sqrt{s} = 900$ GeV (left) and $\sqrt{s} = 7$ TeV (right) for different p_T^{lead} thresholds. The error bars show the statistical uncertainty while the shaded areas show the total errors.

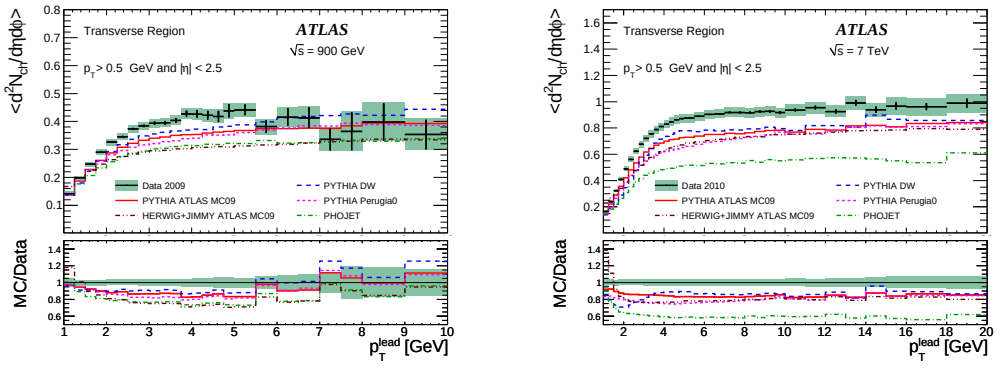

Figure 3. Charged particle densities in the transverse region as a function of the p_T of the leading charged particle in p-p collisions at 900 GeV (left) and 7 (right) TeV.

transverse momentum of the leading particle. The density value at the plateau is a factor two larger with respect to the multiplicity measured in minimum bias events and this is due to the fact that the high-p_T track selection required for the leading track implies more momentum exchange and a lack of diffractive contribution in the plateau region. All the models taken into account show at least 10-15% lower activity in the plateau region with respect to data. The PYTHIA DW tune is the closest model to data for the transverse region while the larger difference between data and MC is seen for the PHOJET generator [12]. Since the JIMMY [13] model requires at least one hard scattering, the strong deviation of HERWIG+JIMMY from the data for low-p_T^{lead} is expected because it cannot be applicable in this region while is evident the improvement for HERWIG+JIMMY predictions from 900 GeV to 7 TeV for high-p_T^{lead}. An UE analysis has also been performed by the ATLAS experiment using calorimetric information [4].

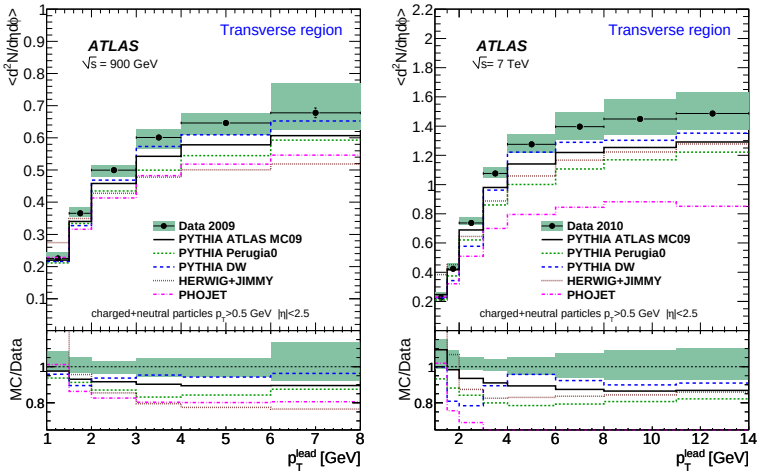

Figure 4. Particle densities in the transverse region as a function of the p_T of the leading particle in p-p collisions at 900 GeV (left) and 7 (right) TeV.

This incorporates the results obtained by the track based analysis and is also sensitive to the neutral component. Figure 4 shows the particle densities (charged and neutral) in the transverse region as a function of the p_T of the leading particle for 900 GeV and 7 TeV data. The measured densities are 40% higher with respect to the UE analysis using only charged tracks, due to the neutral component. Again the various MC predictions underestimate the data, with PYTHIA DW generating predictions closest to the data and PHOJET the largest deviations. All these measurements may be used to improve the MC descriptions of the complete final state produced in proton-proton collisions.

4. Two-particle angular correlations

The study of the correlations between final state particles can be used for investigating the underlying mechanisms of particle production [5, 14, 15, 16]. Moreover additional dynamical information can be identified and included in models to improve the description of the multi-particle production mechanism in soft interactions. The inclusive two-particle correlation function is given by:

$$R\left(\Delta\eta, \Delta\phi\right) = \frac{\left\langle \left(N_{ch} - 1\right) F\left(N_{ch}, \Delta\eta, \Delta\phi\right)\right\rangle_{ch}}{B\left(\Delta\eta, \Delta\phi\right)} - \left\langle N_{ch} - 1\right\rangle_{ch}. \tag{2}$$

where $F\left(N_{ch}, \Delta\eta, \Delta\phi\right)$ represents the correlations between emissions in a single event (including correlated and uncorrelated pairs) normalized by the total number of events while $B\left(\Delta\eta, \Delta\phi\right)$ is the distribution of uncorrelated pairs normalized by its integral. Figure 5 shows the corrected inclusive two-particle correlation functions for data at $\sqrt{s} = 900$ GeV and $\sqrt{s} = 7$ TeV. In the full $\Delta\eta$ and $\Delta\phi$ range different components can be identified: the peak at around $\Delta\phi \sim 0$ can be associated to particles coming from the same high-p$_T$ cluster like jets (near-side correlations); the ridge at $\Delta\phi \sim \pi$ comes from back-to-back jets (away-side correlations); a gaussian-shaped distribution across

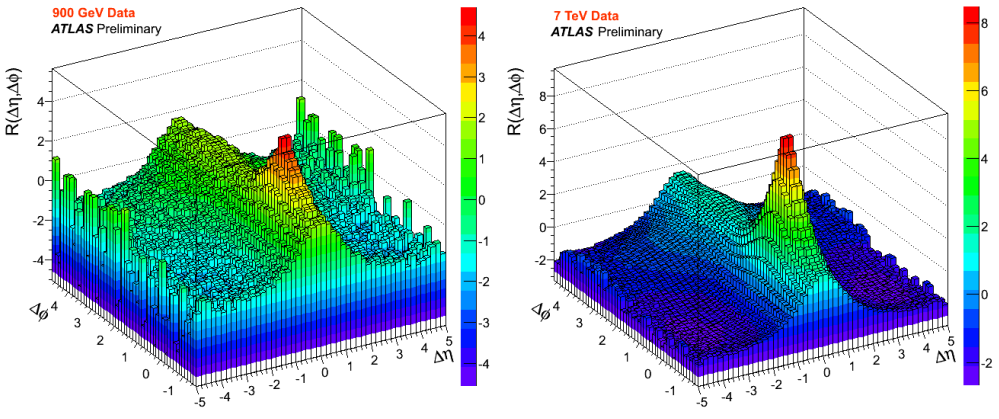

Figure 5. Corrected two-particle correlation distribution functions in $\Delta\eta$ and $\Delta\phi$ for 900 GeV (left) and 7 TeV.

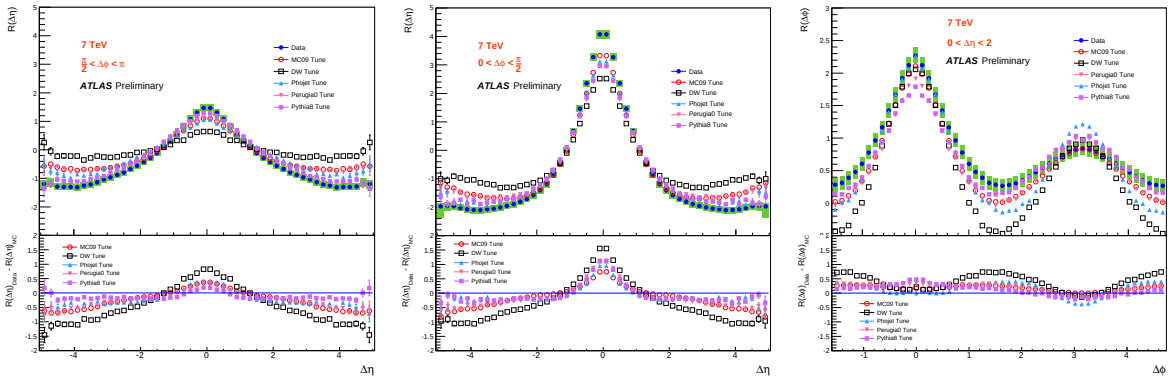

Figure 6. Away-side (left), near-side (center) and short-range (right) two-particle correlation distributions obtained by integrating over the $\Delta\phi$ ranges ($\frac{\pi}{2} - \pi$ and $0 - \frac{\pi}{2}$) and $\Delta\eta$ range ($0 < \Delta\eta < 2$) for data and different MC tunes at 7 TeV. In data, the green bands correspond to the total uncertainties (statistical and systematic, added in quadrature) while the blue lines are the statistical errors.

all $\Delta\phi$ with a width of $\Delta\eta \sim 2$ is related to resonances, string fragmentations and high-p_T clusters (short-range correlations). In order to study in detail the structure of the correlations, the two-dimensional correlation function has been projected along $\Delta\eta$ and $\Delta\phi$. These are shown in Figure 6 for collision data at $\sqrt{s} = 7$ TeV compared with several MC tunes. For the away-side correlations there is a good agreement between data and Pythia 8 in the full $\Delta\eta$ range; for the near-side correlations, none of the MC tunes describes correctly the shape of the data, with Pythia 8 being the closest to the data in the tails. In the case of short-range correlations, the different tunes taken into account agree with data only in localized $\Delta\phi$ regions. Similar results have been obtained for 900 GeV data.

5. Conclusions

Charged particle distributions, underlying event distributions and two-particle correlations in p-p collisions at 900 GeV and 7 TeV measured by the ATLAS detector have been presented. These are important inputs for MC tuning purposes, since most of the pre-LHC models do not show a satisfactory agreement with data. The new AMBT1 tune represents the first improvement for minimum bias results.

References

[1] The ATLAS Collaboration "Charged-particle multiplicities in pp interactions measured with the ATLAS detector at the LHC", New J Phys 13 (2011) 053033, arXiv:1012.5104v2

[2] The ATLAS Collaboration, "Charged-particle multiplicities in pp interactions at $\sqrt{s} = 900$ GeV measured with the ATLAS detector at the LHC", Phys. Lett. B688 (2010) 21-42, arXiv:1003.3124v2

[3] The ATLAS Collaboration, "Measurement of underlying event characteristics using charged

particles in pp collisions at $\sqrt{s}$ =900 GeV and 7 TeV with the ATLAS detector", Phys. Rev. D 83 (2011) 112001, arXiv:1012.0791v2

[4] The ATLAS Collaboration, "Measurements of underlying event properties using neutral and charged particles in p-p collisions at 900 GeV and 7 TeV with the ATLAS detector at the LHC", Submitted to EPJC, arXiv:1103.1816v2

[5] The ATLAS Collaboration, "Measurement of Inclusive Two-Particle Angular Correlations in Proton-Proton Collisions at $\sqrt{s}$ =900 GeV and 7 TeV", ATLAS-CONF-2011-055

[6] The ATLAS Collaboration, "The ATLAS Experiment at the CERN Large. Hadron Collider", JINST 3 (2008) S08003

[7] The ATLAS Collaboration, "Performance of the Minimum Bias Trigger in p-p Collisions at $\sqrt{s}$ = 7 TeV", ATL-CONF-2010-068

[8] The ATLAS Collaboration, "Charged particle multiplicities in pp interactions at $\sqrt{s}$ = 0.9 and 7 TeV in a diffractive limited phase-space measured with the ATLAS detector at the LHC and new PYTHIA6 tune", ATLAS-CONF-2010-031

[9] The ATLAS Collaboration, "ATLAS Monte Carlo tunes for MC09", ATL-PHYS-PUB-2010-002

[10] M. G. Albrow et al., "Tevatron-for-LHC Report of the QCD Working Group", arXiv:hep-ph/0610012

[11] The CDF Collaboration, "Underlying event in hard interactions at the Fermilab Tevatron $p\bar{p}$ collider", Phys. Rev. D 70 (2004) 072002

[12] R. Engel, "Photoproduction within the two component dual parton model. 1. Amplitudes and cross-sections", Z. Phys. C66 (1995) 203-214

[13] J. M. Butterworth, J. R. Forshaw, and M. H. Seymour, "Multiparton interactions in photoproduction at HERA," Z. Phys. C72 (1996) 637-646

[14] K. Eggert et al., "Angular Correlations Between the Charged Particles Produced in pp Collisions at ISR Energies", Nucl. Phys. B86 (1975) 201-215

[15] The UA5 Collaboration, "Charged particle correlations in anti-p p collisions at c.m. energies of 200, 546 and 900 GeV", Z. Phys. C37 (1988) 191-203

[16] The PHOBOS Collaboration, "Cluster properties from two-particle angular correlations in p+p collisions at $\sqrt{s}$ = 200 and 410 GeV", Phys. Rev. C75 (2007) 054913

Monte Carlo Simulation for Elastic Energy Loss of High-Energy Partons in Quark-Gluon Plasma

J. Auvinen, K. J. Eskola, H. Holopainen and T. Renk

Department of Physics, P.O. Box 35, FI-40014 University of Jyväskylä, Finland
Helsinki Institute of Physics, P.O. Box 64, FI-00014 University of Helsinki, Finland

E-mail: jussi.a.m.auvinen@jyu.fi

Abstract. We examine the significance of $2 \to 2$ partonic collisions as the suppression mechanism of high-energy partons in the strongly interacting medium formed in ultrarelativistic heavy ion collisions. For this purpose, we have developed a Monte Carlo simulation describing the interactions of perturbatively produced, non-eikonally propagating high-energy partons with the quarks and gluons from the expanding QCD medium. The partonic collision rates are computed in leading-order perturbative QCD (pQCD), while three different hydrodynamical scenarios are used to model the medium. We compare our results with the suppression observed in $\sqrt{s_{NN}} = 200$ GeV Au+Au collisions at the BNL-RHIC. We find the incoherent nature of elastic energy loss incompatible with the measured data and the effect of the initial state fluctuations small.

1. Introduction: A substantial suppression of high-energy hadrons has been measured in $\sqrt{s_{NN}} = 200$ GeV Au+Au collisions at the BNL-RHIC [1]. This is believed to be a consequence of the energy loss of hard partons traversing a strongly interacting medium.

To study the relevant physics of this phenomenon in as detailed manner as possible, we have developed a Monte Carlo (MC) simulation for the hard parton's interaction with the medium [2, 3, 4]. This is similar to the (perhaps even more ambitious) MC models JEWEL (Jet Evolution With Energy Loss) [5] and MARTINI (Modular Algorithm for Relativistic Treatment of heavy IoN Interactions) [6]. However, while JEWEL and MARTINI include both elastic and radiative energy-loss components, we concentrate purely on the elastic energy loss for the time being.

2. The model: We model the elastic energy loss of a hard parton by incoherent partonic $2 \to 2$ processes in pQCD, with scattering partners sampled from the medium. Three different hydrodynamical scenarios are used to model the QCD medium: *i)* a (1+1)-dimensional hydro [7] with initial conditions from the EKRT model [8] for central heavy ion collisions, *ii)* a (2+1)-dimensional hydro [9] with a smooth sWN profile [10] obtained from the optical Glauber model for non-central collisions, and *iii)* an event-by-event hydro [9] with an eBC profile [10] from the Monte Carlo Glauber model to study the effects of the initial state density fluctuations.

Our approach is based on the scattering rate $\Gamma_i(p_1, u(x), T(x))$ for a high-energy parton of a type i with 4-momentum p_1, accounting for all possible partonic processes $ij \to kl$. The flow 4-velocity $u(x)$ and the temperature $T(x)$ of the medium are given by the hydrodynamical model. In the local rest-frame of the fluid, we can express the scattering rate for a process $ij \to kl$ as follows [2]:

$$\Gamma_{ij\to kl} = \frac{1}{16\pi^2 E_1^2} \int_{\frac{m^2}{2E_1}}^{\infty} dE_2 f_j(E_2, T) \int_{2m^2}^{4E_1E_2} ds[s\sigma_{ij\to kl}(s, m^2)]. \quad (1)$$

Here E_1 is the energy of the high-energy parton i in this frame and E_2 is the energy of the thermal particle j with a distribution function $f_j(E_2, T)$, which is the Bose-Einstein distribution for gluons and the Fermi-Dirac distribution for quarks. The scattering cross section $\sigma_{ij\to kl}(s, m^2)$ depends on the standard Mandelstam variable s. A thermal-mass-like overall cut-off scale $m = s_m g_s T$ is introduced in order to regularize the singularities appearing in the cross section when the momentum exchange between partons approaches zero. Here g_s is the strong coupling constant, which we keep fixed with momentum scale. The free parameters of our model are thus s_m and $\alpha_s = \frac{g_s^2}{4\pi}$.

The hard parton is propagated through the plasma in small time steps Δt. At each step, the probability for a collision is given by the Poisson distribution $1 - e^{-\Gamma_i \Delta t}$. We always assume there is no significant interaction between the high-energy parton and the fully hadronic medium, and thus no collisions happen in regions with temperature below the decoupling temperature $T_{\rm dec}$. The medium-modified distribution of high-energy partons obtained in the end can be convoluted with a fragmentation function to calculate the nuclear modification factor $R_{AA}(P_T, y, \phi) = \frac{dN_{AA}/dP_T dy d\phi}{\langle N_{\rm BC}/\sigma_{NN}\rangle\, d\sigma^{pp}/dP_T dy d\phi}$.

3. Results: In the following, our interest is in the high-P_T neutral pions produced in $\sqrt{s_{NN}} = 200$ GeV Au+Au collisions. To achieve roughly the right amount of nuclear modification in the 0-10% centrality bin and to emulate also the incoherent higher-order processes, we set $\alpha_s = 0.5$ and $s_m = 1.0$.

The simulation results for the 0-10%, 40-50% and 50-60% centrality bins, compared with the measurements, are shown in Fig. 1. While the P_T-behaviour of the obtained R_{AA} is compatible with the data within the studied transverse momentum range, it is clear from the figure that our model cannot reproduce the reaction plane angle dependence seen in the PHENIX experiment. Also the inclusive, angle-averaged nuclear modification factor fails to match with the experimental data: The computed suppression decreases too slowly as one advances to the more peripheral collisions.

In Figure 2 we compare the angular dependence of the partonic R_{AA} for fluctuating initial state geometry with the result for smooth initial conditions. While the variation in R_{AA} between events can be considered notable, the angular variation within a single event is rather weak. The average over 20 events with fluctuating initial conditions, keeping the same value $\alpha_s = 0.5$ for the fluctuating and smooth cases, equals the smooth initial condition scenario with fairly good accuracy. However, in non-central collisions case the average over 20 events with fluctuating initial conditions is found to be systematically above the smooth initial conditions curve, although the statistical uncertainties

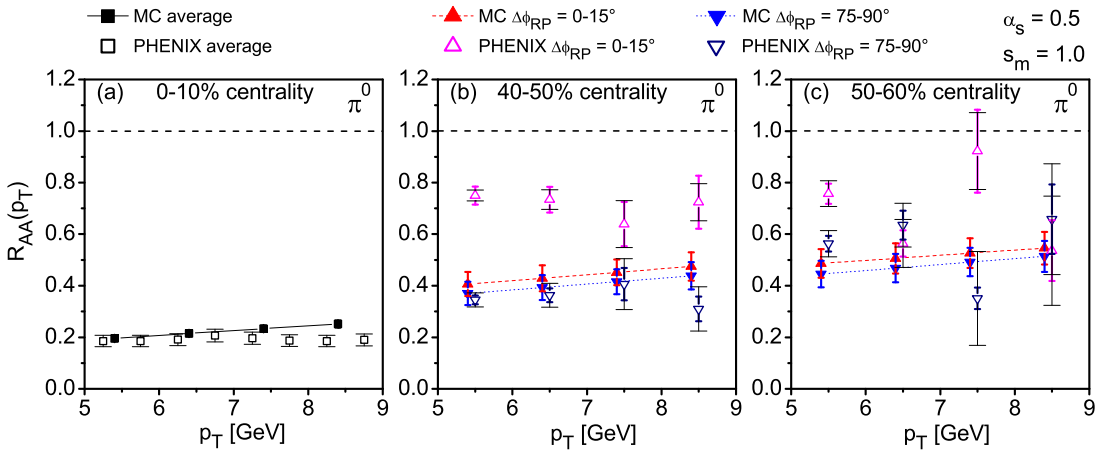

Figure 1. (Color online) Left panel: The π^0 nuclear modification factor for 0-10% centrality, averaged over the reaction plane angle. Middle and right panel: The π^0 nuclear modification factor dependence on the reaction plane angle $\Delta\phi$ for 40-50% (middle panel) and 50-60% centrality (right panel). The simulation points (solid squares and triangles) are connected with lines to guide the eye. The PHENIX data are from [11] (0-10% centrality, open squares) and [12] (40-50% and 50-60% centrality, open triangles). Colored bars with small cap represent statistical errors; black bars with wide cap are systematic errors.

indicated by the asymmetry of the upper curve make the difference almost negligible.

4. Summary: Our result for $R_{AA}(\phi)$ in non-central collisions demonstrates that a purely incoherent energy-loss framework contradicts the present RHIC data. The weak sensitivity of the elastic energy loss model to the angle-dependent observables is clearly seen also in the fluctuating initial state study. In the central collisions, no difference is seen between the fluctuating and the smooth initial conditions when an average over 20 events has been taken. In the non-central collisions the fluctuating conditions do appear to produce somewhat smaller suppression compared to the smooth background.

Acknowledgments: J.A. gratefully acknowledges the grant from the Jenny and Antti Wihuri Foundation. This work was also supported by the national Graduate School of Particle and Nuclear Physics, the Academy research program of the Academy of Finland (Project No. 130472) and Academy Project 133005. CSC – IT Center for Science Ltd. is acknowledged for the allocation of computational resources.

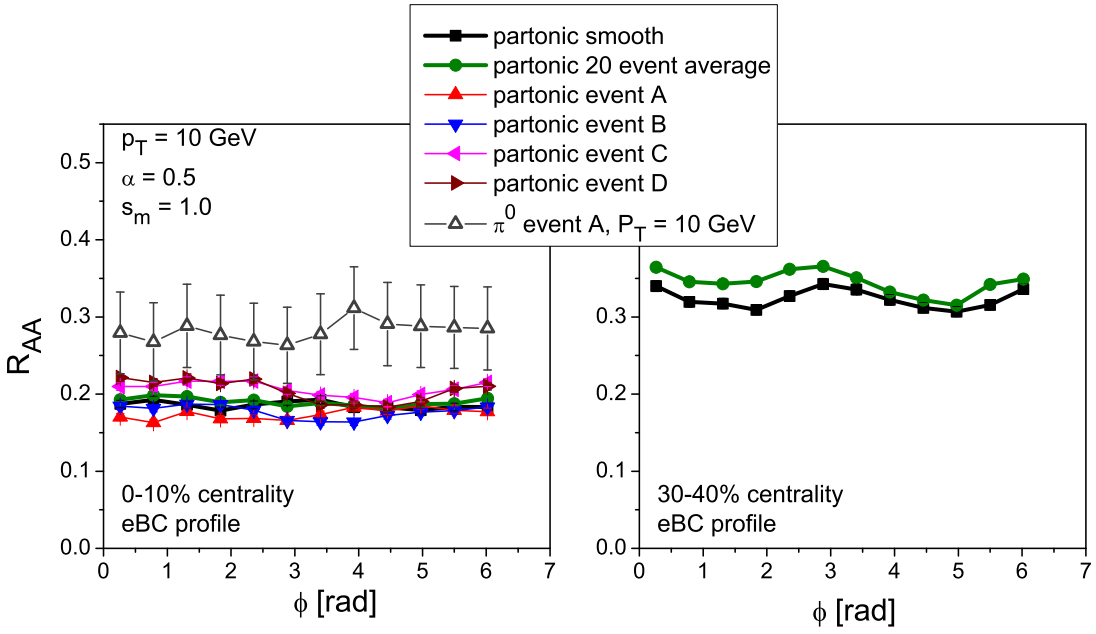

Figure 2. The partonic nuclear suppression factor R_{AA} for central 200 AGeV Au-Au collisions at $p_T = 10$ GeV as a function of the angle of outgoing partons with respect to the event plane. The left panel includes plots for smooth initial conditions, for four different events with fluctuating initial conditions and for an average over 20 fluctuation events in 0-10% centrality. The nuclear suppression factor for π^0 at $P_T = 10$ GeV in one event is also displayed. The right panel includes plots for smooth initial conditions and for an average over 20 fluctuation events in 30-40% centrality.

References

[1] S.S. Adler *et al.* [PHENIX Collaboration], Phys. Rev. Lett. **96**, 202301 (2006).
[2] J. Auvinen, K. J. Eskola and T. Renk, Phys. Rev. C **82**, 024906 (2010).
[3] J. Auvinen, K. J. Eskola, H. Holopainen and T. Renk, Phys. Rev. C **82**, 051901 (2010).
[4] T. Renk, H. Holopainen, J. Auvinen and K. J. Eskola, arXiv:1105.2647 [hep-ph].
[5] K. Zapp, G. Ingelman, J. Rathsman, J. Stachel and U. A. Wiedemann, Eur. Phys. J. C **60**, 617 (2009).
[6] B. Schenke, C. Gale and S. Jeon, Phys. Rev. C **80**, 054913 (2009).
[7] K. J. Eskola, H. Honkanen, H. Niemi, P. V. Ruuskanen, S. S. Räsänen, Phys. Rev. C **72**, 044904 (2005).
[8] K. J. Eskola, K. Kajantie, P. V. Ruuskanen, K. Tuominen, Nucl. Phys. B **570**, 379 (2000).
[9] H. Holopainen, H. Niemi and K. J. Eskola, Phys. Rev. C **83**, 034901 (2011).
[10] P. F. Kolb, U. W. Heinz, P. Huovinen, K. J. Eskola and K. Tuominen, Nucl. Phys. A **696**, 197 (2001).
[11] A. Adare *et al.* [PHENIX Collaboration], Phys. Rev. Lett. **101**, 232301 (2008).
[12] S. Afanasiev *et al.* [PHENIX Collaboration], Phys. Rev. C **80**, 054907 (2009).

Parton-medium interaction from RHIC to LHC — a systematic approach

T Renk

Department of Physics, P.O. Box 35, FI-40014 University of Jyväskylä, Finland

E-mail: thorsten.i.renk@jyu.fi

Abstract. Despite a wealth of experimental data for high p_T processes in heavy-ion collisions, discriminating between different models of hard parton-medium interactions has been difficult. One important reason is that the pQCD parton spectrum at RHIC kinematics is so steeply falling that distinguishing even a moderate shift in parton energy from complete parton absorption is almost impossible in observable quantities. In essence, energy loss models are effectively only probed in the vicinity of zero energy loss and as a result, only the pathlength dependence of energy loss offers some discriminating power at RHIC kinematics. At LHC, this is no longer the case: Due to the much flatter shape of the parton spectra originating from 2.76 AGeV collisions, the available observables probe much deeper into the model dynamics. A simultaneous fit of the nuclear suppression both at RHIC and LHC kinematics has thus a huge potential to discriminate between various models with equally good description of RHIC data alone.

1. Introduction

The suppression of the high transverse momentum P_T hadron yield in heavy-ion (A-A) collisions as compared to the scaled expectation from p-p collisions, often referred to as 'jet quenching', has long been considered one of the most important probes of the medium created in heavy-ion collisions [1, 2, 3, 4, 5, 6]. Yet, despite a wealth of experimental data and several years of theoretical efforts, even solid qualitative statements such as to the nature of parton-medium interaction remain elusive.

Several reasons contribute to the problem. First, there is an inherent ambiguity between modelling the parton-medium interaction and modelling the spacetime evolution of the underlying medium: an increased medium density or spatial size can usually compensate for a decrease of interaction strength. Second, primary parton spectra in perturbative Quantum Chromodynamics (pQCD) are steeply falling functions of p_T, and thus even a moderate shift in parton momentum is indistinguishable from an absorption of a parton by the medium [7]. Finally, the problem itself is a genuinely difficult one, involving the hard scales of the perturbative process, the soft scales of medium dynamics and the transition region.

In this work, we show that a systematic comparison of combinations of medium evolution and parton-medium interaction models is capable of resolving the inherent ambiguities to a large degree, whereas the increased kinematic reach of the LHC as compared to RHIC significantly increases the dependence of observable quantities on model details.

2. Modelling outline

We start by selecting both a model for the medium spacetime evolution as well as a model for the parton-medium interaction. The spacetime evolution for RHIC conditions is chosen out of a range of fluid dynamical models which are constrained by bulk observables, a 3+1d ideal hydrodynamical model [8], a 2+1d ideal model [9] and a viscous hydrodynamical code [10] (the latter with both a Glauber (vGlb) and a CGC-type (vCGC) initial condition).

Hard interactions are assumed to take place inside this evolving medium distributed in the transverse plane with a binary collision profile. From a given collision vertex, partons are propagated outward and undergo interactions with the medium. Here, we consider two main classes of parton-medium interaction models: full in-medium showers and leading parton energy loss models. In an in-medium shower evolution model, the yield of high P_T hadrons can be computed from the expression

$$d\sigma_{\rm med}^{AA\to h+X} = \sum_f d\sigma_{vac}^{AA\to f+X} \otimes \langle D_{MM}^{f\to h}(z,\mu^2)\rangle_{T_{AA}} \tag{1}$$

where f sums over all parton flavours, $d\sigma_{vac}^{AA\to f+X}$ is the vacuum pQCD cross section for producing parton f and $\langle D_{MM}^{f\to h}(z,\mu^2)\rangle_{T_{AA}}$ is the geometry-averaged medium modified fragmentation function (MMFF) for fractional momentum z at scale μ^2. The MMFF is the output of a parton-medium interaction model given the path through the medium. Here we use the Monte Carlo (MC) code YaJEM [11, 12, 13] to compute it. The geometry averaging is done over all possible initial vertices, either with a given orientation with respect to the event plane or averaged over all orientations. In leading parton energy loss models, the MMFF is approximated by

$$\langle D_{MM}^{f\to h}(z,\mu^2)\rangle_{T_{AA}} = \langle P(\Delta E)\rangle_{T_{AA}} \otimes D^{f\to h}(z,\mu^2) \tag{2}$$

i.e. by a convolution of the vacuum fragmentation function $D^{f\to h}(z,\mu^2)$ with a geometry-averaged energy loss probability distribution $\langle P(\Delta E)\rangle_{T_{AA}}$. This latter quantity is computed within a given leading parton energy loss framework. In the present study we consider a radiative energy loss model [14] (ASW), a parametrized elastic energy loss model [15] (elastic) as well as a MC model for elastic pQCD interactions [16] (eMC) and an AdS/CFT inspired model for energy loss in a strongly coupled medium [17] (AdS).

In each of these models, a single parameter K_{med} regularizes the proportionality between powers of thermodynamical quantities such as energy density ϵ or temperature T and the interaction strength. Unless stated otherwise, we adjust K_{med} for any combination of medium evolution and parton-medium interaction model such that

the nuclear suppression factor R_{AA} in central 200 AGeV Au-Au collisions at RHIC is reproduced and compute for other centralities, different $\sqrt{s}$ or other observables without additional free parameters.

3. Pathlength dependence

Different parton-medium interaction models show different response to the pathlength L of a parton propagating in a constant medium. This can be exploited to discriminate between models. For instance, any incoherent process (e.g. elastic or eMC) counts the number of interactions along the path by $n_{scatt} = L/\lambda$ where λ is the mean free path. If the energy loss of a parton to the medium is proportional to n_{scatt}, a linear pathlength dependence of the total lost energy $\Delta E \sim L$ follows. On the other hand, in coherent radiative processes, the virtuality Q of a gluon with energy ω from the virtual cloud surrounding a parton must be brought on-shell by random transverse kicks from the medium. While the number of kicks is proportional to L, there is also a coherence condition which states that interactions within the formation time $\tau \sim \omega/Q^2$ need to be summed coherently. This implies a quadratic pathlength dependence $\Delta E \sim L^2$ [14] (ASW). If however in addition finite energy corrections are accounted for, such a quadratic dependence effectively reverts back to a linear dependence for experimentally relevant kinematics [13] (YaJEM). In a strongly coupled medium where an AdS/CFT description may be applicable, the gluons from the virtual cloud surrounding the parent parton are not brought on-shell by random transverse kicks but by the action of a drag force of order T^2. Coherence time arguments in this case lead to $\Delta E \sim L^3$ [17] (AdS). Finally, an in-medium shower corresponds to the evolution from a high initial virtuality scale down to a low scale Q_0. If one takes into account that the medium can only affect a shower above $Q_{med} = \sqrt{E/L}$ where E is the parent parton energy, an explicit non-linear behaviour of the medium effect with pathlength and energy E emerges [13] (YaJEM-D).

Thus, the different physics assumptions underlying various models are reflected in the expected dependence of medium modification on pathlength. Experimentally this is accessible e.g. through the emission of high P_T hadrons as a function of the angle ϕ with the event plane, or specifically in the difference of in-plane and out of plane emission. However, while interesting to characterize models, pathlength dependence in a constant medium is not relevant for the experimental situation. In a real hydrodynamical evolution, the spatial density profile, longitudinal and transversal flow, viscous reheating and fluctuations in the initial state all have noticeable influence [19, 20], underlining the need for realistic hydrodynamically modelling and an assessment of the uncertainties associated with the medium model.

In Fig. 1 we show some results of a systematic investigation [19] of pathlength dependent observables for different combinations of medium evolution and parton-medium interaction model. Clearly, both elements have a pronounced influence on the results. Summarizing the findings of [19], we can state that the spread between in plane and out of plane emission grows whenever energy loss happens late. This may be due

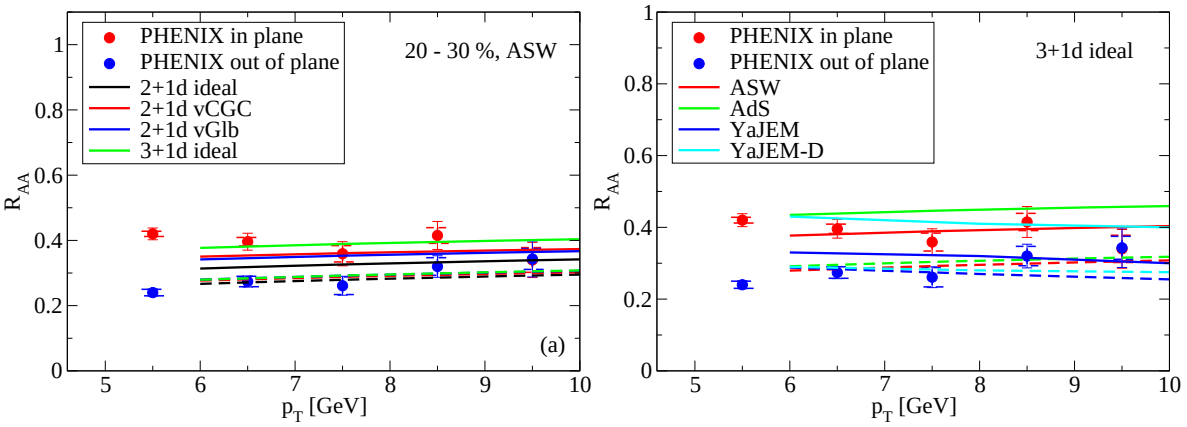

Figure 1. Left panel: $R_{AA}(P_T)$ for 30-40% cental 200 AGeV Au-Au collisions for in plane (solid) and out of plane (dashed) emission computed for the same energy loss model (ASW) with different hydrodynamical backgrounds, compared with PHENIX data [21]. Right: same as left panel, but for the same 3+1d ideal hydrodynamical model and different parton-medium interaction models.

to the L^3 dependence of AdS or the strong non-linear dependence of YaJEM-D, but can also be driven by the hydrodynamical component. Here, differences are unrelated to the dimensionality of the simulation, rather factors like initialization time, equation of state, viscosity or freeze-out conditions matter. There is no single factor which influences the spread, rather a combination of various effects contributes with almost equal magnitude.

Several combinations of models are viable, however for instance an L dependence as characteristic for incoherent interactions or of radiative energy loss with finite energy corrections fails no matter what medium is assumed [13, 15, 16]. Other models work conditionally, for instance the AdS model works fine with the 2+1d hydrodynamics but overestimates the spread seen in the data for the 3+1d model, whereas the ASW model behaves the opposite way. Thus, while pathlength dependent observables clearly have some power to distinguish various scenarios of parton-medium interaction and/or do medium tomography, additional constraints are needed.

4. Hydrodynamics with fluctuating initial conditions

Before assessing the potential of a larger kinematic lever-arm to discriminate in more detail between various model calculations, let us discuss a potentially troublesome issue connected with modelling the medium. It has recently become apparent that event-by-event fluctuations in the initial conditions are crucial to understand details of the hydrodynamical evolution of the medium in A-A collisions. In other words, it matters if the initial state is first averaged and then the evolution of an average final state is computed, or if the evolution for each initial state is computed and only the final state is averaged. One may thus wonder if the same is true for hard partons interacting with such a medium. Potentially, there are several effects that might create a difference. First, R_{AA} is a non-linear function of medium density which responds stronger to a decreasing

density than to an increasing density (even an arbitrarily high density cannot push R_{AA} below zero). Thus, fluctuations in the initial state may decrease the observed amount of suppression. However, 'hotspots' in the hydrodynamical initial state are typically associated with binary collision vertices. Taking this correlation into account implies that produced partons tend to be produced in regions with higher-than-average density, which would decrease the amount of suppression as compared to a smooth, initial-state averaged medium. In addition, there is also the effect of a very irregular initial flow field, for which the sign is *a priori* unknown. Finally, the fact that the event plane is not identical with the reaction plane needs to be taken seriously — if the reaction plane is used as reference plane for $R_{AA}(\phi)$, then the magnitude of the spread between in-plane and out of plane emission is artificially decreased by a trivial averaging effect.

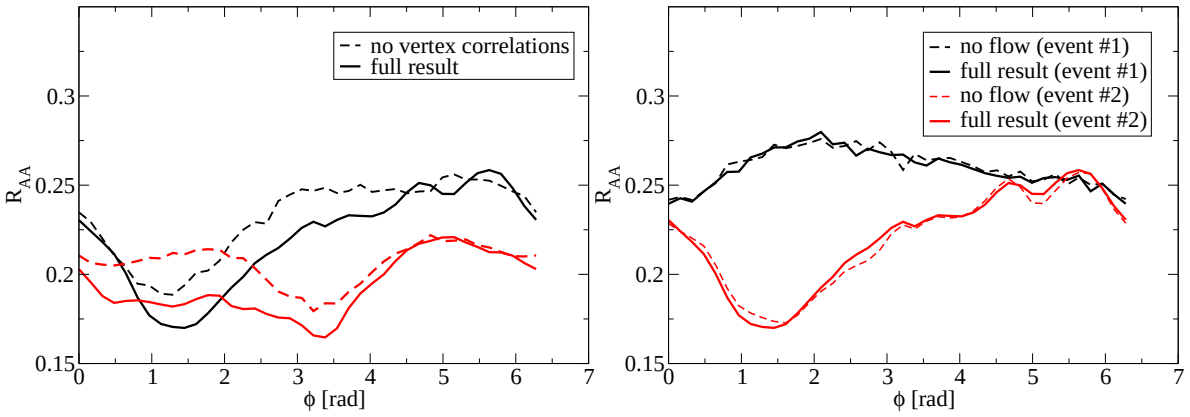

Figure 2. Left: $R_{AA}(\phi)$ computed in the ASW model for two different events, with (solid) and without (dashed) taking the correlation between binary collisions and hotspots into account. Right: same as left, but with (solid) and without (dashed) taking the irregular fluctuation-driven flow field into account.

In order to investigate the role of fluctuations, we use the ASW energy loss model in combination with a 2+1d ideal hydrodynamical model with initial state fluctuations and study $R_{AA}(\phi)$ at fixed $P_T = 10$ GeV [20]. In Fig. 2 we show for two events each the effects of the correlation of the production vertex with hotspots and of the irregular flow field. We find that both inter- and intra-event fluctuations are sizeable. The net effect of the correlation is indeed a downward shift of R_{AA} as expected, whereas the effect of the fluctuation-driven flow field is very mild. In central events the cancellation between nonlinearity and vertex-hotspot correlation is very good. When we perform a 20 event average and aim for a best fit to the data we obtain a K_{med} which is less than 20% different from the smooth case. In non-central collisions, the cancellation becomes imperfect and dependent on the size scale of the fluctuations, resulting in a decrease of suppression for small-scale fluctuations. This can potentially be used to constrain the physics origin of fluctuations. Our study would indicate relatively large-scale O(0.8) fm fluctuations. All in all, the observed magnitude of effects does not suggest that fluctuations in the hydrodynamical initial state are a sizeable effect for high P_T probes, thus conclusions obtained using smooth hydrodynamical models remain essentially valid.

Qualitatively similar results have also been obtained with the eMC model [16].

5. P_T dependence of R_{AA} at larger $\sqrt{s}$

As mentioned initially, for a steeply falling parton spectrum even small shifts in parton momentum lead to a large suppression in hadron yield, which makes observables at RHIC insensitive to details of the parton-medium interaction [7]. At LHC kinematics with 2.76 ATeV, this is no longer the case since the spectra are much harder. Thus, the P_T dependence of R_{AA} is now not only visible, but carries information about model details. However, in order to take advantage of this fact, one needs to overcome the ambiguity due to the modelling of the soft medium evolution. Ideally, one would like to run 'the same' hydro at larger $\sqrt{s}$ in order to connect with RHIC results, but in practice a hydro code does not take $\sqrt{s}$ as input parameter but rather an initial condition in terms of entropy distribution and thermalization time and a breakup condition. Thus, additional modelling is required to constrain the $\sqrt{s}$ dependence of these quantities.

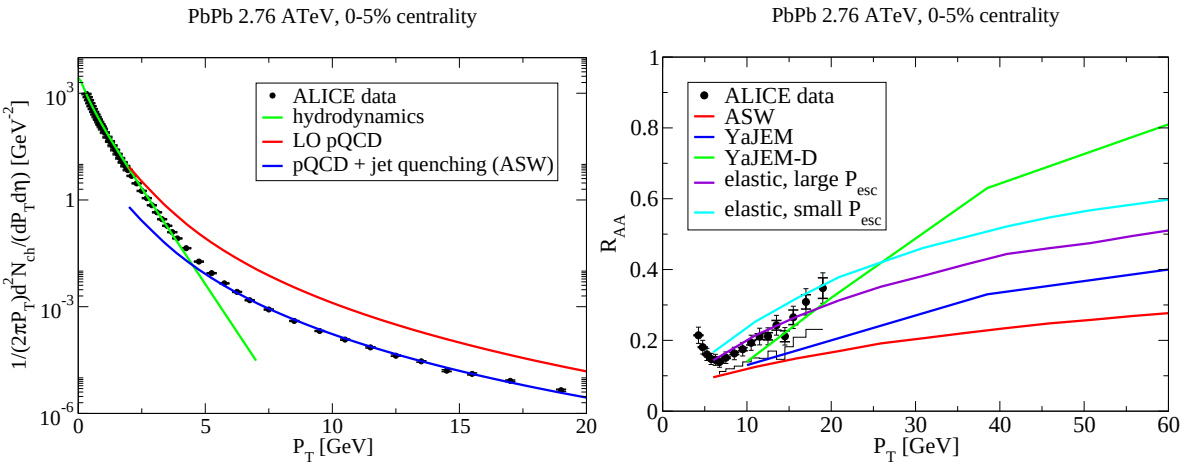

Figure 3.

Here, we use the EKRT initial state saturation model [22] and results from a dynamical freeze-out criterion [23] to constrain the extrapolation of the medium evolution from RHIC to LHC [24]. In Fig. 3 left, we demonstrate that this procedure combined with a pQCD + parton-medium interaction component can give good agreement throughout the whole P_T range measured by the ALICE collaboration [25]. In Fig. 3 right, we show that, as expected, the various parton medium interaction models tuned to RHIC data predict very different results at LHC kinematics. While currently a large systematic uncertainty in the measurement prevents any firm conclusions, this shows, in combination with pathlength dependent observables, the potential to uncover that nature of the parton-medium interaction.

6. Conclusions

While fully reconstructed jets are the observable most closely reflecting the QCD dynamics of parton evolution in the medium, they also suffer from conceptual problems separating jet from medium at soft scales. In contrast, the study presented here demonstrates that a systematic investigation of model combinations against a significant body of single inclusive high P_T hadron data (as well as correlation) has the potential to identify or at least significantly constrain the physics of parton-medium interaction without running into scale sepataion problems. Future high-precision data from the LHC experiments will therefore quickly identify viable models for jet productions in medium if the constraints from leading hadron and hadron correlation physics are taken seriously.

Acknowledgements

Fruitful collabortion with K. J. Eskola, H. Holopainen, J. Auvinen, R. Paatelainen, C. Marquet, U. Heinz and C. Shen is gratefully acknowledged. This work is supported by the Academy Researcher program of the Finnish Academy (Project 130472).

[1] M. Gyulassy and X. N. Wang, Nucl. Phys. **B420**, 583 (1994).
[2] R. Baier, Y. L. Dokshitzer, A. H. Mueller, S. Peigne and D. Schiff, Nucl. Phys. **B484**, 265 (1997).
[3] B. G. Zakharov, JETP Lett. **65**, 615 (1997).
[4] U. A. Wiedemann, Nucl. Phys. **B588**, 303 (2000).
[5] M. Gyulassy, P. Levai and I. Vitev, Nucl. Phys. **B594**, 371 (2001).
[6] X. N. Wang and X. F. Guo, Nucl. Phys. **A696**, 788 (2001).
[7] T. Renk, Phys. Rev. **C74** , 034906 (2006).
[8] C. Nonaka, S. A. Bass, Phys. Rev. **C75** , 014902 (2007).
[9] K. J. Eskola, H. Honkanen, H. Niemi, P. V. Ruuskanen, S. S. Rasanen, Phys. Rev. **C72** , 044904 (2005); H. Holopainen, H. Niemi, K. J. Eskola, Phys. Rev. **C83**, 034901 (2011).
[10] H. Song and U. W. Heinz, Phys. Lett. **B 658** 279 (2008); Phys. Rev. **C 77** 064901 (2008); Phys. Rev. **C78** 024902 (2008).
[11] T. Renk, Phys. Rev. **C78**, 034908 (2008).
[12] T. Renk, Phys. Rev. **C79**, 054906 (2009).
[13] T. Renk, Phys. Rev. **C83**, 024908 (2011).
[14] C. A. Salgado and U. A. Wiedemann, Phys. Rev. D **68**, 014008 (2003).
[15] T. Renk, Phys. Rev. **C76** , 064905 (2007).
[16] J. Auvinen, these proceedings.
[17] C. Marquet, T. Renk, Phys. Lett. **B685** , 270-276 (2010).
[18] T. Renk, K. Eskola, Phys. Rev. **C75**, 054910 (2007).
[19] T. Renk, H. Holopainen, U. Heinz, C. Shen, Phys. Rev. **C83** , 014910 (2011).
[20] T. Renk, H. Holopainen, J. Auvinen, K. J. Eskola, [arXiv:1105.2647 [hep-ph]].
[21] S. Afanasiev *et al.* [PHENIX Collaboration], Phys. Rev. C **80**, 054907 (2009).
[22] K. J. Eskola, K. Kajantie, P. V. Ruuskanen and K. Tuominen, Nucl. Phys. **B570**, 379-389 (2000).
[23] K. J. Eskola, H. Niemi, P. V. Ruuskanen, Phys. Rev. **C77**, 044907 (2008).
[24] T. Renk, H. Holopainen, R. Paatelainen, K. J. Eskola, [arXiv:1103.5308 [hep-ph]].
[25] K. Aamodt *et al.* [ALICE Collaboration], Phys. Lett. **B696**, 30-39 (2011).

Underlying Events in pp Collisions at LHC Energies

András G. Agócs[1,2], Gergely G. Barnaföldi[1] and Péter Lévai[1]

[1]KFKI Research Institute for Particle and Nuclear Physics of the HAS
29-33 Konkoly-Thege Miklós Str. H-1121 Budapest.

[2]Eötvös University, Faculty of Sciences
1/A Pázmány Péter sétány, H-1117 Budapest.

E-mail: agocs@rmki.kfki.hu

Abstract. Hadron production is investigated in proton-proton (pp) collisions at $\sqrt{s} = 7$ TeV LHC energy – especially outside the cones of identified jets. We improved the original CDF definition of underlying event and introduce surrounding rings/belts (SB) around the cone of identified jets. We compare the characteristics of hadron production using the original CDF-based and the new SB-based via analysing PYTHIA generated fluxes of these hadrons within the geometrical regions of pp collisions.

1. Introduction

The physics of hadron showers (jets) started with the analysis of earlier LEP and TEVATRON experiments and have been continued by the measurements of the RHIC at BNL and the LHC at CERN. During the last two decades these experiments mainly focus on electron-positron (e^-e^+) and proton-(anti)proton (pp,$p\bar{p}$) collisions and tested successfully various methods of jet-identification in these reactions.

Investigating jets – created in high-energy hadron-hadron collisions – is a golden way to understand the complex physics of strong interaction and even theories beyond the Standard Model. Recent state-of-the-art analysis techniques [1, 2] reached the point to able to analyse events more deeply: the inner structure of jets, surrounding area of hadron showers, off-jet directions in nucleon-nucleon, and jet-matter interaction in nucleus-nucleus collisions. These latter studies are in the liu of the Quark Gluon Plasma (QGP) researches, which strongly require the separation or at least estimation of non-perturbative, soft background part of the reactions.

To identify soft or semi-hard remnants of a high-energy collision the Underlying Event (UE) was introduced by the CDF Collaboration at TEVATRON energies [3]. Since multiple jet events were very rare, then UE has denoted the remaining hadrons of a $p\bar{p}$ collisions, after a leading jet was identified. The CDF-definition corresponds to jet identification in one-jet events, where the second jet is assumed to move automatically into the away side. The CDF definition can be generalize to apply for multi-jet events via introducing and investigate Surrounding Belts (SB) around identified jets [4, 5]. The comparison of the two methods is presented here on a PYTHIA generated data sample.

2. The New Definition of UE and the Concept

The CDF definition of the underlying event is a simple and practical tool since opens the jet (and the away-jet) angle acceptances to the maximum sizes: 1/3 to the near and 1/3 to the away, finally 1/3 for the two transverse regimes named as the UE. Moreover, the CDF event geometry can be fixed easily, since the position of the leading jet defines the *toward region*, and the *away region* will be chosen respectively [3]. Thus, hadrons moving to the *transverse directions* are assigned to be off-jet, background particles. The weakness of the CDF-based UE definition is: it assumes a single or back-to-back jet-event situation, which not always the case at higher energies. In case of multiple jets or jet-matter interaction with secondary collisions the hadron content of the CDF-regions would mixed up. The question is: how can we identify and separate these?

Our idea was to the improved and develop a new UE definition, which is strongly connected to the identified jets (excluding all hadrons from all identified jets), independently on the number of jets. Moreover, jet-matter-interaction secondaries can be also separated and investigated within the surrounding areas around identified jets. By this method the study of pp and AA collisions can be done in the same framework without major changes in jet-finding parameters.

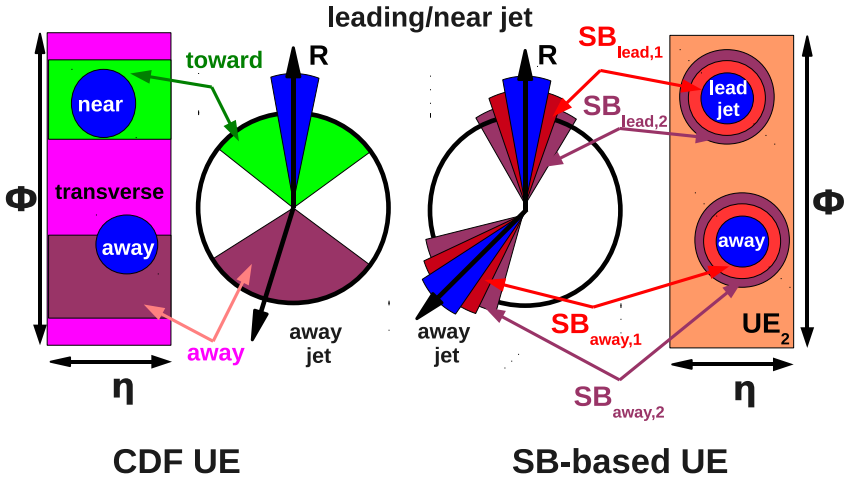

Figure 1. (*Color online.*) The schematic view of the underlying event (UE) defined by the CDF-method (left) and the SB-method (right). Details can be found in Ref. [7].

We introduced a new definition in Refs. [4, 5, 6, 7] in agreement with the layout of the Fig. 1. The left side of displays the CDF-based definition in contrast on the right side SB-based UE is plotted. As it can be seen on Fig. 1, the main difference between the two definition is the multiple application of the jet identification with jet-cone angle $R = \sqrt{\Delta\Phi^2 + \Delta\eta^2}$, then setting an approximate dial-like area, around which concentric bands (or rings), nominated as 'SB_1' and 'SB_2' surrounding belts. The thickness of $\delta R_{SB1} = \delta R_{SB2}$ is about 0.1 at jet-cone values $R = [0.5, 1]$.

3. The Analysis of Underlying Event Definitions

One of the aims of SB-based definition is to separate the jet-like particles from the soft or semi-hard ones. This can be carry out via a comparison of physical quantities e.g.: (i) the average hadron flux within the defined areas relative to the total event multiplicities, and (ii) the flux of the transverse momentum distributions in the discussed regions. Below we recall the original CDF-based and our new SB-based definitions in order to test the validity of the SB-based definition.

We performed an extended study on an earlier SB-based analysis of a simulated data set for pp collisions at 7 TeV – similar to which was published in Refs. [6, 7]. We analysed a data set of 739 500 pp events created by PYTHIA-6 simulation [8], applying the Perugia tune [10]. This sample is similar to the LHC10e14 sample calculated within the ALICE experiment's framework. In the data samples jets are identified by the UA1 method [9], setting $R = 0.4$. We restrict our analysis to a limited sample, where the cuts of $p_{THardMin} = 10$ GeV/c and $p_{THardMax} = 20$ GeV/c have been applied. Applying the cuts we got around 174 452 events, which contains at least one jet partially. Calculating hadron fluxes within the selected specific regions, proper determination of the areas needed. In parallel, selected jets identified or measured partially in the ALICE TPC's acceptance must be counted correctly as well.

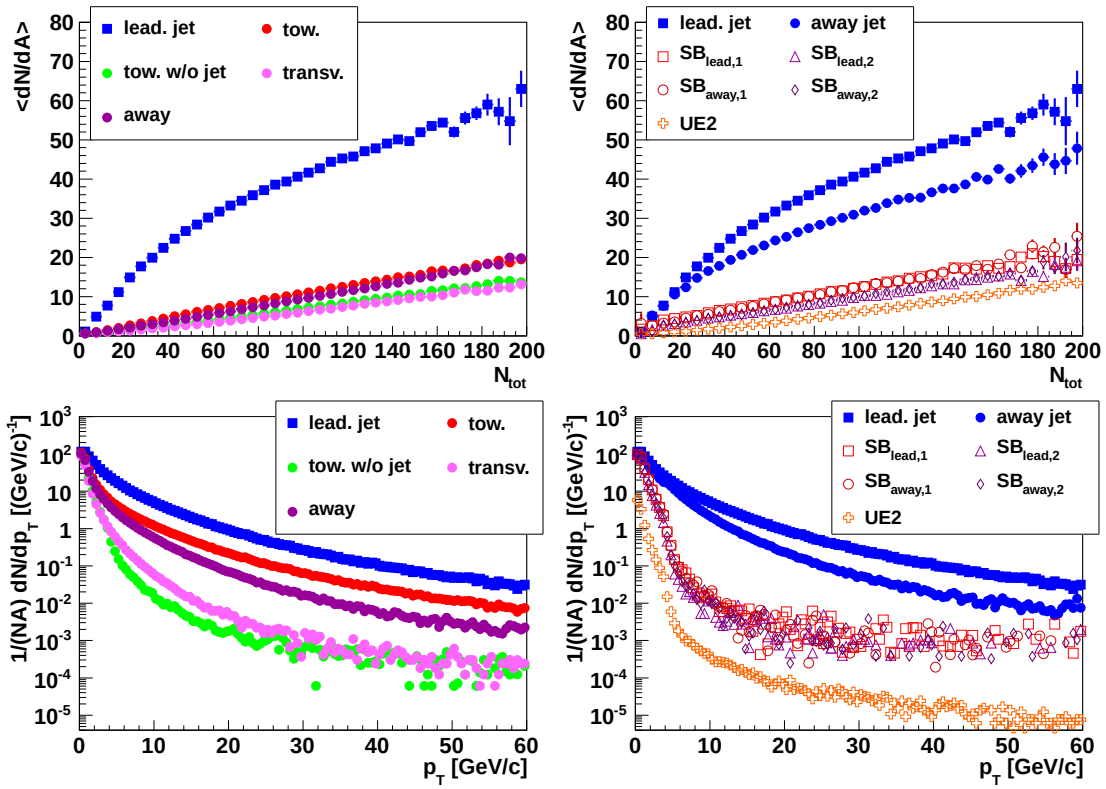

Figure 2. (*Color online.*) *Upper panels*: The charged hadron multiplicity fluxes, dN_i/dA, of the selected areas depending on the total multiplicities of the events, N_{tot}. *Lower panels*: transverse momentum distribution of hadron fluxes. *Left panels* are for CDF-based; *right panels* are for SB-based results. Details can be found in the text.

4. Results and Conclusions

We compared on Fig. 2 the CDF-based (*left*) and SB-based (*right*) definitions applying on *pp* collisions at 7 TeV center of mass energy. *Upper panels* present the charged hadron multiplicity fluxes, dN_i/dA vs. the number of total multiplicity, N_{tot}. *Lower panels* are for the transverse momentum distribution of hadron fluxes in the given regions.

Upper panels of Fig. 2 show the charged hadron multiplicities fluxes were find to be quite similar for both definition on the data sample. The jet-content areas (*blue full squares for near and dots for away sides*) clearly separated with higher flux. Away side (*purple full dots*), surrounding belts (*open circles and triangles*), and underlying event (*pink dots for CDF and orange open crosses for SB*) give similar fluxes in both cases in decreasing order. In both cases the UE has the smallest flux proportional to the N_{tot}. In this way the two definitions give the same result.

The p_T distributions of fluxes for the selected areas are given on the *lower panels* of Fig. 2 using the same notations and colors as above. Similarly to the *upper panels* the distributions are higher for the jet-content areas and getting smaller to the direction of away side, surrounding belts, and underlying event. It is interesting to see for the SB-based case all spectra almost the same, but the separation of jet-content, SBs, and UE are well defined. Moreover, the shapes of the curves clearly reflect the origin of the hadrons: jet-content distributions are power-law like, but the SBs and UE areas are exponential at lower p_Ts, indicating the bulk origin of the hadrons found in these areas.

Summarizing: the SB-method, especially p_T distributions of fluxes gives sophisticated separation of the charged hadron yields from different regions and its general use is support to study the properties of UE and any jet-matter interactions inside the SBs.

Acknowledgments

This work was supported by Hungarian OTKA NK77816, PD73596 and Eötvös University. Author GGB thanks for the János Bolyai Research Scholarship of the HAS.

References

[1] G. P. Salam, Eur. Phys. J. **C67**, (2010) 637.
[2] M. Cacciari, G. P. Salam, S. Sapeta, JHEP **1004**, (2010) 065.
[3] A. A. Affolder *et al.* [CDF Collaboration], Phys. Rev. **D65**, (2002) 092002.
[4] P. Lévai and A. G. Agócs, PoS **EPS-HEP2009**, (2009) 472.
[5] A. G. Agócs, G. G. Barnaföldi, and P. Lévai, J. Phys. Conf. Ser. **270**, (2011) 012017.
[6] G. G. Barnaföldi, A. G. Agócs, and P. Lévai, AIP Conf. Proc. **1348**, (2011) 124.
[7] A. G. Agócs, G. G. Barnaföldi, and P. Lévai, HCBM 2010, Budapest, Hungary, Edited by T.S. Biró; G.G. Barnaföldi; EPJ Web of Conferences, **13**, (2011) 04006.
[8] T. Sjöstrand, S. Mrenna, and P. Z. Skands, JHEP **0605**, (2006) 026.
[9] G. Arnison *et al.* [UA1 Collaboration], CERN-EP/83-118; Phys. Lett. **B132**, (1983) 214.
[10] P. Z. Skands, MCNET-10-08; CERN-PH-TH-2010-113; Phys. Rev. **D82**, (2010) 074018.

Measuring Parton Energy Loss at RHIC compared to LHC

M. J. Tannenbaum†, PHENIX Collaboration

Physics Department, Brookhaven National Laboratory, Upton, NY 11973-5000, USA

E-mail: mjt@bnl.gov

Abstract. The method of measuring $\hat{x}_h = \hat{p}_{Ta}/\hat{p}_{Tt}$, the ratio of the away-parton transverse momentum, $\hat{p}_{T_a}$, to the trigger-parton transverse momentum, $\hat{p}_{T_t}$, using two-particle correlations at RHIC, will be reviewed. This measurement is simply related to the two new variables introduced at LHC for the di-jet fractional transverse momentum imbalance: ATLAS $A_J = (\hat{p}_{Tt} - \hat{p}_{Ta})/(\hat{p}_{Tt} + \hat{p}_{Ta}) = (1 - \hat{x}_h)/(1 + \hat{x}_h)$; and CMS $\langle(\hat{p}_{Tt} - \hat{p}_{Ta})/\hat{p}_{Tt}\rangle = \langle 1 - \hat{x}_h\rangle$. Results from two-particle correlations at RHIC for $\hat{x}_h$ in p-p and A+A collisions will be reviewed and new results will be presented and compared to LHC results. The importance of comparing any effect in A+A collisions to the same effect effect in p-p collisions will be illustrated and emphasized.

1. Introduction

In 1998, at the QCD workshop in Paris, Rolf Baier asked me whether jets could be measured in Au+Au collisions because he had a prediction of a QCD medium-effect (energy loss via soft gluon radiation induced by multiple scattering [1] on color-charged partons traversing a hot-dense-medium composed of screened color-charges [2]). I told him [3] that there was a general consensus [4] that for Au+Au central collisions at $\sqrt{s_{NN}} = 200$ GeV, leading particles are the only way to study jets, because in one unit of the nominal jet-finding cone, $\Delta r = \sqrt{(\Delta\eta)^2 + (\Delta\phi)^2}$, there is an estimated $\pi\Delta r^2 \times \frac{1}{2\pi}\frac{dE_T}{d\eta} \sim 375$ GeV of energy !(!) The good news was that hard-scattering in p-p collisions was originally observed by the method of leading particles and that these techniques could be used to study hard-scattering and jets in Au+Au collisions [5].

2. Hard scattering via single particle inclusive and two-particle correlation measurements

Single particle inclusive and two-particle correlation measurements of hard-scattering have provided a wealth of discoveries at RHIC. Due to the steeply falling power-law invariant transverse momentum spectrum of the scattered parton, $\hat{p}_{T_t}^{-n}$, the inclusive single particle (e.g. π^0) p_{T_t} spectrum from jet fragmentation is dominated by fragments

† Supported by the U.S. Department of Energy, Contract No. DE-AC02-98CH1-886.

with large $z_{\rm trig}$, where $z_{\rm trig} = p_{T_t}/\hat{p}_{T_t}$ is the fragmentation variable, and exponential fragmentation $D_q^{\pi^0}(z) \sim e^{-bz}$ is assumed. This gives rise to several effects which allow precision measurements of hard scattering to be made using single inclusive particle spectra and two particle correlations [6, 7].

The prevailing opinion from the 1970's until quite recently was that although the inclusive single particle (e.g. π^0) spectrum from jet fragmentation is dominated by trigger fragments with large $\langle z_{\rm trig}\rangle \sim 0.6-0.8$, the away-jets should be unbiased and would measure the fragmentation function, once the correction is made for $\langle z_{\rm trig}\rangle$ and the fact that the jets don't exactly balance p_T due to the k_T smearing effect [8]. Two-particle correlations with trigger p_{T_t}, are analyzed in terms of the two variables: $p_{\rm out} = p_T \sin(\Delta\phi)$, the out-of-plane transverse momentum of an associated track with p_T; and x_E, where:

$$x_E = \frac{-\vec{p}_T \cdot \vec{p}_{Tt}}{|p_{Tt}|^2} = \frac{-p_T \cos(\Delta\phi)}{p_{Tt}} \simeq \frac{z}{z_{\rm trig}}$$

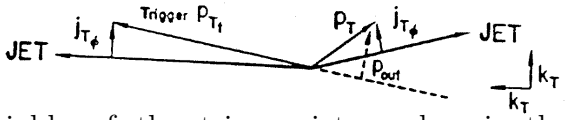

$z_{\rm trig} \simeq p_{Tt}/p_{T\rm jet}$ is the fragmentation variable of the trigger jet, and z is the fragmentation variable of the away jet.

However, in 2006, it was found by explicit calculation that this is not true [9, 6, 7]. The shape of the p_{T_a} spectrum of fragments (from the away-side parton with $\hat{p}_{T_a}$), given a trigger particle with p_{T_t} (from a trigger-side parton with $\hat{p}_{T_t}$), is not sensitive to the shape of the fragmentation function (b), but measures the ratio of $\hat{p}_{T_a}$ of the away-parton to $\hat{p}_{T_t}$ of the trigger-parton and depends only on the same power n as the invariant single particle spectrum:

$$\left.\frac{dP_{p_{T_a}}}{dx_E}\right|_{p_{T_t}} \approx \langle m\rangle\,(n-1)\frac{1}{\hat{x}_h}\frac{1}{(1+\frac{x_E}{\hat{x}_h})^n} \qquad . \tag{1}$$

This equation gives a simple relationship between the ratio, $x_E \approx p_{T_a}/p_{T_t} \equiv z_T$, of the transverse momenta of the away-side particle to the trigger particle, and the ratio of the transverse momenta of the away-jet to the trigger-jet, $\hat{x}_h = \hat{p}_{T_a}/\hat{p}_{T_t}$. The only dependence on the fragmentation function is in the mean multiplicity $\langle m\rangle$ of jet fragments. This functional form was shown previously [9, 10] (and with the present data, see below) to describe the π^0 triggered x_E distribution in p-p collisions and is based only on the following simplifying assumptions: the hadron fragment is assumed to be collinear with the parton direction; the underlying fragmentation functions ($D(z)$) are assumed to be exponential; and for a given p_{T_t}, $\hat{x}_h$ is taken to be constant as a function of x_E over the range of interest. The key issue with Eq. 1 is that it is independent of the slope of an exponential fragmentation function, and only depends on the detected mean multiplicity $\langle m\rangle$ of the jet, the power, n, of the inclusive p_{T_t} spectrum and the ratio of the away jet to the trigger jet transverse momenta, $\hat{x}_h$.

3. Fits to PHENIX π^0-h correlations

The two-particle correlation distributions from π^0 triggers in four intervals of p_{T_t}, 4-5, 5-7, 7-9 and 9-12 GeV/c, with charged hadrons in a fixed range of of associated transverse

momenta, $p_{T_a} \approx 0.7, 1.3, 2.3, 3.5, 5.8$ GeV/c were recently published by PHENIX [11] in terms of the ratio of A+A to p-p collisions, $I_{AA}(p_{T_a})|_{p_{T_t}} = \left.\frac{dP^{AA}/dp_{Ta}}{dP^{pp}/dp_{Ta}}\right|_{p_{T_t}}$ (see Fig. 1).

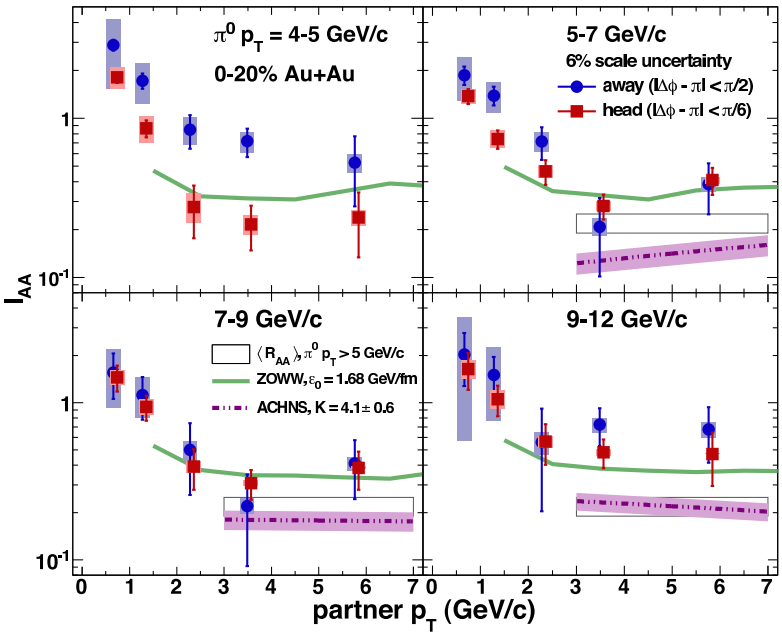

Figure 1. Away-side I_{AA} [11] for a narrow "head" $|\Delta\phi - \pi| < \pi/6$ selection (solid squares) and the entire away-side, $|\Delta\phi - \pi| < \pi/2$ (solid circles) as a function of partner momentum p_{T_a} for various trigger momenta p_{T_t}. Only the head region was used for the present analysis.

We now analyze these distributions separately for p-p and Au+Au collisions, with the statistical error and the larger of the ± systematic errors of the data points added in quadrature. The p-p and Au+Au distributions in $z_T = p_{T_a}/p_{T_t}$ were fit to the formula [9]:

$$\left.\frac{dP_\pi}{dz_T}\right|_{p_{T_t}} = N\,(n-1)\frac{1}{\hat{x}_h}\frac{1}{(1+\frac{z_T}{\hat{x}_h})^n} \qquad , \tag{2}$$

with a fixed value of $n = 8.10$ (± 0.05) as previously determined [12] , where n is the power-law of the inclusive π^0 spectrum and is observed to be the same in p-p and Au+Au collisions in the p_{T_t} range of interest. The fitted value for N is the integral of the z_T distribution which equals $\langle m \rangle$, the mean multiplicity of the away jet in the PHENIX detector acceptance, and $\hat{x}_h \equiv \hat{p}_{T_a}/\hat{p}_{T_t}$ is the ratio of the away jet to the trigger jet transverse momenta.

Fits were performed for the p-p spectra; and also for the Au+Au spectra at two centralities: 0-20% and 20-40% upper-percentiles. The parameters of the p-p distribution, $\hat{x}_h^{pp}$ and N_{pp}, are determined by fits of Eq. 2 to the p-p data for the four intervals of p_{T_t}; and the parameters $\hat{x}_h^{AA}$ and N_{AA} are determined from the fits to the Au+Au distributions. The fits were performed only for the narrower "head" region, $|\Delta\phi - \pi| < \pi/6$. It should be noted that in Fig. 1, there is no difference in the results (I_{AA}) for the full away side and the head region, for $p_{T_t} \geq 7$ GeV/c, because the non-jet

background becomes sufficiently small so that the "shoulder" [13], now known to be due to a v_3 background modulation [14] for which no correction has been applied in this data, contributes negligibly to the away-side yield.

4. Results of the fits

Examples of the fits for $7 < p_{T_t} < 9$ GeV/c for p-p collisions and Au+Au 0–20% and 20–60% are shown in Figs. 2a and b, respectively. The results for the fitted parameters

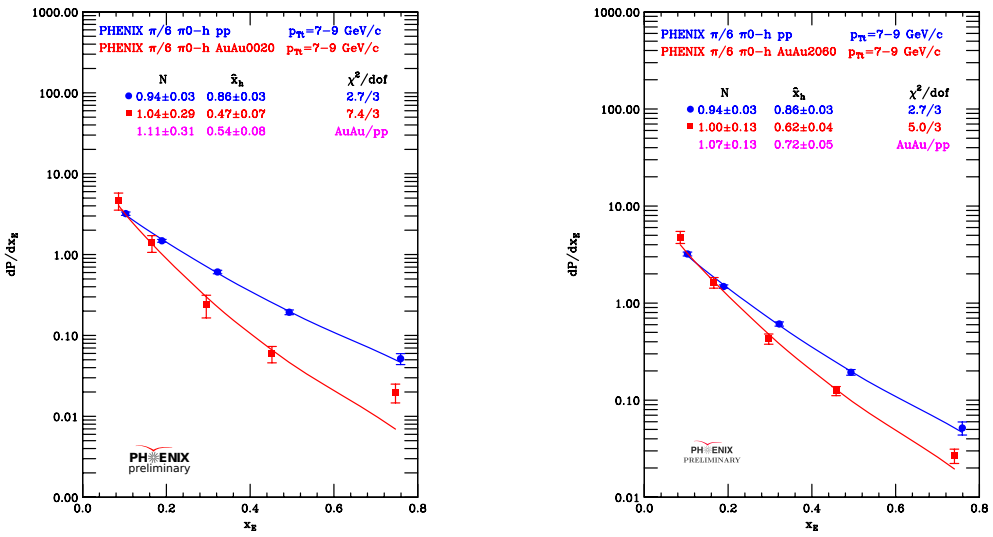

a) b)

Figure 2. p-p (blue circles) and AuAu (red squares) $z_T = p_{T_a}/\langle p_{T_t}\rangle$ distributions for $p_{T_t} = 7 - 9$ GeV/c ($\langle p_{T_t}\rangle = 7.71$ GeV/c), together with fits to Eq. 2 p-p (solid blue line), AuAu (solid red line) with parameters indicated: a) 00-20% centrality, b) 20–60% centrality. The ratios of the fitted parameters for AuAu/pp are also given.

are shown on the figures. In general the values of $\hat{x}_h^{pp}$ do not equal 1 but range between $0.8 < \hat{x}_h^{pp} < 1.0$ due to k_T smearing and the range of z_T covered. For the fixed range of associated p_{T_a} $0.7 - 5.8$ GeV/c, the lowest $p_{T_t} = 4 - 5$ GeV/c trigger provides the most balanced same and away side jets, with $\hat{x}_h \approx 1.0$, while as p_{T_t} increases up to 9–12 GeV/c, for the fixed range of p_{T_a}, the jets become unbalanced towards the trigger side in p-p collisions due to k_T smearing. Thus, in the present data, the p_{T_t} and z_T ranges are identical for the p-p and Au+Au comparison. Furthermore, in order to take account of the imbalance ($\hat{x}_h^{pp} < 1$) observed in the p-p data, the ratio $\hat{x}_h^{AA}/\hat{x}_h^{pp}$ is taken as the measure of the energy of the away jet relative to the trigger jet in A+A compared to p-p collisions.

It is important to note that the away jet energy fraction in AuAu relative to p-p, $\hat{x}_h^{AA}/\hat{x}_h^{pp} = 0.47/0.86 = 0.54 \pm 0.08$ in Fig. 2a, is significantly less than 1, indicating energy loss of the away jet in the medium. Also since the away-jet may suffer different

energy losses for a given trigger jet $\hat{p}_{T_t}$ due to variations in the path-length through the medium, $\hat{x}_h^{AA}$ should be understood as $\left\langle \hat{x}_h^{AA} \right\rangle$.

5. LHC Results

In very exciting first results from the LHC heavy ion program, ATLAS [15] observed dijet events in Pb+Pb central collisions at $\sqrt{s_{\rm NN}} = 2.76$ TeV with a large energy asymmetry which they characterized by a new quantity $A_J = (1-\hat{x}_h^{AA})/(1+\hat{x}_h^{AA})$. Shortly thereafter, CMS [16] presented a plot of $\langle 1 - p_{t,2}/p_{t,1} \rangle = 1 - \left\langle \hat{x}_h^{AA} \right\rangle$, the fractional jet imbalance as a function of E_{T1} up to 200–220 GeV with a cut $E_{T2} \geq 50$ GeV (Fig. 3). If there were no cuts on the p-p jets used in this measurement, then this variable should be identical to the one we call $1 - \hat{x}_h^{AA}/\hat{x}_h^{pp}$, the away-parton fractional energy loss (or imbalance) in A+A relative to p-p. However, due to the cut used in the CMS data, the sample of di-jets

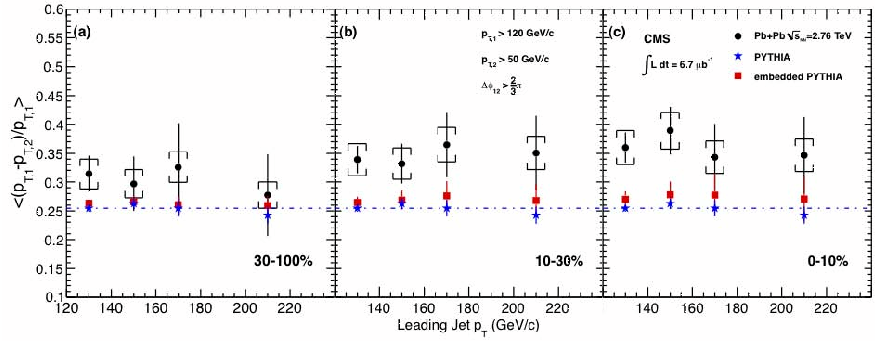

Figure 3. CMS [16] plot of $\langle 1 - p_{t,2}/p_{t,1} \rangle$, the fractional jet imbalance, as a function of $p_{T,1}$ for 3 centralities in p-p and Pb+Pb collisions.

in p-p used to compare with A+A suffers from a large imbalance of 0.25, independent of E_{T1} (Fig. 3). We correct this by calculating $\hat{x}_h^{AA}$ and $\hat{x}_h^{pp}$ for CMS from their given values of $1-\hat{x}_h^{AA}$ and $1-\hat{x}_h^{pp}$ and then correcting to $1-\hat{x}_h^{AA}/\hat{x}_h^{pp}$. For instance, in Fig. 3c for $E_{T1} = 130$ GeV, $\langle 1 - \hat{x}_h^{pp} \rangle = 0.255$ (i.e. $\langle \hat{x}_h^{pp} \rangle = 0.745$), while $\left\langle 1 - \hat{x}_h^{AA} \right\rangle = 0.36$ (i.e. $\left\langle \hat{x}_h^{AA} \right\rangle = 0.64$), so that $1 - \left\langle \hat{x}_h^{AA} \right\rangle / \langle \hat{x}_h^{pp} \rangle = 1 - (0.64/0.745) = 0.141$.

The corrected points are shown together with the PHENIX data for $1 - \hat{x}_h^{AA}/\hat{x}_h^{pp}$, which we denote for simplicity $\langle 1 - \hat{x}_h \rangle$, the observed fractional jet imbalance in A+A relative to p-p (Fig. 4). Of course the CMS result is directly measured with jets, while the PHENIX value is deduced from the fragments of the dijets using a few simple assumptions, as noted above. The PHENIX data are plotted at the presumed mean trigger parton transverse momentum $\langle \hat{p}_{T_t} \rangle = p_{T_t} / \langle z_{\rm trig} \rangle$, where the average fragmentation fraction of the trigger particle, $\langle z_{\rm trig} \rangle \approx 0.7$, was derived in Ref. [9]. There is a clear difference in fractional jet imbalance in going from RHIC to LHC in central collisions—the jet-imbalance or fractional energy loss is much smaller at LHC. This is different from the first impression [15]. Also at RHIC, there is less fractional energy loss or jet imbalance in less central collisions.

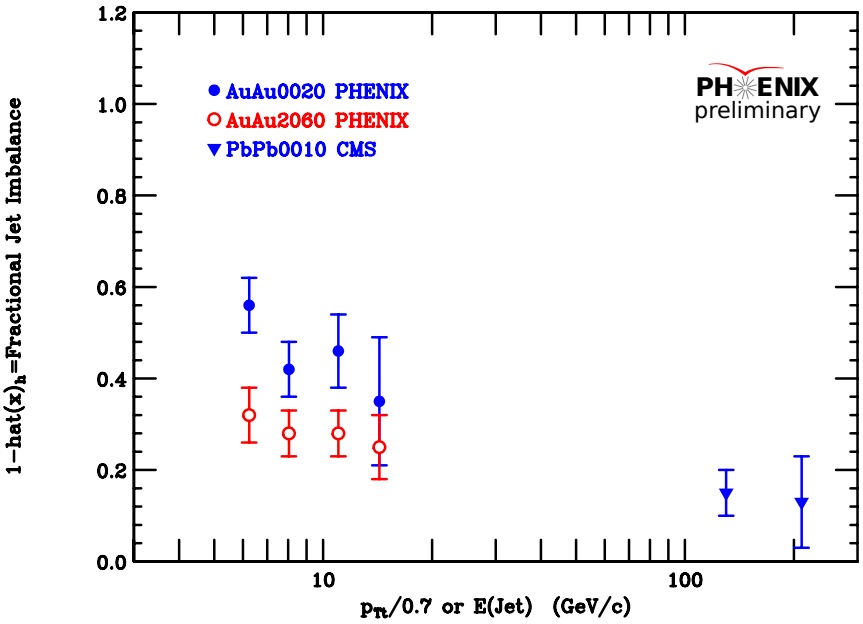

Figure 4. Away-jet fractional imbalance or energy loss in A+A relative to p-p, $1-\hat{x}_h$, as a function of $p_{T_t}/0.7$ for PHENIX and E(Jet) for CMS, with centralities indicated.

The large difference in fractional jet imbalance between RHIC and LHC c.m. energies could be due to the difference in jet $\hat{p}_{T_t}$ between RHIC ($\sim$ 20 GeV/c) and LHC ($\sim$ 200 GeV/c), the difference in n for the different $\sqrt{s}$, or to a difference in the properties of the medium. Future measurements will need to sort out these issues by extending both the RHIC and LHC measurements to overlapping regions of p_T.

References

[1] R. Baier, Yu. Dokshitzer, S. Peigné and D. Schiff, Phys. Lett. B**345**, 277–286 (1995).

[2] R. Baier *QCD, Proc. IV Workshop-1998 (Paris)* Eds, H. M. Fried, B. Müller (World Scientific, Singapore, 1999) pp 272–279.

[3] M. J. Tannenbaum *ibid.*, pp 280–285, pp 312–319.

[4] e.g. see *Proc. Int'l Wks. Quark Gluon Plsama Signatures (Strasbourg)* Eds. V. Bernard, *et al.*, (Editions Frontieres, Gif-sur-Yvette, France, 1999).

[5] M. J. Tannenbaum, Nucl. Phys. A**749**, 219c–228c (2005).

[6] See Ref. [7] for a more thorough treatment with a full list of references.

[7] M. J. Tannenbaum, PoS(CFRNC2006)001.

[8] R. P. Feynman, R. D. Field and G. C. Fox, Nucl. Phys. B**128**, 1–65 (1977).

[9] S. S. Adler, *et al.* PHENIX Collaboration, Phys. Rev. D**74**, 072002 (2006).

[10] A. Adare, *et al.* PHENIX Collaboration, Phys. Rev. D**82**, 072001 (2010).

[11] A. Adare, *et al.* PHENIX Collaboration, Phys. Rev. Lett. **104**, 252301 (2010).

[12] A. Adare, *et al.* PHENIX Collaboration, Phys. Rev. Lett. **101**, 232301 (2008).

[13] A. Adare, *et al.* PHENIX Collaboration, Phys. Rev. C**77**, 011901(R) (2008).

[14] A. Adare, *et al.* PHENIX Collaboration, arXiv:1105.3928v1, submitted to Phys. Rev. Lett.

[15] G. Aad, *et al.* (ATLAS Collaboration), Phys. Rev. Lett. **105**, 252303 (2010).

[16] The CMS Collaboration, arXiv:1102.1957v2, submitted to Phys. Rev. C.

Leading charged particle correlations at ALICE

F. Krizek for the ALICE collaboration

Department of Physics, P.O. Box 35, University of Jyväskylä, Jyväskylä 40014, Finland

E-mail: filip.krizek@cern.ch

Abstract. A leading charged particle correlation analysis was performed on $p+p$ data measured by the ALICE experiment at $\sqrt{s} = 7$ TeV. The main emphasis was on the x_{E} distributions for a given charged hadron trigger momentum p_{Tt}. It was observed that dN/dx_{E} is driven by the imbalance function at low x_{E}. At high x_{E} it shows exponential behavior and the extracted slope can be related to $\langle z_t \rangle$ of the trigger particle.

1. Introduction

In 2010, the ALICE collaboration at CERN collected a large amount of $p+p$ minimum bias data at $\sqrt{s} = 7$ TeV. We use the two-particle correlation method to study the hard scattering phenomena in a similar way as described e.g. in [1]. The leading charged particle (that with the highest transverse momentum p_{Tt} in an event) is paired with other tracks from the same event which have magnitude of transverse momentum in the range $p_{\mathrm{T,cut}} \leq p_{\mathrm{Ta}} \leq p_{\mathrm{Tt}}$. The lower cut, $p_{\mathrm{T,cut}} = 1$ GeV/c, was introduced to suppress uncorrelated background from soft QCD processes. Here we focus on an analysis of x_{E} distributions. The quantity x_{E} is defined as

$$x_{\mathrm{E}} \equiv -\frac{\vec{p}_{\mathrm{Tt}} \cdot \vec{p}_{\mathrm{Ta}}}{p_{\mathrm{Tt}}^2} = -\frac{p_{\mathrm{Ta}}}{p_{\mathrm{Tt}}} \cos\Delta\phi \tag{1}$$

where p_{Tt} and p_{Ta} are the trigger and associated transverse momenta and $\Delta\phi = \angle(\vec{p}_{\mathrm{Tt}}, \vec{p}_{\mathrm{Ta}})$ is the angle between them. The subtraction of the remaining background from the measured dN/dx_{E} distributions will be discussed later.

In earlier work at CCOR [2], the x_{E} quantity was used to estimate the fragmentation variable of the away side jet $z_{\mathrm{a}} \simeq p_{\mathrm{Ta}}/\hat{p}_{\mathrm{Ta}}$, where $\hat{p}_{\mathrm{Ta}}$ is the initial transverse momentum of a parton fragmenting into the associated hadron with a momentum p_{Ta}. At that time it was assumed that fragmentation on the trigger side does not affect fragmentation on the away side. In the limit of back-to-back jets, the fragmentation variable of the away side jet would then be equal to x_{E} corrected for the mean energy fraction carried by the trigger particle $\langle z_{\mathrm{t}} \rangle$, as can be seen from the following chain of limits

$$x_{\mathrm{E}} \equiv -\frac{\vec{p}_{\mathrm{Tt}} \cdot \vec{p}_{\mathrm{Ta}}}{p_{\mathrm{Tt}}^2} \xrightarrow{\Delta\phi\to\pi} \frac{\hat{p}_{\mathrm{Ta}} z_{\mathrm{a}}}{\hat{p}_{\mathrm{Tt}} \langle z_{\mathrm{t}} \rangle} \xrightarrow{k_{\mathrm{T}}\to 0} \frac{z_{\mathrm{a}}}{\langle z_{\mathrm{t}} \rangle} \xrightarrow{z_{\mathrm{t}}\to 1} z_{\mathrm{a}} \tag{2}$$

where $z_{\rm t} \simeq p_{\rm Tt}/\hat{p}_{\rm Tt}$ denotes the trigger particle fragmentation variable. Partonic transverse momentum, which is responsible for the momentum imbalance ($\hat{x}_{\rm h} = \hat{p}_{\rm Ta}/\hat{p}_{\rm Tt} \neq 1$) and acoplanarity of the produced jets, is denoted $k_{\rm T}$. In the limit when $k_{\rm T}$ is small ($k_{\rm T} \ll p_{\rm T}$), both effects vanish and $\hat{x}_{\rm h} = 1$. The last limit, $z_{\rm t} \to 1$, corresponds to the situation when the trigger particle carries the whole energy of the initial parton or the trigger is a direct photon. However, it has been observed that in the case that the trigger and associated particle are hadrons, keeping $p_{\rm Tt}$ fixed while changing $p_{\rm Ta}$ changes not only $z_{\rm a}$ but also $z_{\rm t}$ [1]. Therefore $x_{\rm E}$ extracted from di-hadron correlations does not correspond to the fragmentation variable.

2. Results

The presented results are based on an analysis of $\approx 3 \times 10^8$ minimum bias $p+p$ events at $\sqrt{s} = 7$ TeV corresponding to about 5 nb^{-1}. Charged primary tracks were selected within $|\eta| < 0.8$ using the ALICE central tracking system [3].

The left panel of Fig. 1 shows an example of di-hadron $dN/d\Delta\phi$ distribution. Pairs which are used to construct the away side $dN/dx_{\rm E}$ distribution are located in the hatched region, ranging from $\Delta\phi = (0.5, 1.5)$ rad$/\pi$. The hatched peak corresponds to the pairs where the associated particles originate from the away side jet fragmentation and are thus correlated with the trigger in azimuth. The pedestal under the away side peak is populated by particles emerging from underlying events. These can involve processes such as initial state radiation or multi-partonic interactions which produce particles angularly uncorrelated with the trigger. Hence, the measured $dN/dx_{\rm E}$ distribution always contains contributions from pairs where associated particles are correlated (jet fragmentation) and uncorrelated (underlying event) with the trigger in azimuth. In this analysis, the latter contribution is considered as a background.

The background yield can be estimated assuming that this component is isotropic in $\Delta\phi$ and the transverse momentum distribution of associated particles from the underlying event for a fixed trigger $p_{\rm Tt}$ is known: $dN_{\rm bg}/dp_{\rm Ta}|_{p_{\rm Tt}} = B_{p_{\rm Tt}}(p_{\rm Ta})$. Under these assumptions we can write

$$\frac{dN_{\rm bg}}{dx_{\rm E}} \propto \int_{p_{\rm Tt,min}}^{p_{\rm Tt,max}} \int_{\pi/2}^{3\pi/2} \int_{p_{\rm T,cut}}^{p_{\rm Tt}} \frac{dN_{\rm trigg}}{dp_{\rm Tt}} \frac{dN_{\rm bg}}{dp_{\rm Ta}}\bigg|_{p_{\rm Tt}} \delta\left(x_{\rm E} + \frac{p_{\rm Ta}}{p_{\rm Tt}} \cos\Delta\phi\right) dp_{\rm Ta}\, d\Delta\phi\, dp_{\rm Tt}\,,$$

where $dN_{\rm trigg}/dp_{\rm Tt}$ is the distribution of the trigger transverse momentum within the range $p_{\rm Tt,min} < p_{\rm Tt} < p_{\rm Tt,max}$. The integration was performed over the available phase space such that the integral over $\Delta\phi$ covers the region below the away side peak and the associated transverse momentum is integrated only in the range $p_{\rm T,cut} < p_{\rm Ta} < p_{\rm Tt}$. The upper limit is dictated by the requirement that the trigger is the leading particle in the event and $p_{\rm T,cut}$ is the lower border of the selected $p_{\rm Ta}$ range. The Dirac δ-function selects pairs with a given $x_{\rm E}$ from the available phase space. Assuming that trigger transverse momentum follows a power-law distribution within the selected $p_{\rm Tt}$ bin, i.e.,

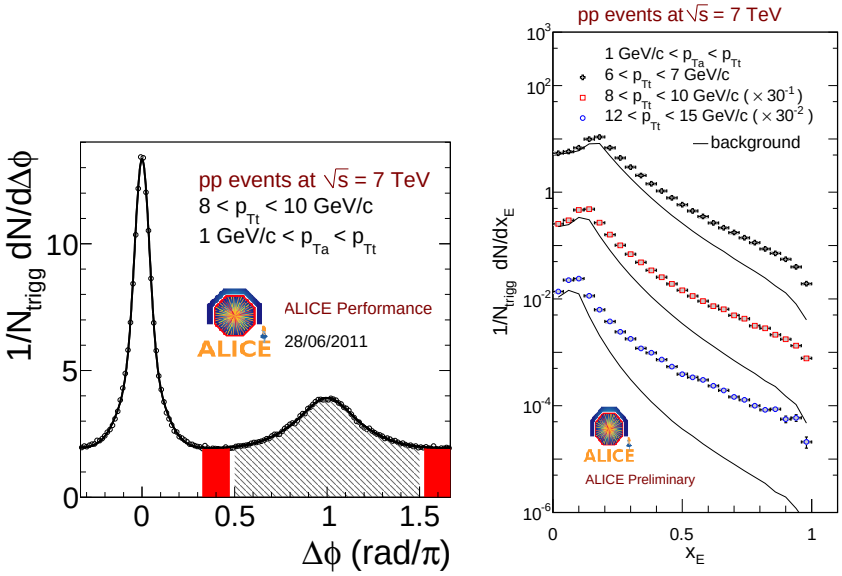

Figure 1. Left: An example of the per trigger normalized $dN/d\Delta\phi$ distribution. Here $\Delta\phi$ is the relative angle between associated particle and the trigger. Away side hemisphere is marked with the hatched area. The solid regions on both sides of the away side hemisphere mark the regions where we assume that the underlying event is the dominant source of associated particles. Right: Examples of measured $dN/dx_{\rm E}$ distributions for three trigger $p_{\rm Tt}$ bins. Transverse momenta of associated particles are in the range $1{\rm GeV}/c < p_{\rm Ta} < p_{\rm Tt}$. Solid lines represent corresponding background calculated according to (3). See text for more details.

$dN_{\rm trigg}/dp_{\rm Tt} \propto p_{\rm Tt}^{-n}$, we see that

$$\frac{dN_{\rm bg}}{dx_{\rm E}} \propto \int_{p_{\rm Tt,min}}^{p_{\rm Tt,max}} \int_{\Delta\phi_1}^{\Delta\phi_2} p_{\rm Tt}^{-n}\, B_{p_{\rm Tt}}\left(-x_{\rm E}\frac{p_{\rm Tt}}{\cos\Delta\phi}\right) \frac{p_{\rm Tt}}{\cos\Delta\phi}\, d\Delta\phi\, dp_{\rm Tt} \qquad (3)$$

where $\Delta\phi_1 = \arccos\left({\rm Max}\left[-x_{\rm E}\, p_{\rm Tt}/p_{\rm T,\,cut}\,;\,-1\right]\right)$ and $\Delta\phi_2 = \arccos(-x_{\rm E})$. The integration limits on $\Delta\phi$ follow from the condition $p_{\rm T,\,cut} \le p_{\rm Ta} \le p_{\rm Tt}$. Taking into account only such $p_{\rm Ta}$ for which the argument of the δ function equals zero we obtain $p_{\rm T,\,cut} \le -x_{\rm E}\, p_{\rm Tt}/\cos\Delta\phi \le p_{\rm Tt}$. Whence it can be seen that $\Delta\phi_1$ and $\Delta\phi_2$ have to fulfill $-\cos\Delta\phi_1 \le {\rm Min}\left[x_{\rm E}\, p_{\rm Tt}/p_{\rm T,\,cut}\,;1\right]$ and $x_{\rm E} \le -\cos\Delta\phi_2$. We assume that the function $B_{p_{\rm Tt}}(p_{\rm Ta})$ can be estimated with the $dN/dp_{\rm Ta}|_{p_{\rm Tt}}$ spectrum of the associated particles that are in the two regions around the minima of $dN/d\Delta\phi$ distribution for a given trigger bin, as shown in the left panel of Fig. 1. Associated particles which contribute to these $\Delta\phi$ regions are assumed to originate mainly from the underlying event. The number of pairs which form the background is equal to the number of pairs under the pedestal below the away side peak in $dN/d\Delta\phi$ distribution. Examples of the measured $dN/dx_{\rm E}$ distributions together with the corresponding background calculated according to (3) are shown in the right panel of Fig. 1.

In the left panel of Fig. 2 we present background subtracted $dN/dx_{\rm E}$ distributions. For clarity, spectra are scaled down by factors of five as otherwise they would be difficult to distinguish from one another. In order to quantify this scaling, the tail of the

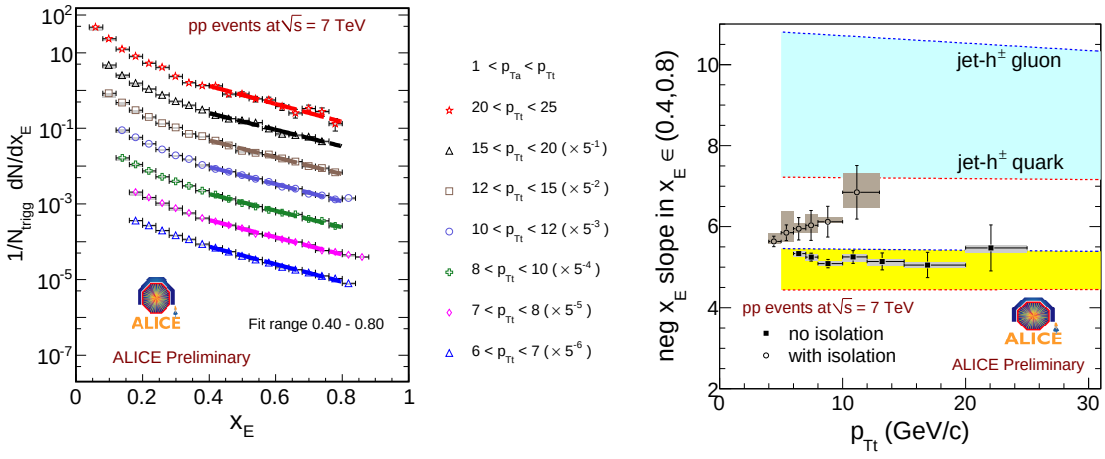

Figure 2. Left: Per trigger normalized background subtracted dN/dx_{E} distributions for several trigger p_{Tt} bins. The trigger was a non-isolated leading charged hadron in the pseudorapidity range $|\eta| < 0.8$. Distributions are fit with an exponential function in the range $x_{\mathrm{E}} \in (0.4, 0.8)$. Transverse momenta given in the legend are in units of GeV/c. Right: Negative x_{E} slopes obtained from a fit of dN/dx_{E} distributions in the range $x_{\mathrm{E}} \in (0.4, 0.8)$ as a function of trigger p_{Tt}. As the trigger we used charged leading particle either without or with an isolation cut. See text for more details.

distribution was fit with an exponential function of the form $\exp(-\alpha\, x_{\mathrm{E}})$ in the range $x_{\mathrm{E}} \in (0.4, 0.8)$. Obtained values of the parameter α (negative x_{E} slope) are presented as a function of trigger p_{Tt} in the right panel of Fig. 2. Two cases were considered: (i) the trigger is a leading charged particle in $|\eta| < 0.8$ and (ii) trigger is an isolated leading charged particle in $|\eta| < 0.4$. The purpose of the isolation cut was to increase $\langle z_{\mathrm{t}} \rangle$ of the trigger. The isolation cut was performed using a cone of radius $R = 0.4$ rad. The sum of the transverse momenta of other tracks having $p_{\mathrm{T}} > 0.5$ GeV/c inside the cone was required to be less than 10 % of the trigger particle p_{Tt}. As can be seen from the right panel of Fig. 2, larger $\langle z_{\mathrm{t}} \rangle$ also increases the value of the negative x_{E} slope. The data points are also compared with predictions of a simple fragmentation model based on the Parent-Child Relationship [4], where we further assume that $k_{\mathrm{T}} = 0$ GeV/c ($\Delta\phi = \pi$). As originally pointed out by Bjorken in [4] the universality of the fragmentation function and the power law nature of the final state parton spectrum implies that particle and jet invariant cross sections have the same power law shape. According to the Bjoerken's prescription, the p_{T} cross section can be calculated as an integral over the all kinematically allowed values of parton momenta, $\hat{p}_{\mathrm{T}} \geq p_{\mathrm{T}}$ to $\hat{p}_{\mathrm{T}max} = \sqrt{s}/2$,

$$\frac{1}{p_{\mathrm{T}}}\frac{d\sigma_h}{dp_{\mathrm{T}}} = \int_{x_{\mathrm{T}}}^{1} \left(\frac{p_{\mathrm{T}}}{z}\right)^{-n} D_{\mathrm{u,d}}^{\mathrm{h}\pm}(z)\, \frac{dz}{z^2} = p_{\mathrm{T}}^{-n} \int_{x_{\mathrm{T}}}^{1} D_{\mathrm{u,d}}^{\mathrm{h}\pm}(z) z^{n-2} dz \;\propto\; p_{\mathrm{T}}^{-n}\,. \quad (4)$$

Here, $\hat{p}_{\mathrm{T}}$ is the parton transverse momentum, $x_{\mathrm{T}} = 2p_{\mathrm{T}}/\sqrt{s}$, and $D_{\mathrm{u,d}}^{\mathrm{h}\pm}(\mathrm{z})$ is the fragmentation function. Thus the inputs to our fragmentation model were: (i) the power law exponent of the p_{T} spectrum of partons, which was estimated based on the inclusive invariant cross section of hadrons and (ii) the KKP parameterization of the quark and gluon fragmentation functions [6]. In the right panel of Fig. 2, the upper (lower) borders

of calculated bands correspond to the case where the negative x_{E} slope was calculated using the gluon (quark) fragmentation function. The upper band represents the case $z_{\mathrm{t}} = 1$, i.e. what one would expect in the case of ideal direct gamma triggered correlations. The lower band is found when the trigger also fragments ($\langle z_{\mathrm{t}} \rangle \approx 0.5$ in the case of $p + p$ at 7 TeV). The slope of the tail of the x_{E} distribution thus reflects the mean momentum fraction $\langle z_{\mathrm{t}} \rangle$ carried by the trigger.

References

[1] S. S. Adler et al., *Phys. Rev. D* **74**, 072002 (2006).
[2] A.L.S. Angelis et al., *Physica Scripta* **19**, 116-123 (1979).
[3] Alice collaboration, *J. Instrum.* **3**, S08002 (2008).
[4] J. D. Bjorken, *Phys. Rev. D* **8** , 4098 (1973).
[5] S. M. Berman, J. D. Bjorken, and J. B. Kogut, *Phys. Rev. D* **4**, 3388 (1971).
[6] B.A. Kniehl, G. Kramer and B. Pötter, *Nucl. Phys.* **B** 582, 514 (2000).

Jets in QCD media: onset of color decoherence

Yacine Mehtar-Tani†, Carlos A. Salgado†, Konrad Tywoniuk‡

† Departamento de Física de Partículas, Universidade de Santiago de Compostela, E-15782 Santiago de Compostela, Galicia-Spain

‡ Department of Astronomy and Theoretical Physics, Lund University, Sölvegatan 14A, SE-223 62 Lund, Sweden

E-mail: ymehtar@gmail.com, carlos.salgado@usc.es, konrad.tywoniuk@thep.lu.se

Abstract. We study the effect of an extended, color deconfined medium on interferences between emitting projectiles which in vacuum leads to the condition of angular ordering.

The fragmentation process of the highly virtual partons that emerge from a hard interaction process in $e^+e^-$and p+p collisions reveal many of the fundamental properties of QCD. In particular, color interference effects give rise to coherent emissions respecting angular ordering of subsequent branchings. The jet fragmentation process is expected to be modified by the presence of an extended color deconfined medium. This situation applies, e.g., for jet production in heavy-ion collisions. Indeed, strong medium effects are observed for both single-inclusive leading particle spectra [1, 2, 3] and two-particle correlations [4, 5] in experiments both at the Relativistic Heavy-Ion Collider (RHIC) at BNL, for Au+Au collisions at $\sqrt{s_{NN}} = 200$ GeV/c, and at the Large Hadron Collider (LHC) in CERN, for Pb+Pb at $\sqrt{s_{NN}} = 2.76$ TeV/c. Experimentally more demanding, recently one also has reconstructed full jets in heavy-ion collisions and observed a striking asymmetry of transverse jet energy [6, 7].

While the former, single- and double-inclusive observables mainly pin down the physics of energy loss of the leading particle in the jet, the latter measurements require a proper treatment of all secondaries in the shower which mainly populate the soft sector. This poses a challenge to theoretical models of radiative processes in colored plasmas since, as in the case of a vacuum cascade, one needs to consider multiple emitters to be sensitive to the effects of QCD color coherence [8, 9, 10]. The well-established calculations of medium-induced gluon emission up to now only account for the radiation off a single, independent emitter [11, 12, 13, 14]. This simple picture could break down for multiple emissions in the cascade.

Recently, we studied color coherence effects between emitters, identical to those responsible for angular ordering in vacuum, for the medium-induced spectrum off a $q\bar{q}$ antenna with a fixed opening angle [15, 16]. We found that the resulting, coherent spectrum differs strongly from the one off an independent emitter for a large range of

opening angles due to the non-trivial and sizable contributions from the interferences between the quark and the antiquark. In particular, the interferences give rise to terms which are infrared divergent and antiangular ordered, in contrast to radiation in vacuum. Thus, these soft gluons are responsible for the onset of decoherence which ultimately leads to the breakdown of angular ordering of a shower in medium.

1. Onset of decoherence in opaque media

The radiation of soft gluons can be described in terms of a classical gauge field, A^a_μ, which is a solution of the classical Yang-Mills (CYM) equations. In the presence of the current generated by the quark and antiquark propagation, J^μ, the CYM equations read

$$[D_\mu, F^{\mu\nu}] = J^\mu \tag{1}$$

where $D_\mu = \partial_\mu - igA_\mu$, $F_{\mu\nu} = \partial_\mu A_\nu - \partial_\nu A_\mu - ig[A_\mu, A_\nu]$ and g is the gluon coupling constant. The currents, which in vacuum are given by $J^{\mu,a}_{q(0)} = g\, p^\mu/E\delta^{(3)}(\vec{x} - \vec{p}/Et)\Theta(t)Q^a_q$ for the quark, where $p \equiv (E, \vec{p})$ is the energy and 3-momentum and Q^q_q the color charge, and analogously for the antiquark such that $J = J_q + J_{\bar{q}}$, are found through the continuity equation, $[D_\mu, J^\mu] = 0$. Finally, the amplitude of emitting a gluon with momentum $k \equiv (\omega, \vec{k})$ is given by

$$\mathcal{M}^a_\lambda(\vec{k}) = \lim_{k^2\to 0} -k^2 A^a_\mu(k)\epsilon^\mu_\lambda(\vec{k})\,, \tag{2}$$

where $\epsilon^\mu_\lambda(\vec{k})$ is the gluon polarization vector. In the following, we will work in light-cone gauge $A^+ = 0$.†

Treating the medium as a static background field, $A_{\rm med}$, to solve Eq. (1) amounts to finding the linear response of the induced gauge field [17]. In the soft limit, $\omega \to 0$, the solution takes a particularly simple form [16]. The amplitude for soft gluon emission reads

$$\mathcal{M}^a_\lambda(k) = -ig\Big[\frac{\kappa\cdot\epsilon_\lambda}{x(p\cdot k)}U^{ab}_p(L,0)Q^b_q + \frac{\bar{\kappa}\cdot\epsilon_\lambda}{\bar{x}(\bar{p}\cdot k)}U^{ab}_{\bar{p}}(L,0)Q^b_{\bar{q}}\Big]\,, \tag{3}$$

where $\kappa^i = k^i - xp^i$ $(i = 1, 2)$, $x = k^+/p^+$ is the gluon light-cone momentum fraction and L is the longitudinal extent of the medium.‡ The interaction with the medium is described by the Wilson line along the trajectory of the quark

$$U_p(x^+, 0) = \mathcal{P}_+ \exp\Big[ig\int_0^{x^+} d\xi\, T\cdot A^-_{\rm med}(\xi, \xi\,\mathbf{p}/p^+)\Big] \tag{4}$$

where $(T^b)^{ac}$ is the structure constant of the adjoint representation. The amplitude in vacuum is recovered in the zeroth order expansion of the Wilson line, $U \to 1$. Focussing for the moment on the singlet antenna configuration, i.e., $\gamma^* \to q\bar{q}$, we find the spectrum, after squaring and summing over physical gluon polarizations, to be given by

$$dN_{\gamma^*} = \frac{\alpha_s\, C_F}{(2\pi)^2}\Big[\mathcal{R}_q + \mathcal{R}_{\bar{q}} - 2(1 - \Delta_{\rm med}(L,0))\mathcal{J}\Big]\frac{d^3k}{(k^+)^3} \tag{5}$$

† Light-cone vectors are defined as $k^\pm = (k^0 \pm k^3)/\sqrt{2}$, and $\mathbf{k} = (k^1, k^2)$ will denote the perpendicular components.

‡ Variables with an overline involve the antiquark momentum, $\bar{p}$.

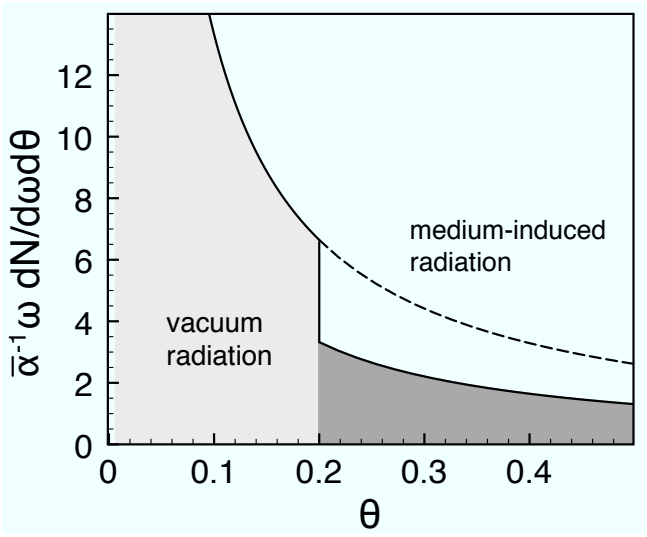

Figure 1. The coherent soft gluon emission spectrum off a quark in the presence of a medium for a $q\bar{q}$ pair with opening angle $\theta_{q\bar{q}} = 0.2$ and $\Delta_{\rm med} = 0.5$ (solid line). Here $\bar{\alpha} \equiv \alpha_s C_F/\pi$. The limit of opaque medium, i.e., $\Delta_{\rm med} \to 1$, is marked by the dashed line.

where

$$\Delta_{\rm med}(L,0) = 1 - \frac{1}{N_c^2-1}\langle \mathbf{Tr}\, U_p(L,0) U_{\bar{p}}^\dagger(L,0)\rangle\,, \tag{6}$$

is the medium decoherence parameter which will be discussed at length below. The spectrum in Eq. (5) is given by the sum of two independent spectra off the quark and antiquark, denoted by $\mathcal{R}_{q(\bar{q})}$, respectively, and interferences between the emitters, encoded in $\mathcal{J}$. Finally, the brackets $\langle\cdots\rangle$ in Eq. (6) indicate medium averages. For further details, see [16].

The total spectrum in the presence of a medium in Eq. (5) is very transparent. All the information about the medium resides in the definition of the medium decoherence parameter $\Delta_{\rm med}$ while the emission vertexes are vacuum-like. In particular, in the absence of medium effects $\Delta_{\rm med} \to 0$ and the spectrum becomes identical to the angular ordered one in vacuum. In the opposite case of a dense medium $\Delta_{\rm med} \to 1$, since it is constrained by unitarity, and all interference terms drop out. In effect the total spectrum becomes the superposition of the two independent emissions off quark and antiquark, respectively. Note that these conclusions are developed without the need to specify a particular model for the medium. In other words, Eq. (5) describes in a completely general way the onset of decoherence of QCD radiation in the presence of spatially extended, interacting color charges and the breakdown of angular ordering.

Projecting on the coherent emission off, for instance, the quark and taking the average over the azimuthal angle with respect to its direction we can rewrite Eq. (5) as

$$dN_{\gamma^*,q} = \frac{\alpha_s\, C_F}{\pi}\frac{d\omega}{\omega}\frac{d\theta}{\theta}\Big[\Theta(\theta_{q\bar{q}}-\theta) + \Delta_{\rm med}(L,0)\Theta(\theta-\theta_{q\bar{q}})\Big]\,, \tag{7}$$

in the limit of small angle emissions. Here, θ is the emission angle with respect to the

quark and $\theta_{q\bar{q}}$ is the opening angle of the $q\bar{q}$ antenna. The spectrum is depicted in Fig. 1. Note that vacuum radiation is confined with in a cone $\theta < \theta_{q\bar{q}}$, as expected, while the medium-induced radiation is geometrically separated from it and emitted at angles $\theta > \theta_{q\bar{q}}$.

In the general case of a color-charged antenna, e.g., originating from the splitting of a virtual gluon, $g^* \to q\bar{q}$, the above conclusion generalizes. The radiation off the total charge of the antenna comes with the same emission factor as the interferences in the singlet spectrum in Eq. (5), namely with $(1 - \Delta_{\rm med})\mathcal{J}$. Thus, in the limit of opaque media there is no radiation off the total charge. This result is also striking and implies a sort of "memory loss" effect due to the strong color screening: In the soft limit the partons radiate independently without taking notice of any other color charge in the system.

2. Medium-induced antiangular ordering of soft gluons

The striking simplicity of the results in the previous section are rooted in the fact that the soft gluon does not interact with the medium. To see how the picture generalizes when we allow for this interaction it is instructive to consider the exact solution of Eq. (1) at first order in the background field [15]. The truncation of the expansion is only valid for relatively dilute media, which nevertheless are relevant for many situations in heavy-ion collisions.

Presently it is instructive to assume a simple model for the medium in order to illustrate the features of QCD coherence. We assume the medium background field to consist of random, non-correlated scattering centers moving on the x^- light-cone. The medium average is then defined as

$$\langle \mathcal{A}^a_{\rm med}(x^+,\mathbf{q})\mathcal{A}^{*b}_{\rm med}(x'^+,\mathbf{q}')\rangle \equiv \delta^{ab}\, n_0\, m_D^2\, \delta(x^+ - x'^+)\,(2\pi)^2\,\delta^{(2)}(\mathbf{q}-\mathbf{q}')\mathcal{V}^2(\mathbf{q})\,, \tag{8}$$

where $\mathcal{A}_{\rm med}(x^+,\mathbf{q})$ is the medium background potential in the mixed representation, $\mathbf{q}$ denoting the exchanged momentum. In Eq. (8), $\mathcal{V}(\mathbf{q}) = 1/(\mathbf{q}^2 + m_D^2)$ is the medium interaction potential, m_D is the Debye mass and n_0 is the 1-dimensional density of scattering centers. The amplitude of gluon radiation off the quark is then given by

$$\mathcal{M}^a_{q,(1)} = ig^2 \int \frac{d^2\mathbf{q}}{(2\pi)^2}\int_0^L dx^+ [T\cdot\mathcal{A}_{\rm med}(x^+,\mathbf{q})]^{ab} Q_q^b\, e^{i(k^- - v^-)x^+} \times \left[\frac{\nu\cdot\epsilon}{p\cdot v}\left(1 - e^{i\frac{p\cdot v}{p^+}x^+}\right) + \frac{\kappa\cdot\epsilon}{p\cdot k} e^{i\frac{p\cdot v}{p^+}x^+}\right], \tag{9}$$

where $v \equiv (v^+ = k^+, v^- = \mathbf{v}^2/2k^+, \mathbf{v} = \mathbf{k} - \mathbf{q})$ and $\nu^i = v^i - x\,p^i$. The first term in Eq. (9) corresponds to the interaction of the emitted gluon with the medium, denoted $\mathcal{M}^g_q$, while the second term corresponds to the interaction of the quark before the bremsstrahlung emission of the gluon, denoted $\mathcal{M}^{\rm brem}_q$.

Among the various contributions to the spectrum, we recover the terms proportional to $|\mathcal{M}_q|^2 + |\mathcal{M}_{\bar{q}}|^2$ which correspond to the independent medium-induced spectra off quark

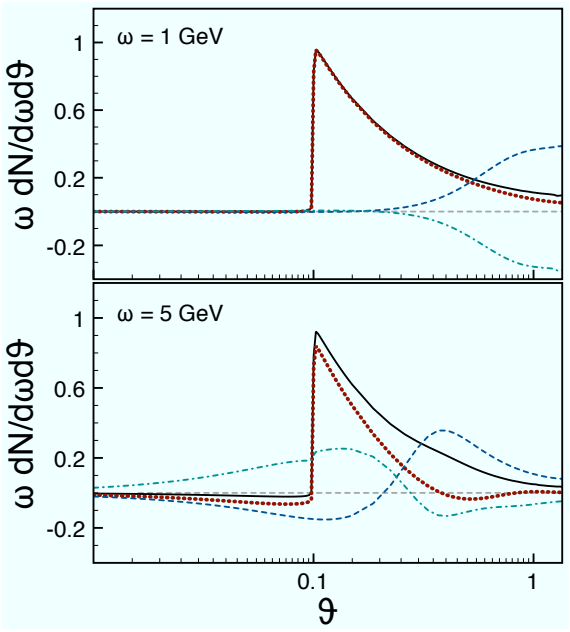

Figure 2. The angular distribution of the medium-induced gluon spectrum for ω=1 and 5 GeV for a $q\bar{q}$ pair with opening angle $\theta_{q\bar{q}} = 0.1$; see the text for details. The dotted (red) line corresponds to the dominant contribution in the soft limit, while the short-dashed (blue) curve is the sum of GLV contributions from the quark and the antiquark and the dash-dotted (green) curve depicts the remaining terms. The solid line corresponds to the total spectrum.

and antiquark [13, 14], denoted by $\mathcal{I}_{\rm GLV}$ in the following. Additionally, we also get novel contributions stemming from the interference. The latter can be further divided into two contributions, namely $\mathcal{I}_{\rm brems} \propto 2\,{\rm Re}\,\mathcal{M}_q^{\rm brem}\mathcal{M}_{\bar{q}}^{*\rm brem}$, which is the only term exhibiting a soft divergence, and the remaining ones, involving at least one gluon interaction with the medium, denoted by $\mathcal{I}_{\rm interf}$.

The three contributions are plotted in Fig. 2, where we have evaluated the angular distribution of the full spectrum off a $q\bar{q}$ pair with opening angle $\theta_{q\bar{q}} = 0.1$ traversing a medium with thickness $L = 4$ fm ($m_D = 0.5$ GeV, $\alpha_s = 1/3$ and $n_0 L = 1$) numerically for $\omega = 1$ and 5 GeV. We note that, in both cases, the three terms add up to zero at small angles, leaving the cone delimited by the pair angle empty. Notably, the vacuum-like pattern persists at the higher energy caused by an intricate cancellation between the different contributions. In fact, these cancellations extend up to energies $\omega < (\theta_{q\bar{q}}^2 L)^{-1}$ [15] in this situation.

3. Conclusions

The fragmentation of a highly virtual parton in the final state involves copious production of soft secondaries. The structure of the jet propagating in vacuum is dictated by the condition of angular ordering in the leading logarithmic approximation. On the other hand, a strong medium modification in jet production in heavy-ion

collisions, characterized by an abundance of soft particle production at large angles compared to the jet axis, is observed in experiment.

From QCD arguments, large-angle radiation is affected by interferences between emitters. We have demonstrated how these effects are modified in the presence of an extended, color deconfined medium. In the limit of soft gluon emissions, the onset of decoherence is controlled by the parameter $\Delta_{\rm med}$ which contains information about the medium density and spatial extension [15, 16]. Furthermore, now in the limit of relatively dilute media, we showed that the vacuum-like emission pattern extends up to gluon energies $\omega < (\theta_{q\bar{q}}^2 L)^{-1}$, rendering the coherent emission spectrum very different from the one expected if the emissions were independent. Furthermore, our results do not rely on the specific situation of a $q\bar{q}$ antenna but applies to all situations for soft gluon production of two generic emitters, e.g., off a $q^* \to qg$ system.

In short, our results imply that the presence of the medium induces logarithmically enhanced soft radiation at large angles, geometrically separated from the vacuum fragmentation by the jet opening angle. This is in qualitative agreement with the experimental data [6, 7]. For dense media and gluon energies away from the soft sector there arises additional medium-induced radiation that is sensitive to longitudinal coherence effects [18, 19]. Finally, having the complete antenna radiation spectrum at hand we anticipate the transparent emerging structure of soft gluon radiation to be an important building block for the calculus of distributions inside fully developed jets in the presence of a medium.

[1] S. S. Adler *et al.* [PHENIX Collaboration], Phys. Rev. **C69** (2004) 034910.
[2] J. Adams *et al.* [STAR Collaboration], Phys. Rev. Lett. **91** (2003) 172302.
[3] K. Aamodt *et al.* [ALICE Collaboration], Phys. Lett. B **696** (2011) 30.
[4] J. Adams *et al.* [STAR Collaboration], Phys. Rev. Lett. **91** (2003) 072304.
[5] S. S. Adler *et al.* [PHENIX Collaboration], Phys. Rev. Lett. **97** (2006) 052301.
[6] G. Aad *et al.* [Atlas Coll.], [arXiv:1011.6182 [hep-ex]];
[7] S. Chatrchyan *et al.* [CMS Coll.], [arXiv:1102.1957 [nucl-ex]].
[8] A. Bassetto, M. Ciafaloni, G. Marchesini and A. H. Mueller, Nucl. Phys. **B207**, 189 (1982).
[9] A. Bassetto, M. Ciafaloni and G. Marchesini, Phys. Rept. **100**, 201 (1983).
[10] Yu. L. Dokshitzer, V. A. Khoze, A. H. Mueller and S. I. Troyan, "Basics Of Perturbative QCD," *Gif-sur-Yvette, France: Ed. Frontieres (1991) 274 p. (Basics of perturbative QCD)*
[11] R. Baier, Yu. L. Dokshitzer, A. H. Mueller, S. Peigné and D. Schiff, Nucl. Phys. **B483**, 291 (1997); **484**, 265 (1997).
[12] B. G. Zakharov, JETP Lett. **63**, 952 (1996); **65**, 615 (1997).
[13] M. Gyulassy, P. Levai and I. Vitev, Phys. Rev. Lett. **85**, 5535 (2000); Nucl. Phys. **B594**, 371 (2001).
[14] U. A. Wiedemann, Nucl. Phys. **B588**, 303 (2000)
[15] Y. Mehtar-Tani, C. A. Salgado, K. Tywoniuk, Phys. Rev. Lett. **106** (2011) 122002.
[16] Y. Mehtar-Tani, C. A. Salgado, K. Tywoniuk, [arXiv:1102.4317 [hep-ph]].
[17] Y. Mehtar-Tani, Phys. Rev. C **75** (2007) 034908.
[18] Y. Mehtar-Tani, K. Tywoniuk, [arXiv:1105.1346 [hep-ph]].
[19] J. Casalderrey-Solana and E. Iancu, [arXiv:1105.1760 [hep-ph]].

Fast Embedding of Jets in Heavy-Ion Collisions for Background Studies with ALICE

B Bathen, for the ALICE Collaboration

Wilhelm-Klemm-Strasse 9, 48149 Münster, Germany

E-mail: Bastian.Bathen@cern.ch

Abstract. Jet reconstruction in heavy-ion collisions is strongly affected by soft background from the underlying event. For an appropriate interpretation of the jet observables it is essential to understand the influence of the background and its fluctuations on the reconstructed jets. For this purpose we study random cones and the response of known probes embedded in heavy-ion events. The embedded probe can be a single high-p_{T} track or a jet from a simulated or real p–p event. This allows a detailed study of background fluctuations and verification of the performance of background subtraction methods.

1. Introduction

We present our results on region-to-region energy fluctuations of the soft background in Pb–Pb collisions at the LHC ($\sqrt{s_{\mathrm{NN}}} = 2.76\,\mathrm{TeV}$) measured with the ALICE experiment. The studies are based on charged tracks with a low p_{T} cut of $150\,\mathrm{MeV}/c$. We used the two different methods *random cones* and *fast embedding* to investigate the background. For *fast embedding* we discuss the case of embedded single high-p_{T} tracks.

A good knowledge of the background fluctuations is mandatory for the interpretation of jet measurements. For example, it has been argued that the impact of background fluctuations is of particular interest since the first measurements of imbalanced jets in Pb–Pb collisions at the LHC have been published [1, 2, 3].

2. Background Subtraction

The average background has to be estimated and subtracted on event-by-event basis. For this purpose, the heavy-ion event is clusterized with the $\mathrm{k_T}$-algorithm from the FastJet package [4]. We assume that most of these clustered objects consist of soft background, even though this is not the case for all of them. We call these *background jets* in the following. The clustering procedure eliminates regions with strong deviations from the average background, as we determine the background density ρ of the event as the median of those background jets:

$$\rho = \mathrm{median}(p_{\mathrm{T}}^{i}/A_{jet}^{i}),$$

where p_{T}^{i} is the momentum of the background jet i with the jet area A_{jet}^{i} (in the $\eta - \phi$ plane). For the median we exclude the two hardest jets. In figure 1 ρ is shown as function of centrality (a) and multiplicity (b). The background density increases linearly with the raw number of tracks† (multiplicity).

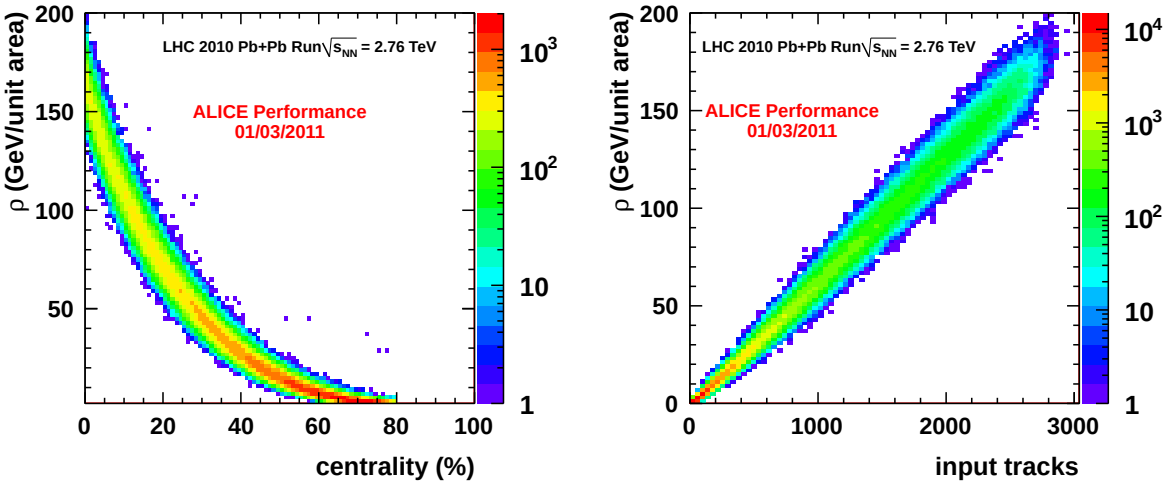

(a) (b)

Figure 1. Background density ρ in Pb–Pb collisions at $\sqrt{s} = 2.76\,\mathrm{TeV}$ as function of centrality (a) and multiplicity (b) with low track p_{T} cut off at $150\,\mathrm{MeV}/c$. Multiplicity is in this case the raw (uncorrected) number of tracks in the event, which is the number of input tracks for the jet finder.

$\rho \times A_{jet}$ is the expected amount of background energy which contributes to the jet momentum. For a jet radius of $R = 0.4$ and corresponding jet area of $A_{jet} = 0.5$ the background is between $50\,\mathrm{GeV}/c$ and $100\,\mathrm{GeV}/c$ for the 10 % most central events. The average background ρ is estimated event-by-event and $\rho \times A_{jet}$ is subtracted from the reconstructed jet momentum. What still persists are the region-to-region background fluctuations, which can not be corrected event-by-event and need to be convoluted.

3. Jet Reconstruction

The k_{T} algorithm [5, 6] sequentially combines the tracks i and j with the smallest distance parameter $d_{ij} = \min(p_{\mathrm{T},i}^{2}, p_{\mathrm{T},j}^{2})\frac{\Delta R_{i,j}^{2}}{R^{2}}$, where $\Delta R_{i,j} = \sqrt{(\Delta\eta)^{2} + (\Delta\phi)^{2}}$ and R is the radius parameter. The k_{T} algorithm is especially convenient for background jets. Since the $d_{i,j}$ is weighted with the squared transverse momentum $p_{\mathrm{T},(i,j)}^{2}$, it basically starts clustering with low-p_{T} tracks and it therefore is sensitive to soft contributions.

† Raw number of reconstructed charged tracks after quality cuts, which is the number of input tracks for the jet finder.

This is disadvantageous for the reconstruction of real jets in an environment of large soft background (see e.g. [7, 8]).

The anti-k_{T} algorithm on the contrary weights the distance between the tracks with the inverse transverse momentum $\min(1/p_{\mathrm{T},i}^2, 1/p_{\mathrm{T},j}^2)$. So it starts clustering with high-p_{T} particles and it is much more robust against soft background in terms of area stability and back reaction [8]. Hence, we use the anti-k_{T} algorithm for real jet reconstruction in Pb–Pb collisions. The jets are reconstructed with $R = 0.4$ in a pseudorapidity range of $|\eta| < 0.4$ in terms of the jet axis.

4. Fast Embedding

One of the methods we use to determine the background fluctuations is the embedding of a known probe into a real heavy-ion event (see e.g. [9]). The probes can be single high-p_{T} toy tracks or fully simulated (e.g. PYTHIA + GEANT) or real p–p jet events. Here we discuss only the results from embedded single tracks, which are taken as jets with only one (high-p_{T}) track. This method is called *fast embedding*, since the embedding is done for already reconstructed tracks and does not take into account possible effects of reconstruction, like possible merging of track clusters with influence on the tracking efficiency and resolution.

Since we know the transverse momentum of the embedded probe we can calculate the background fluctuations δp_{T} by subtracting the median of the background and the momentum of the embedded probe [7, 9]:

$$\delta p_{\mathrm{T}} = p_{\mathrm{T},jet}^{rec} - \rho \times A_{jet} - p_{\mathrm{T},jet}^{probe}.$$

This allows us to study in detail the influence of the soft background on the reconstructed jet observables. We also can verify the performance of the background subtraction methods we use. If the average background is correctly subtracted the mean of the δp_{T} distribution is zero, otherwise a systematic shift in δp_{T} will occur.

A matching of the embedded probe and the reconstructed jet in the heavy-ion event is necessary. For embedded single tracks we just match the track with the reconstructed jet which contains the track. As additional requirement both jets (probe and reconstructed) need to be in the jet acceptance.

The single tracks are randomly embedded over full jet $\eta - \phi$ acceptance ($|\eta| < 0.4$) with a flat p_{T} distribution from $50\,\mathrm{GeV}/c$ to $250\,\mathrm{GeV}/c$. We need to keep in mind that the probes are embedded in a flat centrality distribution, that does not equate to a corresponding centrality distribution of an inclusive jet spectrum, since the cross-section of jet production in a heavy-ion event increases with the number of binary collisions.

5. Random Cones

An alternative method to study the background of heavy-ion events are *random cones*. Here cones with an fixed size of $R = 0.4$ are randomly placed in the heavy-ion event and

the p_{T} in the cones are summed up to *background jets*. The background is subtracted as described earlier, so we directly get the background fluctuations:

$$\delta p_{\mathrm{T}} = p_{\mathrm{T,jet}}^{rndm} - \rho \times A_{jet}.$$

6. Results

Figure 2 shows the background fluctuations δp_{T} for two centrality classes comparison the two discussed methods *random cones* and *fast embedding* of single tracks. Figure 2(a) shows the results for the 10 % most central events. Since the δp_{T} distribution is mainly caused by uncorrelated Poissonian fluctuations it is expected to be a gamma-distribution[10]. However, for a large number of input tracks, which is the case for the most central events, the distribution can be well described with a Gauss in the ideal case of only uncorrelated fluctuations. In addition heavy-ion events contain already jets, and those cause the tail on the right-hand side of the δp_{T} distribution. We specify the distribution with a Gaussian fit on the left-hand side as a first assumption. More precisely it is a iterative fit with a fit range from $\mu - 3\,\sigma$ to $\mu + 0.5\,\sigma$ with the mean μ and width σ of the Gaussian fit. The termination condition is a shift of μ less than $0.1\,\mathrm{GeV}/c$, the maximum number of iterations is 20.

The results from *random cones* and *track embedding* agree pretty well. For both the mean is close to zero. This demonstrates that the background subtraction method works as desired and the impact of the average background in the event to the reconstructed jet can successfully be corrected. This also is valid for all centrality classes with different amount of background, as shown in figure 2(b) for peripheral events (centrality $50 - 80\,\%$).

The width of δp_{T} is about $10\,\mathrm{GeV}/c$ in the most central events ($0 - 10\,\%$) and decreases for more pheripheral events ($50 - 80\,\%$), where it is about $1 - 2\,\mathrm{GeV}/c$. However, the Gaussian fit does not describe the distribution very well in such peripheral events with low number of tracks.

In addition to the random cones from all (background) jets the δp_{T} distribution from the random cones without the two leading jets is shown (fig.2, open circles). Here, the tail on the right-hand side almost disappears. This indicates that the tail indeed comes from some jets in the heavy-ion events and are not part of the soft background contribution.

The measured background, of course, directly depends on the chosen low p_{T} cut off. In the studies presented so far we benefit from the good tracking capabilities of ALICE for tracks of very low p_{T} down to $150\,\mathrm{MeV}/c$. However, in view of jet reconstruction a higher p_{T} cut can help to reduce the influence of the background. In centrality class $0 - 10\,\%$ is the average background $\rho = 136\,\mathrm{GeV}/c$ for the track-p_{T} cut of $0.15\,\mathrm{GeV}/c$, it decreases to $\rho = 61\,\mathrm{GeV}/c$ for $p_{\mathrm{T}} > 1.0\,\mathrm{GeV}/c$ and further to $\rho = 13\,\mathrm{GeV}/c$ for $p_{\mathrm{T}} > 2.0\,\mathrm{GeV}/c$. The main advantage is the smaller background fluctuations which we can expect due to the reduced number of tracks. The effect for those track-p_{T}

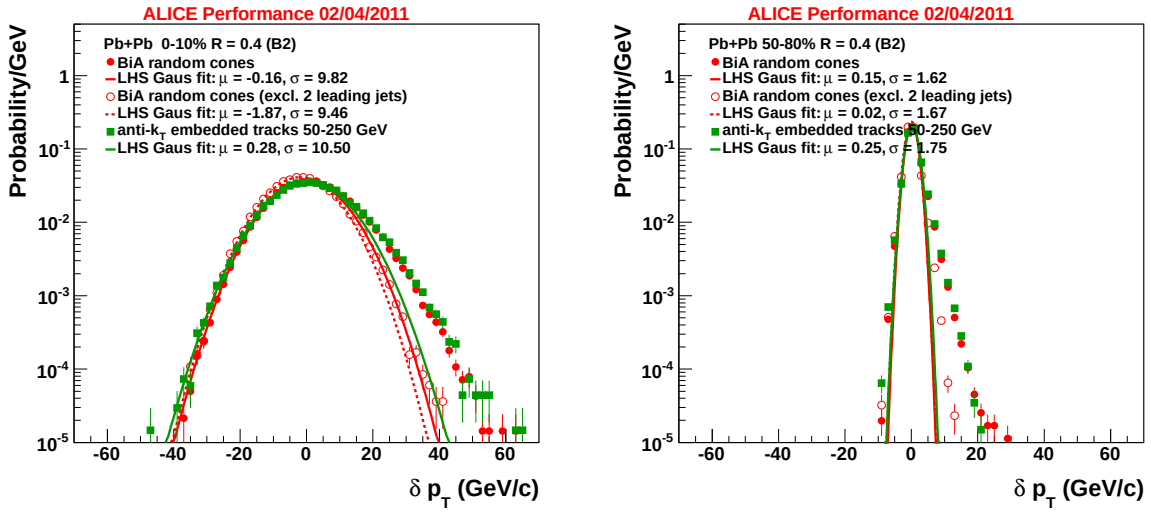

(a) (b)

Figure 2. Background fluctuations δp_{T} in Pb–Pb collisions at $\sqrt{s} = 2.76\,\mathrm{TeV}$ for central $(0-10\,\%)$ (a) and peripheral events $(50-80\,\%)$ (b) with track $p_{\mathrm{T}} > 150\,\mathrm{MeV}/c$.

cuts is shown in figure 3. For $p_{\mathrm{T}} > 2.0\,\mathrm{GeV}/c$ is $\sigma = 3.2\,\mathrm{GeV}$, while the mean of the distribution basically stays close to zero. That means that the background subtraction method also works for higher p_{T} cuts. However, such a cut would introduce a bias on a hard fragmentation, and makes the situation worse for the reconstruction of quenched jets.

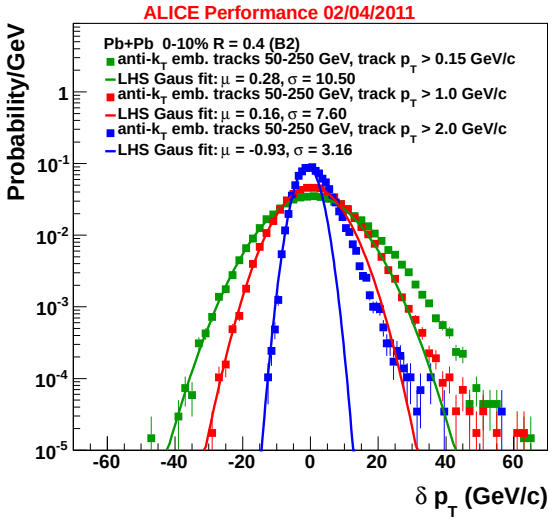

Figure 3. Background fluctuations δp_{T} in central collisions $(0-10\,\%)$ for track $p_{\mathrm{T}} > 0.15\,\mathrm{GeV}/c$, $p_{\mathrm{T}} > 1.0\,\mathrm{GeV}/c$ and $p_{\mathrm{T}} > 2.0\,\mathrm{GeV}/c$.

7. Conclusion

We presented the first measurement of the background fluctuations in heavy-ion events for charged tracks with a low p_{T} cut-off of $150\,\mathrm{MeV}/c$. Based on the different methods *random cones* and *fast embedding* we see a good agreement with a background fluctuation of $\sigma \approx 10\,\mathrm{GeV}/c$ in the most central events. The subtraction of the average background is well under control also for events with a large number of tracks. To reduce the fluctuations for the reconstruction of jets at low p_{T} it might be necessary to use a higher track-p_{T} cut.

8. Outlook

We did not discuss our studies of the background fluctuations as function of multiplicity. The dependence of the number of tracks allows a comparison with the Poissonian limit. The background fluctuations are expected to approach the Poissonian limit in case they are caused by uncorrelated sources only.

Also other effects contribute to a broadening of the fluctuations. E.g. we estimate the background fluctuations for different orientations to the event plane for this purpose.

Furthermore we investigate the background fluctuations with embedding of full PYTHIA jet events and quenched jets (QPYTHIA and PYQUEN). With those probes our sample becomes more realistic, but also more biased by the jet finder, so we observe jet splitting and have signs of back reaction.

References

[1] The ATLAS Collaboration. *PRL*, 105:252303, 2010, arXiv:hep-ex/1011.6182v2.
[2] The CMS Collaboration, 2011, arXiv:nucl-ex/1102.1957v2.
[3] M. Cacciari, G.P. Salam, and G. Soyez, 2011, arXiv:hep-ph/1101.2878v2.
[4] M. Cacciari and G.P. Salam. *Phys. Lett.*, B641, 2006, arXiv:hep-ph/0512210.
[5] S. Catani, Y.L. Dokshitzer, M.H. Seymour, and B.R. Webber. *Nucl. Phys. B*, 406:187–224, 1993.
[6] S.D. Ellis and D.E. Soper. *Phys. Rev. D*, 48:3160, 1993, arXiv:hep-ph/9305266.
[7] M. Cacciari, J. Rojo, G.P. Salam, and G. Soyez. 71:1539, 2011, arXiv:hep-ph/1010.1759v1.
[8] M. Cacciari, G.P. Salam, and G. Soyez. *JHEP*, 0804:063, 2008, arXiv:hep-ph/0802.1189.
[9] P.M. Jacobs, 2010, arXiv:hep-ex/1012.2406v2.
[10] M.J. Tannenbaum. *Phys. Lett.*, B498:29–43, 2001.

Jet Production in p+p and Pb+Pb collisions from ATLAS

Monica Dunford for the ATLAS Collaboration
CERN, Geneva CH-1211Switzerland
E-mail: Monica.Dunford@cern.ch

Abstract. At the LHC, measurements of jet production cross sections are important tests of the Standard Model in a new unexplored energy region. In addition, the study of jets is of great relevance to searches for new particles and new interactions as Standard Model processes often represent a significant background. In this work, results on the inclusive, dijet, multi-jet and W+jet cross sections are presented. Other properties of jets such as jet shapes, azimuthal decorrelation in dijet events and the fraction of dijet events without additional jets in the rapidity region bounded by the dijet system are also discussed. Results of dijet asymmetry observed in Pb+Pb collisions are also presented.

1. Introduction

The study of jet production cross sections is an important test of quantum chromodynamics (QCD), the theory of the strong interactions. At the LHC, jet cross sections and properties can be measured in a new, unexplored energy region including a larger jet rapidity range, an extended jet p_{T} range and greater dijet invariant masses. Precision tests of the Standard Model using jets represent a particularly rich field. In addition to cross section measurements of the inclusive, dijet and multi-jet processes, the study of jet properties like the measurement of the jet shapes provides information about the details of the parton-to-jet fragmentation process and other tests of non-perturbative QCD.

In 2010, the LHC also ran with Pb+Pb collisions. Collisions of heavy ions at ultra-relativistic energies are expected to produce an evanescent hot, dense state, with temperatures exceeding two trillion kelvins, in which the relevant degrees of freedom are not hadrons, but quarks and gluons. In this medium, it is possible to have strong jet energy loss resulting in a large dijet asymmetry, not observed in proton+proton collisions.

2. ATLAS detector

The ATLAS detector [1, 2] consists of an inner tracking system (inner detector, or ID) surrounded by a thin superconducting solenoid providing a 2T magnetic field,

electromagnetic and hadronic calorimeters and a muon spectrometer (MS). The ID consists of pixel and silicon microstrip (SCT) detectors, surrounded by the transition radiation tracker (TRT). The electromagnetic calorimeter is a lead liquid-argon (LAr) detector, split into barrel ($|\eta| < 1.475$) and endcap ($1.375 < |\eta| < 3.2$) regions. Hadron calorimetry is based on two different detector technologies. The barrel ($|\eta| < 0.8$) and extended barrel ($0.8 < |\eta| < 1.7$) calorimeters are composed of scintillator/steel; the hadronic endcap calorimeter ($1.5 < |\eta| < 3.2$) are LAr/Cu. The forward calorimeters ($3.1 < |\eta| < 4.9$) are instrumented with LAr/Cu and LAr/W that provide electromagnetic and hadronic energy measurements, respectively. The MS is based on three large superconducting toroids arranged with an eight-fold azimuthal coil symmetry around the calorimeters, and a system of three stations of chambers for the trigger and for precise measurements. The nominal pp interaction point at the centre of the detector is defined as the origin of a right-handed coordinate system. The positive x-axis is defined by the direction from the interaction point to the centre of the LHC ring, with the positive y-axis pointing upwards, while the beam direction defines the z-axis. The azimuthal angle ϕ is measured around the beam axis and the polar angle θ is the angle from the z-axis. The pseudorapidity is defined as $\eta = -\ln\tan(\theta/2)$ and rapidity is defined as $y = 0.5 \times \ln[(E + p_z)/(E - p_z)]$.

3. Jet cross sections

The following sections discuss several jet cross section measurements. This discussion includes the inclusive jet cross section, the cross sections of dijet and multijet events and the jet cross section in association with a W-boson.

3.1. Inclusive cross sections

Jets for the inclusive jet cross section are defined using the anti-k_t algorithm. Two different radius parameters of $R = 0.4$ and 0.6 are chosen in order to be sensitive to different non-perturbative QCD effects such as the jet size and the underlying event. Jets are reconstructed at the electromagnetic scale, using three-dimensional topological clusters built from calorimeter cells as input to the jet algorithm. Events were recorded with three different triggers: the Minimum Bias Trigger (MBTS), used to select minimum bias events; the central jet trigger, covering $|\eta| < 3.2$; and the forward jet trigger, spanning $3.1 < |\eta| < 4.9$. Jets are required to have $p_T > 20$ GeV and rapidity $|y| < 4.4$.

The double-differential inclusive jet cross section [3] is shown in figure 1 for R=0.4 jets. The measurement extends from jet p_T of 20 GeV to almost 1.5 TeV, spanning two orders of magnitude in p_T and seven orders of magnitude in cross section. The systematic uncertainty on this measurement is dominated by the jet energy scale (JES) uncertainty. NLO pQCD NLOJet++ predictions are generally in agreement with the experimental results, although some differences are observed at high jet p_T and rapidity.

The data have also been compared with the predictions obtained with different PDF sets as well as NLO predictions using Powheg. Good agreement with data is observed for the different PDF sets. The Powheg predictions are consistent with data although there is a trend for Powheg to predict larger cross sections than the data at low p_{T}, and smaller cross sections than NLOJet++ (but closer to the data) in the high-p_{T} region.

3.2. Dijet cross sections

For the dijet mass measurements, events are selected in which the leading jet has a $p_{\mathrm{T}} > 30$ GeV and $|y| < 4.4$ and has at least one sub-leading jet with $p_{\mathrm{T}} > 20$ GeV and $|y| < 4.4$. The trigger is the same as that used for the inclusive jet cross section except that the logical OR of the central and forward jet triggers is used in order to be fully efficient at sufficiently high jet p_{T}.

Dijet double-differential cross sections [3] are measured as a function of the dijet mass, m_{12} and binned in the maximum rapidity of the two leading jets ($|y|_{max}$). Events must have $|y|_{max} < 2.8$, due to complexity of triggering dijet events outside this acceptance using a combination of central and forward jet triggers. Figure 1 shows dijet double-differential cross sections as a function of m_{12}. The cross section falls rapidly with mass, and extends up to dijet masses of 4 TeV. The data are compared to NLOJet++ predictions as well as NLO Powheg predictions. The effect of using different PDF sets is also investigated. There is a reasonable agreement between Powheg and the data for R = 0.4 and between NLOJet++ and the data for both radius parameters. For R = 0.6, Powheg systematically predicts higher cross sections at low dijet mass compared to the data and the NLOJet++ predictions.

3.3. Multi-jet cross sections

Similar to the inclusive jet cross section measurements, in the multi-jet cross section analysis [4] jets are defined using the anti-k_{t} algorithm with a radius parameter of $R = 0.4$. Events are triggered using two-jet and three-jet triggers which have been shown to be fully efficient for multi-jet events with at least one jet with $p_{\mathrm{T}} > 60$ GeV. An event must contain at least two jets with one jet having $|y| < 2.8$ and $p_{\mathrm{T}} > 80$ GeV. All other jets are required to have $|y| < 2.8$ and $p_{\mathrm{T}} > 60$ GeV in order to be counted. To remove jets from additional proton-proton interactions overlapping in the event (pile-up), jets are only accepted if at least 70% of their charge particle p_{T} comes from the event vertex.

The uncertainty due to JES is the dominant systematic uncertainty but other jet-related uncertainties were considered. These additional factors include uncertainties on the JES for jets that have near-by activity, uncertainties due to additional energy in the jet from the presence of pile-up and uncertainties in the admixture of quark- and gluon-initiated jets. Figure 2 shows the cross section as a function of the inclusive jet multiplicity, compared to several Monte Carlo predictions. Good agreement between data and theoretical predictions is seen.

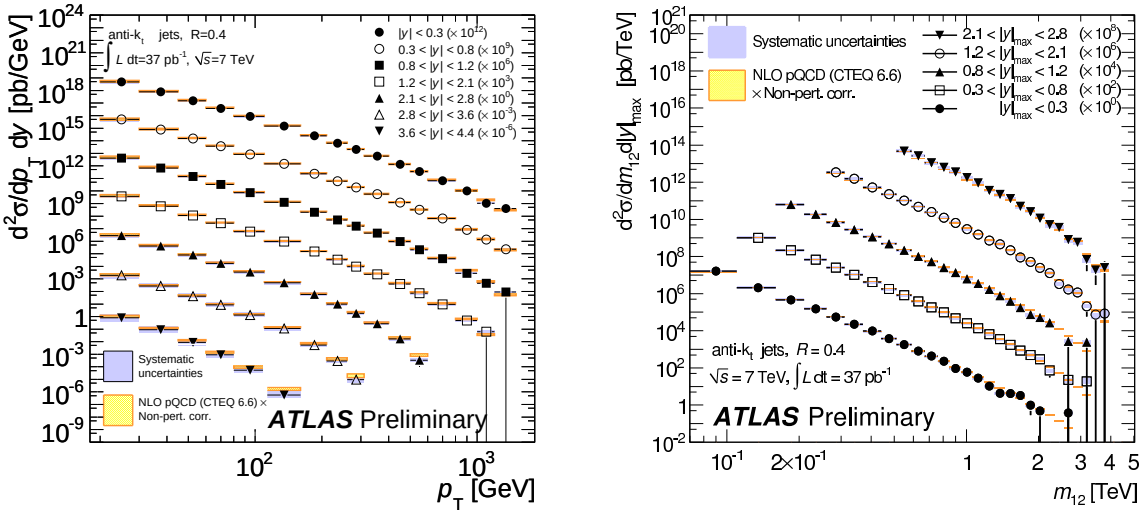

Figure 1. Left: Inclusive jet double-differential cross sections as a function of jet p_{T} in different regions of y. Right: Dijet double-differential cross section as a function of the dijet mass, binned in the maximum rapidity of the two leading jets $|y|_{max}$. In both figures, results for R=0.4 jets are shown and the data are compared to NLO pQCD calculations to which non-perturbative corrections have been applied.

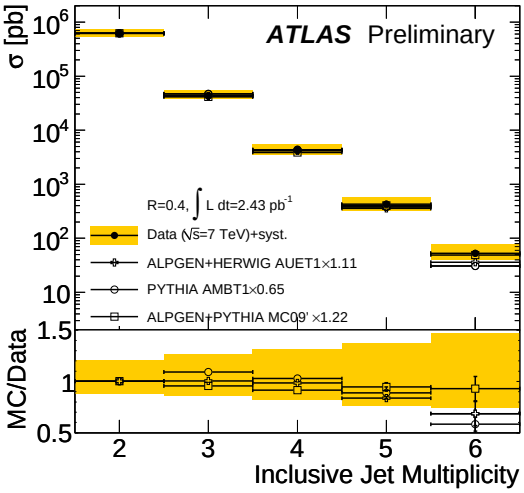

Figure 2. Total inclusive jet cross section as a function of multiplicity. The data are compared to leading order Monte Carlo simulations (ALPGEN + HERWIG AUET1, ALPGEN + PYTHIA MC09 and PYTHIA AMBT1) normalized to the measured two-jet inclusive jet multiplicity bin. AUET1, MC09 and AMBT1 refer to different tunings of the underlying event.

3.4. Jets in associated with a W Boson

The study of massive vector boson (V, where V=W or Z) production in association with one or more jets is an important test of QCD. To select W+jet events [8], one and only one good electron (muon) within a $|\eta| < 2.47$ (2.4) with $p_{\mathrm{T}} > 20$ GeV is required. The jets are selected using the anti-k_{t} algorithm with a radius parameter $R = 0.4$. The jet p_{T} must be greater than 20 GeV and the jet η within 2.8. All jets within $\Delta R < 0.5$ of a good electron or muon were removed, regardless of the jet p_{T} or η. Events were required to have $E_{\mathrm{T}}^{\mathrm{miss}} > 25$ GeV and a transverse mass, $M_{\mathrm{T}} > 40$ GeV.

The major backgrounds to this analysis are from QCD processes and from events

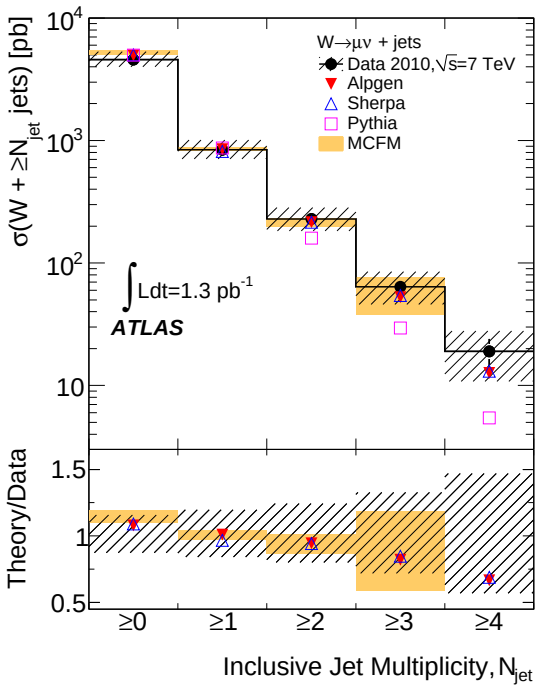

Figure 3. W+jets cross section ratio results as a function of corrected jet multiplicity for the muon channel. For the data, the statistical uncertainties are shown by the vertical bars, and the combined statistical and systematic uncertainties are shown by the black-hashed regions. Also shown are predictions from ALPGEN, SHERPA, PYTHIA and MCFM, and the ratio of theoretical predictions to data (PYTHIA is not shown in the ratio). The theoretical uncertainties are shown only for MCFM (NLO prediction for $N_{\text{jet}} \leq 2$ and a LO prediction for $N_{\text{jet}} = 3$)

with electroweak decays. The latter consist of $W \rightarrow \tau\nu$ where the tau decays leptonically, $Z \rightarrow ll$ where one lepton is not identified and hadronic energy in the event is mismeasured, $Z \rightarrow \tau\tau$ events and leptonic $t\bar{t}$ decays ($t\bar{t} \rightarrow b\bar{b}qq'e\nu$). The QCD background in the electron channel has two components, one where a light flavor jet passes the electron selection and additional energy mismeasurement in the event results in large $E_{\text{T}}^{\text{miss}}$, and the other where a bottom- or charm-hadron decays to an electron. For the muon channel, the QCD background arises from semileptonic heavy flavor decays in multi-jet events. The QCD background in the electron channel is estimated using a data-driven method while all other backgrounds are modeled using MC.

The dominant sources of systematic uncertainties in the cross section measurements for both electron and muon channels are the uncertainties in the jet energy scale, uncertainties due to QCD background estimates and uncertainties in the lepton reconstruction efficiency. The measured W+jets cross sections for the muon channel (multiplied by the leptonic branching ratio) as a function of the corrected jet multiplicity are shown in figure 3. The particle level expectations from ALPGEN and SHERPA simulations as well as a NLO calculation using MCFM agree well with the data. As PYTHIA is a LO calculation, it does not provide a good description of the data for jet multiplicities greater than one.

4. Jet properties

The following sections discusses several measurements related to the properties of jets and events with jets. This includes measurements of jet shapes in inclusive jet production, azimuthal decorrelations between the two central jets in multi-jet events

and the fraction of dijet events that do not contain an additional jet in the rapidity region bounded by the dijet system.

4.1. Jet Shapes

The shape of the jet depends on the type of partons (quark or gluon) that gives rise to jets in the final state, and is sensitive to non-perturbative fragmentation effects and underlying event (UE) contributions from the interaction between proton remnants. For this measurement [5], events are triggered using the MBTS and central jet triggers and are required to have one and only one reconstructed primary vertex with a position along the beam direction within 10 cm of the origin of the coordinate system. This requirement suppresses contributions from pile-up, beam-related backgrounds and cosmic rays. There must be at least one jet with $p_{\mathrm{T}} > 30$ GeV and $|y| < 2.8$. Jets are selected using the anti-k_{t} algorithm with a radius parameter $R = 0.6$.

The internal structure of the jet is studied in terms of the differential and integrated jet shapes. The differential jet shape is defined as the average fraction of the jet p_{T} that lies inside an annulus of R=0.1 around the jet axis, whereas the integrated jet shape is defined as the average fraction of the jet p_{T} that lies inside a cone of radius r concentric with the jet cone. The dominant systematic uncertainty is due to the absolute energy scale of the individual clusters belonging to the jet.

At low p_{T}, more than 80% of the transverse momentum is contained within a cone of radius $r = 0.3$ around the jet direction. This fraction increases up to 95% at very high p_{T}, showing that jets become narrower as p_{T} increases. The data are compared to predictions from HERWIG++, ALPGEN, PYTHIA-Perugia2010, and PYTHIA-MC09 and to predictions from PYTHIA-DW and PYTHIA-Perugia2010 with and without UE contributions. Different tunings of the underlying event have also been investigated. The jet shapes predicted by PYTHIA-Perugia2010 provide a reasonable description of the data, while HERWIG++ predicts broader jets than the data at low and very high p_{T}. The PYTHIA-DW predictions are in between PYTHIA-Perugia2010 and HERWIG++ at low p_{T} and produce jets which are slightly narrower at high p_{T}. ALPGEN is similar to PYTHIA-Perugia2010 at low p_{T}, but produces jets significantly narrower than the data at high p_{T}. PYTHIA-MC09 tends to produce narrower jets than the data in the whole kinematic range under study.

4.2. Azimuthal decorrelation

Measurement of the decorrelation in the azimuthal angle [6] between the two most energetic jets ($\Delta\phi$), as a function of the number of partons produced is an important test of pQCD. Experimentally, this measurement has the distinct advantage of testing calculations of multi-jet production without requiring measurements on the additional jets. The results presented here measure the dijet azimuthal decorrelations with jet p_{T} up to 1.3 TeV, which is beyond the reach of previous colliders.

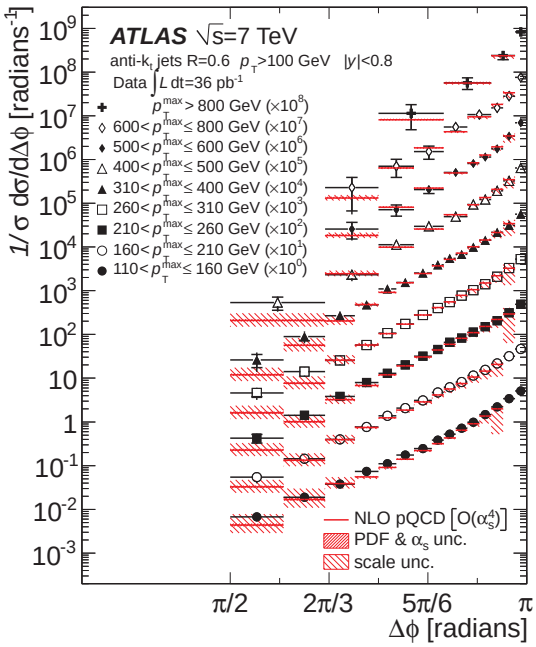

Figure 4. The differential cross sections binned in p_{T}^{max} regions. Also shown are the results from the NLO pQCD calculations

Jets are selected using the anti-k_{t} algorithm with a radius parameter $R = 0.6$. Only jets with $p_{\mathrm{T}} > 100$ GeV and $|y| < 2.8$ are considered. The two leading jets, used for the $\Delta\phi$ definition, are required to satisfy $|y| < 0.8$. Although this measurement has limited reliance on the jet energy scale, the systematic uncertainties are still dominated by JES as well as unfolding uncertainties.

Figure 4 shows the normalized differential cross sections for different values of the highest p_{T} jet in the event (p_{T}^{max}). As p_{T}^{max} increases and the probability for the emission of a third jet is reduced, the fraction of events near π becomes larger. Also shown are the NLO predictions which agree well with the data.

4.3. Dijet production with jet veto

The dijet production with jet veto measurement [7] tests models of perturbative QCD radiation in dijet systems in two limits: large jet rapidity separation and large jet transverse momentum. The measurement is defined in two ways: the fraction of dijet events that do not have an additional jet with a transverse momentum p_{T} greater than a given veto scale Q_0 in the rapidity region bounded by the dijet system (called gap fraction) and the mean number of jets in the rapidity region bounded by the dijet system.

Jets are selected using the anti-k_{t} algorithm with a radius parameter $R = 0.6$. Events must have only a single primary vertex and at least two jets with $p_{\mathrm{T}} > 20$ GeV and $|y| < 4.5$. The average transverse momentum of the boundary jets must be greater than 50 GeV. The measurement is dominated by JES and unfolding uncertainties.

The data is compared to theoretical predictions from Powheg and HEJ. HEJ, a parton-level Monte Carlo generator following an all-order resummation based on the

BFKL kernel, does not describe the data well in some cases such as large values of the average p_{T} and for the gap fraction large values of Δy. In general, Powheg describes the data well. The only disagreement is observed at large Δy, where Powheg slightly underestimates the gap fraction regardless of the generator used to shower and hadronise the events.

5. Dijet asymmetry in Pb+Pb collisions

Using data taken during the LHC Pb+Pb running period, the centrality-dependent dijet asymmetry was measured[9]. Events are selected using the minimum bias trigger. Jets are selected using the anti-k_{t} algorithm with a radius parameter $R = 0.4$. The inputs to the jet algorithm are towers of calorimeter cells of size $\Delta\eta \times \Delta\phi = 0.1 \times 0.1$. For each event, the average transverse energy density was calculated in each calorimeter layer in bins of width $\Delta\eta = 0.1$, and averaged over azimuth. In this averaging, jets where the ratio of the maximum tower energy over the mean tower energy was greater than 5, were excluded. The average energies were subtracted layer-by-layer for the cells that make up each jet.

The subtraction of the average energies results in no change in topological features of the events nor are any jets removed by or in the subtraction procedure. HIJING+PYTHIA simulations were used to check the overall linearity and resolution of the jet reconstruction with respect to the primary jet energy. Although the jet shapes should be similar compared to those in proton-proton collisions as discussed earlier, the efficiency, linearity, and resolution for reconstruction of jets in Pb+Pb collisions may be poorer if the jets are substantially modified by the medium. To check the sensitivity to such effects, the jet shape, characterized here as the ratio of the "core" energy (integrated over $\sqrt{\Delta\eta^2 + \Delta\phi^2} < 0.2$) to the total energy, was studied. This ratio shows only a weak dependence on centrality. This gives confidence that the high-energy jets do look approximately like jets measured in proton-proton collisions, and that the energy subtraction procedure does not introduce significant biases.

Events are required to have a leading jet with $E_T > 100$ GeV and $|y| < 2.8$. To calculate the dijet asymmetry, a second jet in the opposite hemisphere is required to have $E_T > 25$ GeV.

A striking feature of this sample is the appearance of events with only one high E_T jet and no high E_T jet in the opposite hemisphere. The dijet asymmetry and $\Delta\phi$ distributions are shown in figure 5 for different centrality bins, where centrality is characterized using the total transverse energy in the forward calorimeters. For comparison, HIJING+PYTHIA simulated events as well as proton-proton collision data events are also shown. As clearly seen in the figure, the dijet asymmetry in peripheral Pb+Pb events is similar to both proton-proton collisions and simulations. As the events become more central, the Pb+Pb data distributions become increasingly asymmetric. The $\Delta\phi$ distributions show that the leading and second jets are primarily back-to-back in all centrality bins; however, a systematic increase is observed in the rate of second

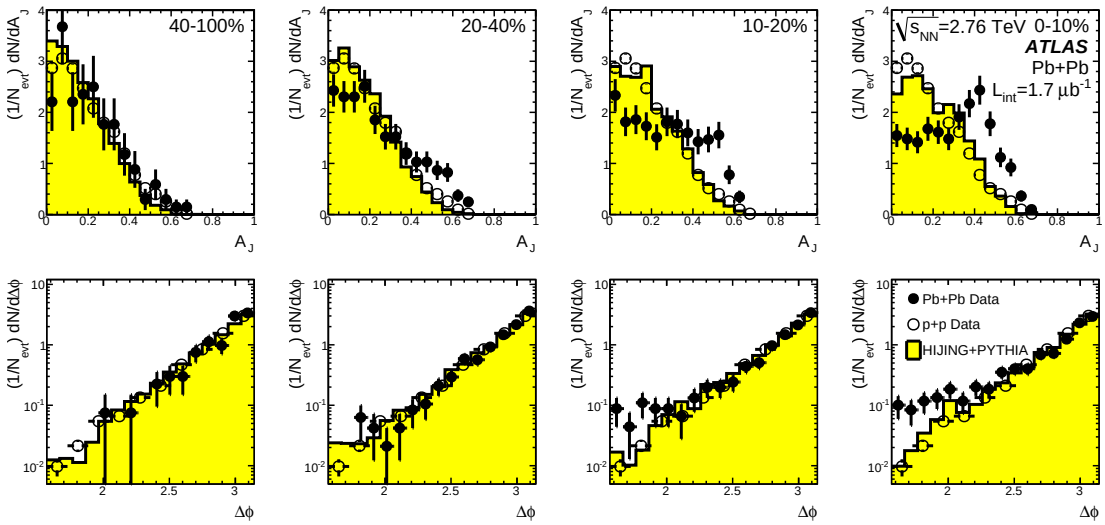

Figure 5. (top) Dijet asymmetry distributions for data (points) and unquenched HIJING with superimposed PYTHIA dijets (solid yellow histograms), as a function of collision centrality (left to right from peripheral to central events). Proton-proton data from $\sqrt{s} = 7$ TeV, analyzed with the same jet selection, is shown as open circles. (bottom) Distribution of $\Delta\phi$, the azimuthal angle between the two jets, for data and HIJING+PYTHIA, also as a function of centrality.

jets at large angles relative to the recoil direction for more central events. Numerous studies have been performed to verify that the events with large asymmetry are not produced by backgrounds or detector effects.

These highly asymmetric events have a natural interpretation in terms of QCD energy loss, where the second jet is attenuated, in some cases leading to striking highly-asymmetric dijet events. This observation is the first of an enhancement of such large dijet asymmetries, which are not observed in proton-proton collisions, which may point to an interpretation in terms of strong jet energy loss in a hot, dense medium.

6. Conclusion

This work presents a summary of jet cross section and jet property measurements made using the ATLAS detector in both p+p and Pb+Pb collisions. Measurements of the inclusive jet, dijet, multi-jet and W-boson plus jet cross sections are shown. All of these cross section measurements show good agreement to NLO predictions. In addition measurement of jet properties are also presented including measurements of jet shapes in inclusive jet production, azimuthal decorrelations between the two central jets in multi-jet events and the fraction of dijet events that do not contain an additional jet in the rapidity region bounded by the dijet system. With the exception of some cases, NLO predictions describe the data well. In Pb+Pb collisions, a large dijet asymmetry has been observed which is consistent with the interpretation of strong jet energy loss in a hot, dense medium.

[1] ATLAS Collaboration 2008 *JINST* **3** S08003
[2] ATLAS Collaboration 2009 arXiv:0901.0512 [hep-ex]
[3] ATLAS Collaboration 2011 ATLAS-CONF-2011-047
[4] ATLAS Collaboration 2011 ATLAS-CONF-2011-043
[5] ATLAS Collaboration 2011 *Phys. Rev. D* **83** 052003
[6] ATLAS Collaboration 2011 *Phys. Rev. Lett.* **106** 172002
[7] ATLAS Collaboration 2011 ATLAS-CONF-2011-038
[8] ATLAS Collaboration 2011 *Phys. Lett. B* **698** 325-345
[9] ATLAS Collaboration 2010 *Phys. Rev. Lett.* **105** 252303

Studies of Jet Quenching in PbPb collisions at CMS

Matthew Nguyen for the CMS Collaboration

CERN, Meyrin, Switzerland

E-mail: Matthew.Nguyen@cern.ch

Abstract. Jets are an important tool to probe the hot, dense medium produced in ultra-relativistic heavy-ion collisions. At the collision energies available at the Large Hadron Collider (LHC), there is copious production of hard processes, such that high p_{T} jets may be differentiated from the heavy-ion underlying event. The multipurpose Compact Muon Solenoid (CMS) detector is well designed to measure hard scattering processes with its high quality calorimeters and high precision silicon tracker [1]. Jet quenching has been studied in CMS in PbPb collisions at $\sqrt{s_{NN}} = 2.76$ TeV. As a function of centrality, dijet events with a high p_{T} leading jet were found to have an increasing momentum imbalance that was significantly larger than predicted by simulations. The angular distribution of jet fragmentation products has been explored by associating charged tracks with the jets measured in the calorimeters. By projecting the momenta of charged tracks onto the leading jet axis it is shown that the apparent momentum imbalance of the leading dijet pair can be recovered if low p_{T} tracks are considered. A large fraction of the balancing momentum carried by these soft particles is radiated at large angle relative to the jets.

Jets associated with the hard scattering of partons are a powerful probe of the hot, dense matter created in heavy-ion collisions, which is believed to be a Quark-Gluon Plasma (QGP). Previous data, mostly in the form of single and di-hadron observables show that jets are strongly modified by the medium, a phenomenon known as jet quenching [2]. The large PbPb collision energies at the LHC provide an abundance of jets of $p_{\mathrm{T}} > 100$ GeV/c, facilitating the direct reconstruction of jets. We review recent studies of jet quenching in PbPb collisions at a nucleon-nucleon center-of-mass energy of $\sqrt{s_{NN}} = 2.76$ TeV collected in 2010 using the Compact Muon Solenoid (CMS) detector. The results presented in these proceedings are a subset of those found in [3].

Jets are reconstructed from the energy deposited in the lead-tungstate crystal electromagnetic calorimeter (ECAL) and the brass/scintillator hadron calorimeter (HCAL) covering $|\eta| < 3$. The steel/quartz-fiber Cherenkov Hadron Forward (HF) calorimeter, covering $3 < |\eta| < 5.2$ is used for centrality determination. Calorimeter cells are grouped into towers of granularity $\Delta\eta \times \Delta\varphi = 0.087 \times 0.087$ in the barrel region ($|\eta| < 1.5$), and a somewhat coarser segmentation in the endcaps.

The CMS tracking system, located inside the calorimeters, consists of pixel and silicon-strip layers covering $|\eta| < 2.5$. It provides track reconstruction down to $p_{\mathrm{T}} \approx 100$ MeV/c, with a track momentum resolution of about 1% at $p_{\mathrm{T}} = 100$ GeV/c. The tracking system and central calorimeters are embedded in a solenoid with 3.8 T

central magnetic field. A set of scintillator tiles on the inner side of the HF calorimeters, the Beam Scintillator Counters (BSC), provide triggering and beam-halo rejection.

Jet events were selected using the High Level Trigger, requiring a jet with $p_{\mathrm{T}} > 50$ GeV/c, where the jet p_{T} value is uncorrected for the calorimeter response. The trigger becomes fully efficient for collisions with a leading jet with corrected p_{T} greater than 100 GeV/c. The large underlying event in heavy-ion collisions is subtracted on an event-by-event basis according to the procedure described in [4]. Jets are reconstructed using an iterative cone algorithm [5]. Jet corrections for the calorimeter response have been applied, as determined in studies for pp collisions [6].

To obtain a pure sample of dijets the following selection was applied:

- Leading jet: corrected jet $p_{\mathrm{T},1} > 120$ GeV/c and $|\eta_1| < 2$
- Subleading jet: corrected jet $p_{\mathrm{T},2} > 50$ GeV/c and $|\eta_2| < 2$
- Azimuthal angle between the jets of $\Delta\phi_{12} > 2\pi/3$ radians

Prior to jet finding on the selected events, a small contamination of noise events from uncharacteristic ECAL and HCAL detector responses was removed using signal timing, energy distribution, and pulse-shape information [7]. As a result, about 2.4% of the events were removed from the sample.

As a baseline for quenching effects the data are compared to dijets in PYTHIA, representing a sample with no quenching. To simulate the effects of the heavy-ion underlying event these dijet events are embedded into both real PbPb data and simulated PbPb data using the HYDJET generator [8]. Both embedded samples were propagated through the standard reconstruction and analysis chain.

Figure 1 shows distributions of $\Delta\phi_{12}$ between leading and subleading jets which pass the respective p_{T} selections. Figure 1 (a) shows pp data at 7 TeV compared to PYTHIA simulations, while Fig. 1 (b)-(f) show PbPb data in five centrality bins, compared to PYTHIA+DATA simulations. In general, the distributions agree quite well with the PYTHIA reference simulations. The more central events show an excess of events with azimuthally misaligned dijets ($\Delta\phi_{12} < 2$), compared with more peripheral events. A similar trend is seen for the PYTHIA+DATA simulations, although the fraction of events with azimuthally misaligned dijets is smaller in the simulation. The tails of these distributions in central events can be understood as the result of the increasing rate of fake jets or mismatched jets which come from another hard scattering. The effect is larger in data than in simulation, as the subleading jet can undergo a sufficiently large energy loss to fall below the 50 GeV/c selection criteria.

To characterize the p_{T} balance of the dijet, the asymmetry variable A_J is used, where $A_J \equiv (p_{\mathrm{T},1} - p_{\mathrm{T},2})/(p_{\mathrm{T},1} + p_{\mathrm{T},2})$. The A_J distribution for pp collisions at 7 TeV, plotted In Fig. 2 for pp (a), agrees well with PYTHIA. The centrality dependence of A_J for PbPb collisions can be seen in Figs. 2 (b)-(f), in comparison to PYTHIA+DATA simulations. Whereas the dijet angular correlations show only a small dependence on collision centrality, the dijet momentum balance exhibits a dramatic change in shape for the most central collisions. In contrast, the PYTHIA simulations only exhibit a modest

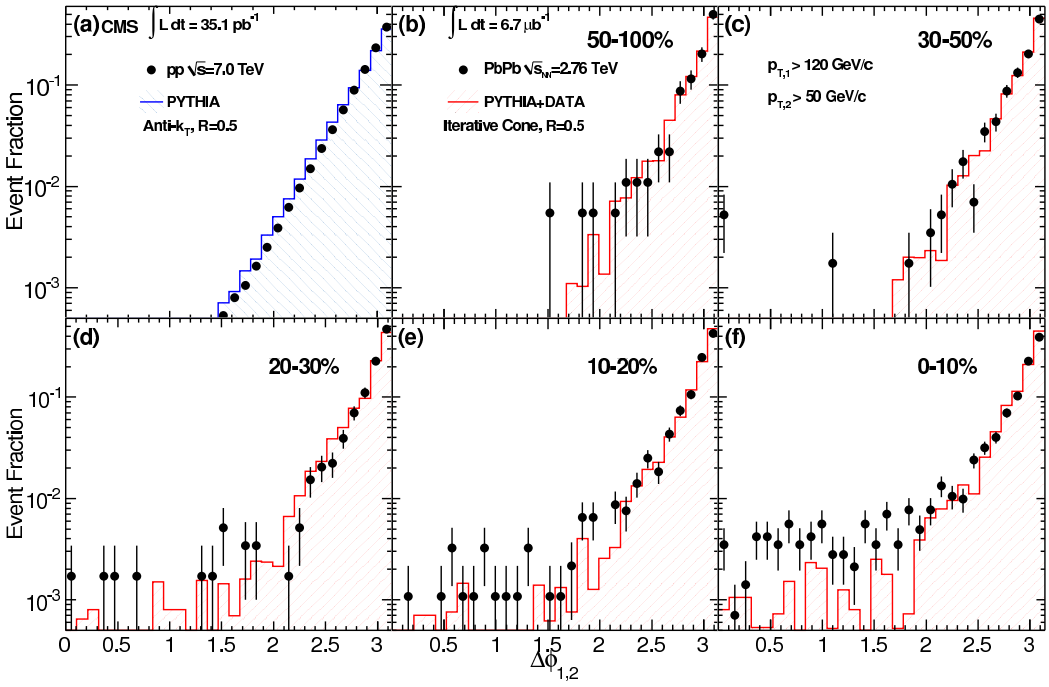

Figure 1. $\Delta\phi_{12}$ distributions for leading jets of $p_{\mathrm{T},1} > 120$ GeV/c with subleading jets of $p_{\mathrm{T},2} > 50$ GeV/c for 7 TeV pp collisions (a) and 2.76 TeV PbPb collisions in several centrality bins: (b) 50–100%, (c) 30–50%, (d) 20–30%, (e) 10–20% and (f) 0–10%. Data are shown as points, while the histograms show (a) PYTHIA events and (b)-(f) PYTHIA events embedded into PbPb data. The error bars show the statistical uncertainties.

broadening, even when embedded in the highest multiplicity PbPb events. The large rate of highly imbalanced jets indicates a strong jet quenching effect in which energy no longer reaches the calorimeters inside the jet cone. The absence of any modification to the $\Delta\phi_{12}$ distributions suggests that this energy is not transferred via hard radiation.

To fate of the "lost" energy was studied in greater detail by looking at correlations of the jets with charged tracks. The distribution of jet-associated tracks was studied as a function of both track p_{T} and ΔR from the leading and subleading jet axis (not shown). The background of combinatorial jet-track pairs was explicitly subtracted. It was found, however, that the size of the background limited the study to tracks with $p_{\mathrm{T}} > 1.0$ GeV/c and $\Delta R < 0.8$. To pursue the fate of the lost energy outside of this domain, a more inclusive quantity was studied. The overall momentum balance in the dijet events can be obtained using the projection of missing p_{T} of reconstructed charged tracks onto the leading jet axis. For each event, this projection was calculated as

$$\not{p}_{\mathrm{T}}^{\parallel} = \sum_{\mathrm{i}} -p_{\mathrm{T}}^{\mathrm{i}} \cos\left(\phi_{\mathrm{i}} - \phi_{\text{Leading Jet}}\right),$$

where the sum is evaluated over all tracks with $p_{\mathrm{T}} > 0.5$ GeV/c and $|\eta| < 2.4$. The results were then averaged over events to obtain $\langle \not{p}_{\mathrm{T}}^{\parallel} \rangle$. No explicit background subtraction is applied in this method, as the heavy-ion underlying event is not expected

to give a net p_{T} contribution along the leading jet axis.

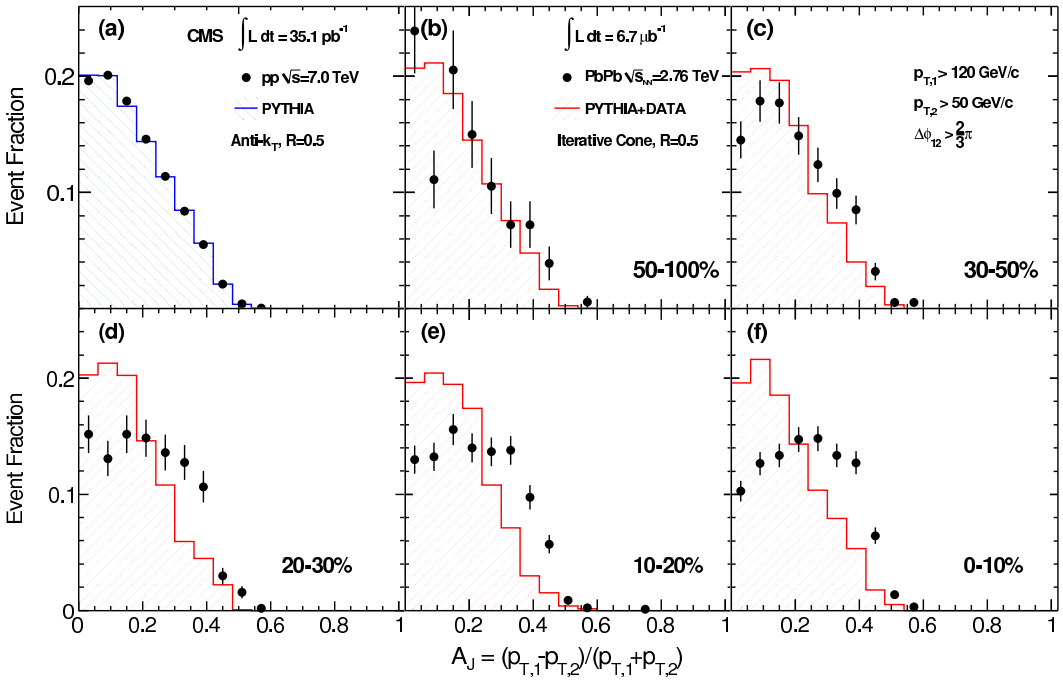

Figure 2. Dijet asymmetry ratio, A_J, for leading jets of $p_{\mathrm{T},1} > 120$ GeV/c, subleading jets of $p_{\mathrm{T},2} > 50$ GeV/c and $\Delta\phi_{12} > 2\pi/3$ for 7 TeV pp collisions (a) and 2.76 TeV PbPb collisions in several centrality bins: (b) 50–100%, (c) 30–50%, (d) 20–30%, (e) 10–20% and (f) 0–10%. Data are shown as points, while the histograms show (a) PYTHIA events and (b)-(f) PYTHIA events embedded into PbPb data. The error bars show the statistical uncertainties.

In Fig. 3, the solid markers show $\langle p_{\mathrm{T}}^{\parallel} \rangle$ as a function of A_J for two centrality bins, 30–100% (left) and 0–30% (right). The top row shows simulation (PYTHIA embedded in HYDJET), while the bottom row shows PbPb data. Even for large A_J dijet events, the charged tracks above $p_{\mathrm{T}} > 0.5$ GeV/c show no net momentum balance with respect to the leading jet axis in data or simulation. The figure also shows the contributions to $\langle p_{\mathrm{T}}^{\parallel} \rangle$ for five transverse momentum ranges from 0.5–1 GeV/c to $p_{\mathrm{T}} > 8$ GeV/c. The vertical bars for each range denote statistical uncertainties. For data and simulation, a large negative contribution to $\langle p_{\mathrm{T}}^{\parallel} \rangle$ (i.e., in the direction of the leading jet) by the $p_{\mathrm{T}} > 8$ GeV/c range is balanced by the combined contributions from the 0.5–8 GeV/c regions. Looking at the $p_{\mathrm{T}} < 8$ GeV/c region in detail, important differences between data and simulation emerge. For PYTHIA+HYDJET both centrality ranges show a large balancing contribution from the intermediate p_{T} region of 4–8 GeV/c, while the contribution from the two regions spanning 0.5–2 GeV/c is very small. In peripheral PbPb data, the contribution of 0.5–2 GeV/c tracks relative to that from 4–8 GeV/c tracks is somewhat enhanced compared to the simulation. In central PbPb events, the relative contribution of low and intermediate-p_{T} tracks is actually the opposite of that seen in PYTHIA+HYDJET. In data, the 4–8 GeV/c region makes almost no contribution

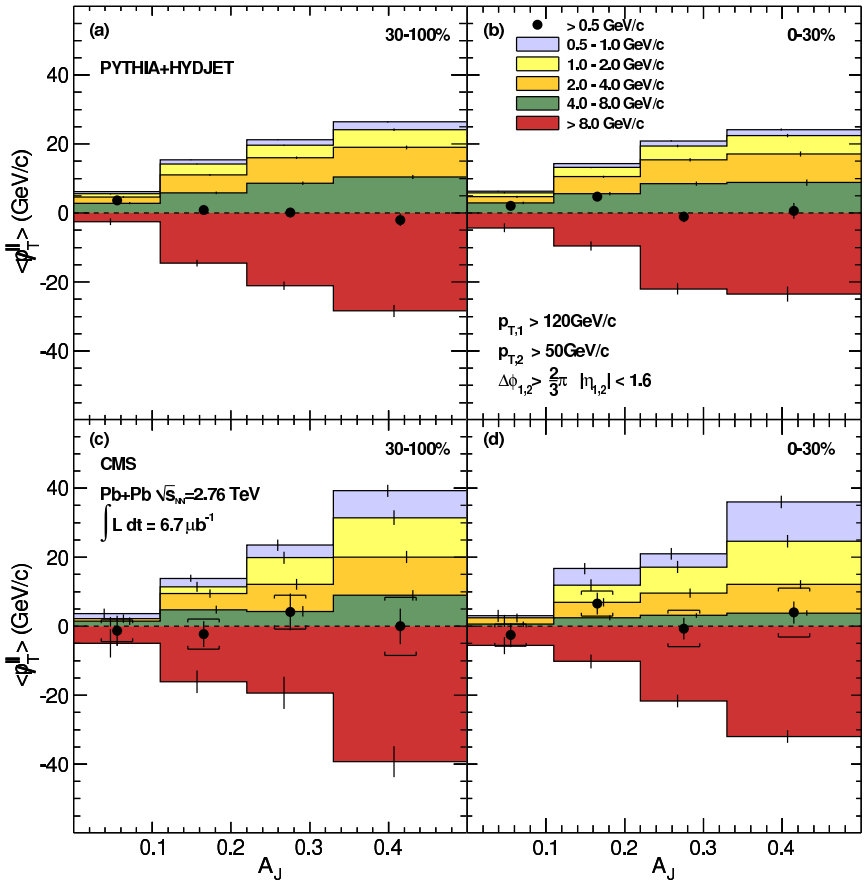

Figure 3. Average missing transverse momentum, $\langle \not{p}_{\mathrm{T}}^{\parallel} \rangle$, for tracks with $p_{\mathrm{T}} > 0.5$ GeV/c, projected onto the leading jet axis (solid circles). The $\langle \not{p}_{\mathrm{T}}^{\parallel} \rangle$ values are shown as a function of dijet asymmetry A_J for 30–100% centrality (left) and 0–30% centrality (right). For the solid circles, vertical bars and brackets represent the statistical and systematic uncertainties, respectively. Colored bands show the contribution to $\langle \not{p}_{\mathrm{T}}^{\parallel} \rangle$ for five ranges of track p_{T}. The top and bottom rows show results for PYTHIA+HYDJET and PbPb data, respectively. For the individual p_{T} ranges, the statistical uncertainties are shown as vertical bars.

to the overall momentum balance, while a large fraction of the negative imbalance from high p_{T} is recovered in low-momentum tracks.

Further insight into the radial dependence of the momentum balance can be gained by studying $\langle \not{p}_{\mathrm{T}}^{\parallel} \rangle$ separately for tracks inside cones of size $\Delta R = 0.8$ around the leading and subleading jet axes, and for tracks outside of these cones. The results of this study for central events are shown in Fig. 4 for the in-cone balance and out-of-cone balance for MC and data. One observes that for both data and simulation an in-cone imbalance of $\langle \not{p}_{\mathrm{T}}^{\parallel} \rangle \approx -20$ GeV/c is found for the $A_J > 0.33$ selection. In both cases this is balanced by a corresponding out-of-cone imbalance of $\langle \not{p}_{\mathrm{T}}^{\parallel} \rangle \approx 20$ GeV/c. However in simulation, more than 50% of the balance is carried by tracks with $p_{\mathrm{T}} > 4$ GeV/c, as might be expected from multijet production, whereas in data the balance is carried

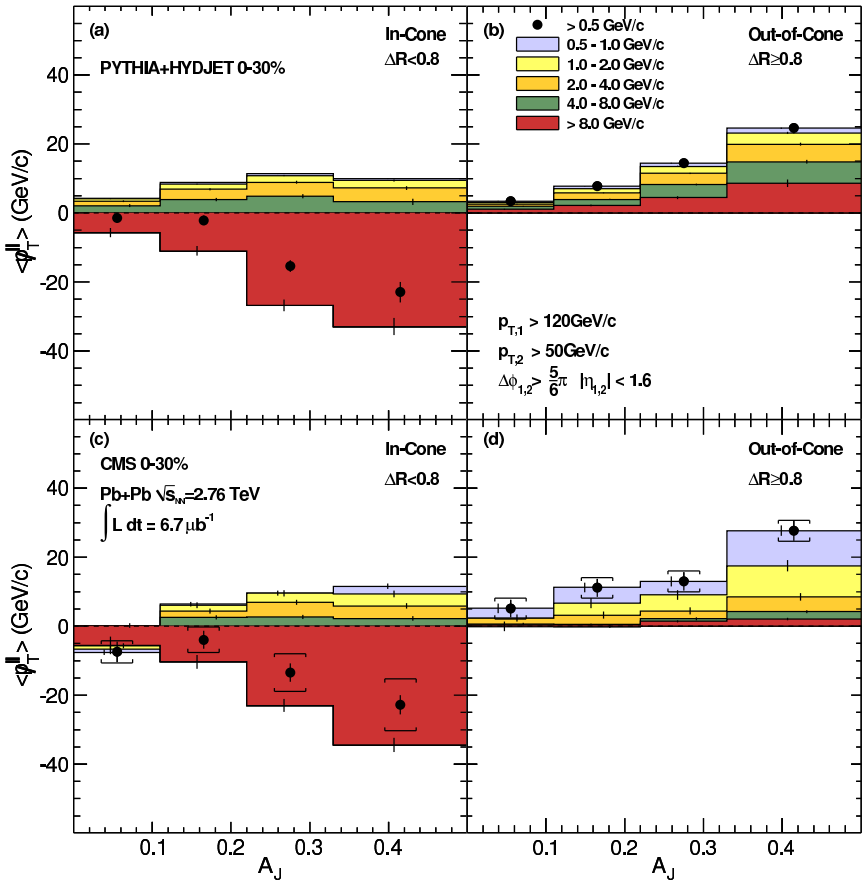

Figure 4. Average missing transverse momentum, $\langle p_{\mathrm{T}}^{\parallel} \rangle$, for tracks with $p_{\mathrm{T}} > 0.5$GeV/c, projected onto the leading jet axis (solid circles). The $\langle p_{\mathrm{T}}^{\parallel} \rangle$ values are shown as a function of dijet asymmetry A_J for 0–30% centrality, inside ($\Delta R < 0.8$) one of the leading or subleading jet cones (left) and outside ($\Delta R > 0.8$) the leading and subleading jet cones (right). For the solid circles, vertical bars and brackets represent the statistical and systematic uncertainties, respectively. For the individual p_{T} ranges, the statistical uncertainties are shown as vertical bars.

almost entirely by tracks with $0.5 < p_{\mathrm{T}} < 4$ GeV/c.

To conclude, detailed studies of dijet in PbPb collisions have been performed. The increase in the frequency of imbalanced dijets in central events demonstrates that a sizeable amount of energy is transferred out of the subleading jet. The absence of any strong angular decorrelation of the jet pairs disfavors a scenario in which this energy takes the form of hard radiation. By examining the p_{T} balance of charged tracks with respect to the leading dijet axis, it was found that asymmetric dijet events are balanced when tracks are considered down to p_{T} of 500 MeV/c. In PbPb data this balance is dominated by tracks below ~ 2 GeV/c. By studying the balance of charged tracks both inside and outside a cone of R = 0.8, it was found that the majority of this energy is distributed at large angle with respect to the jet axis.

References

[1] CMS Collaboration, "The CMS experiment at the CERN LHC", JINST 3 (2008) S08004.

[2] For a review of jet quenching, see D. dEnterria, "Jet quenching", Landolt-Boernstein, Springer-Verlag Vol. 1-23A (2010) 99, arXiv:0902.2011.

[3] CMS Collaboration, "Observation and Studies of Jet Quenching in PbPb Collisions at $\sqrt{s_{NN}} = 2.76$ TeV". 2011. arXiv:1102.1957v2.

[4] O. Kodolova et. al, "The performance of the jet identification and reconstruction in heavy ions collisions with CMS detector", *Eur. Phys. J.* **50** (2007) 117.

[5] J. E. Huth, N. Wainer, K. Meier et al., "Toward a standardization of jet definitions", in Research Directions For The Decade: Snowmass 90. 1990. FERMILAB-CONF-90-249-E.
CMS Collaboration, CMS physics: Technical Design Report Volume 1: Detector Performance and Software, CERN-LHCC-2006-001 (2006).

[6] CMS Collaboration, "Determination of the Jet Energy Scale in CMS with pp Collisions at $\sqrt{s} = 7$ TeV", CMS Physics Analysis Summary CMS-PAS-JME-10-010 (2010).

[7] CMS Collaboration, "Electromagnetic calorimeter commissioning and performance with 7 TeV data", CMS Note 10-002 (2010).
CMS Collaboration, "Identification and Filtering of Uncharacteristic Noise in the CMS Hadron Calorimeter", JINST 5 (2010) T03014, arXiv:0911.4881. doi:10.1088/1748-0221/5/03/T03014.

[8] I. P. Lokhtin and A. M. Snigirev, "A model of jet quenching in ultrarelativistic heavy ion collisions and high-pT hadron spectra at RHIC", Eur. Phys. J. C45 (2006) 211, arXiv:hep-ph/0506189. doi:10.1140/epjc/s2005-02426-3.

Jet reconstruction and jet studies in PHENIX

A. Iordanova, for the PHENIX Collaboration

University of California, Riverside, CA, 92521 USA

E-mail: anetai@ucr.edu

Abstract. Jets of particles in localized regions of phase space are produced from partonic hard-scatterings of quarks and gluons contained within protons and neutrons. In *pp* and d+Au collisions the produced jets fragment into many hadrons, which can then be reconstructed in the PHENIX detector. In contrast, jets in heavy-ion collisions (for example Cu+Cu) may propagate through the created hot, dense medium which, in turn, could lower the energy of the jet. This energy loss has several consequences including modification of the expected rate of (final) particle production and jet-shapes. By directly studying the jets measured in heavy-ion collisions, we can start to understand the properties of the hot, dense medium. However, the large non-jet backgrounds make such measurements difficult. In this talk, I will discuss the latest PHENIX results involving jets, jet reconstruction and high-$p_{\rm T}$ phenomena in the context of our current understanding of heavy-ion collisions.

1. A brief story of jets at RHIC

Single particle spectra provided the earliest measurements of jets at the Relativistic Heavy Ion Collider (RHIC) [1]. At high-$p_{\rm T}$, a large suppression of this single particle production in Au+Au, relative to that in *pp* collisions, was observed and interpreted as an effect of "in medium" parton energy loss, or jet quenching. From this measurement alone it is difficult to derive quantitative information for the level of radiative versus collisional energy loss or the type of energy loss process – perturbative or non perturbative.

Two particle correlations were the next technique used by the RHIC experiments and yielded more direct evidence of jets and jet quenching [2, 3]. The disappearance of the backward jet in central Au+Au collisions was interpreted as direct evidence for suppression due to parton energy loss. Further extensive studies showed that the jet "reappears" at low momentum, where its shape is found to be modified. No quenching was observed at high-$p_{\rm T}$. Although such statistical approaches advanced our knowledge of the parton-medium interactions in heavy-ion collisions there are still uncertainties in the energy scale of the jet and in the modification to the parton fragmentation function (expected softening and broadening of the jets). There are still many open questions left concerning the geometrical aspects of this type of measurement: what is the position

of the hard scattering in the collision overlap area? and as a result, what is the path length traversed in the medium? Is the energy lost by the trigger or the backward jet?

Another correlation analysis, γ-hadron, is considered to be better suited for studying high-$p_{\rm T}$ phenomena in heavy-ion collisions as it removes some ambiguities from the hadron-hadron correlation approach. There is no trigger or surface bias as the γ emerges from the hot, dense matter unscathed. The jet yield (which corresponds to the opposite side jet in these two particle correlations) is averaged over all path lengths. By measuring the γ there is no uncertainty in the jet energy scale. The jet fragmentation function can be measured and its modification can be interpreted as effects from parton energy loss in the medium.

Full jet reconstruction is a relatively recent probe at RHIC, providing a direct observation of parton-medium interaction. Also, di-jet correlations and varying the reconstructed jet size could provide more information on jet broadening and medium response. The reason for the delayed start of the full jet reconstruction is two-fold. Firstly, the jet production rate in heavy-ion collisions at RHIC energies is low due to the low underlying pp cross-section, discussed below. Secondly, the detection of a relatively low-$p_{\rm T}$ jet signal is inhibited by the large background from the underlying event multiplicity, especially for central collisions. In addition, the traditional jet reconstruction algorithms, when applied to a heavy-ion environment, give rise to a substantial false jet production rate due to the particle number and localized energy fluctuations on an event-by-event basis.

The full jet reconstruction in PHENIX has faced its own specific challenges. The greatest obstacle is the limited acceptance of the central arms, which are the main detectors used in the jet reconstruction.

2. Jet reconstruction

Full jet reconstruction in PHENIX utilizes the two mid-rapidity spectrometer arms, which cover $|\eta| < 0.35$ and $\Delta\phi{=}\pi/2$. The specific detector subsystems used in the reconstruction are the Drift Chamber (DC) and Pad Chamber (PC 1&3) for the momentum measurement of charged particles. The Electromagnetic Calorimeter (EMCal) is used to reconstruct the energy of photons (to reconstruct π^0 and η). More details of the PHENIX detector and its subsystems can be found in Ref. [4, 5, 6].

The jet reconstruction algorithm uses a Gaussian filter to first locate the jet and then reconstruct its energy [7, 9]. This cone-like algorithm has no sharp angular cut-off, which ensures the collinear and infrared safety of the reconstructed jets. The reconstruction starts with convolution of the event $p_{\rm T}$ density in $\eta - \phi$ space with a Gaussian distribution. The Gaussian distributed weights enhance the signal from the center of the jet relative to its periphery and thus optimizes the signal-to-background ratio whilst also defining the background. The local maxima in the filter output are the positions of the reconstructed jets in the event, Fig. 1, left panel. The filter kernel size is chosen to be $\sigma = 0.3$, unless otherwise specified. This parameter could be

approximately related to the size parameter of the iterative cone algorithm, where $\sigma = R/\sqrt{2}$. The Gaussian weighting is found to be best for the limited detector acceptance of the PHENIX detector; it smoothly dampens the large angle fragments or the lack of them if they fall outside the detector's coverage.

The jet reconstruction is based solely on individual track momenta and electromagnetic cluster energies. Several factors may modify the reconstructed jet energy. For example, loss of energy from long-lived neutral hadrons due to the lack of a hadronic calorimeter, worsening of the track momentum resolution at higher momenta, the angular weighting in the jet reconstruction algorithm. A correction to the true jet energy scale is difficult and cannot be done via a single multiplicative factor alone. Instead, the measured jet spectrum is unfolded by using an energy transfer matrix.

The jet algorithm utilizes a fake jet rejection scheme [9]. No statistical evaluation and subtraction of the background is carried out, instead a trade-off between reconstructed efficiency and acceptable fake rejection rate is made. This method for background rejection is inspired, again, by the Gaussian filter algorithm. The Gaussian weighted p_T^2 distribution arround the reconstructed jet axis (η, ϕ) serves as a jet shape discriminant, $g_{\sigma_{dis}}(\eta, \phi)$, which is defined in Eq. 1.

$$g_{\sigma_{\rm dis}}(\eta, \phi) = \sum_{i \in \rm fragment} p_{T,i}^2 e^{-((\eta_i - \eta)^2 + (\phi_i - \phi)^2)/2\sigma_{\rm dis}} \quad (1)$$

Here the size of the kernel is $\sigma_{dis} = 0.1$ and is the characteristic size of the background particle separation in the event. After studies, the discriminant threshold cut-off is set to be greater than $17.8\,({\rm GeV}/c)^2$. All jets which have $g_{\sigma_{dis}}$ below this value are considered to be fake. For example, for jets with $7.5{<}p_{\rm T}{<}11.5\,{\rm GeV}/c$ in the most central 0-20% Cu+Cu collisions at $\sqrt{s_{\rm NN}} = 200\,{\rm GeV}$, the fake contribution is less than 10% of the jet yield. This fixed threshold results in jet reconstruction efficiency, which is nearly centrality independent.

3. Results

The jet reconstruction results for *pp* and Cu+Cu system [8, 9] from RHIC Run 5 are obtained using the Gaussian filter with size $\sigma = 0.3$.

The inclusive jet cross-section for *pp* collisions at $\sqrt{s} = 200\,{\rm GeV}$ is shown in Fig. 1, right panel. The total luminosity for the data used in this analysis was $\mathcal{L} = 2.2\,pb^{-1}$. The data is compared with different models. Owing to the differences in the jet reconstruction algorithms a full agreement is not expected, although above $p_{\rm T}{>}15\,{\rm GeV}/c$ the deviation in the shapes is small. The data is also compared with the STAR High Tower jet spectrum [10].

The jet spectrum for Cu+Cu collisions at $\sqrt{s_{\rm NN}} = 200\,{\rm GeV}$ is shown in the left panel of Fig. 2. The data is divided into four centrality classes. The spectrum is unfolded to the energy scale of the reconstructed jet in *pp* collisions ($p_T^{{\rm rec}-pp}$ on the x-axis). A centrality dependent transfer matrix is used for this unfolding. The data is corrected for the geometrical acceptance and efficiency, which includes the fake background rejection.

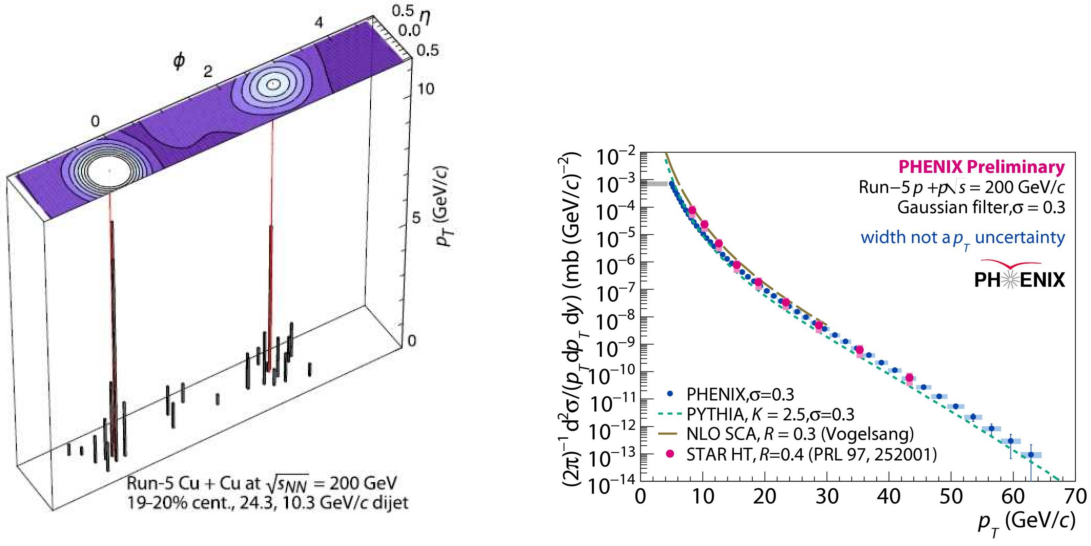

Figure 1. In the left panel, an example for jet reconstruction in a Cu+Cu event is shown, illustrating the event p_{T} distribution (black) and the reconstructed jet positions (red). In the right panel, the jet cross-section for pp collisions at 200 GeV is shown. The data are plotted as blue circles. The shaded boxes are point-to point systematic uncertainties, error bars are statistical. The grey box on the left represents the normalization uncertainty. The two lines correspond to models using different jet reconstruction algorithms. The STAR result using anti-k_T algorithm with size 0.4 is also show for comparison.

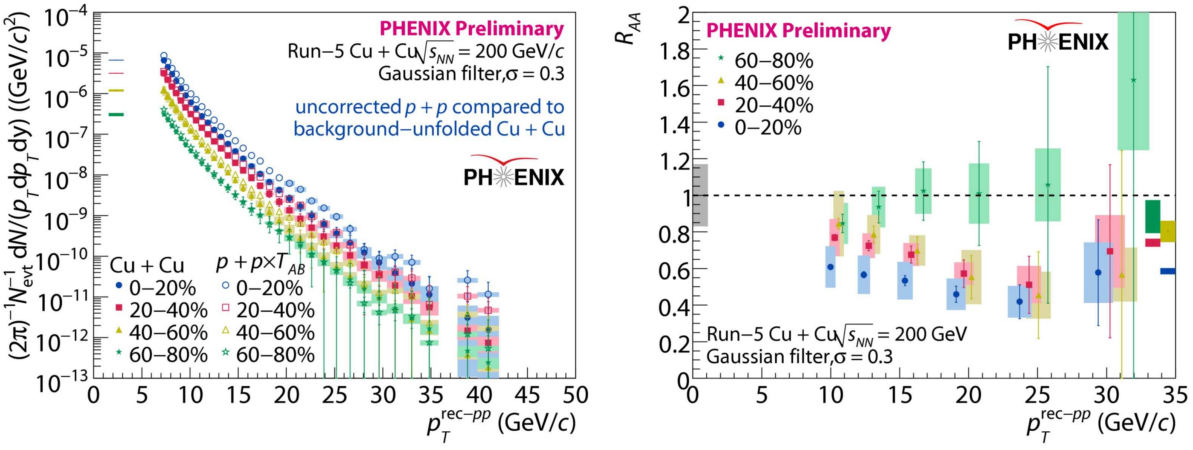

Figure 2. The left panel shows the Jet spectrum for 200 GeV Cu+Cu collisions. The data is shown as closed points for four centrality bins, represented by different marker shapes/colors. The shaded boxes are point-to point systematic uncertainties, error bars are statistical. The boxes on the left represents the normalization uncertainty. The Cu+Cu jet spectrum is unfolded to the jet energy in pp collisions. The pp spectrum jet energy is not corrected and is multiplied by the corresponding T_{AB} factor for each centrality bin. The right panel shows the jet R_{AA} for 200 GeV Cu+Cu collisions.

Only the data where the efficiency is greater than 75% is shown, which is reflected in the absence of the lowest-p_{T} data. For comparison, the reconstructed pp jet spectrum

is also shown, where no correction has been applied for its energy scale. The *pp* result is scaled by the corresponding value for the nuclear overlap density function, T_{AB}, for each centrality bin. For central collisions the scaled *pp* exceeds the Cu+Cu yield. The difference between the jet spectra in the two systems is better understood when the ratios for each centrality bin are formed.

The jet nuclear modification factor, R_{AA}, and its centrality dependence for $\sqrt{s_{NN}} = 200\,\mathrm{GeV}$ Cu+Cu collisions is shown in the right panel of Fig. 2. The nuclear modification factor is defined in Eq. 2,

$$R_{AA} = \frac{1}{N_{\mathrm{evt}}} \frac{1}{\langle T_{AB} \rangle} \frac{d^2 N_{\mathrm{Cu}}/dp_T dy}{d^2\sigma_{pp}/dp_T dy} \tag{2}$$

where T_{AB} is the nuclear overlap density function. Indeed, the maximum difference between the jet spectrum in *pp* and Cu+Cu systems is observed in central collisions. This suppression gradually decreases with centrality and the yield appears to be unmodified in peripheral collisions. The R_{AA} is independent of the jet energy scale used. The ratios of the spectra formed at the energy scale of the jets in Cu+Cu collisions shows the same features with centrality. For this test, the Cu+Cu jet spectra is left uncorrected and the *pp* spectra is reconstructed at the energy scale of the Cu+Cu jets by embedding the *pp* jets into Cu+Cu data.

The strong jet R_{AA} suppression in central Cu+Cu collisions is found to be at the same level as the one for single-π^0 spectra [11], for the overlapping p_T range †.

The sensitivity of the R_{AA} to the jet reconstruction and in particular to the jet cone size used was discussed by [12]. The increase of the jet opening angle is expected to lead to increase of the jet R_{AA} and to give more information on the jet-medium interaction and jet broadening. In order to explore this possibility, the jet R_{AA} was obtained by using a Gaussian filter with larger size, $\sigma = 0.4$, in the jet reconstruction algorithm (not shown in this proceedings). Although R_{AA} appears to increase for the larger cone size, the background fluctuations also enlarge the statistical errors on that measurement. As a result, no definite conclusion about the jet broadening can be currently made by this study. Further insight into jet broadening in the medium can be made by using di-jets. The angular correlation in $\Delta\phi$ for symmetric jets with $7.5 < p_T < 11.5\,\mathrm{GeV}/c$ was formed for the Cu+Cu system at 200 GeV. For the four centrality classes the resulting di-jet distributions were the same within the statistical errors. This leads one to conclude that jets are not deflected more in central than in peripheral collisions and to the acknowledgment that more systematic studies are needed to complete the parton energy loss picture at RHIC.

Medium modification of the jet fragmentation function in heavy-ion collisions is a direct measure of parton energy loss. The jet fragmentation function in *pp* serves as a baseline for any measurement of the jet fragmentation properties. The charged and neutral jet fragmentation functions in *pp* collisions at $\sqrt{s} = 200\,\mathrm{GeV}$ are measured using

† It should be noted that the R_{AA} for single-π^0 spectra is at a different energy scale than the reconstructed jets

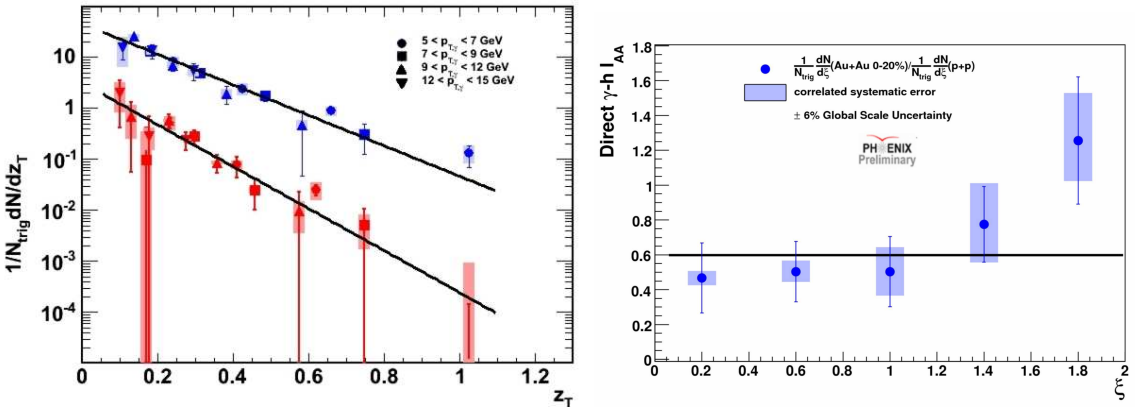

Figure 3. The left panel shows the extracted hadron jet fragmentation function from the away side in γ-hadron correlation at 200 GeV. Symbols corresponding to different γ $p_{\rm T}$ bins. The functions on the top are for pp collisions (blue markers, scale by a factor of 10), the one on the bottom are for Au+Au 0-20% central collisions (red markers). The lines correspond to an exponential fit function. The x-axis is $z_{\rm T} = {p_{\rm T}}^h/{p_{\rm T}}^\gamma$. The right panel shows the jet yield ratio I_{AA} in central Au+Au and min bias pp collisions. The line is for guidance. The x-axis is the $\xi \propto lnz$.

the Gaussian filter jet reconstruction algorithm [13]. We are also investigating the jet fragmentation functions in the heavy-ion system, but no results are currently available. Instead, we can look at the γ-jet results.

The hadronic jet fragmentation function in Au+Au collisions at 200 GeV is extracted from a narrow region on the away-side ($|\Delta\phi - \pi| < \pi/5$ rad) of the γ-hadron correlation [14, 15]. The fragmentation function in Au+Au collisions is shown in Fig. 3, left panel, for four $p_{\rm T}$-bins of the reconstructed $\gamma(p_{T,\gamma})$. The fragmentation functions, within a collision system, have the same behavior with $z_{\rm T}$, independent of $p_{T,\gamma}$. This $z_{\rm T}$ scaling, expected in pp collisions, shows that the created medium in heavy-ion collisions modifies the hadronic part of the jet fragmentation function in the same way, independent of the energy scale. A universal fit with an exponential function to all data is performed to better understand the difference between the two collision systems. The extracted value for the slope in Au+Au is 1.3σ larger compared to that in pp ($b_{pp} = 6.9 \pm 0.8$, $b_{Au+Au} = 9.5 \pm 1.4$). This could be interpreted as the hadronic fragmentation in Au+Au being closer to gluon fragmentation [15].

As the γ+jet events are not expected to have a surface bias, the observed $z_{\rm T}$ scaling in heavy-ions is somewhat surprising. The right panel of Fig. 3 shows the ratio of the hadronic jet yields in central Au+Au and minimum bias pp, for the full away-side region. The Au+Au measurement is extended to a higher ξ (lower $z_{\rm T}$) by lowering the $p_{\rm T}$ of the hadron from 1.0→0.5 GeV. This ratio provides a closer look at the modification of the fragmentation function in heavy-ion collisions. We observe that there is a suppression (i.e., the ratio is below unity) at a lower ξ with no shape modification. At high ξ (low $z_{\rm T}$) the fragmentation function in central Au+Au is enhanced. This is especially important, since model predictions diverge at low $z_{\rm T}$ [16, 17, 18]. MLLA predicts the

medium modification of hadronic jets at a low $z_{\rm T}$ and expects an enhancement as a result of gluon splitting, similarly to what we observe in our results.

4. Summary

The presented jet reconstruction algorithm for a Gaussian filter with fake jet rejection is an effective way to study parton-medium interaction at RHIC. With this jet finder we have measured spectra and jet fragmentation functions in pp collisions at $\sqrt{\rm s} = 200\,{\rm GeV}$. A strong jet suppression for central heavy-ion collisions is observed, when the jets are reconstructed in 200 GeV Cu+Cu data. The results are not sensitive to the cone size change, within the systematics. The level of suppression is the same for the jet $\rm R_{AA}$ in central heavy-ion collisions and for the single π^0 for the overlapping jet-π^0 $p_{\rm T}$ range. No significant $\Delta\phi$ broadening from di-jet correlations is observed.

Direct γ-hadron correlations provide closer look into the parton-medium interaction in heavy-ion collisions. The hadronic jet yield in Au+Au is suppressed at low ξ but the shape of the fragmentation function appears to be unmodified with respect to pp collisions. Moving toward higher ξ and considering the full away side of the γ-hadron correlation function the shape does change and enhancement is observed.

[1] K. Adcox *et al.* (PHENIX Collaboration), Phys. Rev. Lett. **88**, 022301 (2001).
[2] C. Adler *et al.* (STAR Collaboration), Phys. Rev. Lett. **90**, 082302 (2003).
[3] J. Adams *et al.* (STAR Collaboration), Phys. Rev. Lett. **91**, 072304 (2003).
[4] K. Adcox *et al.* (PHENIX Collaboration), NIM **A499**, 469-479 (2003).
[5] K Adcox *et al.* (PHENIX Collaboration), NIM **A499**, 489-507 (2003).
[6] L. Aphecetche *et al.* (PHENIX Collaboration), NIM **A499**, 521-536 (2003).
[7] Y. Lai and B. A. Cole, arXiv:0806.1499.
[8] Y. Lai (PHENIX Collaboration), Nucl. Phys. **A830**, 251-254 (2009).
[9] Y. Lai (PHENIX Collaboration), arXiv:0911.3399.
[10] B. I. Abelev *et al.* (STAR Collaboration), Phys. Rev. Lett. **97**, 252001 (2006).
[11] A. Adare *et al.* (PHENIX Collaboration), Phys. Rev. Lett. **101**, 162301 (2008).
[12] I. Vitev and B.-W. Zhang, Phys. Rev. Lett. **104**, 132001 (2010).
[13] Y. Lai (PHENIX Collaboration), arXiv:1005.2801.
[14] A. Adare *et al.* (PHENIX Collaboration), Phys. Rev. **C80**, 024908 (2009).
[15] M. Connors (for the PHENIX Collaboration), Nucl. Phys. **A830**, 447-450 (2009).
[16] N. Borghini and U. A. Wiedemann, arXiv:hep-ph/0506218, CERN-PH-TH-2005-100, BI-TP/2005/20.
[17] H. Zhang *et al.*, Phys. Rev. Lett. **103**, 032302 (2009).
[18] T. Renk, arXiv:0904.3806.

Jet studies with STAR at RHIC: jet algorithms, jet shapes, jets in AA

J Kapitán (for the STAR Collaboration)

Na Truhlarce 38/64, Praha 8, Czech Republic

E-mail: kapitan@rcf.rhic.bnl.gov

Abstract. Hard scattered partons are predicted to be well calibrated probes of the hot and dense medium produced in heavy ion collisions. Interactions of these partons with the medium will result in modifications of internal jet structure in Au+Au events compared to that observed in the p+p/d+Au reference. Full jet reconstruction is a promising tool to measure these effects without the significant biases present in measurements with high-p_{T} hadrons.

One of the most significant challenges for jet reconstruction in the heavy ion environment comes from the correct characterization of the background fluctuations. The jet momentum irresolution due to background fluctuations has to be understood in order to recover the correct jet spectrum. Recent progress in jet reconstruction methodology is discussed, as well as recent measurements from p+p, d+Au and Au+Au collisions at $\sqrt{s_{\mathrm{NN}}} = 200$ GeV.

1. Introduction

Jets are remnants of hard-scattered partons, which are the fundamental objects of perturbative QCD. At Relativistic Heavy Ion Collider (RHIC), they can be used as a probe of the hot and dense matter created in heavy ion collisions. Interaction and energy loss of energetic partons in the medium lead to jet quenching in heavy ion collisions. Until recently, jet quenching was studied indirectly using single particle spectra and di-hadron correlations [1]. These measurements are however limited in the sensitivity to probe partonic energy loss mechanisms due to biases toward hard fragmentation and small energy loss [2].

Developments in theory (for example [3, 4]) and experiment (detector upgrades, increased RHIC luminosity) finally enabled full jet reconstruction in heavy ion collisions [5]. Full jet reconstruction reduces the biases of indirect measurements and enables access to qualitatively new observables such as energy flow and fragmentation functions. As a baseline measurement for heavy ion jet studies, p+p collisions at the same energy are used. To isolate initial state effects from medium modification, measurements in d+Au are essential.

We present current jet analyses at STAR, starting with recent results on initial state effects (d+Au). Status of jet spectra analysis in Au+Au follows, including studies

of background fluctuations and their effect on the measurement of jet spectra. Finally we discuss recent results on correlations in Au+Au triggered by fully reconstructed jets: di-jet analysis and jet-hadron correlations.

2. Jet reconstruction

The present analysis is based on $\sqrt{s_{\rm NN}} = 200$ GeV data from the STAR experiment, recorded during 2006-2008. The Barrel Electromagnetic Calorimeter (BEMC) detector is used to measure the neutral component of jets, and the Time Projection Chamber (TPC) detector is used to measure the charged particle component of jets. In the case of a TPC track pointing to a BEMC tower, its momentum is subtracted from the tower energy to avoid double counting (electrons, MIP and possible hadron showers in the BEMC). Pseudorapidity acceptance for jets is $|\eta| < 0.6$ in p+p and Au+Au and $|\eta| < 0.55$ in the case of d+Au collisions.

Recombination jet algorithms $k_{\rm T}$ and anti$-k_{\rm T}$, part of the FastJet package [3], are used for jet reconstruction. To subtract the background, a method based on active jet areas [4] is applied event-wise: ${p_{\rm T}}^{\rm Rec} = {p_{\rm T}}^{\rm Candidate} - \rho \cdot A$, with ρ estimating the background density per event and A being the jet active area.

An important aspect of underlying event background are its fluctuations. We discuss data-driven methods used to correct the jet observables for these fluctuations.

3. Initial state: d+Au

This analysis is based on minimum bias triggered $\sqrt{s_{\rm NN}} = 200$ GeV data from the STAR experiment, recorded during RHIC run 8 (2007-2008). The Beam Beam Counter detector, located in the Au nucleus fragmentation region, was used to select the 20% highest multiplicity events in d+Au collisions. 10M events after event cuts were used for jet finding (anti$-k_{\rm T}$ algorithm) with a resolution parameter $R = 0.4$ and $p_{\rm T} > 0.2$ GeV/c cut was applied to tracks and towers.

PYTHIA 6.410 and GEANT detector simulations (adjusted to match the realistic TPC tracking efficiency in d+Au run 8 running) were used for jet corrections to hadron level. Embedding into real d+Au events at level of reconstructed tracks and towers was used to correct for background fluctuations. A bin-by-bin correction was applied to the jet spectrum [6].

To compare the per event jet yield in d+Au to jet cross section measurements in p+p collisions, MC Glauber studies were utilized: $\langle N_{\rm bin} \rangle = 14.6 \pm 1.7$ for 0-20% highest multiplicity d+Au collisions and $\sigma_{\rm inel,pp} = 42$ mb. These factors were used to scale the p+p jet cross section measured previously by the STAR collaboration [7] using a Mid Point Cone (MPC) jet algorithm with a cone radius of $R = 0.4$. The resulting d+Au jet $p_{\rm T}$ spectrum is shown in Figure 1 together with the scaled p+p jet spectrum. Within the systematic uncertainties, the d+Au jet spectrum scales with $\langle N_{\rm bin} \rangle$.

The leading systematic uncertainty is the Jet Energy Scale (JES) that is driven

by imprecise knowledge of TPC tracking efficiency for tracks in jets with realistic run 8 d+Au detector backgrounds. This will be considerably improved by embedding jets in raw d+Au data. With better handle on JES and by measuring jet spectrum in run 8 p+p collisions and in peripheral d+Au collisions, we'll be able to construct $R_{\rm AA}$ and $R_{\rm CP}$ for jets, respectively.

4. Inclusive jet spectra and background fluctuations in Au+Au

Preliminary results on jet $p_{\rm T}$ spectrum in Au+Au collisions at $\sqrt{s_{\rm NN}}$ = 200 GeV were reported in [8]. In this analysis, the background fluctuations were estimated by generating PYTHIA jets and embedding them into real central Au+Au events. The resulting spectrum distortion was parametrized by Gaussian, for $R = 0.4$ the width is $\sigma = 6.8$ GeV with systematic uncertainty ± 1 GeV. This parametrization was then used for a regularized matrix inversion to unfold the measured jet spectrum. Resulting $R_{\rm AA}$ is shown in Figure 2. The systematic uncertainties prevent us from precisely quantifying the suppression for $R = 0.4$ jets (their reduction will be the subject of the next paragraphs). However, it is clear that these jets are less suppressed than jets with $R = 0.2$ and charged hadrons ($R_{\rm AA} \approx 0.2$). This is consistent with a picture of jet profile broadening from $R = 0.2$ to $R = 0.4$ in central Au+Au collisions with respect to p+p, which is illustrated by spectra ratios in Figure 3.

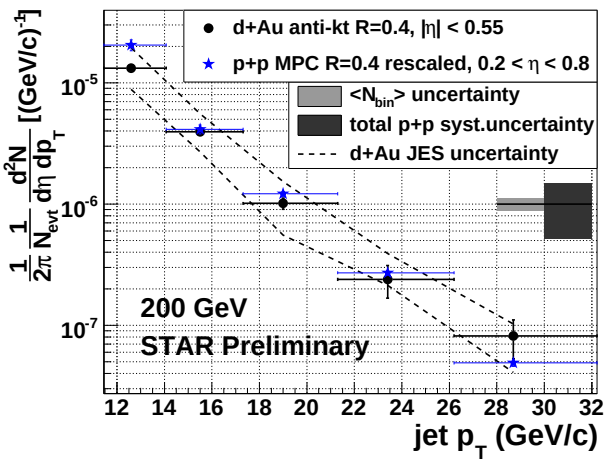

Figure 1. Jet $p_{\rm T}$ spectrum from d+Au collisions [6] compared to $\langle N_{\rm bin}\rangle$ scaled p+p spectrum [7].

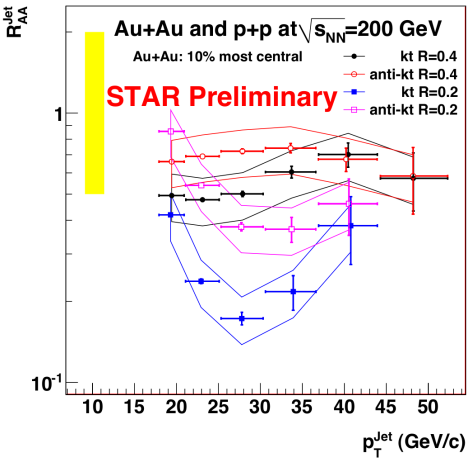

Figure 2. $R_{\rm AA}$ of jets in central Au+Au collisions for $k_{\rm T}$ and anti$-k_{\rm T}$ algorithms and $R = 0.2, 0.4$ [8].

Precise characterization of underlying event background fluctuations is essential to reduce systematic uncertainties in jet measurements. These are hence a subject of intense study, both theoreticlly [9] and experimentally. We summarize here recent results of STAR studies of background fluctuations [10].

To quantify the background fluctuation, a method is used where a probe "jet" (single particle, PYTHIA jet, QPYTHIA jet) is embedded into real central Au+Au

events. This allows to extract the shape of the fluctuations (they are known to be non-Gaussian) and also to check if they are independent of the fragmentation pattern of the probe (this is essential as jet fragmentation is modified in Au+Au collisions). We embed an object of known $p_{\rm T} = {p_{\rm T}}^{\rm embed}$ and apply jet reconstruction on the hybrid event (anti$-k_{\rm T}$ algorithm with $R = 0.4$). We match a reconstructed jet containing more than 50% of probe $p_{\rm T}$ to the probe jet and quantify the response of the hybrid system to the embedded jet via:

$$\delta p_{\rm T} = {p_{\rm T}}^{\rm reco} - \rho \cdot A^{\rm reco} - {p_{\rm T}}^{\rm embed}, \tag{1}$$

where $A^{\rm reco}$ is the area of the matched reconstructed jet and ρ is determined prior to the embedding step. This definition is identical to Eq. (1) in [9]. The normalized distribution of $\delta p_{\rm T}$ is the probability distribution to find jet energy (after event-wise background correction) ${p_{\rm T}}^{corr} = {p_{\rm T}}^{true} + \delta p_{\rm T}$. If there were no background fluctuations, $\delta p_{\rm T}$ would be a delta function at zero. For very low $p_{\rm T}$ probes, areas of anti$-k_{\rm T}$ jets get very small, so a cut $A^{\rm reco} > 0.4$ was applied. With this cut, $\delta p_{\rm T}$ distribution turns out to be largely independent of ${p_{\rm T}}^{\rm embed}$ [10].

We have investigated dependence of $\delta p_{\rm T}$ on jet fragmentation pattern. Figure 4 shows the overlay of multiple $\delta p_{\rm T}$ distributions for single particle jets and for jets with both low and high $p_{\rm T}$ generated by PYTHIA and Q-PYTHIA ($\hat{q} = 5$ GeV^2/fm). In order to compare their shapes directly, the distributions were aligned horizontally by fitting a Gaussian function to $\delta p_{\rm T} < 0$ and aligning the centroids by shifting relative to one reference distribution. The shifts are shown in the insert and are typically smaller in magnitude than 1 GeV. The overlay shows that the $\delta p_{\rm T}$ distribution is to a large extent universal, within a factor ~ 2 at $\delta p_{\rm T} = 30$ GeV, especially in region $\delta p_{\rm T} > 0$ which drives the smearing of the inclusive jet spectrum. Further quantification of this observation and its application to deconvolution of the measured inclusive jet spectrum in central Au+Au collisions is in progress.

5. Jet triggered correlations

A highly biased jet population was used as *trigger* in di-jet and jet-hadron correlations. Trigger jets are required to contain a BEMC tower with $E_{\rm T} > 5.4$ GeV to achieve a longer in-medium pathlength on the recoil (away side). To limit the effect of background fluctuations, trigger jets are reconstructed using only TPC tracks and BEMC towers with $p_{\rm T} > 2$ GeV/c. A 2 GeV systematic uncertainty on trigger jet energy was used to account for any remaining effect.

Recoil jet $p_{\rm T}$ spectrum was measured in p+p and Au+Au (0-20% most central) collisions [11]. A Gaussian model of background fluctuations was used to unfold the Au+Au spectrum with systematic uncertainty ± 1 GeV. Figure 5 shows a significant suppression of recoil jet $p_{\rm T}$ spectrum in Au+Au compared to p+p for $R = 0.4$, which suggests jet broadening beyond $R = 0.4$. Considering also the observation from inclusive jet analysis (suggestive of jet broadening from $R = 0.2$ to $R = 0.4$) there appears to be a smooth jet broadening trend. Note that the recoil jet $p_{\rm T}$ spectrum is much

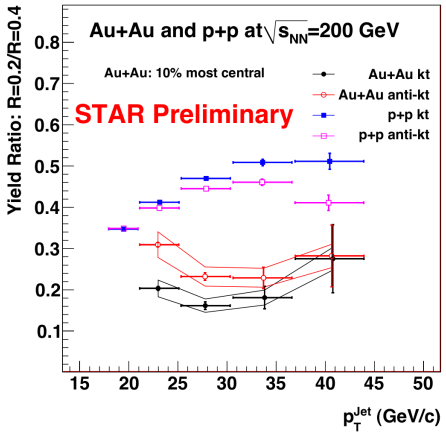

Figure 3. Ratio of $R = 0.2/R = 0.4$ jet p_{T} spectra in p+p and Au+Au collisions [8].

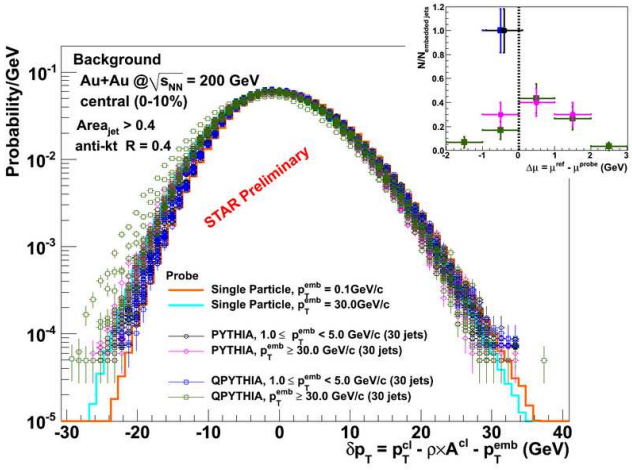

Figure 4. Quantifying the background fluctuations and their dependence on probe p_{T} and fragmentation [10].

flatter (harder) than the inclusive one, therefore impact of uncertainties on background fluctuations is much reduced.

Full jet reconstruction is not feasible for $R > 0.4$ due to large background fluctuations. To investigate the jet broadening on the away side of the trigger jet, jet-hadron (JH) azimuthal correlations between trigger jet and charged hadrons (detected by the TPC detector) are measured [12]. The raw azimuthal correlation is parametrized via two Gaussian peaks (near and away side jet) and v_2 modulated background (with fixed v_2 values). The uncertainties in the (a priori unknown) jet v_2 value were chosen to cover the extreme cases of no v_2 and 50% higher than $v_2\{2\}$ at $p_{\mathrm{T}} = 6$ GeV/c (default is $v_2\{2\}$ at $p_{\mathrm{T}} = 6$ GeV/c). The associated track v_2 values and uncertainties follow the analysis in [13]. Due to ambiguities of ZYAM for broad jet structures, the background level was determined by the fit. For comparison ZYAM was applied (as expected for broad structures it leads to an underestimation of the correlated away-side yields for lower associated p_{T}).

Figure 6 shows the awayside Gaussian width of JH in p+p and $0-20\%$ most central Au+Au collisions. There is a significant broadening (Au+Au w.r.t. p+p) for $p_{\mathrm{T}}^{assoc} < 3$ GeV/c, while no broadening at higher p_{T}^{assoc} is observed. I_{AA}, the ratio of per-trigger associated yields, is plotted in Figure 7. There is a significant suppression of high p_{T} particles on the away side accompanied by an enhancement at low p_{T}^{assoc}. In order to quantify the energy redistribution on the away side, it's better to instead of I_{AA} use D_{AA}:

$$D_{\mathrm{AA}}(p_{\mathrm{T}}^{assoc}) = p_{\mathrm{T}}^{assoc} \cdot (Y_{\mathrm{AA}}(p_{\mathrm{T}}^{assoc}) - Y_{\mathrm{pp}}(p_{\mathrm{T}}^{assoc})), \tag{2}$$

where $Y_{\mathrm{AA,pp}}$ are per-trigger associated yields in AA,pp. Away side D_{AA} for JH is shown in Figure 8. In fact, the energy "lost" at high p_{T} is approximately compensated by low p_{T} enhancement [14]: jet quenching in action.

Given the observed broadening for $p_{\rm T}^{assoc} < 3$ GeV/c, no broadening for high $p_{\rm T}^{assoc}$ and $I_{\rm AA}$ shape independent of $p_{\rm T}^{assoc}$ at high $p_{\rm T}^{assoc}$, one can speculate that the original parton loses energy by emission of soft radiation (and therefore the original jet direction changes little: no broadening is observed at high $p_{\rm T}^{assoc}$). These soft fragments traverse the medium, receive transverse kicks and therefore appear at large angles with respect to the original parton direction. The energy loss is followed by a possibly vacuum-like fragmentation of a parton with reduced energy.

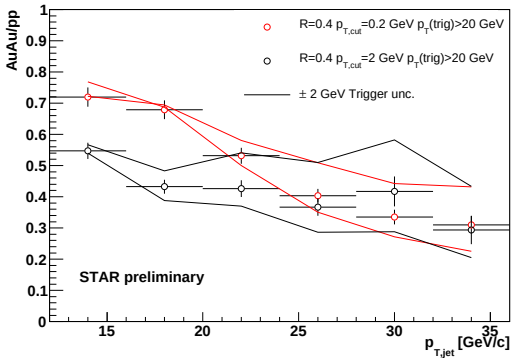

Figure 5. Ratio of recoil jet $p_{\rm T}$ spectra in Au+Au/p+p [11].

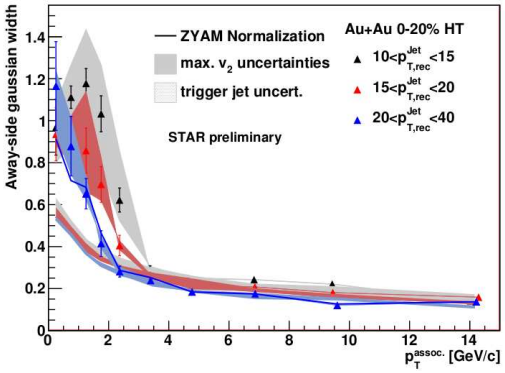

Figure 6. Away side Gaussian width in JH correlations [12].

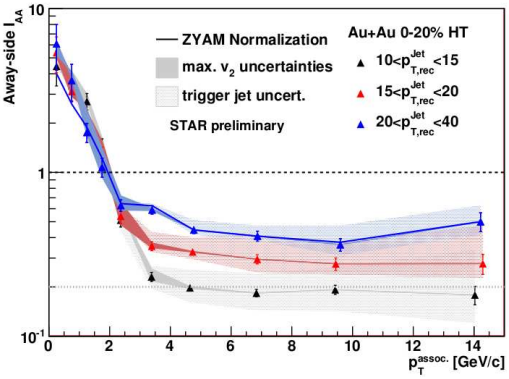

Figure 7. Away side $I_{\rm AA}$ in JH correlations [12].

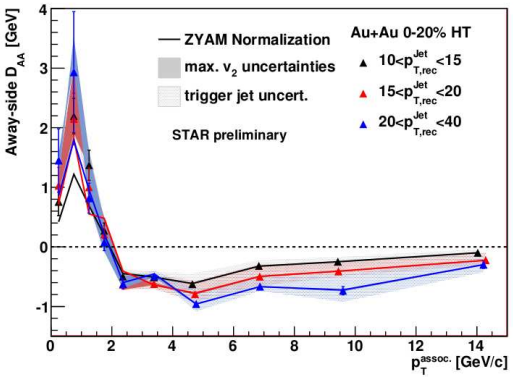

Figure 8. Away side $D_{\rm AA}$ in JH correlations [12].

6. Summary

We have presented STAR results on full jet reconstruction in d+Au collisions. Within current systematics there appears to be binary collision scaling compared to p+p collisions, but the final measurements (jet $R_{\rm AA}$ and $R_{\rm CP}$) with reduced systematic uncertainties are yet to be completed. The study of background fluctuations $\delta p_{\rm T}$ in Au+Au collisions suggests its independence of ${p_{\rm T}}^{\rm embed}$ and the probe jet fragmentation pattern. The shape of $\delta p_{\rm T}$ will be used to unfold the measured jet $p_{\rm T}$ spectrum to obtain the final result with decrased systematic uncertainties. The hints of jet broadening obtained first in inclusive jet $p_{\rm T}$ spectrum and di-jet correlations were further studied using jet-hadron correlations, where significant broadening and enhancement at low

p_{T}^{assoc} was accompanied by suppression (and no broadening) at high p_{T}^{assoc}. This is consistent with the picture of pQCD-like energy loss to soft fragments followed by (possibly vacuum-like) fragmentation of a parton with reduced energy.

Acknowledgement

This work was supported in part by grants LC07048 and LA09013 of the Ministry of Education of the Czech Republic.

References

[1] I. Arsene *et al*, Nucl. Phys. **A757**, 1-27 (2005). B. B. Back *et al*, Nucl. Phys. **A757**, 28-101 (2005). J. Adams *et al*, Nucl. Phys. **A757**, 102-183 (2005). K. Adcox *et al*, Nucl. Phys. **A757**, 184-283 (2005).
[2] T. Renk, Phys. Rev. **C78**, 034904 (2008).
[3] M. Cacciari, G. Salam, Phys. Lett. **B641**, 57 (2006). M. Cacciari, G. Salam, G. Soyez, JHEP **0804**, 063 (2008).
[4] M. Cacciari, G. Salam, Phys. Lett. **B659**, 119 (2008). M. Cacciari, G. Salam, G. Soyez, JHEP **0804**, 005 (2008).
[5] J. Putschke (for the STAR Collaboration), Eur. Phys. J. **C61**, 629-635 (2009). S. Salur (for the STAR Collaboration), Eur. Phys. J. **C61**, 761-767 (2009). M. Ploskon (for the STAR Collaboration), Nucl. Phys. **A830**, 255c-258c (2009). E. Bruna (for the STAR Collaboration), Nucl. Phys. **A830**, 267c-270c (2009).
[6] J. Kapitan (for the STAR Collaboration), Nucl. Phys. **A855**, 412-415 (2011).
[7] B. I. Abelev *et al*, Phys. Rev. Lett. **97**, 252001 (2006).
[8] M. Ploskon (for the STAR Collaboration), Nucl. Phys. **A830**, 255c-258c (2009).
[9] M. Cacciari, J. Rojo, G. Salam, G. Soyez, Eur. Phys. J. **C71**, 1539 (2011).
[10] P. Jacobs (for the STAR Collaboration), Nucl. Phys. **A855**, 299-302 (2011).
[11] E. Bruna (for the STAR Collaboration), arXiv:1010.3184.
[12] J. Putschke (for the STAR Collaboration), Nucl. Phys. **A855**, 83-91 (2011).
[13] B. I. Abelev *et al*, Phys. Rev. **C80**, 064912 (2009).
[14] A. Ohlson (for the STAR Collaboration), arXiv:1106.6032.

Physics opportunities with an Electron-Ion Collider

Vadim Guzey

Jefferson Lab, 12000 Jefferson Avenue, Newport News, VA 23606, USA

E-mail: vguzey@jlab.org

Abstract.

I briefly present main science goals, basics of design, and key measurements at a planned Electron-Ion Collider.

1. Nucleon and nuclear structure in QCD and the EIC project

Understanding the internal structure of the nucleon and nuclei on the basis of the fundamental theory of strong interactions, Quantum Chromodynamics (QCD), is one of the central problems of nuclear physics today. The outstanding fundamental questions include (i) the dynamical origin of mass in the visible Universe, (ii) the behavior of matter at astrophysical densities and temperatures, and (iii) the nuclear structure and reactions from first principles. While decades of experiments at SLAC, CERN, Fermilab, DESY, and Jefferson Lab and advances in theory have thoroughly explored the internal structure of hadrons, several key questions remain open:

- What is the internal landscape of the nucleon? In particular, what role do sea quarks and gluons play in the nucleon structure? What is their polarization and how do they distribute in space (and in the longitudinal and transverse momentum)?
- What is the role of gluons and their self-interactions in nuclei? What is the density of gluons in nuclei and the role of gluon collective (non-linear) effects?
- What governs the transition (hadronization) of quarks and gluons in pions and nucleons? How does color charge of QCD interact with nuclear matter?

These major science questions define main goals and form the science case for a future Electron-Ion Collider (EIC), a polarized electron-polarized proton and electron-nucleus collider that has been embraced by the U.S. nuclear science community and which received an informal recommendation in 2007 DOE/NSF NSAC Long Range Plan [1].

2. Basic characteristics and designs of EIC

The design of an EIC is driven by its science goals. The basic requirements for a future EIC include:

- Lepton beam which provides a clean and well-understood probe,
- Range of c.m. energies from s=few 100 GeV^2 to s=few 1000 GeV^2; the energy should be variable and upgradeable:
  - electrons with energy up to $20-30$ GeV,
  - protons with energy up to $250-325$ GeV and ions with energy up to $100-130$ GeV/A,
- Polarized electron and proton beams (polarization $> 70\%$) including longitudinal and transverse polarization of the proton beam, polarized light nuclei, e.g., ^{3}He,
- High luminosity of the order of 10^{34} cm^{-2}s^{-1} ($>$ 100 times that of HERA),
- Range of nuclei, from deuterium to ^{208}Pb.

From the start of the EIC project, there have been two competing designs of an EIC: ELIC at Jefferson Lab and eRHIC at Brookhaven National Laboratory (BNL), see figure 1. ELIC assumes a ring-ring design with the existing CEBAF as an injector;

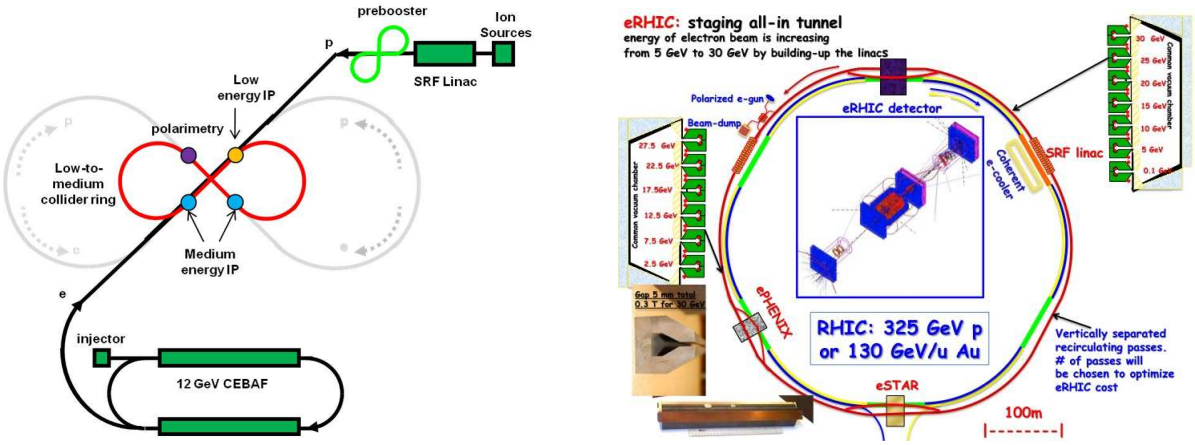

Figure 1. Two competing designs of an EIC: (left) ELIC at Jefferson Lab, (right) eRHIC at BNL.

the hadron complex and accelerator ring need to be constructed; up to four interaction points are considered. The accelerator ring is envisioned to have the shape of the figure eight (for polarization transport) and to be realized in two stages: (i) an initial medium-energy option (MEIC) with a 1-km long ring providing $3-11$ GeV/c electrons on 60/95 GeV/c protons (the nuclear momentum scales as Z/A, where Z is the charge and A is the atomic mass number), (ii) followed by an upgrade (ELIC) to a larger 2.5-km ring with $3-11$ GeV/c electrons on 250 GeV/c protons. The aimed luminosity is $\sim 10^{34}$ cm^{-2}s^{-1}.

The eRHIC at BNL assumes a linac-ring design with the existing RHIC complex; energy-recovering linacs for electrons need to be built and they can be placed in the existing RHIC tunnel. The project is also envisioned to take place in two stages: (i) an initial medium-energy stage (MeRHIC) with 5 GeV/c electrons on $250-325$ GeV/c

protons, (ii) followed by un upgrade (eRHIC) to $20-30$ GeV/c electrons on $250-325$ GeV/c protons. The aimed luminosity is $\sim 10^{33,34}$ cm^{-2}s^{-1}; it is also discussed to re-use the existing RHIC detectors (ePHENIX and eSTAR).

During 2010-2011 the Jefferson Lab and BNL EIC designs have significantly converged: the aimed c.m. energies and luminosities are now rather similar; both designs assume staging (energy upgrade). At the same time, the designs are different in technological challenges and cost. For detailed and up-to-date information on the EIC accelerator designs, see [2].

3. Key measurements at an EIC

The nucleon/nucleus in QCD is a many-body system whose wave function consists of an infinite number of configurations containing valence and sea quarks and gluons. The high-energy and high-luminosity EIC will study the sea quark and gluon structure of the nucleon/nuclei as well as their propagation in nuclear matter. Some key measurements at the EIC are summarized below.

Mapping the spin and spatial structure of quarks and gluons in the nucleon.

One of the key measurements at the EIC is the measurement of the gluon helicity distribution $\Delta g(x,Q^2)$. Measurements of the polarized structure function g_1 in a wide range in Bjorken x and Q^2 will dramatically extend the available data set and will enable one to extract $\Delta g(x,Q^2)$ using global QCD fits down to $x \approx 10^{-4}$ at stage-1 (medium-energy EIC) and down to $x \approx 3\times 10^{-5}$ at stage-2 (full-energy EIC). Additional constraints on $\Delta g(x,Q^2)$ can be obtained from the measurements of charm and jet production in polarized DIS. It will significantly reduce the present uncertainty associated with the first moment $\int_0^1 dx \Delta g(x,Q^2)$ (which is expected to be determined with 10% accuracy) and, thus, with the gluon contribution to the nucleon spin sum rule.

While the polarization of valence quarks is known fairly well and will be further constrained by the measurements at Jefferson Lab at 12 GeV, the polarization and flavor dependence (asymmetry) of sea quarks is poorly known. One example is polarized strange quark distributions $\Delta s(x)$ and $\Delta\bar{s}(x)$: while the available data prefers small and positive $\Delta s(x)$ and $\Delta\bar{s}(x)$, the first moment of $\Delta s(x)$ is negative and sizable due to the constraints from hyperon decays. The flavor dependence of polarized parton distributions (PDFs) will be studied at an EIC using the combination of inclusive and semi-inclusive polarized DIS. In the latter, the quark flavor will be "tagged" by selecting $\pi^\pm$ and $K^\pm$ produced from its fragmentation. The kinematic coverage and detection capabilities of a discussed future detector for an EIC (good particle ID in a wide kinematic range) are uniquely suited for such measurements. In addition to semi-inclusive DIS, flavor decomposition of polarized PDFs can be performed in charged-current (W^+ and W^-) inclusive polarized DIS; these measurements do not require the knowledge of fragmentation functions.

A more detailed information about the nucleon structure can in principle be obtained from hard exclusive processes (exclusive electroproduction of a real photon or

a vector or pseudoscalar meson) which access generalized parton distributions (GPDs). GPDs provide the distributions and correlations of partons both in the longitudinal light-cone fraction(s) and transverse coordinate (impact parameter). Therefore, it is often said that GPDs provide the spatial, three-dimensional snapshot of the nucleon. Additionally, GPDs quantify the fundamental decomposition of the nucleon spin in terms of the quark and gluon helicities and orbital moments (Ji's spin sum rule). Various deep exclusive processes access different flavor and spin combinations of GPDs: production of a real photon or deeply virtual Compton scattering (DVCS) and production of light vector mesons (ρ, ω, ϕ) probe unpolarized sea quark and gluon GPDs, production of J/ψ probes the unpolarized gluon GPD, production of pseudoscalar mesons (π, K) probes the non-strange and strange polarized GPDs. Such measurements require differential measurements of low-rate exclusive processes which will be possible at an EIC due to its high luminosity; the possibility to longitudinally and transversely polarize the proton beam will help to disentangle different kinds of GPDs.

In parallel to the nucleon imaging program, deep exclusive processes with nuclei (DVCS, J/ψ production) will access impact parameter dependence of nuclear PDFs and will obtain the spatial image of nuclear shadowing of sea quarks and gluon in nuclei. This information is essential for perturbative calculations for pA scattering at RHIC and the LHC.

Other relevant EIC measurements include PDFs at large x and a program of measurements of transverse momentum dependent distributions (TMDs) in semi-inclusive DIS.

The gluon structure of nuclei.

One of manifestations of the role of QCD in nuclear physics is the nuclear modifications of structure functions and parton distributions. The pattern of the deviations of the nuclear structure function $F_{2A}(x,Q^2)$ from the sum of the nucleon structure functions $AF_{2N}(x,Q^2)$ has been established in fixed-target experiments and looks as follows: suppression for small $x < 0.05$ (nuclear shadowing), slight enhancement for $0.05 < x < 0.2$ (antishadowing), suppression for $0.2 < x < 0.8$ (EMC effect), and rapid enhancement for $x > 0.8$ (Fermi motion). This trend of nuclear modifications translates into a similar pattern of modifications of quark and gluon distributions in nuclei when these are extracted using global QCD fits. However, in the small x region, the gluon PDF in nuclei is essentially unconstrained by such fits and sea quark PDFs are poorly constrained. At an EIC, one will accurately determine the gluon PDF in a range of nuclei down to $x = 10^{-3}$ and the sea quark PDFs down to approximately 5×10^{-4} due to: (i) a wide $x - Q^2$ range probing deep in the shadowing region (the collider kinematics will allow one to simultaneously have small x and sufficiently large range in Q^2 such that the gluon distribution can be reliably determined from scaling violations), (ii) direct access to gluons via the longitudinal structure function $F_L^A(x,Q^2)$ (via the measurements at different beam energies), (iii) complimentary measurements of charmed structure functions $F_{2A}^{(c)}(x,Q^2)$ and $F_L^{A(c)}(x,Q^2)$, (iv) measurements of light-quark and heavy-quark jets in DIS.

At very small x, the gluon density rapidly increases and one expects an onset of a new high-gluon density (non-linear) regime of the strong interactions. Such a scenario is realized in the framework of the Color Glass Condensate (CGC) formalism, where the regime of high parton densities is characterized by a new dynamical scale Q_s^2. While even the full-energy EIC will not be capable to look for saturation effects with the proton beam, the hope to achieve the saturation regime at the EIC rests on the nuclear enhancement of $Q_s^2 \sim A^{1/3}$ (one needs to have $Q_s^2 \geq 1$ GeV^2 for the validity of the parton picture). It is impossible to unambiguously establish the presence of parton saturation in one kind of experiment since saturation effects can be masked, e.g., by a suitable adjustment of the input parton densities. Therefore, at the EIC, one considers a host of different measurements aimed at a search of the non-linear regime of high-gluon density in nuclei including inclusive, diffractive and exclusive DIS.

Turning to the medium and large x region, $0.05 < x < 0.8$, one notes that the quark PDFs in nuclei in this region have been rather thoroughly investigated in fixed-target experiments and will be further studied at Jefferson Lab at 12 GeV. At the same time, the behavior of the gluon PDF in this region is poorly constrained. Using the same probes and methods as in the studies of nuclear shadowing in the gluon channel (see above), one will be able to study antishadowing and the EMC effect in the gluon channel at the EIC.

Other relevant EIC measurements include tagged structure functions of light nuclei (D, ^{3}He) and studies of medium modifications of bound nucleons.

Emergence of hadronic matter from quarks and gluons.

The transition of colored partons to colorless hadrons—hadronization—still lacks an understanding from the first principles in QCD: there compete several mechanisms (parton energy loss, prehadron re-interactions inside the nuclear medium, etc.) involving several time scales. To disentangle these mechanisms, probably the best experimental tool is DIS with nuclei. At an EIC, the combination of high energy and high luminosity will bring the studies of hadronization to a qualitatively new level. Indeed, the large Q^2 range will permit measurements in the fully perturbative regime with enough leverage to determine nuclear modifications of the fragmentation functions; the high luminosity will permit for multidimensional binning necessary for separating the many competing mechanisms and detecting rare processes. The large $\nu \approx 10 - 1000$ GeV range will allow one to isolate in-medium parton propagation effects (large ν) and cleanly extract color neutralization and hadron formation times (small ν). For the first time, one will also be able to study hadronization of open charm and open bottom mesons and in-medium propagation of heavy mesons; these studies are crucial for understanding of quark-gluon plasma at RHIC. Also, within a collider environment, one would be able to separate target from current fragmentation adding a new dimension to hadronization studies.

The second aspect of hadronization studies at an EIC is the possibility to use colored probes to study the gluon distribution in nuclei. In addition, for the first time one will be able to to measure jets and their substructure in eA collisions.

4. The EIC project status and timeline

After the informal recommendation by NSAC Long Range Plan in 2007 [1], the EIC collaboration was formed. Now the collaboration includes more than 100 scientists from about 20 institutions. The EIC collaboration functions as follows: the activities are coordinated by the EIC Steering Committee; the status and progress are reported at semi-annual collaboration meetings; regular reviews of physics and updates on the accelerator designs take place and are overseen by the International EIC Advisory Committee. For more information, see [3, 4].

Also, a series of Jefferson Lab Users workshops on EIC was held in 2010 [5, 6, 7] and the EIC science was discussed at 2010 Institute for Nuclear Theory program INT 10-03 in Seattle [8].

Now the EIC Collaboration and EIC enthusiasts are working towards a full recommendation by the NSAC LRP in 2013.

[1] 2007 DOE/NSF NSAC Long-Range Plan, http://science.energy.gov/np/nsac

[2] Y. Zhang, *Progress in MEIC and ELIC Design and Development*, and V. Litvinenko, *Progress in eRHIC Design and Development*, talks at EIC Advisory Committee meeting, Jefferson Lab, April 10, 2011, http://conferences.jlab.org/eic2011/program.html.

[3] http://www.jlab.org/meic

[4] http://www.eic.bnl.gov

[5] http://www.physics.rutgers.edu.np/2010rueic-home.html

[6] http://michael.tunl.duke.edu/workshop; M. Anselmino *et al.*, Eur. Phys. J. A **47** (2011) 35 [arXiv:1101.4199 [hep-ex]].

[7] http://www.phy.anl.gov/mep/EIC-NUC2010

[8] http://www.int.washington.edu/PROGRAMS/10-3.

From QCD color coherence to inclusive distributions and correlations in jets

Redamy Pérez-Ramos

Dr. Moliner 50, S-46100 Burjassot, Spain

E-mail: redamy.perez@uv.es

Abstract. In this paper we briefly review some examples of inclusive energy-momentum distributions and correlations in QCD intra-jet cascades. Emphasis is given to the role of gluon coherence effects in final states hadron spectra. These observables provide tests of the Local Parton Hadron Duality (LPHD) hypothesis.

The high energy annihilation e^+e^- into hadrons, deep inelastic lepton-hadron scattering (DIS) and hadron-hadron collisions are classical examples of hard processes where high transverse momentum jets are produced [1]. In fact, the observation of quark and gluon jets has played a crucial role in establishing Quantum Chromodynamics (QCD) as the theory of strong interaction within the Standard Model of particle physics. Jets, narrowly collimated bundles of hadrons produced at high virtuality Q, reflect configurations of quarks and gluons at short distances. As is well known, perturbative QCD (pQCD) controls the relevant observables to be measured at colliders but its applicability fails as the evolution of the jet reaches the hadronization stage. In other words, at short quark-gluon distances, the perturbative approach is suitable due to the weak strength of the coupling constant $\alpha_s(Q^2) \ll 1$ while, as the jet evolves towards hadronization occurring at larger $\alpha_s(k_\perp^2) \sim 1$ ($k_\perp^2 < Q^2$ for secondary partons emitted off the leading parton) and larger quark-gluon distance, the expanded series do not converge any longer. Therefore, the perturbative approach fails to describe the forthcoming evolution of partons into final hadrons that hit the detectors. That is why, it is advocated the Local Parton Hadron Duality hypothesis after the emission of gluons inside the jet reaches the infrared cut-off Q_0, which mainly consists of comparing the shape and normalization of the obtained distribution with the corresponding data sets [2].

Jet physics is mainly dominated by soft gluon bremsstrahlung. As a consequence of QCD color coherence, the emission of successive soft gluons inside the jet has been demonstrated to form a cascade where the emission angles decrease towards the hadronization stage, the so-called Angular Ordering (AO) [1]. Perturbative schemes, like the Double Logarithmic Approximation (DLA) and the Modified Leading Logarithmic Approximation (MLLA), which allow for the resummation of soft-collinear and hard-collinear gluons, have been implemented. One of the most impressive predictions of

perturbative QCD (pQCD) is the existence of the hump-backed plateau (HBP) of the inclusive energy distribution of hadrons, later confirmed by experiments at colliders like the LEP [3] and the Tevatron [4]. Within the same formalism, the transverse momentum distribution, or $k_\perp$-spectrum of hadrons produced in $p\bar{p}$ collisions at center of mass energy $\sqrt{s} = 1.96$ TeV at the Tevatron [5], was well described by MLLA and next-to-MLLA (NMLLA) predictions inside the validity ranges provided by such schemes, both supported by the LPHD [6, 7]. Thus, inclusive observables like the inclusive energy distribution and the inclusive transverse momentum $k_\perp$ spectra of hadrons have shown that the perturbative stage of the process is dominant and the LPHD hypothesis is successful in treating one-particle inclusive observables. The study of particle correlations in intrajet cascades, which are less inclusive observables, provides a refined test of the partonic dynamics and the LPHD. Two-particle correlations were measured by the OPAL collaboration in the e^+e^- annihilation at the Z^0 peak, that is for $\sqrt{s} = 91.2$ GeV at LEP [8]. Though the agreement with theoretical predictions turned out to be rather good for the description of the data, a discrepancy still subsists pointing out a possible failure of the LPHD for less inclusive observables or the existence of non-trivial hadronization effects not regarded in the evolution equations. However, these measurements were redone by the CDF collaboration in $p\bar{p}$ collisions at the Tevatron for mixed samples of quark and gluon jets [4]. The agreement with theoretical predictions turned out to be rather good, in particular for very soft particles ($x \ll 0.1$) with very close energy fractions. However, a discrepancy showed up and still stays unclear between the OPAL and CDF analysis.

The inclusive energy spectrum of soft gluon bremsstrahlung partons in QCD jets $D^{ch}(\ln(1/x)) = \mathcal{K}^{ch}\frac{1}{N}\frac{dN}{d\ln(1/x)}$ has been obtained in the MLLA, and supported with the LPHD hypothesis for charged hadrons [1]. This approximation takes into account all essential ingredients of parton multiplication in the next-to-leading order, which are parton splitting functions responsible for recoil effects at each $q \to qg$, $g \to q\bar{q}$, $g \to gg$ vertex, the running coupling $\alpha_s(k_\perp^2) \ll 1$ depending on the relative transverse momentum of the two offspring and the exact AO. Gluon coherence suppresses indeed multiple production of very soft gluons such that, only particles with intermediate energies multiply most efficiently. As a consequence, the energy spectrum of charged hadrons acquires the hump-backed shape with an asymptotic energy peak in the logarithmic scale $\ell_{max} = \ln(1/x_{max}) \to \frac{1}{2}\ln(Q/Q_0)$ in the limit where the perturbative approach, regularized by the infrared cut-off Q_0, equals Λ_{QCD}, the so-called limiting spectrum. At the end, the shape and normalization are compared with the experiment; a constant $\mathcal{K}^{ch}$ is chosen, which normalizes the number of soft gluons to the number of charged detected hadrons (mostly pions and kaons), giving support to the similarity between parton and hadron spectra [1]. This is exactly what is observed in Fig.1 (left) for the e^+e^- data [3] at the Z^0 peak. The description of the OPAL data, to cite one example, are well described by the MLLA one-particle inclusive distribution in the limiting spectrum approximation ($Q_0 \sim \Lambda_{QCD}$). Though the coupling constant α_s diverges in this limit, the hadron spectra turns out to be Collinear and Infrared Safe (CIS), describing

the data even in the region of x, $x \sim 1$ where the MLLA is not valid. Originally, for $Q_0 \neq \Lambda_{QCD}$, the single inclusive spectrum is $\propto \mathcal{K}^h(\omega, \ln(Q_0/\Lambda_{QCD}))$ in Mellin space, which is written in terms of Bessel functions. In the limit $Q_0 \sim \Lambda_{QCD}$ however, any influence of this factor disappears such that $\mathcal{K}^h(\omega, 0) = 1$. Other experiments like ALEPH, CDF, DELPHI, HERA and TASSO also show results that are in agreement with MLLA calculations [4].

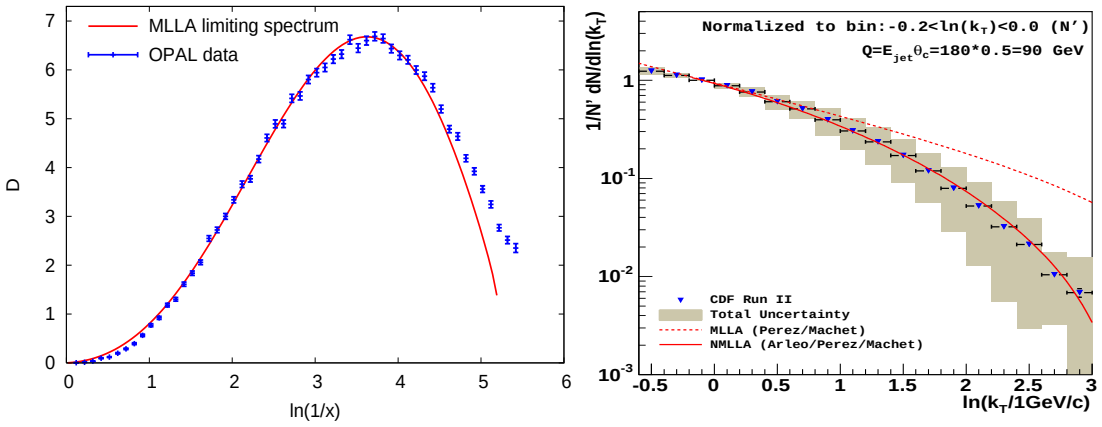

Figure 1. Hump-backed plateau (left) as a function of $\ln(1/x)$ for fixed $Q = 91.2$ GeV in the process $e^+e^- \to q\bar{q}$ and $k_\perp$-spectra (right) for a mixed sample of quark and gluon jets for a dijet with $Q = 90$ GeV in $p\bar{p}$ collisions with $\mathcal{K}^{ch} \sim 1$.

Secondly, the $k_\perp$-spectra of charged hadrons $\mathcal{K}^{ch} \frac{1}{N} \frac{dN}{d \ln k_\perp}$ was measured at the Tevatron [5]. It was also found to follow the MLLA and NMLLA expectations and to give further support to the LPHD hypothesis [7]. Computing the single inclusive $k_\perp$-distribution requires the definition of the jet axis. The starting point of the approach consists in considering the correlation between two particles (h1) and (h2) of energies E_1 and E_2 which form a relative angle Θ inside one jet of total opening angle $\Theta_0 > \Theta$ [6]. Weighting over the energy E_2 of particle (h2), this relation leads to the correlation between the particle (h=h1) and the energy flux, which can be identified with the jet axis [6]. Since soft particles are less sensitive to the energy balance, in the soft approximation $x \ll 1$ the previous correlation disappears and the computation of this observable becomes straightforward. As an example, in Fig. 1 (right), as taken from [5], we display the $k_\perp$-spectra of charged hadrons inside a jet of virtuality $Q = 90$ GeV in $p\bar{p}$ collisions at $\sqrt{s} = 1.96$ TeV [5], together with the MLLA predictions of [6] and the NMLLA calculations [7], both in the limiting spectrum approximation ($Q_0 = \Lambda_{QCD} = 230$ MeV); the experimental distributions suffering from large normalization errors, data and theory are normalized to the same bin, $\ln(k_\perp/1) = -0.1$. The results in the limiting spectrum approximation are found to be in impressive agreement with measurements by the CDF collaboration, unlike what occurs at MLLA, pointing out small overall non-perturbative contributions. Moreover, NMLLA predictions are reliable in a much larger $k_\perp$ range than MLLA. Coherence also plays the same role in this case at very small $k_\perp$. However,

the size of higher order corrections $\mathcal{O}(\sqrt{\alpha_s})$ as $k_\perp \to \Lambda_{QCD}$ becomes huge in such a way that coherence suffers screening due to the running of α_s [6] and hence, data and theory can not be compared for $\ln(k_\perp/1) < -0.1$. The agreement between NMLLA predictions and CDF preliminary data in $p\bar{p}$ collisions at the Tevatron is good, indicating very small overall non-perturbative corrections and giving further support to LPHD hypothesis [2].

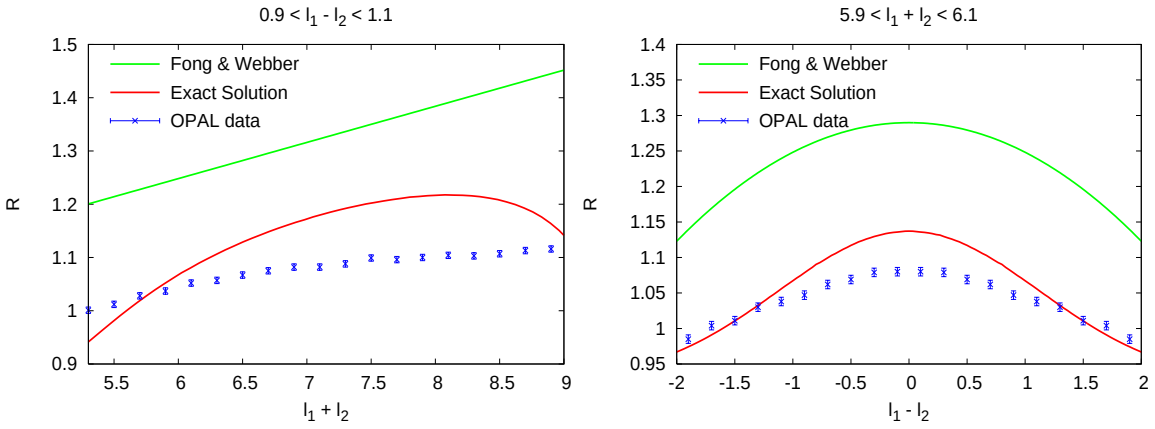

Figure 2. Two-particle correlations in two quark jets $R = \frac{1}{2} + \frac{1}{2}\mathcal{C}_q^{(2)}$ in the process $e^+e^- \to q\bar{q}$ as a function of $\ell_1 + \ell_2 = |\ln(x_1x_2)|$ for $\ell_1 - \ell_2 = \ln(x_2/x_1) = 1.0$ (left) and $\ell_1 - \ell_2 = |\ln(x_2/x_1)|$ for $\ell_1 + \ell_2 = \ln(x_1x_2) = 6.0$ (right).

So far, the MLLA, NMLLA expectations and LPHD for one-particle inclusive distributions have been shown to provide a good description of the data. Correlations, defined as the n-particle cross section normalized by the product of the single inclusive distribution (HBP) of each parton, is important because the resulting observable becomes independent of the constant $\mathcal{K}^{ch}$, thus providing a refined test of QCD dynamics at the parton level. However, for less inclusive observables like n-particle energy-momentum correlations and multiplicity correlators, non-trivial hadronization effects may appear and spoil the agreement between theory and experiment. First, the MLLA evolution equations for two-particle correlations, quite similar to those giving the HBP, were written and solved iteratively in terms of the logarithmic derivatives of $D^h(\ln(1/x), \ln(k_\perp/Q_0))$ (HBP) [9]. That is how, the result previously obtained by Fong and Webber in [10], only valid in the vicinity of the maximum ℓ_{max} of the HBP, was extended to all possible values of x. Consequently, as displayed in Fig.2, the normalization of the more accurate solution of the evolution equations is lower and reproduces some features of the OPAL data at the Z^0 peak $Q = 91.2$ GeV of the e^+e^- annihilation, like the flattening of the slopes towards smaller values of x [9]. Also, the correlation vanishes ($\mathcal{C}^{(2)} \to 1$) when one of the partons becomes very soft, thus describing the hump-backed shape of the one-particle distribution. The reason for that is dynamical rather than kinematical: radiation of a soft gluon occurs at larger angles and therefore are emitted independently from the rest of jet ensemble. Qualitatively, our MLLA expectations agree better with available OPAL data than the Fong–Webber predictions [9]. There remains however a significant discrepancy, markedly at very small

x. In this region non-perturbative effects are likely to be more pronounced. They may undermine the applicability to particle correlations of the LPHD considerations that were successful in translating parton level predictions to hadronic observations in the case of more inclusive single particle energy spectra [1]. These measurements were redone by the CDF collaboration for $p\bar{p}$ collisions at center of mass energy $\sqrt{s} = 1.96$ TeV for mixed samples of quark and gluon jets [4]. For comparison with CDF data, the 2-particle correlator was normalized by the corresponding multiplicity correlator of the second rank, which defines the dispersion of the mean average multiplicity inside the jet. In this case, the MLLA solution by Fong and Webber [10], the more accurate MLLA solution [9] and the NMLLA solution [7] were compared with the CDF data. The Fong-Webber predictions turned out to be in good agreement with CDF data in a range from large to small x, also covering the region of the phase space where MLLA predictions should normally not be reliable, that is for $x > 0.1$, see Fig.3. As these figures were taken from [4], different notations have been used in this case, for instance, $\ell = \xi = \ln(1/x)$, $\Delta\xi = \xi - \xi_{max}$ ($\xi_{max} = \ell_{max} = \frac{1}{2}\ln(Q/Q_0)$) such that $\Delta\xi_1 + \Delta\xi_2 = \ell_1 + \ell_2 - \ln(Q/Q_0)$ and $\Delta\xi_1 - \Delta\xi_2 = \ell_1 - \ell_2$.

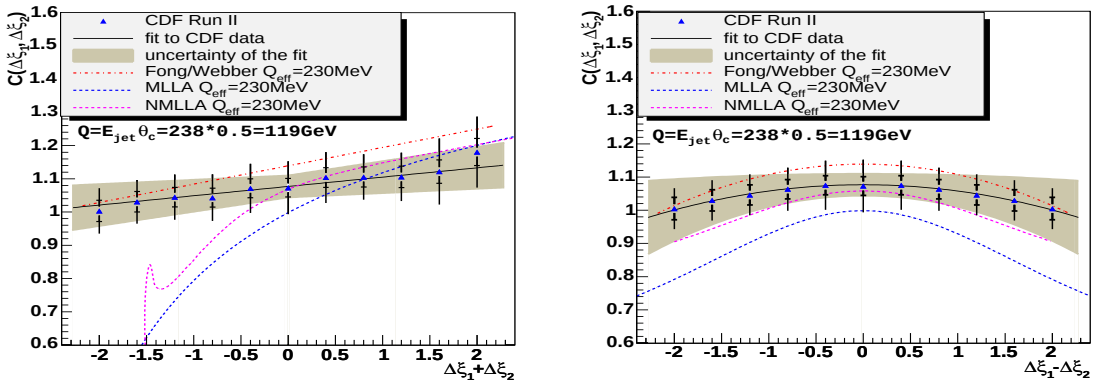

Figure 3. Two-particle correlations in a mixed sample of gluon and quark jets in $p\bar{p}$ collisions as a function of $\Delta\xi_1 + \Delta\xi_2 = |\ln(x_1x_2)| - \ln(Q/Q_0)$ for $\Delta\xi_1 = \Delta\xi_2$ (left) and $\Delta\xi_1 - \Delta\xi_2 = |\ln(x_2/x_1)|$ for $\Delta\xi_1 = -\Delta\xi_2$ (right).

As observed in Fig.3 (left), the data is well described by the three cases in the interval $\Delta\xi_1 + \Delta\xi_2 > -0.5$, that is at very small x. However, the Fong-and-Webber solution also describes the data for $\Delta\xi_1 + \Delta\xi_2 < -0.5$, that is for larger values of x where the MLLA is no longer valid. QCD color coherence for Fig.3 (left, the peak at $\Delta\xi_1 + \Delta\xi_2 = -1.5$ is due to numerical uncertainties) should be observed if the analysis is extended to $\Delta\xi_1 + \Delta\xi_2 > 2.5$. Moreover, the NMLLA solution [7] extends the region of applicability to larger values of x. In [4], it was concluded that despite the disagreement with the OPAL data in Fig.2, the LPHD stays successful for the description of less inclusive energy-momentum correlations. Therefore, forthcoming data from the LHC becomes necessary in order to clarify this mismatch. In case the LHC data agrees with CDF, the LPHD would stay safe for such observables. Finally, we

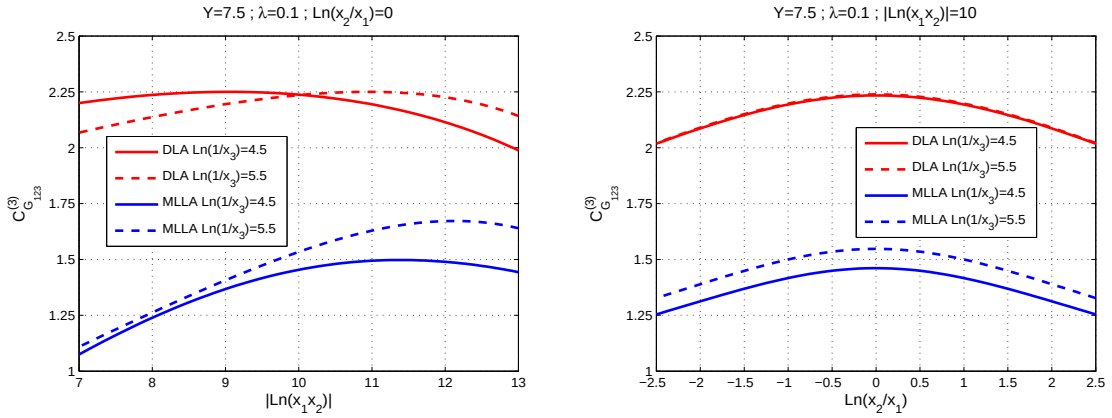

Figure 4. Gluon jet 3-particle correlator as a function of $|\ln(x_1x_2)|$ for $x_1 = x_2$ and $\ln(1/x_3)$ and as a function of $\ln(x_2/x_1)$ for fixed $|\ln(x_1x_2)|$ and $\ln(1/x_3)$ (right).

perform theoretical predictions for three-particle correlations for the LHC in the limiting spectrum approximation ($Q_0 \approx \Lambda_{QCD}$) [11]. The correlators are functions of the total hardness Q of the jet and the three x_i ($i = 1, 2, 3$) energy fractions: $\mathcal{C}^{(3)}_{G_{123}}(\ell_1, \ell_2, \ell_3, Y)$ and $\mathcal{C}^{(3)}_{Q_{123}}(\ell_1, \ell_2, \ell_3, Y)$. In Fig.4, the DLA and MLLA three-particle correlators inside a gluon jet are displayed, as a function of the difference $(\ell_1 - \ell_2) = \ln(x_2/x_1)$ for two fixed values of $\ell_3 = \ln(1/x_3) = 4.5, 5.5$, fixed sum $(\ell_1 + \ell_2) = |\ln(x_1x_2)| = 10$ and, finally, fixed $Y = 7.5$ (virtuality $Q = 450$ GeV and $\Lambda_{QCD} = 230$ MeV), which is realistic for LHC phenomenology. The representative values $\ell_3 = \ln(1/x_3) = 4.5, 5.5$ ($x_3 = 0.011$, $x_3 = 0.004$) have been chosen according to the range of the energy fraction $x_i \ll 0.1$, where the MLLA scheme can only be applied. From Fig.4, the gluon correlator is observed to be the strongest when particles have the same energy and to decrease when one parton is harder than the others, which as for the one and two-particle distributions, follows as a consequence of coherence. Moreover, the observable increases for softer partons with x_3 decreasing, which is for partons less sensitive to the energy balance. This observable becomes useful so as to extend the domain of applicability of the LPHD such that it can be measured together with two-particle correlations at the LHC. Same conclusions and trends hold for the quark correlator but the normalization is higher, showing stronger correlations inside a quark jet [11]. Finally, after jets are properly reconstructed, the measurement of the one-particle spectrum, two and three-particles correlations becomes extremely important at the LHC in order to further test the LPHD hypothesis.

[1] Yuri L. Dokshitzer, Valery A. Khoze, Alfred H. Mueller, and S. I. Troian (ed.), *Basics of perturbative QCD* (Ed.Frontieres, Paris, 1991).

[2] Yakov I. Azimov, Yuri L. Dokshitzer, Valery A. Khoze, and S. I. Troyan, *Z. Phys. C* **27** (1985) 65-72.

[3] M. Z. Akrawy et al., *Phys. Lett.* **B247** (1990) 617.

[4] T. Aaltonen et al., *Phys. Rev.* **D77** (2008) 092001.

[5] T. Aaltonen et al., *Phys. Rev. Lett.* **102** (2009) 232002.

[6] Redamy Perez-Ramos and Bruno Machet, *JHEP* **04** (2006) 043.
[7] Francois Arleo, Redamy Pérez Ramos, and Bruno Machet, *Phys. Rev. Lett.* **100** (2008) 052002.
[8] P. D. Acton et al., *Phys. Lett.* **B287** (1992) 401.
[9] Redamy Perez Ramos, *JHEP* **06** (2006) 019.
[10] C. P. Fong and B. R. Webber, *Nucl. Phys.* **B355** (1991) 54.
[11] Redamy Perez Ramos, Vincent Mathieu, and Miguel-Angel Sanchis-Lozano, arXiv:1104.1973 [hep-ph].

Heavy flavor production at STAR

Jaroslav Bielcik for the STAR Collaboration

Department of Physics, Faculty of Nuclear Science and Physics Engineering, Czech Technical University in Prague, Brehova 7, Prague, Czech Republic

E-mail: jaroslav.bielcik@fjfi.cvut.cz

Abstract. The properties of the hot and dense nuclear matter produced at RHIC can be investigated in multiple ways by heavy flavor production. The STAR experiment has capability to study both open heavy flavor and quarkonia. Heavy quarks are produced in early stage of the collision and the mechanisms of their interaction with nuclear matter is not yet well understood. This can be studied by non-photonic electrons originating from semileptonic decays of heavy flavor mesons. For the interpretations of the experimental data contributions from charm and bottom mesons have to be separated. The heavy quarkonium production is expected to be sequentially suppressed depending on the temperature of the produced nuclear matter. In this contribution we report recent results from STAR on non-photonic electrons, direct reconstruction of charm mesons, J/ψ as well Υ in p+p, Cu+Cu and Au+Au collisions at $\sqrt{s_{NN}}$ =200 GeV.

1. Introduction

Relativistic heavy ion collisions allow to study the properties of hot and dense nuclear matter in laboratory. Lattice QCD predicts the phase transition from confined hadrons to deconfined quarks and gluons at an energy density of about 1 GeV/fm^3 and at temperature of about 170 MeV. Most of the investigated experimental observables are based on the measurement of hadrons containing light quarks and gluons [1]. The particles containing heavy charm and bottom quarks are a unique probe to study this system. Heavy quarks are produced due to their large mass at the beginning phase of the collision and it is expected that they interact with the nuclear medium differently than light quarks. STAR is a large acceptance, multipurpose experiment that can study heavy flavor physics in multiple ways. In this paper we present the results of open heavy flavor and quarkonium measurements from p+p, d+Au, Cu+Cu and Au+Au measurements at $\sqrt{s_{NN}}$ = 200 GeV energy.

2. Open Heavy Flavor

STAR has measured previously open heavy flavor signals from both indirect non-photonic electron channel and directly by reconstructing D meson from its hadronic decay. In hadronic channels, D^0 has been reconstructed in d+Au, Cu+Cu and Au+Au

collisions [2, 3, 4]. Recently also a strong 4σ signal was extracted in p+p collisions measured in year 2009 for D^0 and a 8σ signal for D^* mesons. Non-photonic electrons were measured in p+p, d+Au and Au+Au collisions at 200 GeV [5]. These results were extracted from the data taken with the STAR detector material budget that led to a significant contribution of electrons from π^0 induced γ conversions. This contribution has to be properly subtracted to extract non-photonic electron spectrum. Although the extracted charm cross sections and spectra were self-consistent, the result differed by a factor of about 2 from the PHENIX experiment. In Year 2008 the STAR set-up had significantly lower material budget around the collision point and the new non-photonic electron spectra were extracted in p+p 200 GeV collisions [6]. During the analysis of these new data a mistake was discovered in the analysis of previously published non-photonic electron data that accidentally influenced previous results in all collision systems in about the same way. In Fig. 1a a transverse momentum spectrum (p_T) of non-photonic electrons is shown from the analysis of Year 2008 data and the re-analysis of previous data together with the FONLL QCD calculations. Both results are consistent with each other. In Fig. 1b the data divided by the FONLL calculation are presented and compared to the PHENIX data. All results are consistent with each other and as well as consistent with the upper bound of the FONLL calculation. The nuclear modification factor R_{AA} from the re-analysis of Year 2003/2004 data is shown in Fig. 2. Within the large statistical errors a strong suppression is observed in central Au+Au collisions while no suppression is present in d+Au collisions.

Based on a PYTHIA simulation of electron-hadron azimuthal correlation of charm and bottom electrons, a method to determine a contribution from these two sources to non-photonic electron spectrum was developed. In Fig. 3 a bottom contribution to the total spectrum is pictured. This ratio is consistent with the FONLL predictions and indicates that bottom contribution increases with p_T and is about 50% at $p_T = 5$ GeV/c [7]. This suggests that also the bottom production is significantly suppressed in central Au+Au collisions.

3. J/ψ and Υ measurements

The J/ψ suppression in heavy-ion collisions is considered to be a sensitive probe of color deconfinement in QGP [8]. There are no unique predictions about the exact melting temperatures of various quarkonium states and several competing mechanisms having opposite effects on measured yields, could be important. These include cold nuclear matter effects (nuclear interaction break-up, shadowing) and recombination. Previous measurements at RHIC show that the suppression of J/ψ as a function of centrality is similar to that observed at the CERN SPS energy. This is puzzling since the temperature and energy density reached in these collisions is significantly lower than at RHIC [9]. Therefore complex measurements are needed to interpret the suppression data properly.

For example, the measurement of J/ψ suppression at high-p_T is sensitive to differences in predictions of various models. In Fig. 4 the nuclear modification factor of

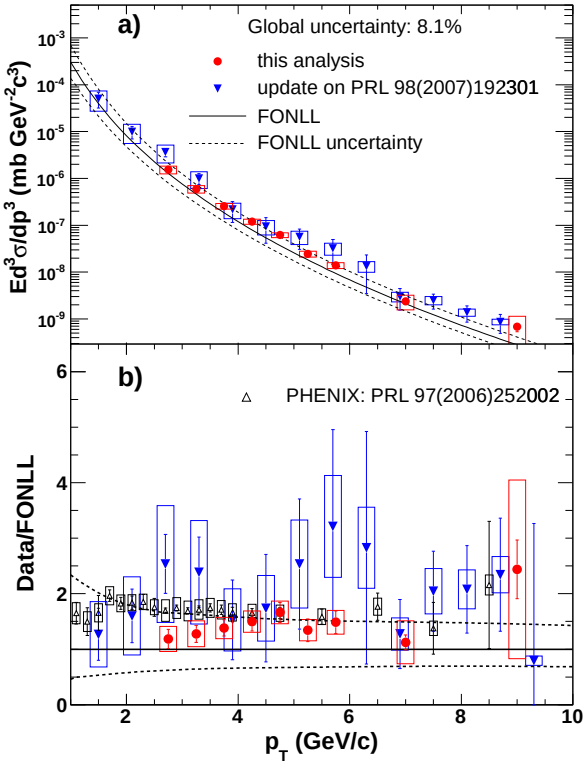

Figure 1. a) The transverse momentum spectrum of non-photonic electrons measured in p+p collisions at $\sqrt{s_{NN}} = 200$ GeV by STAR, b) The ratio of the measured spectra to the FONLL predictions. Taken from [6].

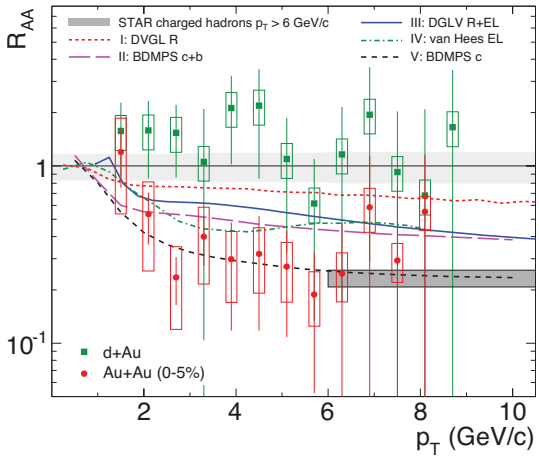

Figure 2. The measurement of R_{AA} for d+Au and Au+Au collisions at $\sqrt{s_{NN}} = 200$ GeV. The lines show model predictions. Taken from [5].

J/ψ as a function of transverse momentum for Cu+Cu collisions at $\sqrt{s_{NN}} = 200$GeV measured by both STAR and PHENIX is shown [10]. R_{AA} for J/ψ is seen to increase with increasing p_T. The average of the two STAR data points at high-p_T at 0-20% centrality is $R_{AA} = 1.4 \pm 0.4$ (stat.)± 0.2 (syst.). This disfavors the theoretical model

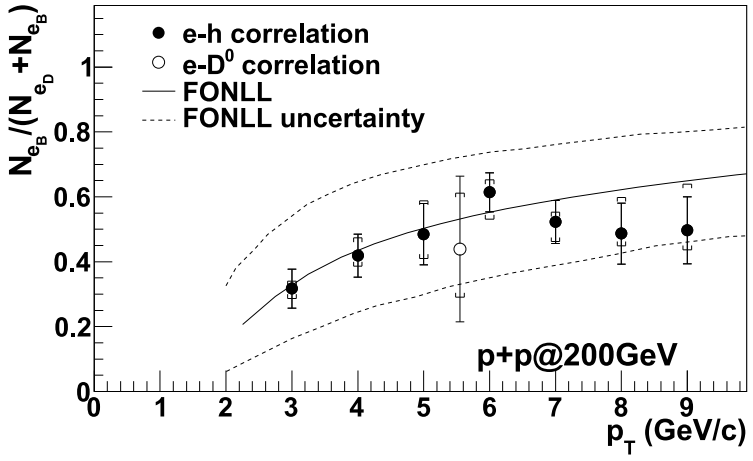

Figure 3. The measurement of relative contribution of bottom decays to non-photonic electron spectra in p+p collisions at $\sqrt{s_{NN}}$ = 200 GeV. Taken from [7].

of quarkonium dissociation in strongly coupled liquid using the AdS/CFT approach. On the other hand the two-component model with finite J/ψ formation time describes the increasing trend of the J/ψ R_{AA} well. It is an interesting question whether this observation will be present also in case of a large system such as Au+Au. This is currently under investigation.

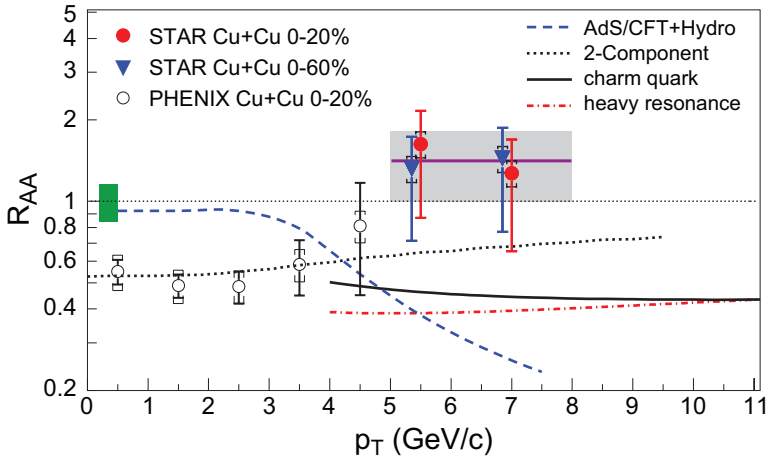

Figure 4. The measurement of R_{AA} vs p_T of J/Ψ production in Cu+Cu collisions at $\sqrt{s_{NN}}$ = 200 GeV by STAR and PHENIX. The lines show model predictions. Taken from [10].

The feed-down from B→J/ψ to high-p_T inclusive J/ψ production decay was shown to be p_T dependent at Tevatron energies, therefore it could be important for understanding of high-p_T results. Since the current STAR set-up does not allow reconstruction of a secondary vertex of B→J/ψ decay, the J/ψ-hadron azimuthal correlations have been used to extract the B feed-down contribution. The PYTHIA based simulations show that while correlations with B feed-down J/ψ dominate the near

side, the direct J/ψ dominates the away side. In Fig. 5 the B→J/ψ feed-down to inclusive production is shown as a function of p_T from p+p collisions at $\sqrt{s_{NN}}$ = 200 GeV. The extracted contribution of 10-25% in the measured range is consistent with the measurements at different energies and in p+$\bar{\text{p}}$ collisions [11].

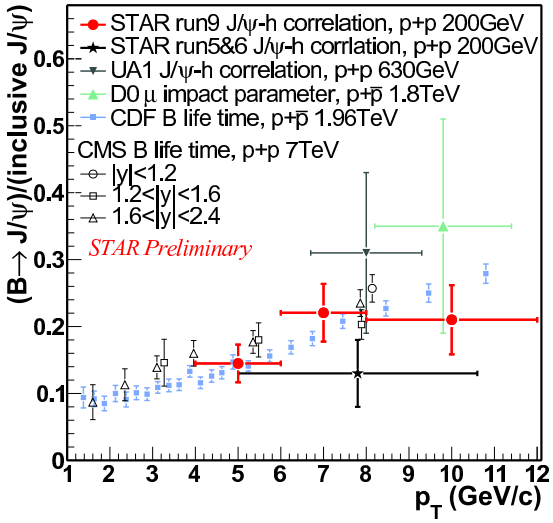

Figure 5. Fraction of B→J/ψ feed-down to inclusive J/ψ spectra measured by STAR in p+p collisions at $\sqrt{s_{NN}}$ = 200 GeV. The measurement from UA1, D0, CDF and CMS experiments are shown for a comparison.

The measurement of the Υ production in heavy-ion collisions is of a great interest, because it is expected that Υ(1S) state does not dissociate at RHIC energies, but Υ(2S,3S) do. This could provide a model independent thermometer of heavy-ion collisions. STAR reported measurements in p+p [13], d+Au [14] and Au+Au [12] collisions. However, so far it was not possible to adress each Υ state separately. It was observed that the extracted production cross section Υ(1S+2S+3S)→e^+e^- at midrapidity is 114 ± 38(stat.)$^{+23}_{-24}$(syst.) pb at $\sqrt{s_{NN}}$ = 200 GeV in p+p collisions and this is consistent with the world trend. No cold nuclear matter effects in d+Au collisions were observed, R_{dA} = 0.78±0.28±20.

In Fig. 6 the invariant mass spectrum of di-electron pairs is shown for 0-60% most central Au+Au collisions. The excess of unlike-sign pairs above like-sign background is observed in the area of expected Υ signal. The signal of 4.6σ was observed. From this, a preliminary nuclear modification factor R_{AA} = 0.78±0.32(stat.)±0.22(syst.,Au+Au)±0.09(syst.,p+p) was obtained. The analysis of a 4-times larger sample from recent Year 2010 measurements is ongoing.

4. Conclusions

In summary, STAR has measured heavy flavor production at RHIC in a complex way. In open heavy flavor sector a new low background measurement of non-photonic electrons in p+p 200 GeV collisions is consistent with the FONLL predictions. The bottom

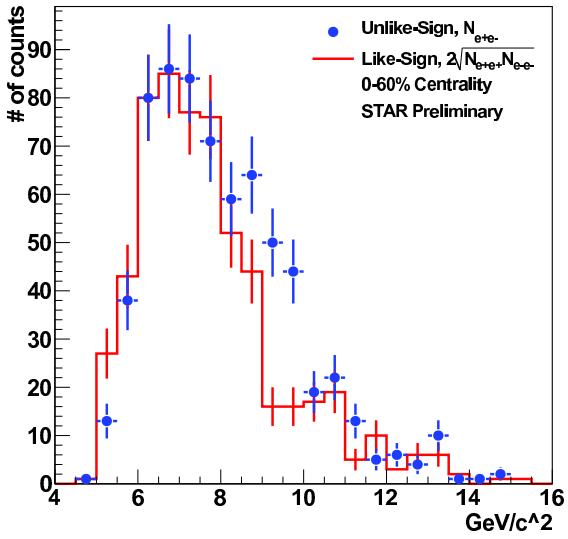

Figure 6. The measurement of invariant mass spectrum of unlike-sign (blue) and like-sign di-electron pairs in Au+Au collisions at $\sqrt{s_{NN}} = 200$ GeV by STAR.

contribution to non-photonic electrons is significant at p_T around 5 GeV/c. The J/ψ seems to be not suppressed at high-p_T in Cu+Cu collisions. The B feed-down to inclusive J/ψ spectra is about $10-25\%$ at high-p_T. The preliminary nuclear modification factor of Υ production is $R_{AA} = 0.78\pm0.32(\text{stat})\pm0.22(\text{syst. Au+Au})\pm0.09(\text{syst. p+p})$ in 0-60% most central. STAR has also collected a large amount of data in Year 2010 and more precise measurements of heavy-flavor observables are expected in near future.

This work was supported by grant INGO LA09013 of the Ministry of Education, Youth and Sports of the Czech Republic.

[1] J. Adams *et al.* [STAR Collaboration], Nucl. Phys. A **757** 102 (2005).
[2] J. Adams *et al.* [STAR Collaboration], Phys. Rev. Lett. **94**, 062301 (2005).
[3] S. Baumgart *et al.* [STAR Collaboration], Eur. Phys. J. **C62**, 3 (2009).
[4] B. I. Abelev *et al.* [STAR Collaboration], arXiv:0805.0364 [nucl-ex].
[5] B. I. Abelev *et al.* [STAR Collaboration], Phys. Rev. Lett. **98**, 192301 (2007).
[6] H. Agakishiev *et al.* [STAR Collaboration], Phys. Rev. **D83**, 052006 (2011).
[7] M. M. Aggarwal *et al.* [STAR Collaboration], Phys. Rev. Lett. **105**, 202301 (2010).
[8] T. Matsui, H. Satz, Phys. Lett. **B178**, 416 (1986).
[9] F. Karsch, D. Kharzeev, H. Satz, Phys. Lett. **B637**, 75 (2006).
[10] B. I. Abelev *et al.* [STAR Collaboration], Phys. Rev. C **80**, 041902 (2009).
[11] Z. Tang [for the STAR Collaboration], Nucl. Phys. **A855**, 396 (2011).
[12] R. Reed [for the STAR Collaboration], Nucl. Phys. **A855**, 440 (2011).
[13] B. I. Abelev *et al.* [STAR Collaboration], Phys. Rev. **D82**, 012004 (2010).
[14] H. Liu [STAR Collaboration], Nucl. Phys. A **830**, 235C (2009).

Open heavy-flavor production in proton-proton collisions at the LHC with ALICE

Rosa Romita, for the ALICE Collaboration

GSI, Plankstrasse 1, Darmstadt, Germany

E-mail: r.romita@gsi.de

Abstract. ALICE is the LHC experiment dedicated to the study of the Quark-Gluon Plasma (QGP) formed in high-energy collisions of lead nuclei. Heavy quarks are sensitive probes of the QGP, since their interactions with the deconfined medium are expected to provide crucial information about its properties. They experience the full collision history and they are expected to be abundantly produced at the LHC. Finally, the understanding of heavy-flavor production in proton-proton collisions is an important test of perturbative QCD calculations, and is an essential reference to interpret the heavy ion results.

We report measurements by ALICE of heavy quark production at central and forward rapidity in pp collisions at $\sqrt{s} = 7$ TeV, via the reconstruction of open charm particles, both exclusively, using a selection of hadronic decay channels, and inclusively, using single leptons. We present cross section measurements of D mesons, electrons and muons from heavy-quark decays in pp collisions.

1. Introduction

Heavy flavor production is a valuable probe of the Quark Gluon Plasma and its properties. Heavy flavor quarks are generated in the initial hard scattering processes and in collisions of heavy nuclei experience the full collision evolution. In particular, measurements of open charm and beauty production probe the energy loss experienced by partons traversing the hot and dense medium formed in high energy nuclear collisions. The energy loss is expeceted to be predominantly due to gluon radiation and is influenced by colour effects (the Casimir factor), which cause the gluons to radiate more energy than the quarks, and by the quark mass (dead cone effect [1]). Thus, the open beauty hadrons are expected, at leading order, to be less quenched than the open charm hadrons at moderate transverse momenta comparable to the quark mass [2].

Proton-proton collisions provide the necessary baseline for the Pb–Pb results, and measurements of charm and beauty cross sections, provide significant tests of perturbative QCD calculations in the new energy regime at the LHC. Heavy quarks are abundantly produced at the LHC: according to next-to-leading order pQCD calculations, the cross section of charm and beauty are expected to increase, respectively, by factors of about 10 and 100 with respect to RHIC energies [3].

ALICE (A Large Ion Collider Experiment) [4] is the LHC experiment dedicated to the study of the properties of the Quark-Gluon Plasma (QGP) formed in heavy ion collisions. It was designed for measuring open heavy flavor down to low momenta, both in the hadronic and leptonic channels, at central and forward rapidity. Its subdetectors provide excellent tracking performance, vertex and impact parameter determination, and particle identification capability. Since the start-up of LHC, high statistics data samples have been collected with proton-proton collisions. In this paper we describe heavy-flavor measurements for 7 TeV pp collisions. In section 2 the detector, its performance and the data samples collected are described. Section 3 presents the preliminary results of open charm reconstruction and the inclusive cross section measurement via hadronic channels (in rapidity -0.9 $< \eta <$0.9). Section 4 and 5 present the heavy-flavor inclusive cross section measurement in leptonic channels: electrons in the central rapidity region (-0.9 $< \eta <$0.9), muons at forward rapidity (-4.0 $< \eta <$-2.5).

2. ALICE detector and data taking

The ALICE detector is composed of a central barrel, in a solenoidal magnetic field of 0.5 T, with tracking, vertexing and particle identification (PID), and a forward muon spectrometer, where muons are reconstructed and identified. Although the ALICE design is optimized for Pb–Pb collisions, it has also significant capabilities for measurements of proton-proton collisions.

2.1. Tracking, vertexing and PID at central rapidity

The detectors of the central barrel (-0.9 $< \eta <$0.9) used for the heavy-flavor analyses presented here are the Inner Tracking System (ITS), the Time Projection Chamber (TPC) and the Time Of Flight (TOF). The ITS is the detector closest to the interaction point and it is composed of three types of silicon detectors: Silicon Pixel (SPD), Silicon Drift (SDD) and Silicon Strip (SSD). It plays a central role in reconstruction of primary and secondary vertices. The primary interaction vertex is reconstructed event by event with a resolution better than 100 μm even in low multiplicity events, while the resolution of the track impact parameter is of the order of a few hundred of μm for low momentum tracks, becoming smaller for larger track momentum, and achieving 75 μm for tracks with transverse momentum larger than 1 GeV/c. Good primary vertex and impact parameter resolution are both important for discrimination of tracks from secondary vertices close to the interaction vertex.

The main ALICE tracking device is the TPC, described in [5]. It is the largest TPC ever built and it has been designed to reconstruct efficiently up to 15000 primary tracks in a single collision. The momentum resolution achieved is better than 1% for tracks with $p < 1$ GeV/c, as verified by measurement of the width of the K^s_0 mass peak.

Particle identification is one of the strengths of ALICE: particle species can be discriminated well by three detectors in different momentum regions. The TPC identifies

particles with intermediate momenta using the information on the specific energy deposit $\mathrm{d}E/\mathrm{d}x$ in its volume, as shown in figure 1(a) [6]. The ITS covers the low momentum region, going down to 0.1 GeV/c, while TOF is able to distinguish, for example, protons up to 3 GeV/c (figure 1(b)). The three detectors cover the p_{T} range relevant for the identification of tracks coming from charmed hadron decays.

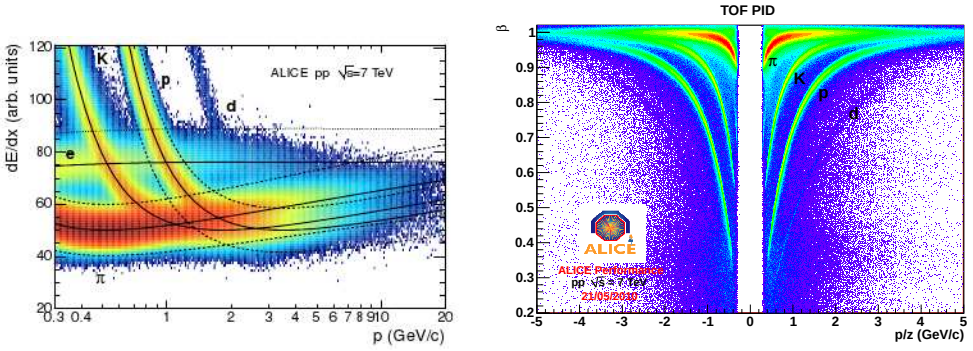

Figure 1. Left panel : Specific ionization energy loss $\mathrm{d}E/\mathrm{d}x$ of various particle species in the Time Projection Chamber, as a function of momentum, for 7 TeV pp collisions. The lines are a parametrization of the Bethe-Bloch function. Right panel: velocity measured by TOF for various particle species as function of signed momentum, for 7 TeV pp collisions.

2.2. The muon spectrometer

The muon spectrometer located at rapidity -4.0 $< \eta <$-2.5 provides a muon trigger to take advantage of the full luminosity delivered by the LHC. It consists of a passive front absorber, a beam shield, a dipole magnet, five stations of high granularity tracking chambers, and two trigger stations, equipped with two planes of Resistive Plate Chambers. The main goal of the ALICE muon spectrometer is the study of quarkonia states and inclusive heavy-flavor production in the muon channel. The design is optimized for operation in the high multiplicity environment of the Pb–Pb collisions.

2.3. Data samples

The following data samples are used for the analyses described here: 1×10^8 minimum bias events at 7 TeV (corresponding to 1.6 nb^{-1} integrated luminosity) for D mesons analysis; 1.8×10^8 minimum bias events at 7 TeV (corresponding to 2.6 nb^{-1} integrated luminosity) for single electrons; 2.2×10^6 muon triggers at 7 TeV (corresponding to 3.5 nb^{-1}) for single muons; The detectors used for issuing the minimum bias trigger are the SPD and the VZERO scintillator arrays covering the rapidity ranges 2.8$< \eta <$5.1 and -3.7$< \eta <$-1.7 and placed at 3.4 m and 0.9 cm from the IP, respectively. the segmented scintillator counter VZERO. The trigger requires at least one hit in the SPD, combined

in logical or with one signal in the VZERO counters , triggering in this way on one track anywhere in the eight units of pseudorapidity covered by the two trigger detectors.

3. Open charm via hadronic decay channels

Open charm mesons (D^0, D^+, D^{*+}, D_s^+) and baryon (Λ_c) are exclusively reconstructed using their hadronic decay channels into 2, 3 or 4 charged particle final states. This is done by identifying their decay vertex, which is typically displaced by a few hundreds of microns from the interaction vertex, with their $c\tau$ ranging from 60 μm for Λ_c to 300 μm for D^+. The decay length of these particles is very small and the combinatorial background is high already in pp collisions, making the measurement particularly challenging.

Decay hadrons are identified by combining tracks with appropriate charge sign, and applying topological cuts to separate the signal from the combinatorial background. Hadrons are identified combining the PID information provided by both TPC and TOF.

The raw yield is obtained by fitting the resulting invariant mass distrubution. The D meson yield is then extracted by applying the corrections for efficiency, acceptance and feed-down from beauty mesons. The efficiency for topological and PID cuts are determined using a Monte Carlo simulation. The measured fraction of prompt charm is inferred from FONLL predictions; this approach is supported by the fact that such theoretical calculations reproduce well beauty production measured in the CMS [7] and LHCb [8] experiments. The p_T differential cross section for the three charmed mesons $D^0 \to K^-\pi^+$, $D^+ \to K^-\pi^-\pi^-$ and $D^* \to D^0\pi^+$, is obtained analyzing 1.6 nb^{-1} integrated luminosity. In the left panel of figure 2(a), the preliminary p_T differential cross section for the D^0 meson is shown in the momentum range $2 < p_T < 12$ GeV/c, together with the comparison with pQCD based calculations: the agreement is good within the errors. In figure 2(b), right panel, the signal for $\Lambda_c^+ \to pK^-\pi^+$ is shown for $p_T > 3$ GeV/c.

4. Electrons from heavy-flavor hadron decays

The inclusive heavy-flavor cross section can be obtained using electrons in the central barrel, due to the $\approx 10\%$ branching ratio of the $c, b \to e$. The electron identification strategy is based on the TPC and TOF detectors. The tracks identified as electrons in the TOF are selected, which rejects most of the kaons and protons. Electrons are identified by the specific ionization energy loss in the TPC, where the electrons are very clearly separated from pions. This electron identification strategy is effective for tracks with momentum up to 4 GeV/c. In the resulting sample, the hadron contamination is estimated to be smaller than 10% for $p_T < 4$ GeV/c, and it is subtracted.

The inclusive electron spectrum contains contributions from many sources other than the charm and beauty decays. The most important background sources are the Dalitz decay of light neutral mesons (the main contribution coming from π^0), photon conversions in the beam pipe and the detector material, the di-electron decays of vector

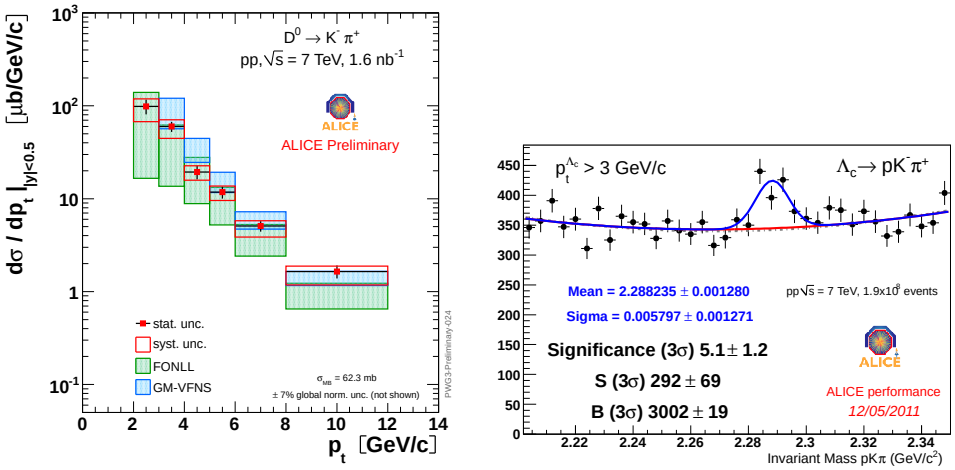

Figure 2. Left panel: Cross section for D^0 in pp collisions at $\sqrt{s} = 7$ TeV (red points), compared with two different pQCD based calcutations (blue and green bands [9], [10]). Right Panel: Invariant mass spectrum of Λ_c candidates with $p_T > 3$ GeV/c are considered.

mesons, heavy quarkonia and electrons from real and virtual QCD photons. These background sources are modeled in a cocktail based on the measured π^0 cross section, with the yield of other light mesons calculated via m_T scaling, and on pQCD calculations for direct photons. The cocktail-subtracted spectrum is a measurement of electrons from heavy-flavor decays. More details of the analysis described below can be found in [11].

The inclusive cross section for non-photonic electron production in pp collisions at $\sqrt{s} = 7$ TeV is shown in figure 3(a), compared to the FONLL prediction for charm and beauty production in the electron channel.

The charm cross section measured with the charmed mesons decays is used to produce a pure charm electron spectrum, (figure 3(b)) and is compared to FONLL predictions. The difference between the two spectra at high p_T can be attributed to the contribution from beauty decays.

5. Muons from heavy-flavor hadron decays

Open heavy-flavor production is studied at forward rapidity in the semi-muonic decay channel. In the inclusive muon p_{T} distribution there are several contributions. It is important to remove all the possible sources of background in order to isolate the contribution from charm and beauty decays. More details of the analysis described below can be found in [12].

Hadrons and low p_{T} muons that do not reach the trigger chambers at the end of the spectrometer are removed. Residual decay muons, originating from decays of light mesons before the front absorber, are removed by subtracting a Monte Carlo p_{T} spectrum normalized to data at low p_{T}. The subtraction of these sources of background is needed

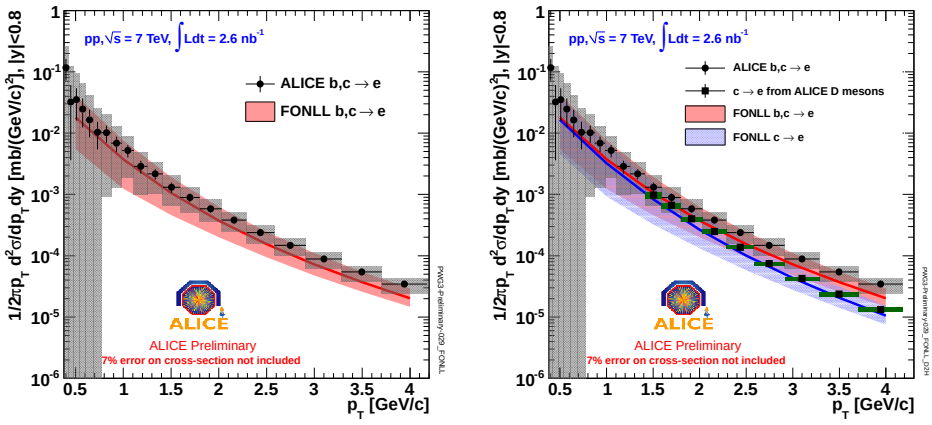

Figure 3. Left panel: Production cross section of electrons from heavy-flavor decays obtained from 1.6×10^8 pp collisions at $\sqrt{s} = 7$ TeV (black points), compared with FONNL predictions for $\mathrm{c, b} \rightarrow \mathrm{e}$ (red line and band). Right panel: inclusive heavy-flavor cross section (black points), FONNL predictions for $\mathrm{c, b} \rightarrow \mathrm{e}$ (red line and band), compared to the charm cross sections for $\mathrm{c} \rightarrow \mathrm{e}$ derived from the D mesons cross section (squares) and the corresponding FONLL prediction (blue line and band).

to extract the heavy-flavor contribution from the single muon spectra. Then, efficiency corrections are applied and systematics are evaluated. The main source of systematic uncertainty is the estimation of the residual background via simulations ($\approx 40\%$). The efficiency correction contribution, related to the description of the detector, is only 5%. The p_{T} differential cross section is shown in figure 4, and is measured in the range $2 < p_{\mathrm{T}} < 6.5$ GeV/c. It has been obtained with 3.5 nb^{-1} of integrated luminosity and is compared with FONLL predictions [9], which describe the measurement within uncertainties.

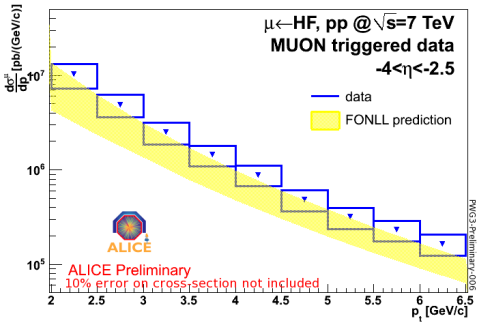

Figure 4. p_{T} differential cross section for muons from heavy flavor decays for pp collisions at $\sqrt{s} = 7$ TeV (blue points), compared to FONLL predictions (yellow band).

6. Conclusions

We have presented the first measurement of heavy-flavor cross sections, both in hadronic and leptonic channels, both at central and forward rapidity, in pp collisions at $\sqrt{s} = 7$ TeV. These measurements represent the essential baseline to understand similar results in Pb–Pb collisions.

[1] Yu.L. Dokshitzer and D.E. Kharzeev, Phys. Lett. B 519, 199 (2001).
[2] N. Armesto et al, Phys.Rev. D71 (2005) 054027
[3] Mangano, Nason, Ridolfi, Nucl. Phys. B 373 (1992) 29.
[4] ALICE Collaboration, K. Aamodt et al., J. Instrum 3, S08002 (2008).
[5] ALICE Collaboration, J. Alme et al., arXiv:1001.1950.
[6] ALICE Collaboration, K. Aamodt et al., arXiv:1105.0380v1 [hep-ex]
[7] V. Khachatryan *et al.* [CMS Collaboration], Eur. Phys. J. C **71** (2011) 1575 [arXiv:1011.4193 [hep-ex]].
[8] R. Aaij *et al.* [LHCb Collaboration], Phys. Lett. B **694** (2010) 209 [arXiv:1009.2731 [hep-ex]].
[9] M. Cacciari, M. Greco, P. Nason, JHEP 9805 (1998) 007; private communication.
[10] B.A. Kniehl et al., Phys. Rev. Lett. 96 (2006) 012001; private communication.
[11] S. Masciocchi [ALICE Collaboration], Nucl. Phys. A **855** (2011) 432.
[12] D. Stocco [ALICE Collaboration], Nucl. Phys. A **855** (2011) 323.

J/Ψ and Z production in p+p and Pb+Pb collisions at the LHC measured with the ATLAS detector.

Matthew Beckingham (on behalf of the ATLAS Collaboration)

Fakultät für Mathematik und Physik, Albert-Ludwigs Universität Freiburg, Hermann-Herder-Strasse 3, D-79104 Freiburg im Breisgau, Germany

E-mail: matthew.beckingham@cern.ch

Abstract. Measurements of the production of J/Ψ mesons and Z bosons at the LHC provide tests of the Standard Model in a new energy regime for proton-proton collisions, as well providing a probe of the matter produced in heavy ion collisions. Presented are measurements of the Z boson production cross section, both inclusive and in association with additional jets, observation of the Z through the decay to tau pairs, and J/Ψ production cross sections in proton-proton data at $\sqrt{s_{pp}} = 7$ TeV performed with the ATLAS detector. Good agreement is seen between the data and Standard Model predictions. Additionally, the production of J/Ψ mesons and Z bosons in lead-lead data at $\sqrt{s_{NN}} = 2.76$ TeV are measured. A decrease in the normalised J/Ψ yield with decreasing centrality is observed. However, no conclusions on the centrality dependence of the normalised Z yield may be drawn.

1. Introduction

Measurements of Standard Model (SM) processes within the new energy regime opened up by the first data delivered by the LHC collider are of great interest. In particular, presented here are measurements of the production of Z bosons and J/Ψ mesons, which provide important tests of SM in proton-proton collisions, may be used to study the predictions of perturbative-QCD (pQCD), as well as providing new constraints on the parton density functions of the proton. Understanding the properties of Z and J/Ψ production is of additional importance, as they form important backgrounds to searches for new physics processes at the LHC. Finally, as particles with well known decay channels, both processes are useful to study the performance of the ATLAS detector. In addition to proton-proton collisions, the clear signatures of J/Ψ and Z decays mean that such particles can be used to probe the matter produced in heavy ion collisions.

The measurements presented here are made with the ATLAS detector [1] using the full dataset delivered by the LHC collider in the year 2010. This corresponds to approximately 42 pb^{-1} of proton-proton data, at a centre of mass energy of $\sqrt{s_{pp}} =$ 7 TeV, and 9.2 μb^{-1} of lead-lead data, at a nucleon-nucleon centre of mass energy of $\sqrt{s_{NN}} = 2.76$ TeV. Further details of the analyses described in these proceedings can be found in the references given near the beginning of each section.

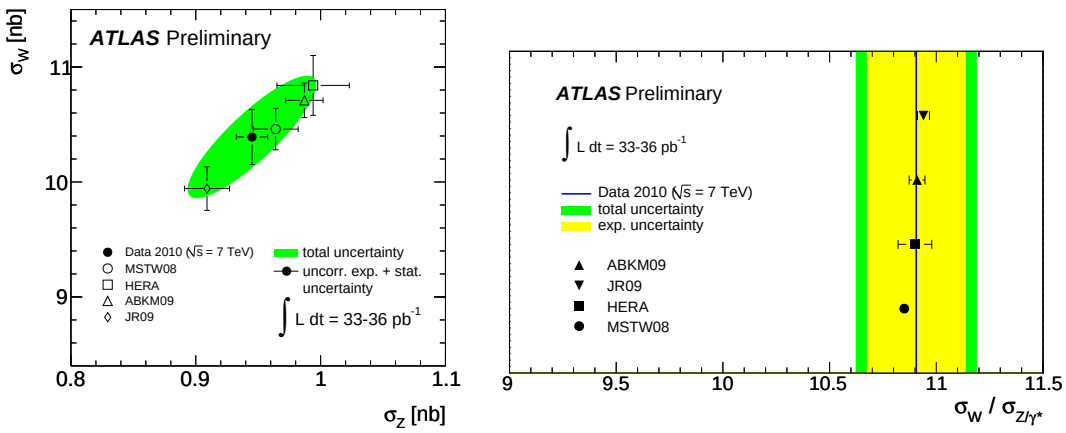

Figure 1. The measured and predicted a) W vs. Z cross sections times leptonic branching ratios and b) W/Z cross section ratio.

2. Z Boson Production in pp Collisions

2.1. Inclusive Z Boson Production Cross Section

The inclusive production cross section for Z bosons is measured using the di-electron and dimuon decay channels of the Z boson [2]. In the electron channel, events are selected by requiring two electrons that pass the "medium" electron identification requirements. In addition, the electrons are required to have a transverse energy $E_T > 20$ GeV, should be within the pseudorapidity range $|\eta| < 2.47$, but outside of the range $1.37 < |\eta| < 1.52$ and have opposite electric charges to each other. Finally, the di-electron invariant mass should be in the range $66 < m_{ee} < 116$ GeV. Similarly, events are selected in the muon channel by requiring two isolated "combined" muons, which are measured by combining the independent measurements of the muon trajectories in the Inner Detector and the Muon Spectrometer. As for the electron channel, the muons should have a transverse momentum $p_T > 20$ GeV, be within the range $|\eta| < 2.47$, have opposite charges and the dimuon invariant mass should be in the range $66 < m_{\mu\mu} < 116$ GeV.

The QCD multijet background to the $Z \to ll$ processes is measured in data, whereas electroweak backgrounds, such as $Z \to \tau\tau$, W boson and top pair events, are estimated using Monte Carlo (MC) simulation. Correction factors, derived using $Z \to ll$ and $W \to l\nu$ data events, are applied to the MC simulations to account for differences with respect to the data of the lepton reconstruction, identification, isolation and trigger efficiencies. Major systematic uncertainties on the measured cross sections arise from the electron and muon reconstruction efficiencies, leading to 3% and 0.8% uncertainties on the final cross sections, respectively. In addition, the uncertainty due to the parton density functions and the luminosity measurement lead to uncertainties on the final cross sections of 4% and 3.4%, respectively. The measured and predicted cross section times leptonic branching ratio for Z and W boson production, and the ratio of these two cross sections, is shown in Figure 1. A good agreement between the measured cross

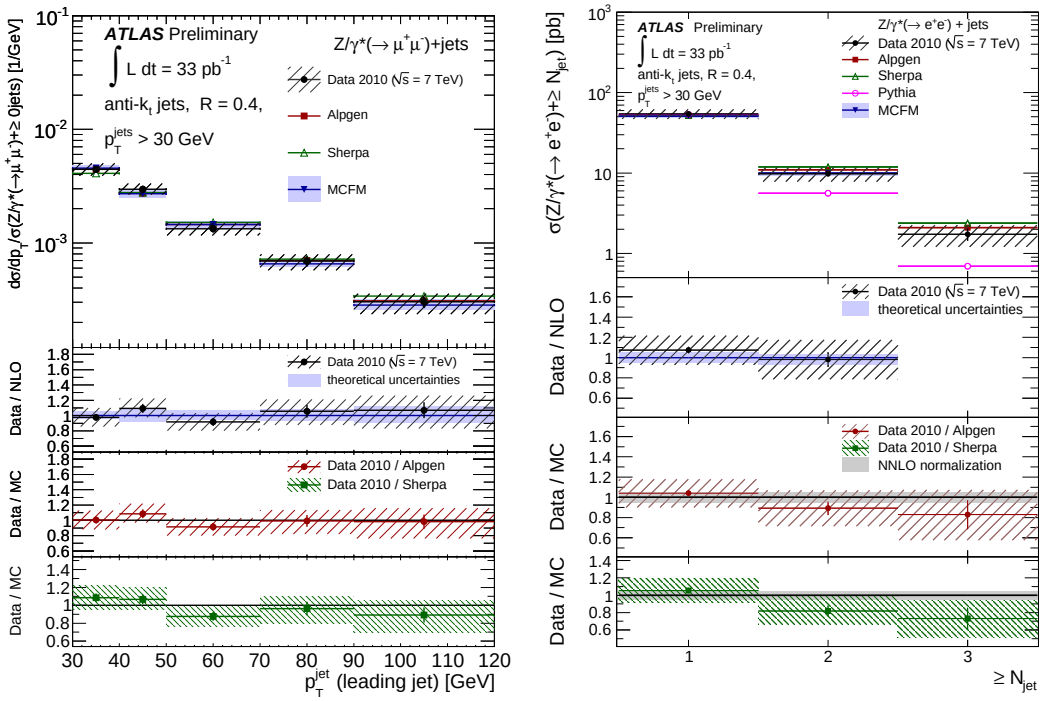

Figure 2. The measured a) cross section for $Z/\gamma* \rightarrow \mu\mu$ production as a function of the inclusive jet multiplicity and b) differential cross section for $Z/\gamma* \rightarrow ee$ as a function of p_T^{jet}, for events with at least one jet with $p_T^{jet} > 30$ GeV and $|\eta_{jet}| < 2.8$ in the final state.

sections and the NNLO predictions is seen.

2.2. Z Boson Production in Association with Jet Cross Section

In addition the cross section for the production of Z bosons in association with jets is measured [3]. Such a process provides a test of pQCD and additionally aids the understanding of an important background to many searches for new physics at the LHC. For both the electron and muon channels, the selection of the Z boson candidate events follows those stated in section 2.1. In addition, events are required to contain at least one jet, where the jets are reconstructed using the anti-k_t jet algorithm with a distance parameter of $R = 0.4$, taking calorimeter clusters as an input. The reconstructed jets are required to have a $p_T > 30$ GeV, lie within the range $|\eta| < 2.8$ and be separated from the lepton candidates by an $\eta - \phi$ distance of $\Delta R > 0.5$.

Differential cross sections for Z boson production in association with jets as a function of inclusive jet multiplicity and p_T^{jet} are shown in Figure 2. The cross section as a function of jet multiplicity is described by the NLO MCFM pQCD prediction and also by the LO with parton shower predictions from the ALPGEN and SHERPA MC generators. The LO prediction from the PYTHIA MC generator is normalised to the data in the $N_{\text{jet}} \geq 1$ multiplicity bin. However, the prediction undershoots the data at large jet multiplicity.

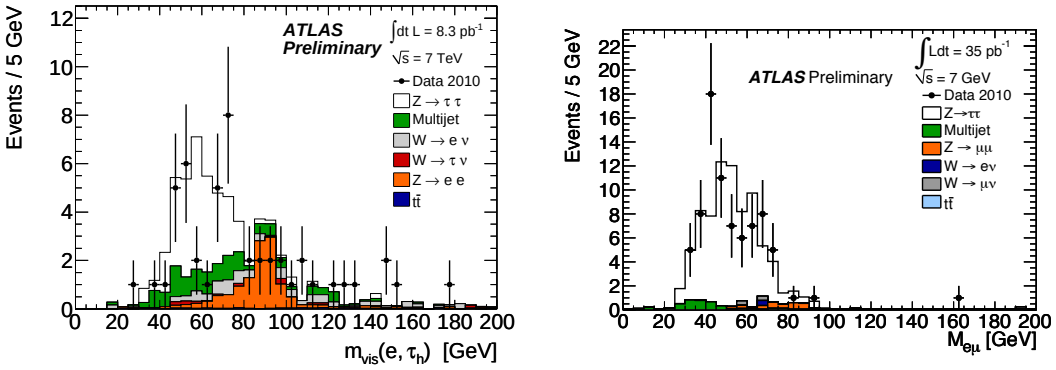

Figure 3. The distributions of the visible mass of the a) muon-tau pairs and b) electron-muon pairs for $\rightarrow \tau\tau$ production.

2.3. Observation of Z Boson Production in the di-tau decay channel

The full quota of leptonic Z boson decay modes is completed by the observation of Z boson production in the di-tau decay channel. Measurements are made in the channels where one tau decays hadronically with the other decaying leptonically to an electron or muon [4], and in the channel where both taus decay leptonically to an electron and a muon [5].

In the lepton-hadron channels, events with exactly one isolated muon or electron with a $p_T > 15$ GeV, in the range $|\eta| < 2.47$, are required. In addition, the selected events should contain exactly one hadronically decaying tau, with a $p_T > 15$ GeV, consisting of either 1 or 3 reconstructed tracks and with an opposite charge to the selected lepton. Furthermore, the sum of the cosine of the difference in the ϕ angle between the lepton and the $\mathrm{E_T^{miss}}$ and the tau and the $\mathrm{E_T^{miss}}$ is required to be greater than $\sum \cos\Delta\phi > -0.15$, the transverse mass of the lepton and the missing transverse energy (E_T^{miss}) should be less than $m_T < 50$ GeV and the lepton-tau invariant mass should be in the range $35 < m_{\mathrm{vis.}} < 75$ GeV. In the electron-muon channel, events are selected containing exactly one isolated electron with $p_T > 15$ GeV and one isolated muon with $p_T > 10$ GeV, with opposite charges. In addition, the variable $\sum \cos\Delta\phi$, calculated using the two final state leptons and the missing transverse energy, is required to be in the range $\sum \cos\Delta\phi > -0.15$, the sum of the E_T of the electron, the p_T of the muon, the p_T of all jets and the E_T^{miss} is required to be in the range $\sum E_T + E_T^{\mathrm{miss}} < 150$ GeV. Finally the electron-muon visible mass is required to be in the range $25 < m_{\mathrm{vis.}} < 80$ GeV. In all channels, the multijet background is estimated using data based techniques, whereas the electroweak and top pair backgrounds are estimated from Monte Carlo. The muon-tau and electron-muon visible mass distributions are shown in Figure 3. In both channels clear excesses of data, which are consistent with the SM expectation, are seen above the estimated background.

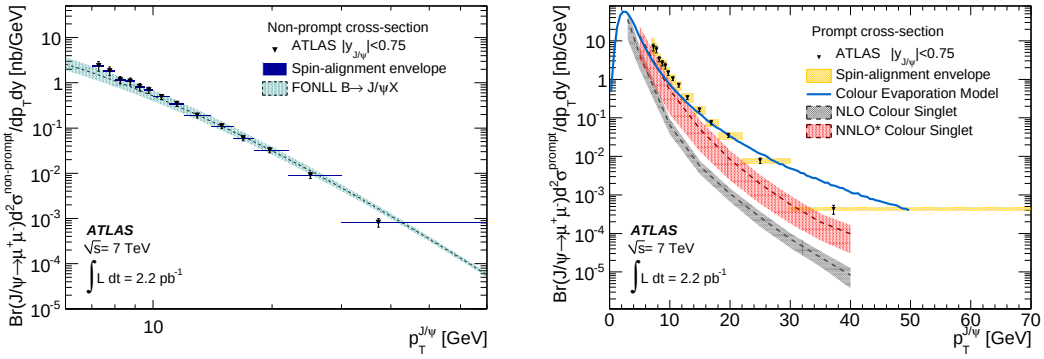

Figure 4. The a) non-prompt and b) prompt J/Ψ production cross-sections as a function of J/Ψ transverse momentum.

3. J/Ψ Cross Section Measurements in p+p Collisions

A key signature in the identification of B-mesons and furthermore a standard candle for the understanding of the ATLAS detector is the production of J/Ψ mesons and their subsequent decay into two muons [6]. Such events are selected by requiring a pair of oppositely charged muons, where the the hardest muon has a $p_T > 4$ GeV and the second muon a $p_T > 2.5$ GeV. The muons should be fitted to the same event vertex and at least one of the muons should be a "combined" muon.

Cross sections are measured by weighting each event by factors to account for the kinematic acceptance, and muon reconstruction and trigger efficiencies. The J/Ψ yield is reconstructed by fitting the dimuon invariant mass spectrum with gaussian forms for the J/Ψ and $\Psi(2S)$ components and a linear fit for the background. The cross sections for prompt J/Ψ production and those produced through the decays of B-mesons are measured. To separate the two components, the pseudo-proper decay time $\tau = \frac{L_{xy} \times m(J/\Psi)}{p_T^{J/\Psi}}$, where L_{xy} is the signed projection of the J/Ψ decay length onto it's flight direction, $m(J/\Psi)$ is the world average mass of the J/Ψ and $p_T^{J/\Psi}$ is the transverse momentum of the J/Ψ. A simultaneous maximum-likelihood fit to τ and the dimuon invariant mass is performed in each p_T and rapidity bin to determine the fraction of prompt and non-prompt J/Ψ mesons. Figure 4 shows the prompt and non-prompt J/Ψ production cross sections as a function of p_T in the central rapidity bin. Good agreement between the measured non-prompt cross section and the prediction from the Fixed Order Next-to-Leading Logarithm prediction is seen. The description of the prompt J/Ψ production cross section by the Colour Singlet Model at NNLO* is an improvement over that at NLO.

4. J/Ψ and Z Boson Measurements in Pb+Pb Collisions

The production of J/Ψ mesons and Z bosons are also measured in the dimuon decay channels in lead-lead collisions, at a centre of mass energy of $\sqrt{s_{NN}} = 2.76$ TeV [7].

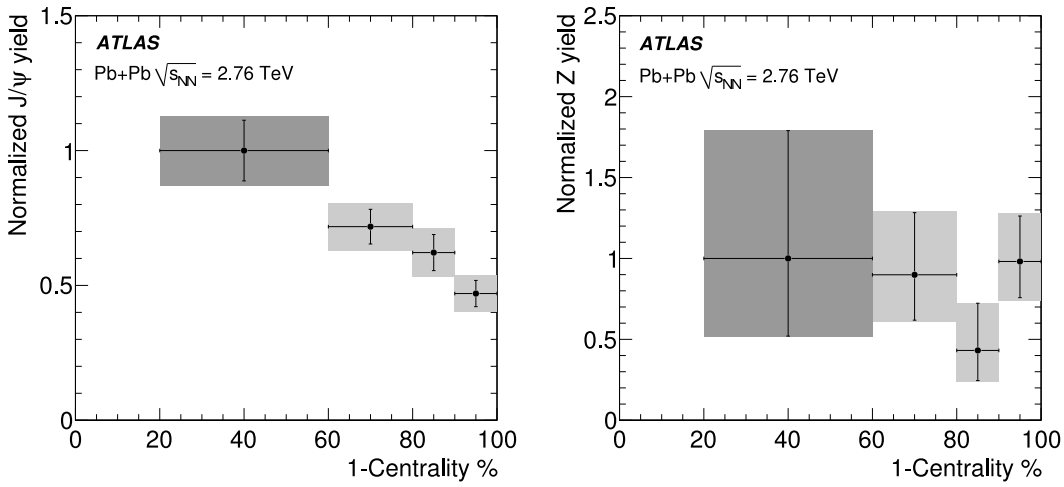

Figure 5. The normalised yield for a) J/Ψ and b) Z production in lead-lead collisions as a function of centrality.

As for the p+p measurements, J/Ψ and Z Bosons are reconstructed using "combined" muons that lie within the range $|\eta| < 2.5$. In the J/Ψ analysis, events containing two such muons with a $p_T > 3$ GeV and opposite charges are required. The J/Ψ yield is obtained from the number of events in the dimuon invariant mass range $2.95 < m_{\mu\mu} < 3.25$ GeV, with the background estimated from sideband subtraction. The yield is furthermore corrected by the $J/\Psi \rightarrow \mu^+\mu^-$ reconstruction efficiency, derived in each centrality bin using MC. The effect of systematics, such as the Inner Detector and Muon Spectrometer reconstruction efficiencies, as a function of centrality are estimated. Figure 5 a) shows the normalised J/Ψ yield, as a function of centrality, calculated as the yield relative to the most peripheral centrality bin (40-80%), normalised by the mean number of binary collisions relative to the most peripheral bin. A significant decrease in the normalised yield is seen with decreasing centrality, similar to that seen in inclusive J/Ψ production in heavy ion collisions at lower energies.

The production of Z Bosons in heavy ions, which is only possible at LHC energies, can act as a reference to the production of J/Ψ mesons, as they not expected to be affected by the hot, dense medium they are produced within. Events are selected containing two muons, as for the J/Ψ analysis above, but each with $p_T > 20$ GeV. In addition, cosmic muons are rejected by requiring that the sum of the two muon pseudorapidities $|\eta_{\mu 1} + \eta_{\mu 2}| > 0.01$ and the dimuon invariant mass is required to be within $66 < m_{\mu\mu} < 116$ GeV. The normalised Z production yield is calculated using the same method as the method as for the J/Ψ normalised yield, including the estimation of the systematic uncertainties, and is shown in Figure 5 b). Due to the large statistical errors on the normalised yield, it is unfortunately not possible to draw strong conclusions on any centrality dependency.

References

[1] The ATLAS Collaboration JINST **3** (2008) S08003
[2] The ATLAS Collaboration 2011 ATLAS-CONF-2011-041
[3] The ATLAS Collaboration 2011 ATLAS-CONF-2011-042
[4] The ATLAS Collaboration 2011 ATLAS-CONF-2011-010
[5] The ATLAS Collaboration 2011 ATLAS-CONF-2011-045
[6] The ATLAS Collaboration *Nucl. Phys. B* **850** (2011) 387
[7] The ATLAS Collaboration *Phys. Lett. B* **697** (2011) 294

Charmonium measurements with ALICE

F. Bossù for the ALICE Collaboration

INFN and University of Turin

E-mail: bossu@to.infn.it

Abstract.

ALICE at the LHC has measured the inclusive J/ψ production in proton-proton collisions at $\sqrt{s} = 7$ TeV. This measurement was carried out at central rapidity in the dielectron decay channel and at forward rapidity in the dimuon one.

Here the inclusive production cross section of the J/ψ and its differential distributions in transverse momentum and rapidity will be presented.

1. Introduction

The interest on heavy quarkonium measurements is driven by the fact that the production mechanism of a bound state is governed by both perturbative and non-perturbative aspects of Quantum Chromodynamics. The models currently available (such as the color evaporation, color singlet and the non relativistic QCD models) [1, 2] are unable to reproduce the production cross section, the distributions in the kinematical variables and the polarization of the heavy quarkonium. Therefore, measurements in a new energy domain, such as the one reachable at LHC, may provide new clues for the understanding of the hadroproduction process.

ALICE [3] is able to measure heavy quarkonia through their leptonic decays. In the central rapidity region ($|y| < 0.9$), this measurement is carried out through the detection of the e^+e^- pair. Various detector systems are embedded in a large solenoid magnet, that provides a magnetic field of 0.5 T. The subdetectors involved in the analysis described here are the Inner Tracking System (ITS) [4] and the Time Projection Chamber (TPC) [5]. The ITS is composed of six cylindrical layers of silicon pixels detectors based on three different technologies (pixels, strips and drift detectors), with a radius varying from 4 to 44 cm. The ITS is designed to localize the primary vertex with a resolution better than 100 μm, to reconstruct the secondary vertexes from the decays of heavy flavour hadrons, to track and identify low momentum particles.

The TPC is a large volume gaseous detector ($85 < r < 247$ cm in the radial direction and 5 m in the longitudinal direction) that is crucial both for the tracking and for the particle identification via specific energy loss measurements.

The forward rapidity region ($-4 < y < -2.5$) is covered by a muon spectrometer [6]. It consists of a front absorber that stops the hadrons coming from the interaction point,

a 3 T $\cdot$ m dipole magnet coupled with five tracking stations of Cathode Pad Chambers (CPC) and after an iron wall of about 1.2 m, two stations of Resistive Plate Chambers (RPC) form the trigger system. Throughout its full length, the spectrometer is shielded against secondary particles produced in the beam pipe by a conical absorber ($\theta < 2^o$). The spectrometer is able to detect muons with a momentum larger than 4 GeV/c. At the trigger level, L0 decisions are delivered if tracks pass a $p_{\rm T}$ cut. The $p_{\rm T}$ thresholds are programmable.

One of the L0 trigger detectors also used for this analysis is the VZERO. It consists of two scintillator arrays covering the range $2.8 < \eta < 5.1$ and $-3.7 < \eta < -1.7$ positioned respectively at $z = 340$ and $z = -90$ cm. This detector provides timing information with a resolution better than 1 ns. It is crucial in the offline rejection of beam-halo and beam-gas events.

2. Data analysis

In 2010, LHC provided pp collisions at $\sqrt{s} = 7$ TeV. In this period the instantaneous luminosity in ALICE was kept to $0.6 - 1.2 \cdot 10^{29}$ cm^{-1}s^{-1} in order to have a collision pile-up in the same bunch crossing smaller than 5%.

The analyzed events were collected in a minimum bias trigger configuration. This trigger is defined as a logical OR between at least one readout chip fired in the pixel layers of the ITS and at least one of the two VZERO detectors fired. It requires a coincidence of the beam pick-up counters signals, indicating the passage of proton bunches. For the muon analysis an additional requirement of at least one triggered muon is applied.

2.1. $J/\psi \rightarrow e^+e^-$

For the dielectron analysis, a sample of about $2.4 \cdot 10^8$ minimum bias events is analyzed. A constraint on the reconstructed vertex position of 10 cm around the nominal position is applied. The tracks have to fulfill requirements on the transverse momentum ($p_{\rm T} > 1$GeV/c), on the number of TPC clusters ($n_{clusters} > 70$ out of 159) and on the χ^2 per point after the global track fit ($\chi^2 < 4$), in order to be accepted in the analysis.

2.1.1. Signal extraction The opposite sign (OS) invariant mass spectrum, Fig. 1, is obtained combining identified electron tracks and partly subtracting the γ conversion background. The TPC is used for the particle identification: $\pm 3\sigma$ inclusion cut for electrons and $\pm 3.5\sigma (3\sigma)$ exclusion cut for pions (protons) were used. In the plot is also shown the like sign (LS) scaled to match the integral of the OS spectrum in the mass interval $3.2 - 5$ GeV/c^2. The necessity of a scale factor is due to misidentified electrons and correlated background. The signal is obtained by subtracting the LS from the OS spectrum. As shown in the bottom panel of Fig. 1, there is a good agreement, both for the bulk of the signal and the for the bremsstrahlung tail, between data and Monte

Carlo simulations. The extracted number of J/ψs is $249 \pm 27(\text{stat}) \pm 20(\text{syst})$ in the mass range $2.92 - 3.16\text{GeV/c}^2$. The systematic error estimation is described in Par.3.

2.1.2. Acceptance and efficiency correction The raw J/ψ yield has to be corrected for the acceptance and the efficiencies of the apparatus and the analysis selection. The determination of this correction factor has been carried out with a Monte Carlo technique: a large sample of signal events is generated according to predictions on the p_{T} and y distributions [8]. The acceptance times efficiency ($A \times \epsilon$) is 10.0% and this correction factor is the product of the kinematic selection on the J/ψ rapidity ($|y| < 0.9$) and on the e^+e^- pseudo-rapidity ($|\eta^{e^+,e^-}| < 0.9$ with $p_{\mathrm{T}}^{e^+,e^-} > 1\text{GeV/c}$), the reconstruction efficiency of the electron pair, the identification efficiency and the signal within the integration range.

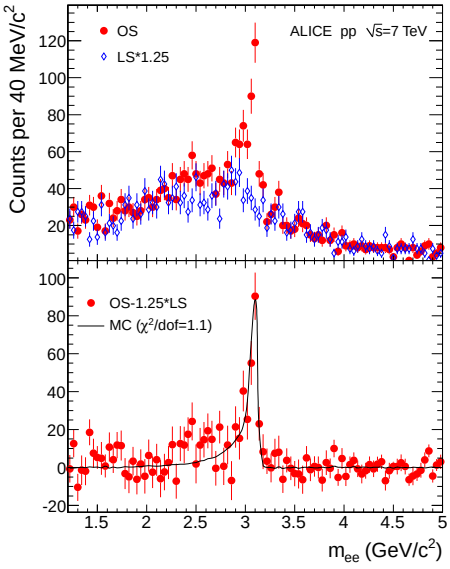

Figure 1. In the top panel the invariant mass distribution for like-sign and opposite-sign electron pairs is shown. In the bottom panel: the difference between these two distributions with the Monte Carlo signal superimposed.

2.1.3. Luminosity normalization For the determination of the production cross section, the number of J/ψs is normalized to the measured cross section of the occurrence of the minimum bias condition itself.

$$\sigma_{J/\psi} = \frac{1}{BR(J/\psi \to l^+l^-)} \frac{N_{J/\psi}}{A \times \epsilon} \times \frac{\sigma_{MB}}{N_{MB}}$$

BR is the branching ratio of the J/ψ in lepton pairs and N_{MB} is the number of minimum bias events.

The minimum bias cross section ($\sigma_{MB} = 62.3 \pm 0.4(\text{stat}) \pm 4.3(\text{syst})$ mb) was obtained relative to the cross section measured in the Van der Meer scan [9, 10],of the coincidence between signals in the two V0 detectors.

2.2. $J/\psi \to \mu^+\mu^-$

For the dimuon analysis, the sample of minimum bias events analyzed is $1.9 \cdot 10^8$ of which $1.0 \cdot 10^7$ have a triggered muon in coincidence with the MB condition. The events are then required to have at least a vertex reconstructed by the pixel detector of the ITS and to have at least one of the two muon candidates that matches a tracklet in the muon trigger system. A cut on the track position at the end of the absorber was applied in order to get rid of small angle muons. Events on the edge of the acceptance were removed requiring that the rapidity of the muon pair is $-4 < y < -2.5$.

2.2.1. Signal extraction The opposite sign invariant mass spectrum (Fig 2) was fitted with Crystal Ball functions [7] for the signal of the J/ψ and the ψ' plus a sum of two exponentials for the underlying continuum. The parameters of the fit were tuned by fitting MC simulations of pure signal. The integral of the signal function in the mass range $2.9 < m_{\mu\mu} < 3.3$ GeV/c^2 is $N_{J/\psi} = 1942 \pm 77(\text{stat}) \pm 144(\text{syst})$ and the width of the peak is $\sigma_{J/\psi} = 94 \pm 8$ MeV/c^2.

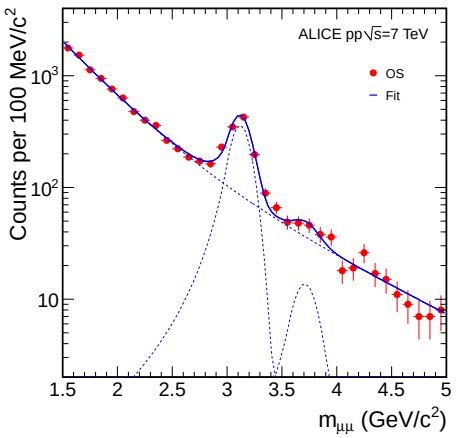

Figure 2. Invariant mass distribution for opposite-sign muon pairs. The fitted J/ψ , ψ' and the background shapes are also shown.

2.2.2. Acceptance and efficiency correction As for the dielectron analysis, the determination of the product $A \times \epsilon$ has been done through MC simulations. The real conditions of the detectors, such us the efficiencies of the tracking and trigger chambers, the dead channels and the residual misalignment, were plugged in the simulation. The value obtained is $A \times \epsilon = 32.9\%$.

2.2.3. Luminosity normalization The requirement of the coincidence of a muon trigger in a minimum bias event slightly modifies the normalization method to obtain the absolute cross-section. The yield of single muons in the acceptance of the spectrometer is taken as the reference process that links the number of J/ψs taken with the corresponding number of minimum bias events.

3. Integrated and differential inclusive J/ψ cross sections

Considering all the details previously described, the inclusive J/ψ production cross sections in pp collisions at $\sqrt{s} = 7$ TeV measured by ALICE are:
$\sigma_{J/\psi}(|y| < 0.9) = 10.7 \pm 1.2(\text{stat}) \pm 1.7(\text{syst}) \,^{1.6}_{-2.3}\ \mu$b and
$\sigma_{J/\psi}(-4 < y < 2.5) = 6.31 \pm 0.25(\text{stat}) \pm 0.80(\text{syst}) \,^{0.95}_{-1.96}\ \mu$b.

The unknown polarization of the J/ψ affects the acceptance values. These were calculated doing MC simulations of pure signal fully transverse or longitudinally polarized in the Collins-Soper and helicity reference frames. The uncertainties are quoted for the frame in which they are largest.

The systematic uncertainties [8] were obtained considering: the uncertainty on the signal extraction, varying the background calculation and the mass range in the dielectron channel while different signal and background shapes were considered for the fit in the dimuon channel; the uncertainty on the acceptance evaluation, estimated varying the input kinematical distributions; the uncertainty on the efficiency

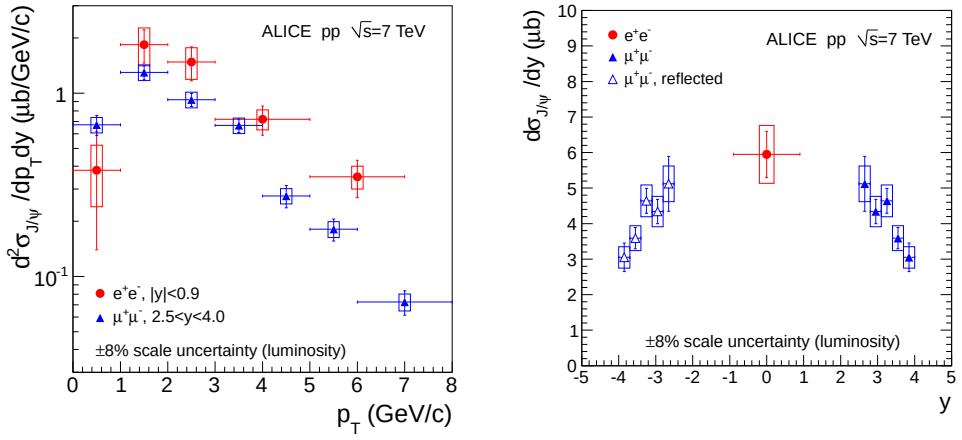

(a) $\mathrm{d}^2\sigma_{J/\psi}/\mathrm{d}p_\mathrm{T}\mathrm{d}y$ (b) $\mathrm{d}\sigma_{J/\psi}/\mathrm{d}y$

Figure 3. The differential inclusive J/ψ cross section distributions in $\mathrm{d}p_\mathrm{T}\mathrm{d}y$ (a) and $\mathrm{d}y$ (b) are shown. The bars represent the statistical errors while the squares the systematic one

reconstruction, evaluated from residual mismatches between data and MC simulations in track quality and particle identification cuts for the dielectron channel and chamber efficiencies in the muon channel; the uncertainty on the muon trigger efficiency, as the difference between $N_{J/\psi}$ collected asking that one or both muons fire the trigger; and the uncertainty on the determination of σ_{MB}, that is mainly due to the beam intensity measurement and the analysis procedure of the VZERO coincidences in the Van der Meer scan.

3.1. Differential cross sections

The differential cross section distributions have been also measured. At mid-rapidity the $\mathrm{d}\sigma_{J/\psi}/\mathrm{d}p_\mathrm{T}$ was measured in 5 transverse momentum bins, between 0 and 7 GeV/c. In the muon channel, the inclusive J/ψ cross section differential behaviour has been studied in the kinematical variables p_T and y.

The steps of the analysis are the same as for the integrated cross section. In Fig 3(a) the $\mathrm{d}^2\sigma_{J/\psi}/\mathrm{d}p_\mathrm{T}\mathrm{d}y$ is shown and in Fig 3(b) the $\mathrm{d}\sigma_{J/\psi}/\mathrm{d}y$ for both mid rapidity and forward analysis.

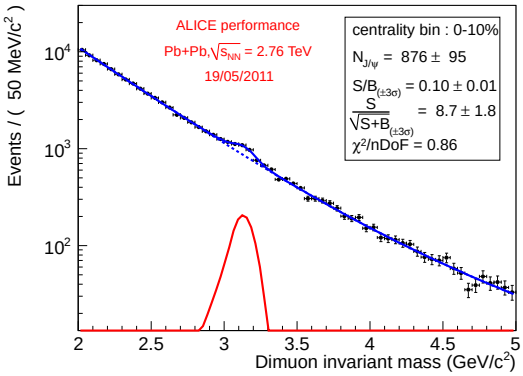

Figure 4. Invariant mass distribution for opposite-sign muon pairs in Pb-Pb collisions, in the centrality bin 0-10%. Centrality is estimated with the V0 detectors

4. Conclusions

ALICE has measured the inclusive J/ψ production cross section through its semileptonic decays in the rapidity range $|y| < 0.9$ and $-4 < y < -2.5$. The details of the analysis as well as the results for the integrated and differential cross sections have been described. In 2010, the LHC delivered one month of Pb-Pb collisions at $\sqrt{s_{NN}} = 2.76$ TeV: analysis on this data sample are ongoing. The J/ψ signal has been already observed (Fig. 4).

References

[1] N. Brambilla et al., *Heavy quarkonium: progress, puzzles, and opportunities*,Eur. Phys. J. **C71**, 1534 (2011).

[2] J.P. Lansberg, *On the mechanisms of heavy-quarkonium hadroproduction*, Eur. Phys. J. **C61**, 693(2009).

[3] K. Aamodt et al. (ALICE Collaboration),*ALICE at the CERN LHC* JINST **3**, S08002 (2008).

[4] K. Aamodt et al. (ALICE Collaboration), *Alignment of the ALICE Inner Tracking System with cosmic-ray tracks*, JINST **5**, P03003 (2010).

[5] J. Alme et al. (ALICE Collaboration), *The ALICE TPC, a large 3-dimensional tracking device with fast readout for ultra-high multiplicity events* , Nucl. Inst. Meth. **A622**, 316 (2010).

[6] F. Bossu (ALICE Collaboration), *The forward muon spectrometer of ALICE: Status and commissioning results*, PoS **BORMIO2010**, 063 (2010).

[7] J.E. Gaiser, *Charmonium spectroscopy from radiative decays of the J/ψ and ψ'*, Ph.D. Thesis, SLAC-R-255 (1982).

[8] K. Aamodt et al (ALICE Collaboration), *Rapidity and transverse momentum dependence of inclusive J/psi production in pp collisions at sqrt(s) = 7 TeV*, [arXiv:1105.0380].

[9] M. Gagliardi, *Measurement of reference cross sections in pp and Pb-Pb collisions at the LHC in van der Meer scans with the ALICE detector.*, EPIC@LHC conference proceedings, arXiv:1109.5369.

[10] S. van der Meer, *Calibration of the effective beam height in the ISR*, ISR-PO/68-31, KEK68-64.

Experimental treatment of Quark and Gluon Jets

Sona Pochybová [1,2]

[1] Eötvös Lórand University, Pazmány Péter sétány 1/A, H-1117, Budapest, Hungary
[2] MTA KFKI RMKI, Konkoly-Thége Miklós út 29-33, H-1121, Budapest, Hungary

E-mail: sona.pochybova@cern.ch

Abstract. The separate study of quark and gluon jets is vital for the interpretation of multiple variables behaviour observed in both high-energy hadron and heavy-ion collisions in the present and future experiments. We propose a set of jet-energy dependent cuts to be used to distinguish between quark and gluon jets experimentally based on a Monte-Carlo study of their properties. Further, we introduce the possibility to calibrate these cuts via gamma-jet and multi-jet events, which represent clean production channels for quark and gluon jets, respectively. The calibration can happen on real data and thus, reduces the dependence of the method performance on Monte-Carlo model predictions.

1. Introduction

Jets are objects produced in hard scatterings of colliding particles. Experimentally we can observe jets as showers of high momentum particles. The character of these showers is determined by the fragmentation properties of the original parton; quark or gluon. In QCD, quarks and gluons carry different color factors [1]. This factor is proportional to the probability of a parton to radiate a soft gluon. Gluons have more than twice the color factor as quarks and as such are expected to form broader and higher multiplicity jets with softer fragmentation function.

Apart from these differences, the gluons are expected to contribute significantly to the baryon production as compared to quarks [2]. All these differences naturally must be demonstrated in the particle spectra observed in an experiment. Previous experiments with e^+e^- [3] and $p\bar{p}$ [4] collisions studying the properties of different parton types have qualitatively proven these expectations.

From the heavy-ion perspective, the study of fragmentation properties of quarks and gluons becomes important for understanding unexpected observation from RHIC explained by different phenomenological models (e.g. coalescence [5], jet flavor conversion [6]), which incorporate the above mentioned differences.

Our aim is to perform a systematic study of the baryon and meson production inside quark and gluon jets. For this, we need to identify the jets first. In the following we introduce a data driven method to distinguish quark and gluon jets and make the study of their properties experimentally feasible.

2. Method description

The experimental treatment of quarks and gluons in proton-proton collisions seems challenging since we only can observe the final state hadrons together with the underlying event. Therefore, our observation is restricted to the experimental definition of a jet in terms of jet finding algorithms. Further, the study of jet properties based on their identification may be biased by our prior expectations incorporated into Monte-Carlo models.

However, experimental data offer the possibility to distinguish between quark and gluon in an unbiased way, by observing their properties in channels, were we are certain of the origin of the jet. Such channels are the multi-jet and gamma-jet events, sources to gluon and quark jets respectively. Observing the properties of jets in such events can help us to identify the leading jets in others.

The study was performed on simulations done using the Pythia 6.4 Monte-Carlo generator with the settings of *Perugia*0 tune [7]. For testing 4 data samples were generated, each containing 1 milion events. The samples involved 3 sets of events with hard scatterings, divided based on the two leading jets into gluon-gluon (GG), quark-quark (QQ) and quark-gluon (QG) samples. In order to study quark-jets, gamma jet sample was created (γQ). To reconstruct the jets, we used anti$-\mathrm{k_T}$ jet-finding algorithm [8] for 2 jet-size parameters; $R = 0.4, 0.7$. To design the cut, we chose to compare the subcone size, which contains 90% of jet's energy - $\Delta R(90\%)$, after the tracks have been sorted in distance from the jet axis. The method introduced is performed in two steps.

1^{st} *step* From each event we select two leading jets and measure their $\Delta R(90\%)$. We plot it as a function of the jet's energy (see Fig. 1, panel (a)). We fit $< \Delta R(90\%) >$ and so we obtain $\Delta R(90\%)_{calc}$ (see Fig. 1, panel (b)). Experimentally this variable can be obtained by actually fitting the $< \Delta R(90\%) >$ measured for reconstructed jets.

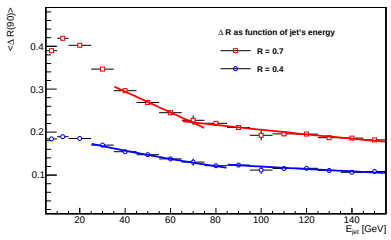

(a)

R	E_{jet} int.	Fit fction	A	B ($\times 10^{-3}$)
0.4	$(25; 85)$	exp	-1.590	-6.556
0.4	$(85; 155)$	exp	-1.878	-2.438
0.7	$(35; 75)$	$pol1$	-0.391	-2.424
0.7	$(75; 155)$	exp	-1.316	-2.666

(b)

Figure 1. Panel (a): $< \Delta R(90\%) >$ as function of jet's energy for $R = \{0.4, 0.7\}$. Lines represent the fits in separate energy intervals. Panel (b): Table with fit parameters. Indicated are the fit functions for different energy intervals, where exp corresponds to $\Delta R(90\%)_{calc} = exp\{A + B \times E_{jet}\}$ and $pol1$ to $\Delta R(90\%)_{calc} = A + B \times E_{jet}$.

$2^{nd} step$ Next we reconstruct jets in multi-jet and gamma-jet events in order to obtain samples of gluon and quark jets. From multi-jet events we select all but the two leading jets, from gamma-jet events we take the jet at $180^o \pm 30^o$ degrees w.r.t. the gamma. We measure $\Delta R(90\%)_{measured}$ for each quark and gluon jet and check how it is distributed around $\Delta R(90\%)_{calc}$, which was obtained from the $< \Delta R(90\%) >$ fit. We obtain a distribution of $DR = \Delta R(90\%)_{calc} - \Delta R(90\%)_{measured}$ plotted in Fig. 2. Based on this distribution we choose a DR cut to be applied to the leading jets (Table 1). The cut was determined from the DR distributions of selected jets from gamma-jet and multi-jet events so, that it maximizes the signal-to-background ratio, signal being the type of jet we want to identify, background the other type of jet. We do this twice, for each type of jet - quark or gluon.

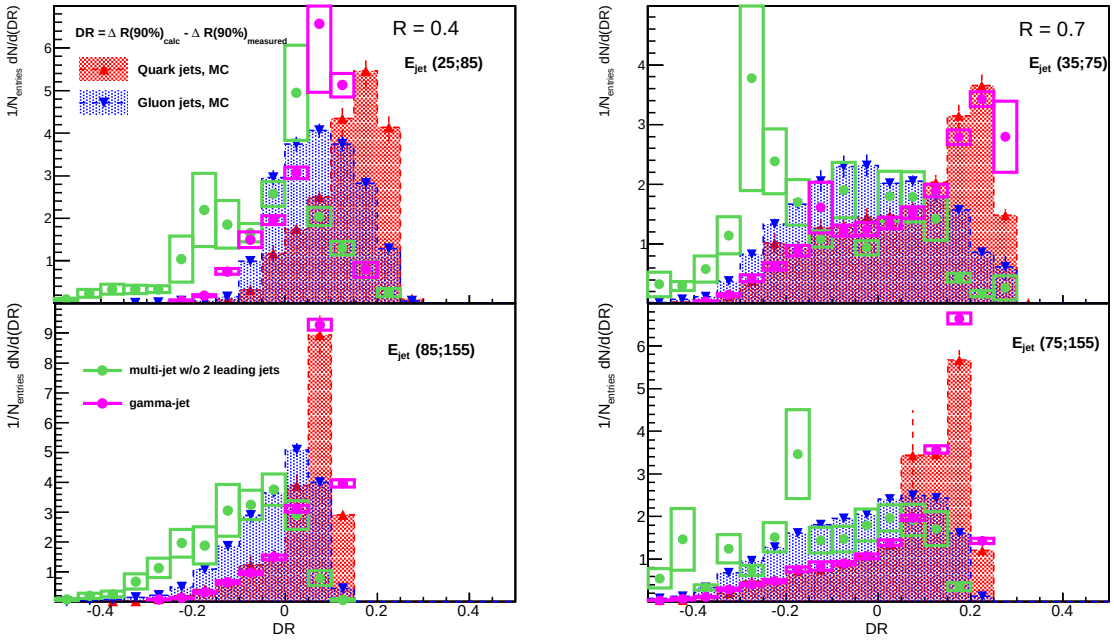

Figure 2. DR variable distribution for $R = \{0.4, 0.7\}$ and different jet energy intervals for MC quark and gluon jets compared to DR distribution of quark and gluon jets obtained from gamma-jet and multi-jet events respectively.

(a)

$R = 0.4$	E_{jet} int.	Q_{cut}	G_{cut}
	$(25; 85)$	0.15	0.10
	$(85; 155)$	0.05	0.00

(b)

$R = 0.7$	E_{jet} int.	Q_{cut}	G_{cut}
	$(35; 75)$	0.15	0.00
	$(75; 155)$	0.10	0.05

Table 1. Cuts to select quark and gluon jets based on gamma-jet and multi-jet distributions of DR in Fig. 2.

3. Discussion

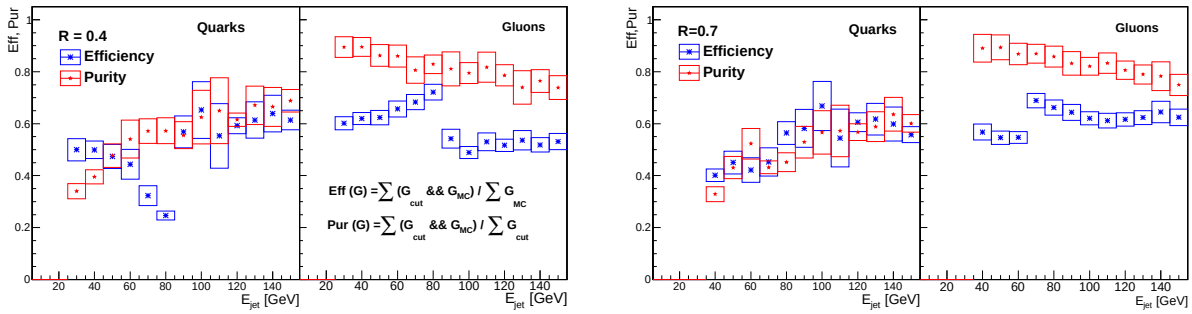

(a) (b)

Figure 3. Performance plots. Efficiency and purity as function of E_{jet}.

We presented a possibility to distinguish between quark and gluon jets experimentally. The main advantage of this method lies in the fact, that the cut on the variable introduced can be calibrated on real data without the necessity to rely on Monte-Carlo information. The cut calibration happens on the samples of quarks and gluons obtained from gamma-jet and multi-jet samples respectively. This way, our selection is not biased by our prior expectations about the differences of quark and gluon jets. As can be seen in Fig. 2, the respective DR distributions of event-identified jets and leading MC jets overlap, especially for higher energy regions and greater jet size. This overlap, however, is not perfect, which is due to the energy dependence of $< \Delta R(90\%) >$ on jet's energy, especially in the lower energy interval (see Fig. 1, panel(a)). This problem has to be investigated in more detail by studying the jets in smaller energy intervals, since the overlap between a MC quarks/gluons and quarks/gluons from specific events is crucial for determining how well our method works.

The performance of the method was determined by the efficiency and purity of the identification of the two leading jets in an event based on the cut obtained from jets in gamma-jet and multi-jet events. We can do this since, eg. a quark from a gamma-jet event and a leading jet whith the same energy and DR will have the same probability of misidentification. Nevertheless, as mentioned above, a detailed study in smaller energy bins is needed to make this statement strong. As can be seen in Fig. 3, for quarks the identification achieves efficiency and purity up to 60% in the higher energy interval. For gluons, efficiency of the selection is better (constant, 60% for higher energy interval), although the purity drops slightly with energy. The rise of purity for quarks and the drop for gluons is however expected since quarks are to form harder jets than gluons. The method performs better for bigger jet size, namely $R = 0.7$ (see Fig. 3, panel(b)).

Acknowledgements

I would like to thank my supervisor Péter Lévai for cooperation and the support of my ideas. The presentation of this work was possible thanks to the funding provided by ELTE and the Hungarian OTKA 77816.

References

[1] R. K. Ellis, W. J. Stirling and B. R. Webber, Camb. Monogr. Part. Phys. Nucl. Phys. Cosmol. **8** (1996) 1.
[2] S. Albino, B. A. Kniehl and G. Kramer, Nucl. Phys. B **725** (2005) 181 [arXiv:hep-ph/0502188].
[3] P. Abreu *et al.* [DELPHI Collaboration], Z. Phys. C **70** (1996) 179.
[4] A. A. Affolder *et al.* [CDF Collaboration], Phys. Rev. Lett. **87** (2001) 211804.
[5] V. Greco, C. M. Ko and P. Levai, Phys. Rev. Lett. **90** (2003) 202302 [arXiv:nucl-th/0301093]. [6]
[6] W. Liu, C. M. Ko and B. W. Zhang, Int. J. Mod. Phys. E **16** (2007) 1930.
[7] P. Z. Skands, Phys. Rev. D **82** (2010) 074018 [arXiv:1005.3457 [hep-ph]].
[8] M. Cacciari, G. P. Salam and G. Soyez, JHEP **0804**, 063 (2008) [arXiv:0802.1189 [hep-ph]].

Calculation of Direct photon production in nuclear collisions

J Cepila

E-mail: jan.cepila@fjfi.cvut.cz

Abstract. Prompt photons produced in a hard reaction are not expected to be accompanied by any final state interaction, either energy loss or absorption and one should not expect any nuclear effects at high p_T. However, data from the PHENIX experiment indicates large-p_T suppression in d+Au and central Au+Au collisions that cannot be accompanied by coherent phenomena. We propose a mechanism based on the energy sharing problem at large p_T near the kinematic limit that is induced by multiple initial state interactions and that improves the agreement of calculations with PHENIX data. We calculate inclusive direct photon production cross sections in p+p collisions at RHIC and LHC energies using the color dipole approach without any additional parameter. Our predictions are in good agreement with the available data. Within the same framework, we calculate direct photon production rates in d+A and A+A collisions at RHIC energy. We also provide predictions for the same process in p+A collisions at LHC energy. Since the kinematic region where the expected suppression manifests can be achieved also at forward rapidity, we present a comparison of forward rapidity to midrapidity behaviour. We also include and analyze the contribution of gluon shadowing as a leading twist shadowing correction that modifies nuclear effects especially at small p_T.

1. Introduction

It is known for a long time that the cross section of the particle production in proton-nucleus collisions is not equal to A times the cross section of the particle production in proton-proton collisions, where A is the mass number of a nucleus. The ratio of these two cross sections is called nuclear modification factor and the deviation of this quantity from unity is a measure of nuclear effects. The suppression of the production rate in the region of high Feynman x_F was first observed in BRAHMS experiment at RHIC collider[1] for the charged hadron production, but later was rediscovered in NA49 experiment at SPS[2] for the pion production and even in E772 experiment at FNAL[3] for the dilepton production. Coherence phenomena(shadowing) are expected to be responsible for the suppression, but one has to interpret it carefully. If a particle with mass M and transverse momentum p_T is produced in a hard reaction with pseudo-rapidity η then the corresponding values of Bjorken variable in the beam and the target are

$$x_{1,2} = \frac{\sqrt{M^2 + p_T^2}}{\sqrt{s}} e^{\pm\eta} \qquad x_F = x_1 - x_2$$

and the region, where coherence phenomena are expected to be strongest, corresponds to forward pseudo-rapidity for energies accessible at RHIC. As a result coherence effects exhibit the x_2 scaling, but as shown in [4] this scaling is known to be broken. The fact, that the suppression has been also observed at any reaction studied so far at any energy suggest that the effect which suppresses particle yields has to be energy independent and as shown in [4] or [5] has to scale with x_F. Such mechanism was formulated in [5, 6] as energy conservation restrictions in the multiple parton rescattering inside the nuclear medium.

In this paper a production of direct photons on nuclear targets is studied. Photons produced in a hard reaction have no final state interactions and so no nuclear effects are expected at high-p_T. However, we show that high-p_T photons are universally suppressed by energy deficit in multiple interactions. We study also a rise of this suppression with η in RHIC and LHC kinematic regions.

2. Energy conservation restrictions in multiple interactions within the color dipole approach calculation

For the calculation of direct photon production cross section, the light-cone color dipole approach is used. The production mechanism is formulated in the rest frame of the target, where the photon emission is treated as bremsstrahlung radiation of a real photon by a projectile quark. On a partonic level, the quark from the incident hadron can fluctuate into the coherent state $|q\gamma>$ of a quark and a photon with the transverse separation ρ where the quark and the photon carries a fraction of the incident momenta p_q of the magnitude of $(1-\alpha)p_q$ and αp_q respectively. The coherence of the fluctuation is disrupted after the coherence length by the interaction with the color field of the target nucleon. The cross section on a partonic level can be calculated[7] as a convolution of the perturbativelly calculated light-cone wave function $\Psi_{\gamma q}(\alpha, \rho)$[8] that describes the probability to produce the fluctuation of the transverse separation ρ and the completely nonperturbative dipole cross section $\sigma^N_{q\bar{q}}(\rho, x)$ of the interaction between the fluctuation and the color field of the nucleon which are obtained from fits to HERA data on the deep inelastic scattering

$$\frac{d\sigma(qN \to \gamma X)}{dln\alpha d^2p_T} = \frac{1}{(2\pi)^2} \sum_{in,f} \int d^2\rho_1 d^2\rho_2 e^{-i\vec{p}_T(\vec{\rho}_1 - \vec{\rho}_2)} \Psi^{*T}_{\gamma q}(\alpha, \rho_1) \Psi^T_{\gamma q}(\alpha, \rho_2) \Sigma(\alpha, \rho_1, \rho_2)$$

$$\Sigma(\alpha, \rho_1, \rho_2) = \frac{1}{2}(\sigma^N_{\bar{q}q}(\alpha\rho_1) + \sigma^N_{\bar{q}q}(\alpha\rho_2) - \sigma^N_{\bar{q}q}(\alpha|\vec{\rho}_1 - \vec{\rho}_2|)),$$

where $\alpha = p^+_\gamma / p^+_q$. In our calculation the GBW approximation to the dipole cross section was used[9]. Consequently, the cross section for the proton - proton collisions on the hadronic level is

$$\frac{d\sigma(pp\to\gamma X)}{d^2p_T}=\frac{x_1}{x_1+x_2}\int_{x_1}^1\frac{d\alpha}{\alpha^2}\sum_q Z_q^2\left(f_q\left(\frac{x_1}{\alpha},Q^2\right)+f_{\bar q}\left(\frac{x_1}{\alpha},Q^2\right)\right)\frac{d\sigma(qN\to\gamma X)}{dln\alpha d^2p_T},$$

where Z_q is the fractional quark charge and the structure function is composed of parton distribution functions $f_{q,\bar q}$ from the GRV98 parametrization[10] at the lowest order at the scale $Q^2=p_T^2$.

For the calculation of the cross section on the nuclear target, one has to discuss the coherence length of the fluctuation. It can be expressed as

$$l_c=\frac{2E_q\alpha(1-\alpha)}{\alpha^2m_q^2+p_T^2}\qquad E_q=\frac{x_1s}{2m_N\alpha},$$

where m_q and m_N is the mass of the projectile quark and nucleon respectively. The limit of the long coherence length(LCL) corresponds to the situation where the coherence length is longer than the nuclear radius R_A. The fluctuation arises long before the quark enters the nucleus and is subject to maximal quark shadowing. Since the transverse size of the fluctuation is "frozen" through the propagation inside the nucleus, different transverse configurations form eigenstates of the interaction in the impact parameter space and the cross section can be eikonalized using the Glauber approximation[11]

$$\sigma^N_{q\bar q}(\rho,x)\to\sigma^A_{q\bar q}(\rho,x)=2\int d^2b\left(1-\left(1-\frac{1}{2A}\sigma^N_{q\bar q}(\rho,x)T_A(b)\right)^A\right),$$

where $T_A(b)$ is the nuclear thickness function. This LCL limit can be safely used in calculations of nuclear effects in RHIC and LHC energy domains especially at forward rapidities. Here higher Fock components containing gluons lead to additional corrections called gluon shadowing (GS). The corresponding suppression factor R_G [12] was included in calculations replacing $\sigma_{q\bar q}$ by $R_G\sigma_{q\bar q}$.

The suppression mechanism can be understood via the survival probability of the large rapidity gap in multiple interactions inside the nucleus. One can see any hard process in the limit $x_1\to 1$ as the large rapidity gap process. The produced particle takes most of the momenta leaving only the small rapidity interval $\Delta y=-ln(1-x_1)$ for the others. The probability to radiate no gluons in the interval Δy is suppressed by Sudakov form factor derived in [13] as $S(x_1)\sim 1-x_1$. The suppression at $x_1\to 1$ can be formulated such that each of the multiple interactions of projectile partons with the nucleus produces an extra factor $S(x_1)$. Corresponding weight factors are related to the Glauber coefficients via Abramovski-Gribov-Kancheli cutting rules [14]. Resuming over the number of scatterings leads to effective parton distribution function[5, 15]

$$f^A_{q/N}(x_1,Q^2)=Cf_{q/N}(x_1,Q^2)e^{-(1-S(x_1))\sigma_{eff}T_A(b)}$$

that correlates with the target and predicts the breakdown of the QCD factorization. The normalization factor C is fixed by Gottfried sum rules and the effective cross section is calculated in [13].

3. Predictions for nuclear effects

First, the cross sections of direct photons in p + p collisions at midrapidity is shown for RHIC and LHC energy. Since there are no relevant data available from LHC yet, the reasonable agreement with data is presented only on PHENIX experiment data(see Fig. 1).

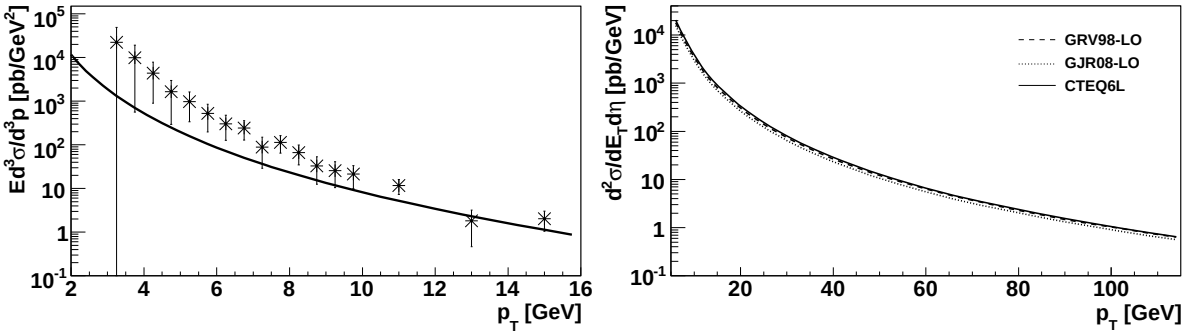

Figure 1. Invariant cross section for direct photon production in p + p collisions at y = 0 at energy of (left) RHIC vs. data from PHENIX experiment[16] (right) LHC for different PDF parametrizations[10, 17, 18]

Since one can approach the kinematic limit by increasing p_T, predictions for nuclear effects at several fixed y for the nuclear modification factor R_{d+Au} at RHIC energy and R_{p+Pb} at LHC energy is presented.

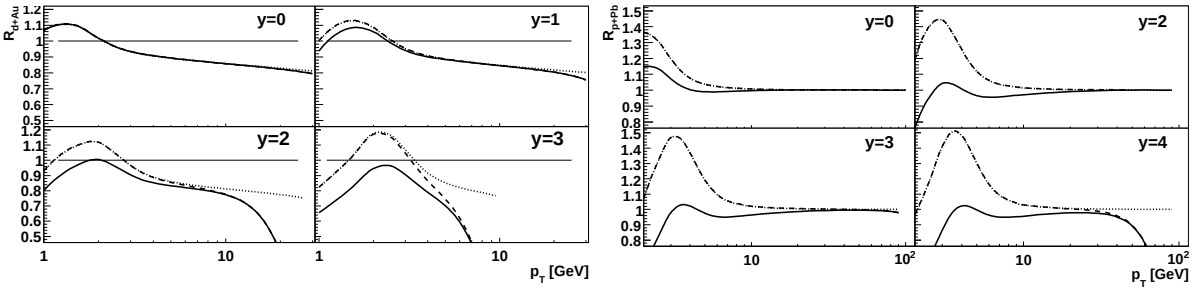

Figure 2. Ratio of the cross sections in (left) d + Au to p + p collisions at $\sqrt{s}$ = 200 GeV (right) p + Pb to p + p collisions at $\sqrt{s}$ = 5,5 TeV and at different values of rapidity. Dotted lines represent calculations without corrections for energy conservation and GS. Dashed lines additionally include corrections for energy deficit and solid lines also GS.

All these figures clearly demonstrate dominance of GS at small and medium p_T and energy conservation effects at high p_T. Both effects rise rapidly with y. Note that unexpected high p_T suppression violating QCD factorization can be tested in the future by new data from RHIC and LHC experiments especially at forward rapidities.

4. Summary

Using the color dipole approach the study of production of direct photons in collisions on nucleon and nuclear targets is presented. The unified approach to large x_1 nuclear

suppression based on energy conservation effects in multiple parton rescattering is discussed. This effect clearly dominates the high p_T region of the production rate mainly at forward rapidity(up to small izotopic corrections in d + Au). Also coherence effects(GS) are demonstrated to be dominant at small and medium p_T. Both effects cause a suppression and rise rapidly with rapidity. First this approach is tested in RHIC kinematic region demonstrating a good agreement with PHENIX data in p + p at midrapidity and also predictions in the LHC kinematic region is presented. Then predictions for p_T behavior of nuclear effects at different fixed rapidities are presented in RHIC and LHC kinematic regions. Quite strong suppression is observed at high p_T in all kinematic regions and it can be tested by future data from LHC and RHIC experiments.

Acknowledgments
This work was supported by grant MSMT LC07048 (Czech Ministry of Education)

References

[1] BRAHMS, Phys. Rev. Lett. 91, 072305 (2003)
[2] B. Boimska, CERN-THESIS-2004-035
[3] E772 Collaboration, Phys. Rev. Lett. 64, 2479 (1990)
[4] PHENIX Collaboration, Phys. Rev. C77, 0214912 (2008)
[5] B.Z.Kopeliovich et al. Phys. Rev. C72,054606 (2005)
[6] J.Nemchik et al.,Phys. Rev. C78, 025213 (2008)
[7] B.Z. Kopeliovich, A. Schafer and A.V. Tarasov, Phys. Rev. C59, 1609 (1999)
[8] S.J.Brodsky, A.Hebecker, E.Quack, Phys. Rev. D55, 2584 (1997)
[9] K.J.Golec-Biernat and M.Wusthoff, Phys. Rev. D60, 114023 (1999)
[10] M.Gluck, E.Reya, A.Vogt, Z. Phys. C67, 433 (1995)
[11] A.B. Zamolodchikov, B.Z. Kopeliovich and L.I. Lapidus, Sov. Phys. JETP Lett. 33, 595 (1981)
[12] B.Z. Kopeliovich, J. Nemchik, A. Sch fer and A. Tarasov, Phys. Rev. C65, 035201 (2002)
[13] B.Z.Kopeliovich, J.Nemchik, I.K.Potashnikova, M.B.Johnson and I.Schmidt, Nucl. Phys. Proc. Suppl. 146, 171 (2005)
[14] V.A.Abramovsky, V.N.Gribov and O.V.Kancheli, Yad. Fiz. 18, 595 (1973) [Sov. J. Nucl. Phys. 18, 308 (1974)]
[15] J. Nemchik et al., Phys. Rev. C78, 025213 (2008)
[16] S.S. Adler et al., [PHENIX Collaboration], Phys. Rev. Lett. 98, 012002 (2007)
[17] M. Gluck, P. Jimenez-Delgado and E. Reya, Eur. Phys. J. C 53 (2008) 355
[18] J. Pumplin, D. R. Stump, J. Huston, H. L. Lai, P. Nadolsky, W. K. Tung, JHEP 0207:012(2002)

VHMPID: ALICE detector upgrade proposal in the high-p_T region

G. Hamar on behalf of the VHMPID Collaboration

29-33 Konkoly-Thege M., Budapest, Hungary

E-mail: hamargergo@rmki.kfki.hu

Abstract. Based on the results in the RHIC heavy ion experiments the identification of very high-p_T particles seems to be extremely interesting at LHC energies. ALICE has an excellent event by event PID below 5 GeV/c even in those high track-densities. However, the track-by-track analysis of the heavy ion data demands further efforts on the experimental side.

We are presenting the idea of an ALICE upgrade detector which is capable to extend the particle identification into the momentum region of 5-25 GeV/c on track-by-track basis. The Very High Momentum Particle Identification Detector (VHMPID) is a gaseous Cherenkov detector, capable to distinguish charged pions, kaons and protons/anti-protons in the above momentum window event by event. This feature gives us the possibility to study the meson/baryon anomaly, multi jet fragmentation function, in medium effects and the same-side and away-side jet correlations.

The paper is focusing on design issues and technical aspects of such a detector, with some insight on present simulations and the prototype test results of the VHMPID.

1. Introduction

ALICE [1] (A Large Ion Collider Experiment) is the dedicated heavy ion experiment at CERN LHC (Large Hadron Collider). The proper particle identification, especially at high transverse momenta, could shed light on the properties of the deconfined hot and dense quark-gluon plasma phase.

ALICE has an excellent particle identification capability up to 5 GeV/c via its various detector system (silicon detectors, time projection chamber, time of flight and transition radiation detectors). We propose here a new detector (VHMPID) which can extend this PID capability up to 25 GeV/c track-by-track.

2. The Very High Momentum Particle Identification Detector

The Very High Momentum Particle Identification Detector (VHMPID) is a gaseous ring imaging Cherenkov detector. The radiator gas (C_4F_{10}) has been chosen to make the detector able to separate pions/kaons/protons in the 5-25 GeV/c momentum range track by track. Spherical mirrors are focusing the Cherenkov light onto the photo sensitive detector forming a ring. The radius of this ring is correlated with the Cherenkov angle and the particle's velocity as well. A simple scratch of the detector can be found on Figure 1. left.

VHMPID will be an excellent tool to analyse jet structure, near side baryon-meson and baryon-antibaryon correlations. One can study multi-hadron fragmentation functions and medium modified fragmentation as well. HMPID and PHOS located in ALICE opposite side as the VHMPID opening the opportunity to measure away-side hadron-hadron and photon-hadron correlations.

3. Research and development issues

Focusing geometry will put the center of the rings independently of the incoming particle allowing us to reduce the photo detector's area. (Figure 1. middle plot shows this feature in a prototype beam test.) Mirrors are tilted to focus at the same spot or near each other, reducing further the cost and area of the photon detection part. However this feature makes mirror alignment a more important task, therefore online information will be served by an alignment measuring laser system inside the detector. The very low number of Cherenkov photons forces us to use state of the art technology for photon detection. According to the large area what should be covered in ALICE cost effective gaseous detectors will be used with CsI. Besides the classic CsI coated MWPC (like in HMPID [4]), TGEM based [2] and TGEM+CCC based detectors are studied and tested. The purity of the Cherenkov gas is crucial, both O_2 and H_2O levels should be kept under 5-10ppm to avoid photon absorption inside the radiator gas volume.

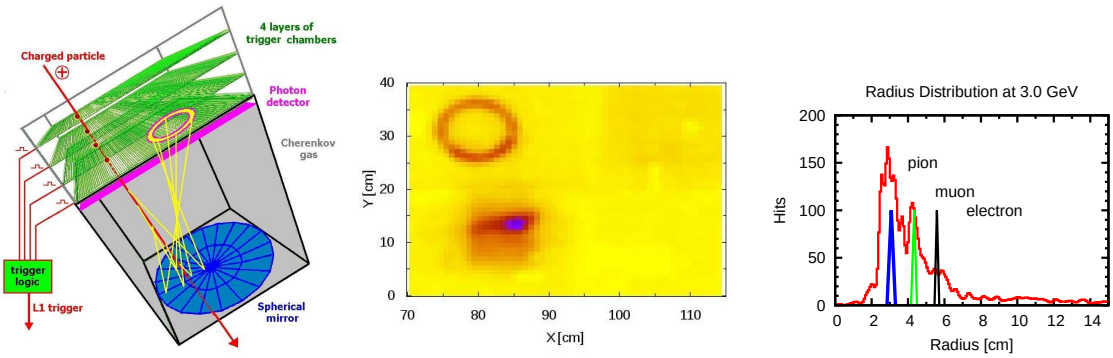

Figure 1. (Left) A simple scratch of one segment of the VHMPID detector. (Middle) Focusing geometry places the ring and its center at the same spot independently from the particle's position. (Right) Three different rings from pions,muons and electrons at the 2010 PS beam tests. The triangles show the theoretical ring radii.

4. Recent beam tests for the VHMPID prototype

We had tests at both CERN PS and SPS with various energy beams and could done many important studies. After gas purification workable O_2 and H_2O levels could be reached. Mirror focusing, and tiltedness were excellent, as Figure 1 left plot shows it. Ring studies and identification capabilities could be tested as well. Radiator lengths studies were made experimentally with an aluminium plate to absorb the Cherenkov light made at the entrance of the particle. Photon detection was made by CsI coated MWPC with strip cathodes on the separation window. Tests have also been carried out with ThickGEM based photon detectors with Cherenkov light obtained from solid and liquid radiators as well.

At PS T10 energies (1-6 GeV/c) one can study how pions start to radiate the Cherenkov photons. Ring radius dependencies, photon detection and radiator length studies have been made. Using a secondary beam, which contains electrons and muons as well, the identification capabilities could be studied. A still noisy but impressive plot can be seen on Figure 1 right.

5. Triggering at high momenta

High-p_T particles are extremely rare therefore a good trigger could highly increase the recorded interesting data. The High PT Trigger Detector [6] (HPTD) will serve three functions:

1. Tracking before and behind the RICH module.
2. L1 triggering at high pT in PbPb and pp collisions.
3. L0 triggering at pp collisions.

HPTD consist of 5+5 layers of gaseous detectors around the Cherenkov part. Each layer should have good spatial resolution and low material budget.

Inside the ALICE magnet charged particles' tracks are bent according to their transverse momenta. Precise measurement of the tracklets allows us to define a set of certain tracklet patters that are generated by the high-p_T particles. Due to the high multiplicities in heavy ion collision and the low yield of interesting particles background suppression is extremely important, one has to filter out decays, secondary particles and specially combinatoric fake patterns. Detector readout, patter recognition, and L1 decision is made by FPGAs within 5 μs required by the ALICE L1 trigger system.

For L0 at pp collisions we use some of the same detectors as for L1. Here large superpads are made to decrease the number of channels, their digital one bit signals go to a purely hardware logic gate system to achieve the 800 ns response for decision.

HPTD does not need to measure the energy loss of the charged particles it only have to detect its tracklet. This simplifies the used electronics into a preamplifier and a discriminator which output is only one bit per channel making it really cost effective. Therefore the detector layers should have narrow pad response function to achieve low enough occupancy with the same number of channels. The Hungarian REGARD Group

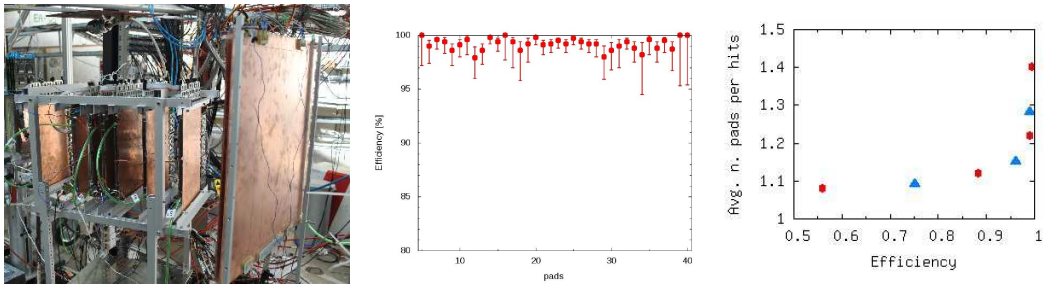

Figure 2. (Left) Seven 20x20 cm2 and one 50x50 cm2 CCC chambers at HPTD's beam test at CERN PS in 2010. (Middle) Uniformity of efficiency in a CCC at the PS tests. (Right) Even at high efficiency the CCC cluster size is reasonably small.

developed a newish multi wire chamber, the "Close Cathode Chamber" [3] with narrow pad response, low material budget and large mechanical tolerance. Several chambers are working for years now, and have proven their reliability in labor, cosmic and beam tests as well. Figure 2 left shows a picture of the beam test setup, the middle plot shows efficiency uniformity of a CCChamber. Figure 2 right shows that even at high efficiency the average cluster size is still moderate ($\sim$ 1.5 pads/hit).

We could test how the Cherenkov and the trigger parts can work together. This close to final setup can be easily compared to the AliROOT simulations. Material budget effects, MIP measurements and especially before+behind pattern appearance were studied.

Summary and Acknowledgement

The detailed jet studies at ALICE needs a proper PID detector in the high momentum region on the event-by-event level. VHMPID will be a gaseous ring imaging Cherenkov detector which can identify π, K, p in the 5-25 GeV/c region. However the project is on the R&D phase, several successfull beamtests have been done with the photon detection, the RICH, the triggering and the tracking parts as well.

This work has been partly supported by the Hungarian OTKA NK 77816 and the NKTH-OTKA CK 77719 and 77815 grants and the Janos Bolyai Research Scholarship of the H.A.S.

[1] K.Aamodt et al. - The ALICE experiment at the CERN LHC, JINST 3 (2008), S08002
[2] V.Peskov et al. - Further evaluation of a THGEM UV-photon detector for RICH - comparison with MWPC, JINST 5 (2010), P11004
[3] D.Varga et al. - Asymmetric Multi-wire Proportional Chamber With Reduced Requirements to Mechanical Precision, Nucl. Instrum. Meth. A D11 (2011) 00130 (accepted)
[4] A.Gallas et al. - Performance of the high momentum particle identification CsI-RICH for ALICE at CERN-LHC, Nucl. Instrum. Meth. A 553 (2005) p 345-350
[5] A.Agocs et al. - Very high momentum particle identification in ALICE at the LHC, Nucl. Instrum. Meth. A 617 (2010) p 424-429.
[6] L.Boldizsar et al. - High-p(T) trigger detector development for the ALICE experiment at CERN, Nucl. Phys. B (Proc.Suppl.) 197 (2009) p 296-301.

HPTD: The High-p$_T$ Trigger Detector for ALICE VHMPID, feasibility and Monte Carlo simulations

L. Boldizsár on behalf of the VHMPID Collaboration

29-33 Konkoly-Thege M. Str., Budapest, Hungary

E-mail: leslie@rmki.kfki.hu

Abstract. ALICE is considering to build a Very High Momentum Particle Identification Detector (VHMPID) in order to extend the momentum range of particle identification to 5–25 GeV/c on track-by-track level. In this short contribution I discuss the design and performance of the High-p_T Trigger Detector (HPTD) which is suppose to generates the level-1 trigger for VHMPID in Pb-Pb collisions within the desired 5μs. The development of the HPTD detector, performance in p+p and heavy-ion collisions will be discussed.

1. ALICE detector upgrade: VHMPID (The Very High Momentum Particle Identification Detector)

ALICE detectors were designed more than a decade ago to discover the properties of QCD matter at high temperatures in the bulk/soft regime. However, after the start of operation of RHIC at BNL in 2000, results from high energy nucleus-nucleus collisions have shown the importance of high momentum particles as hard probes and the need for particle identification in a very large momentum range. The ALICE detector has a unique capability to identify a wide variety of particles up to 5 GeV/c, however its momentum coverage should be extended to meet new physics challenges at LHC. The proposed the Very High Momentum Particle Identification Detector (VHMPID) detector is able to identify charged hadrons on a track-by-track basis in the 5 GeV/c $< p_T <$ 25 GeV/c transverse momentum range, which makes ALICE unique in PID-sense within all LHC experiments. The designed RICH-based detectors will operate with CF_4 and/or C_4F_8O radiator gases, and will cover 12% of the ALICE barrel. [2, 3, 4].

2. Dedicated High-p_T Trigger Detector (HPTD) for VHMPID

Detection of high-momentum particles requires fast triggering which in case of ALICE can be at level-0 (for p-p within 1.3μs) or at level-1 (for Pb-Pb within 6.5μs). For the VHMPID two main strategies are planned to adopt: a trigger, based on the Transition Radiation Detector (TRD); self-triggering by trigger layers implemented directly into VHMPID. This latter option, the *High-p_T Trigger Detector* (HPTD) is

presented here [5]. Moreover this trigger-detector will give a reasonably precise MIP position information for the Cherenkov ring reconstruction.

Our triggering method is based on the fast detection and analysis of particle trajectories projected to the transverse plane in the magnetic field of ALICE L3 solenoid magnet. Within the magnet the particle tracks are circles with a radius proportional to the momentum of the particles ($p_T[GeV/c] = 0.15\ R\ [m]$), but in case of a high-p_T particle track is close to a straight line in the 0.5 T magnetic field of the ALICE.

Measuring the position of the charged particle by the layers of the HPTD one can determine the curling radius and we have the opportunity to select particles under or beyond a threshold momentum (See more on Figure 1 *left*).

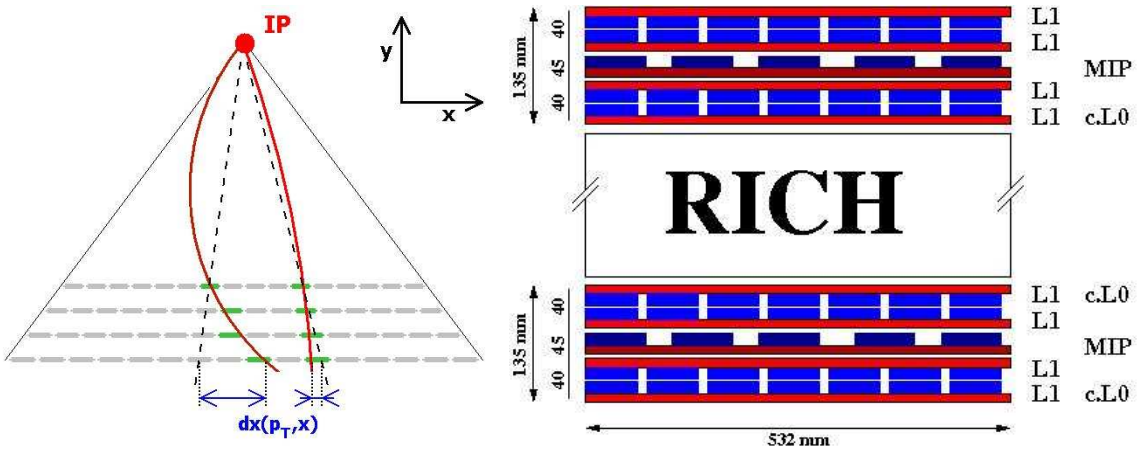

Figure 1. *Left panel*: Curling trajectory of a charged particle inside the ALICE magnet. *Right panel*: Schematic view of the VHMPID detector, as a superposition of the 5+5 layer HPTD and a RICH gas module.

3. HTPD detector layout

The High-p_T Trigger Detector is made of separated layers of "Close Cathode Chambers" [6]. CCCs are multiwire gaseous chambers are similar to 'standard' MWPCs however they have narrow pad response functions. The chambers have segmented pad cathodes especially designed for optimum performance.

The HPTD was optimized with 5 layers above and 5 layers under each VHMPID RICH module. L1 triggering for Pb-Pb collisions needs 4+4 layers with good spatial resolution (4 mm) at ϕ and uses less precise resolution (10 cm) at η just to avoid the occupancy. For technical and budget-saving reasons the HPTD is flat so the width of the pads is slightly increasing with tangential distance from the interaction point. Two layers from the former 4-4 will be used as L0 trigger layers too. In this case beside the pads 'superpads' (2 cm $\times$ 50 cm) are made by grouping together wires by five within the module. Parallel the triggering the MIP detection can be performed with this detector setup. This needs good resolution both in the ϕ and η directions. Therefore the former

setup increased with 1+1 layer with the similar chambers and structure but rotated with 90 degrees. (See MIP layers on the right panel of Figure 1.)

4. HPTD as L1 trigger for Pb-Pb collisions

To get the L1 trigger decision in Pb-Pb collisions needs to exploit the full pad-segmentation of the HPTD detector. When charged particle prolongs on its path in the magnetic field, it leaves pads-prints on each HPTD layers and produces a set of hits as pad-patterns. The obtained pattern-shape correlates with the transverse momentum of the particle. The readout electronics of a pad provides one bit information on each of the pads using a simply and fast electronics: an amplifier and a comparator. Using an FPGA-based pattern recognition algorithm, one can determine if the transverse momentum of the particle is above a certain threshold.

The proposed HPTD detector setup have been studied by Monte Carlo simulations in the AliROOT [7] framework of the ALICE experiment. We optimized the HPTD layout, segmentation and the pattern recognition algorithm. The number of detector layers were studied for triggering for the HMPID best performance. We tested layouts between 6 and 10 number of layers with various distances between the layers (3, 4, and 5 cm). Pad width test were also performed using 3-6 mm and 5-15 cm pads.

Trigger efficiencies as the function of the particle momentum, the trigger rate and purity were simulated by HIJING-based Monte Carlo simulation in Pb-Pb collisions at 5.5 ATeV, using a 10000 event sample [8]. As the Monte Carlo simulations showed the trigger efficiency increase rapidly with the particle momentum at the threshold, it is saturated above 95% and the suppression of low momentum particles which could result large number of fake triggers is very strong. We found the trigger threshold is well tunable by the pad width, and also depends on the other layout parameters.

Figures 2 presents the summary of our results on trigger efficiencies and purities of a realistic event samples as described above. The tested 5 different layer sets with 3 different layer distance-case are shown. Based on these results we found: to larger the layers's distance the efficiency is getting higher. We obtained also to apply more layers lowers the efficiency. On the other hand the purity is higher if we use more layers (i.e. more constraints), and the purity is lower if the layer distance is larger†.

Conclusion of our study: to find the optimal the analysis of setup efficiency and purity could help. Moreover, these parameter also effected by the necessary minimal thickness of the HPTD to ensure enough place to the Cherenkov modul.

The conclusion of the simulation studies we showed that 4+4 layer of HPTD could serve good trigger signal with high efficiency and purity (80-90%) and the simulation studies represent the optimal layout of the proposed HPTD detector module, consists 4+4 L1-layers with 4 cm layer distance (13+13 cm thickness), with pads 4 mm $\times$10 cm.

† This was not true for the cases of 3+3 and 3+4 with 3 cm distance due to the weak constraints.

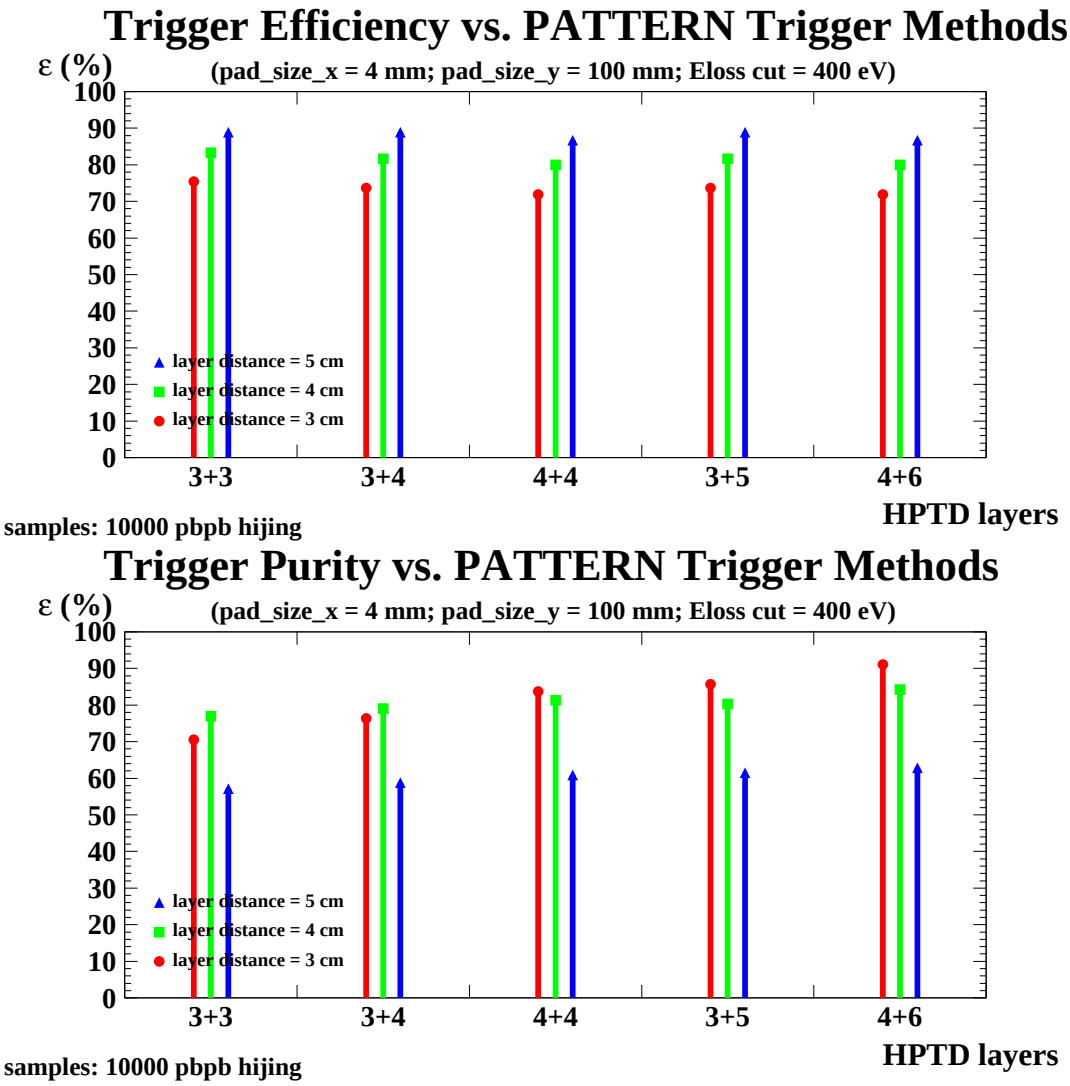

Figure 2. The summary of the trigger efficiencies (*Upper panel*) and purity (*Lower panel*) in realistic event sample based on a 10^4 event sample generated by HIJING at 5.5 ATeV.

5. Acknowledgement

This work is supported by the Hungarian OTKA/NKTH grants NK77816, CK77719 and NK77815 grants, and the János Bólyai Research Scholarship of the HAS.

[1] K. Aamodt et al.: JINST 3 (2008), S08002
[2] The VHMPID Letter of Intent *in preparation* (2011).
[3] G. Volpe et al.: Nucl. Phys. B (Proc. Suppl.) 197 (2009) p 288-291.
[4] A. Agócs et al.: Nucl. Instrum. Meth. A 617 (2010) p 424-429.
[5] L. Boldizsár et al.: Nucl. Phys. B (Proc. Suppl.) 197 (2009) p 296-301.
[6] D. Varga et al.: Nucl. Instrum. Meth. A D11 (2011) 00130 (accepted)
[7] ALIROOT: the ALICE Off-line framework for simulation `http://aliceinfo.cern.ch/Offline/`
[8] Xin-Nian Wang and Miklos Gyulassy, Phys.Rev.D 44, 3501 (1991).

Charged pion identification at high p_{T} in ALICE using TPC $\mathrm{d}E/\mathrm{d}x$

L. Bryngemark (for the ALICE Collaboration)

Department of Physics, Division of Experimental High Energy Physics, Lund University, Box 118, S-221 00 Lund, Sweden

E-mail: Lene.Bryngemark@hep.lu.se

Abstract. The ALICE TPC provides excellent charged particle tracking for the study of pp and Pb-Pb collisions at LHC. The TPC also allows particle identification via the measurement of the specific ionisation $\mathrm{d}E/\mathrm{d}x$. At high p_{T} (p_{T} ¿ 3 GeV/c) this is accomplished in the region of the relativistic rise of the energy loss. From the energy loss distributions the yields of charged pions, kaons, and protons can be determined in bins of p_{T} and p_{T}-spectra are constructed. Here we present the performance of such an analysis in pp collisions at $\sqrt{s}$ = 7 TeV for charged pions up to 10 GeV/c.

1. Introduction

Flow measurements and particle spectra from ultrarelativistic heavy ion collisions at RHIC and LHC have so far given many interesting results in the intermediate and high transverse momentum region $p_{\mathrm{T}} > 2$ GeV/c. In particular, measurements of elliptic flow [1] and high-p_{T} suppression for identified particles [2] at RHIC have given insight in hadronisation mechanisms and the evolution of the quark gluon plasma.

This report presents a method for identifying charged particles at high p_{T} with the TPC in ALICE. Performance results are shown for $3 \leq p_{\mathrm{T}} \leq 10$ GeV/c.

2. The ALICE TPC

The ALICE Time Projection Chamber (TPC) is a gaseous tracking detector with full azimuthal acceptance, covering a pseudorapidity range of $|\eta| < 0.9$ for full track length within the TPC volume [3]. It is a large (90 m^3 gas volume) cylindrical barrel, with read-out at the two end caps. The drift field of 400 V/cm is generated by a central HV cathode. The end caps are segmented into 18 trapezoidal sectors each with Inner and Outer Read-Out Chambers (IROCs and OROCs), equipped with MultiWire Proportional Chambers (MWPCs). Here the signals are read out on 159 pad rows in the radial direction, for a total of about 560 000 pads. Such high read-out granularity is essential for tracking in the high-multiplicity environment of central heavy ion collisions, which is what ALICE is designed for. The front end electronics have on-board digital

filters, allowing baseline restoration, cancellation of signal tails due to ion drift and data reduction via "zero-suppression".

The TPC is used for tracking and measuring charged particle energy loss ($\mathrm{d}E/\mathrm{d}x$) and momentum p, simultaneously. The latter two can be combined and used for particle identification (PID), as energy loss for a given charge follows a single curve in $\beta\gamma = \frac{p}{m}$, m being the particle mass. This curve can be well described by a Bethe-Bloch parametrisation, and the energy loss of each particle species will follow its own curve in p. Figure 1 illustrates energy loss vs p as measured by the ALICE TPC. Bethe-Bloch parametrisation curves for the different particle species are also drawn in the figure. The charge deposited on read-out pads along a track (charge clusters) follows a Landau-like distribution, with a tail of few instances of high-energy transfer. For this reason the energy loss is calculated as a truncated mean (the lowest 60%) of the distribution of track cluster charge. This is referred to as TPC signal in Fig. 1, or simply $\mathrm{d}E/\mathrm{d}x$ in the following.

The ALICE TPC $\mathrm{d}E/\mathrm{d}x$ resolution ($\frac{\sigma_{\mathrm{d}E/\mathrm{d}x}}{\mathrm{d}E/\mathrm{d}x}$) is better than 5% for full length tracks, and the p_{T} resolution $\Delta p_{\mathrm{T}}/p_{\mathrm{T}}$ as of December 2009 was $\sim 7\%$ at 10 GeV/c.

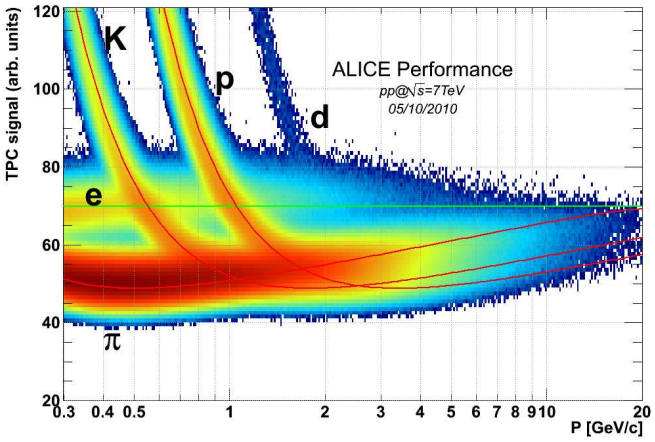

Figure 1. (Colour online) TPC signal as function of momentum in pp collisions at 7 TeV. Pions can be clearly separated at their minimum energy loss around $p = 0.5$ GeV/c.

As is seen in this figure, in the low momentum region of a $\mathrm{d}E/\mathrm{d}x$ vs p histogram, the particle species line up in bands according to their mass and charge. As $\mathrm{d}E/\mathrm{d}x$ and p are both determined from the TPC there is no possibility for mismatches.

On the relativistic rise, $p > 3$ GeV/c, the energy loss curves follow a logarithmically rising behaviour. Here the particle species curves are not separated enough for a unique particle identification on a track-by-track basis. Instead a statistical particle identification for the integrated yields is employed. This method will be described in the following.

3. Method

Event and track selection is carried out following the ALICE unidentified charged hadron p_{T} spectra analysis [4]. An additional cut is applied to reject tracks crossing areas between the TPC read-out sectors which are not instrumented, since these tracks have worse $\mathrm{d}E/\mathrm{d}x$ resolution, due to the smaller number of ionisation measurements. This analysis focuses on high-momentum tracks, which are only bent a little by the magnetic field. With increasing rigidity, only tracks with an original angle pointing to the area between two sectors will be significantly affected.

The method is based on the energy loss, which is parametrised in p. Final results are obtained from fits in p_{T}. The main steps of the method are as follows:

(i) A 2D histogram is filled with $\mathrm{d}E/\mathrm{d}x$ vs p, measured for each track in the TPC.

(ii) This 2D histogram is fitted with a sum of three Gaussians (π, K, p) for each p bin, where the mean of each Gaussian follows a common parametrisation of the Bethe-Bloch curve. The $\langle \mathrm{d}E/\mathrm{d}x \rangle$ vs $\beta\gamma$ dependence is thus extracted in one simultaneous fit. The plateau is extracted using a clean electron sample in the low-p_{T} region.

(iii) For each p_{T} interval, a 1D histogram is filled with $\Delta_\pi \equiv \mathrm{d}E/\mathrm{d}x - \langle \mathrm{d}E/\mathrm{d}x \rangle_\pi$ (for each track).

(iv) The Δ_π histograms are fitted with a sum of four Gaussians: one for each of the particle species p, K, π and e. The yields are the only free parameters; the others (8 out of 12) are fixed in the following way:

- The Bethe-Bloch fit extracted in (ii) is used to fix the means.
- The widths of the Gaussians are fixed to values determined using a clean sample of minimum ionising pions, from the observed relation that the relative width is found to be constant (the width scales with $\langle \mathrm{d}E/\mathrm{d}x \rangle$).

(v) From the fits, particle yields as a function of transverse momentum are determined.

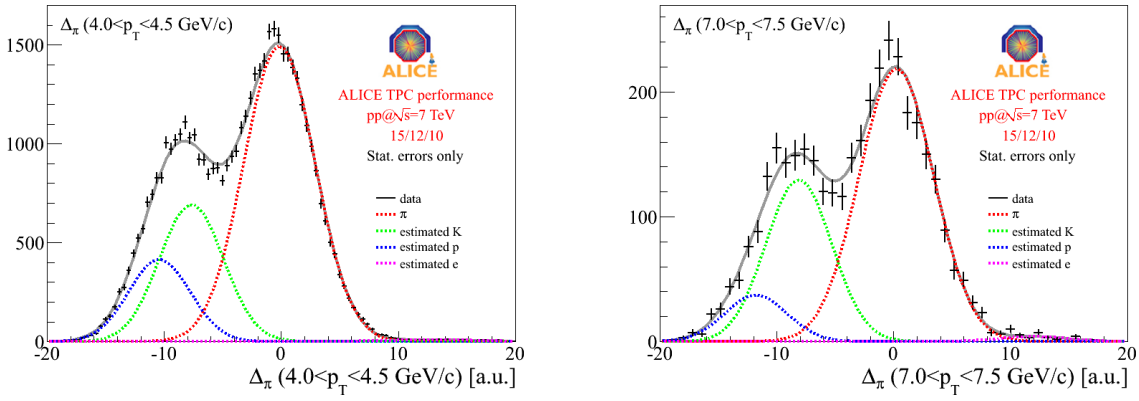

Figure 2. (Colour online) Examples of the Δ_π distribution in two p_{T} bins, fitted with a sum (solid grey line) of four Gaussians (for p, K, π and e, dotted coloured lines). The electron contribution is negligibly small.

Examples of fits are shown for two p_{T} bins in Fig. 2. Positive and negative particles are treated both together, to increase statistics, and separately, to enable the study of antiparticle-to-particle ratios (expected to be close to 1 at mid-rapidity at LHC).

4. Performance of the $\mathrm{d}E/\mathrm{d}x$ analysis

As was seen in the two example fits above, the fit to the π peak is completely determined from the right-hand side, making these fit results very stable (since it is essentially a single Gaussian fit). Protons and kaons have smaller mass ratio than kaons and pions, giving smaller separation. The quality of the fit result for these species is thus harder to verify. For this reason, the remainder of this report focuses on the pions, even though identification of all three species is pursued.

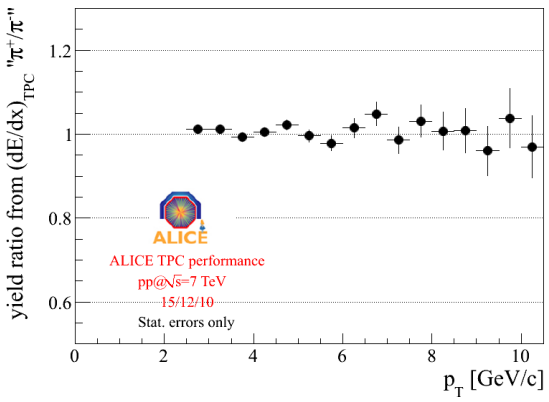

(a) π^+ to π^- raw yield ratio, as a function of p_{T}.

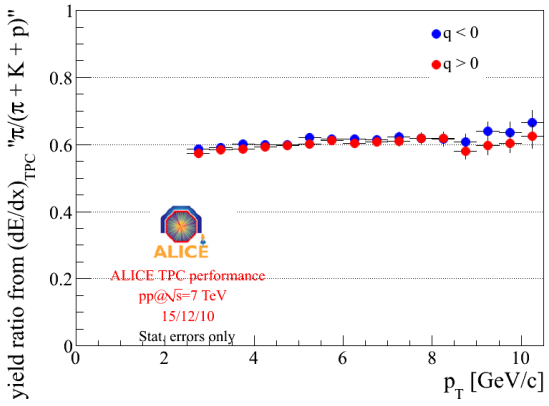

(b) (Colour online) Estimated π^+ and π^- fraction out of the yield of all charged hadrons, as a function of p_{T}.

Figure 3. Uncorrected results as obtained from fits to the Δ_π distributions.

Apart from visually inspecting the fit results, a number of crosschecks are done to assess the performance of the method. This is illustrated in Fig. 3. One consistency check is to take the ratio of the estimated positive and negative pion yields. The raw yield ratio shown in Fig. 3(a) is consistent with the expected value of 1. Figure 3(b) shows the resulting raw π yield fraction out of the total hadron yield, as a function of p_{T}. Here it is seen that the obtained yield fractions of positive and negative pions, respectively, agree within statistical errors over the full p_{T} range. The raw charged pion yield as a function of p_{T} obtained with this method is shown in Fig. 4, without normalisation or other corrections.

5. Conclusion

A method using the TPC $\mathrm{d}E/\mathrm{d}x$ for identification and yield extraction of charged particles at high p_{T} has been presented. The very good performance of the ALICE TPC,

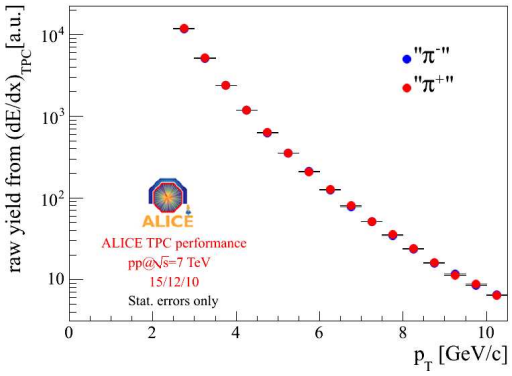

Figure 4. (Colour online) Uncorrected charged pion p_{T} spectrum.

and the stable performance results of the method presented here, are very promising for extracting in particular the charged pion yields.

References

[1] S. S. Adler *et al* (PHENIX Collaboration). *Phys. Rev. Lett.*, **91**:182301, 2003. arXiv:nucl-ex/0305013v2.

[2] K. Adcox *et al* (PHENIX Collaboration). *Phys. Rev. Lett.*, **88**:022301, 2002. arXiv:nucl-ex/0109003v2.

[3] J. Alme *et al*. *Nucl. Instrum. Meth. A*, **622**:316–367, 2010. arXiv:1001.1950.

[4] K. Aamodt *et al* (ALICE Collaboration). *Phys. Lett. B*, **693**:53–68, 2010. arXiv:1007.0719.